Homogénéisation de plaques périodiques épaisses, application aux panneaux sandwichs à âme pliable en chevrons

Arthur Lebée

UNIVERSITÉ PARIS-EST

UNIVERSITÉ PARIS-EST
ECOLE DOCTORALE SCIENCE INGÉNIÉRIE ET ENVIRONNEMENT

THÈSE

présentée pour obtenir le titre de
Docteur en Sciences d'Université Paris-Est
Discipline : Mécanique – Spécialité : Mécanique des structures
par

Arthur Lebée

HOMOGÉNÉISATION DE PLAQUES PÉRIODIQUES ÉPAISSES, APPLICATION AUX PANNEAUX SANDWICHS À ÂME PLIABLE EN CHEVRONS

THICK PERIODIC PLATES HOMOGENIZATION, APPLICATION TO SANDWICH PANELS INCLUDING CHEVRON FOLDED CORE

Thèse soutenue le 15 octobre 2010 devant le jury composé de :

M.	PATRICE CARTRAUD	*Rapporteur*
M.	PAOLO VANNUCCI	*Rapporteur*
M.	GUY BONNET	*Examinateur*
M.	YVES BRECHET	*Président*
Mme.	BERNADETTE MIARA	*Examinatrice*
M.	KARAM SAB	*Directeur de thèse*

Remerciements

C’est de la différence que naissent les projets les plus riches. Karam, au début nous ne parlions pas la même langue. Peut être est-ce encore le cas aujourd’hui. Pourtant, je suis certain que c’est précisément parce que nous avons partagé nos façons de penser et nos cultures que ces années de doctorat ont été si enrichissantes. Pour tes conseils tant scientifiques qu’humains et pour ces années d’attention je tiens à te remercier. J’espère que nous pourrons continuer à faire avancer la “Belle Science”...

Je tiens à remercier Patrice Cartraud et Paolo Vannucci pour avoir été rapporteurs de ma thèse. Leurs conseils profonds et détaillés m’ont beaucoup apporté. De même, je tiens à remercier les membres de mon jury de thèse pour leur écoute attentive et critique. Merci Yves Bréchet de l’avoir présidé. Merci Guy Bonnet et Bernadette Miara d’y avoir participé.

Par ailleurs, je pense que je n’aurais jamais démarré une thèse sans les conseils et l’enthousiasme d’Alain Ehrlacher. Alain, je t’en remercie.

La première manifestation d’un travail de thèse est le mémoire. C’est bien peu en comparaison de tous les moments que j’ai partagés avec les équipes structures hétérogènes et dynamique du laboratoire. Je tiens à vous remercier pour l’entraide et la bonne humeur qui règne, sans lesquels il ne serait pas possible de surmonter les moments vraiment difficiles. Merci à tous. Merci Arnaud, Corinne, Cyril, Duc, Florian, Johanna, Julien, Kien, Laurent, Lina, Malika, Mathieu, Mohammad, Natacha, Philippe, Pooneh, Ramzi, Ronan, Sebastien, Si Hai, Sophie, Sylvain, Thai, Tiffany, Van Anh, Virginie, Wafa et naturellement Marie qui recolle les cœurs...

Parallèlement à ce travail de doctorat il y a eu un projet de développement d’une machine fabriquant le module à chevrons. Ce projet a été l’occasion de rencontres très enrichissantes. Je tiens à remercier tous ceux qui y ont contribué de près ou de loin. Ils se reconnaîtront.

Enfin merci à ma petite femme chérie qui a supporté et supporte encore les joies et déceptions quotidiennes des tenseurs d’ordre six...

à Soraya et Gabriel

Table des matières

Table des figures

Liste des tableaux

Table des Encadrés

Introduction Générale

Ce doctorat a été préparé au sein du Laboratoire Navier et financé par le Ministère de l'Écologie, de l'Énergie, du Développement Durable et de la Mer.

Le point de départ de ce travail de doctorat porte sur l'étude d'un nouveau type d'âme de panneau sandwich fabriqué à partir de techniques de pliage et nommé module à chevrons. Ce type d'âme n'est pas encore répandu dans les panneaux sandwichs et son intérêt économique n'est pas encore parfaitement démontré. Comme on le verra par la suite, le rôle de l'âme dans un panneau sandwich est d'assurer la résistance à l'effort tranchant. Il se trouve que l'étude du comportement d'une plaque à l'effort tranchant pose encore de nombreux problèmes aujourd'hui en raison d'un obstacle d'ordre théorique. Cette étude d'une âme de panneau sandwich est donc l'occasion de revoir en profondeur cette question.

On propose tout d'abord au Chapitre 1 une analyse de la difficulté à déterminer le comportement à l'effort tranchant d'une plaque ainsi qu'une rapide revue bibliographique. Au Chapitre 2, une présentation du module à chevrons ainsi que des contraintes imposées par le marché des panneaux sandwichs sur la conception d'un nouveau type d'âme est effectuée. Il faudra en retenir que la maîtrise du comportement structurel d'un panneau sandwich est un critère déterminant dans cette technologie. Pourtant, une rapide revue bibliographique permet de constater qu'il existe très peu de méthodes permettant de connaître précisement leur comportement.

Au Chapitre 3, la méthode de Kelsey et al. (1958) qui permet de déterminer des bornes pour la raideur à l'effort tranchant des panneaux sandwichs sera appliquée au cas du module à chevrons. Le principal résultat est que ces bornes sont insuffisantes pour estimer précisément la raideur à l'effort tranchant dans le cas d'un panneau sandwich incluant le module à chevrons. En effet la méthode de Kelsey et al. (1958) prend en compte uniquement l'âme du panneau pour calculer cette raideur. Elle ne tient pas compte de l'interaction possible entre l'âme et les peaux.

Cette limitation nous amènera à reconsidérer en profondeur les méthodes existantes pour déterminer le comportement à l'effort tranchant des plaques. En effet, beaucoup de difficultés sont aussi rencontrées dans le cas des plaques stratifiées. On revisite alors au Chapitre 4 les travaux de Reiss-

ner (1945) pour dériver la distribution des contraintes de cisaillement transverse dans le cas d'une plaque homogène en les appliquant au cas d'une plaque stratifiée. Il en résulte la construction d'un nouveau modèle de plaque, le modèle de gradient du moment, qui ne peut être réduit au modèle bien connu de Reissner-Mindlin dans le cas général. Une première validation du modèle est obtenue en le comparant à la solution exacte proposée par Pagano (1969) dans le cas de la flexion cylindrique de plaques stratifiées, au Chapitre 5. On montrera en effet que le modèle de gradient du moment converge avec l'élancement vers la solution exacte lorsque la plaque vérifie la symétrie mirroir.

Le retour vers les panneaux sandwichs est effectué au Chapitre 6 en présentant l'extension de la théorie de gradient du moment au cas des plaques périodiques à l'aide d'un principe d'équivalence énergétique entre champs microscopiques et champs macroscopiques. Dans le cas particulier des panneaux sandwichs, cette nouvelle théorie associée à l'hypothèse de contraste entre la raideur des peaux et la raideur effective de l'âme nous permettra d'élaborer un schéma d'homogénéisation simplifié ainsi que de démontrer les bornes de Kelsey et al. (1958).

L'application du schéma d'homogénéisation associé à la théorie de gradient du moment à un panneau sandwich incluant le module à chevrons sera effectuée au Chapitre 7. Cette mise en œuvre permet tout d'abord de valider une nouvelle fois la théorie de gradient du moment dans le cas périodique mais aussi de mettre en évidence un phénomène de distorsion des peaux du panneau sandwich qui explique l'écart observé entre les bornes de Kelsey et al. (1958).

Enfin, pour illustrer l'intérêt des modèles d'ordre supérieur dont fait partie le modèle de gradient du moment, un modèle de Cosserat multi-particulaire sera présenté au Chapitre 8. Même si ces travaux ne font pas partie de la problématique principale de ce travail de doctorat, ils sont l'occasion de démontrer l'intérêt des modèles de milieux continus généralisés dans la capture des effets de bords.

CHAPITRE

1

Enjeux scientifiques soulevés par les plaques épaisses

Bien qu'extrêmement répandus dans les sciences de l'ingénieur, les modèles de plaque soulèvent encore aujourd'hui des difficultés scientifiques. Dans ce chapitre introductif, on présente tout d'abord en Section 1.1 le modèle naturel de plaque qui prend en compte les efforts membranaires, les moments de flexion et l'effort tranchant. Bien que ce modèle présente un formalisme intuitif pour le fonctionnement des plaques, il ne donne pas la loi de comportement associée. En supposant de plus que la plaque est mince, le modèle naturel peut être simplifié et devient le modèle de Love-Kirchhoff (Section 1.2). Le modèle de Love-Kirchhoff possède une assise théorique forte et permet le calcul d'une loi de comportement mais ne prend pas en compte les effets de l'effort tranchant dans la plaque. De nombreux travaux ont tenté de prendre en compte ces effets dans le modèle naturel mais ils font face à une difficulté fondamentale présentée en Section 1.3.

1.1 Le modèle naturel de plaque

D'une manière générale, une plaque est un objet présentant deux grandes dimensions dans son plan : $L_1 \simeq L_2$, les portées ; et une petite dimension : h, l'épaisseur. Si on considère la plaque comme un objet tridimensionnel on peut y calculer des déformations ε_{ij}^{3D} et des contraintes σ_{ij}^{3D} exactes et localisées. Parce qu'un modèle tridimensionnel est coûteux à calculer et que la plaque est élancée (L/h grand), on souhaite assimiler celle-ci à un plan déformable. Une façon naturelle de le faire consiste à intégrer dans l'épaisseur les contraintes. Ces calculs sont détaillés dans l'Annexe A.1. Ils mènent directement aux efforts réduits $(\mathbf{N}, \mathbf{M}, \boldsymbol{Q})$. $\mathsf{N}_{\alpha\beta}$ est le tenseur 2D des efforts membranaires, $\mathsf{M}_{\alpha\beta}$ le tenseur 2D des moments de flexion et Q_α l'effort tranchant. De même, intégrer l'équation d'équilibre tridimensionnelle $\sigma_{ij,j}^{3D} + f_i = 0$ dans l'épaisseur mène directement aux équations d'équilibre

de plaque [1] :

$$\begin{cases} \mathsf{N}_{\alpha\beta,\beta} + p_\alpha = 0 & \text{(1.1a)} \\ Q_{\alpha,\alpha} + p_3 = 0 & \text{(1.1b)} \\ \mathsf{M}_{\alpha\beta,\beta} - Q_\alpha + \mu_\alpha = 0 & \text{(1.1c)} \end{cases}$$

où $\boldsymbol{p} = (p_\alpha)$ sont les chargements membranaires, p_3 est le chargement transverse et $\boldsymbol{\mu} = (\mu_\alpha)$ sont des couples par unité de surface. Ces équations d'équilibre sont très connues et ont été démontrées de nombreuses manières différentes. On peut se référer à Boussinesq (1871), Reissner (1945) et Mindlin (1951) pour ne citer qu'eux.

En dualisant les équations d'équilibre (formulation faible), on trouve que les efforts de plaque $(\mathbf{N}, \mathbf{M}, \boldsymbol{Q})$ travaillent avec les déformations généralisées qui leurs sont respectivement associées : $\mathbf{e}, \boldsymbol{\chi}, \boldsymbol{\gamma}$ où $\mathsf{e}_{\alpha\beta}$ est la déformation membranaire, $\chi_{\alpha\beta}$ est la courbure et γ_α est la déformation de cisaillement. Ces déformations ont été représentées en Figure 1.1. Elles dérivent de champs de déplacement : U_i et φ_α de la façon suivante :

$$\begin{cases} \mathsf{e}_{\alpha\beta} = \dfrac{1}{2}\left(U_{\alpha,\beta} + U_{\beta,\alpha}\right) & \text{(1.2a)} \\ \chi_{\alpha\beta} = \dfrac{1}{2}\left(\varphi_{\alpha,\beta} + \varphi_{\beta,\alpha}\right) & \text{(1.2b)} \\ \gamma_\alpha = \varphi_\alpha + U_{3,\alpha} & \text{(1.2c)} \end{cases}$$

U_i est le déplacement d'un point du plan moyen de la plaque et φ_α est un vecteur associé à la rotation de ce point par rapport aux axes contenus dans le plan de la plaque.

Pour obtenir un modèle de plaque complet, outre les habituelles conditions aux limites, il est crucial de donner la loi de comportement qui lie les efforts de plaque aux déformations. Dans le cadre de l'élasticité linéaire, cela revient à définir une fonction quadratique des déformations $w\left(\mathbf{e}, \boldsymbol{\chi}, \boldsymbol{\gamma}\right)$ (on parle de densité d'énergie de déformation) ou une fonction quadratique des efforts de plaque $w^*\left(\mathbf{N}, \mathbf{M}, \boldsymbol{Q}\right)$ (densité d'énergie de contraintes). La loi de comportement s'écrit alors formellement :

$$\left(\mathbf{N}, \mathbf{M}, \boldsymbol{Q}\right) = \frac{\partial w\left(\mathbf{e}, \boldsymbol{\chi}, \boldsymbol{\gamma}\right)}{\partial\left(\mathbf{e}, \boldsymbol{\chi}, \boldsymbol{\gamma}\right)} \quad \text{ou} \quad \left(\mathbf{e}, \boldsymbol{\chi}, \boldsymbol{\gamma}\right) = \frac{\partial w^*\left(\mathbf{N}, \mathbf{M}, \boldsymbol{Q}\right)}{\partial\left(\mathbf{N}, \mathbf{M}, \boldsymbol{Q}\right)}$$

La façon la plus naturelle de construire la loi de comportement consiste à trouver le champ de localisation associé aux variables généralisées. On appelle la localisation, une approximation des champs tridimensionnels exacts linéairement dépendante des variables de plaque, $(\mathbf{e}, \boldsymbol{\chi}, \boldsymbol{\gamma})$ pour les déformations ou $(\mathbf{N}, \mathbf{M}, \boldsymbol{Q})$ pour les contraintes (il existe aussi des formulations mixtes). Par exemple pour les plaques stratifiées on écrira les déformations : $\varepsilon_{ij}^{\text{loc}} = f_{ij}\left(\mathbf{e}, \boldsymbol{\chi}, \boldsymbol{\gamma}\right)$, où f est une application

1. Dans tout ce qui suit, les indices grecs varient de 1 à 2 et les indices latins de 1 à 3 et la convention d'Einstein sur les sommations est respectée (sauf spécification).

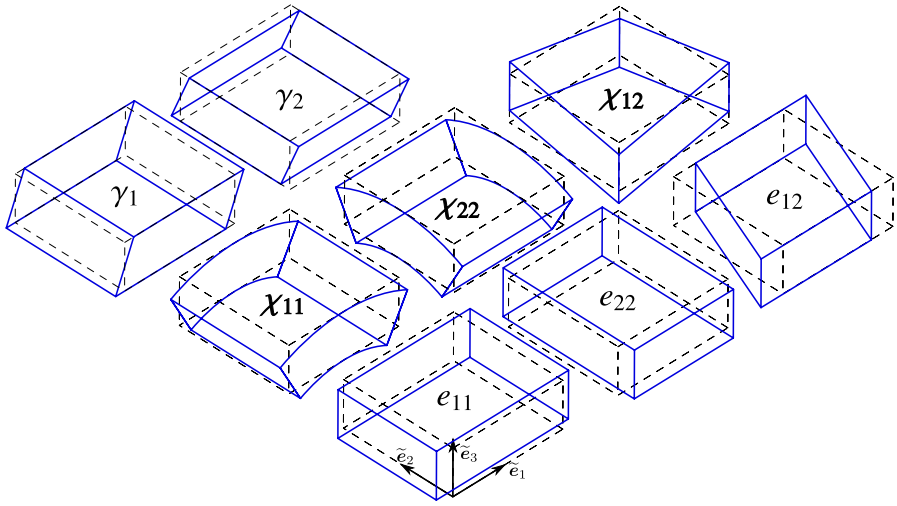

Figure 1.1 – Les déformations volumiques associées aux déformations généralisées (le gauchissement n'est pas représenté pour $\boldsymbol{\gamma}$)

linéaire de $(\mathbf{e}, \boldsymbol{\chi}, \boldsymbol{\gamma})$. Une fois cette approximation construite, la densité d'énergie de déformation s'écrit directement : $w(\mathbf{e}, \boldsymbol{\chi}, \boldsymbol{\gamma}) = \frac{1}{2}\int_{-\frac{h}{2}}^{\frac{h}{2}} \varepsilon_{ij}^{\text{loc}} \mathcal{C}(x_3)_{ijkl} \varepsilon_{kl}^{\text{loc}} dx_3$ où $\mathcal{C}_{ijkl}$ est le tenseur des raideurs élastiques en trois dimensions. Il existe une grande liberté de choix de localisation des champs (pourvu qu'ils soient admissibles) et c'est là qu'intervient la géométrie réelle de la plaque.

Lorsque toutes les variables sont découplées, la densité d'énergie de déformation s'écrit :

$$w(\mathbf{e}, \boldsymbol{\chi}, \boldsymbol{\gamma}) = \frac{1}{2}\left(\mathbf{e} : \boldsymbol{\mathcal{A}} : \mathbf{e} + \boldsymbol{\chi} : \boldsymbol{\mathcal{D}} : \boldsymbol{\chi} + \boldsymbol{\gamma} \cdot \mathbf{F} \cdot \boldsymbol{\gamma}\right)$$

où $\boldsymbol{\mathcal{A}}$ et $\boldsymbol{\mathcal{D}}$ sont des tenseurs d'ordre quatre en dimension deux et $\mathbf{F}$ un tenseur d'ordre deux en dimension deux. $\boldsymbol{\mathcal{A}}$ est la raideur membranaire (*membrane stiffness*), $\boldsymbol{\mathcal{D}}$ la raideur en flexion (*flexural stiffness*) et $\mathbf{F}$ la raideur d'effort tranchant (*shear forces stiffness*).

Le formalisme présenté ne permet pas de déterminer ces trois raideurs. Pour déterminer les raideurs $\boldsymbol{\mathcal{A}}$ et $\boldsymbol{\mathcal{D}}$ il existe des méthodes bien fondées et présentées dans la section qui suit. En ce qui concerne la raideur à l'effort tranchant, il existe encore de nombreuses difficultés présentées en Section 1.3.

1.2 Les plaques minces

On parle d'une plaque mince, lorsque la flèche U_3 générée par les déformations de cisaillement γ_α reste négligeable devant la flèche générée par la courbure de la plaque $\chi_{\alpha\beta}$. Dans le cas d'une plaque homogène isotrope, la part de cisaillement dans la flèche est directement reliée à l'élancement L/h. Plus précisément, la flèche de cisaillement rapportée à la flèche de flexion est proportionnelle

à $\frac{Eh^2}{GL^2}$ où E est le module d'Young et G le module de cisaillement du matériau. Ainsi la flèche de cisaillement est inversement proportionnelle au carré de l'élancement, ce qui en fait dans le cas des plaques homogènes isotropes un phénomène vraiment négligeable et explique la définition de plaque mince. D'une manière plus générale, on obtient une théorie de plaque mince en faisant directement l'hypothèse de Love-Kirchhoff dans le modèle naturel : $\gamma_\alpha = 0$. Ce type de modèle sera nommé par la suite plaque de Love-Kirchhoff.

De nombreux travaux ont été effectués dans ce cadre d'hypothèse et ont été vérifiés expérimentalement. Leur point de départ sont les travaux de Kirchhoff puis Love (1888) dans le cas d'une plaque homogène. Ils ont été étendus aux plaques stratifiées par Reissner and Stavsky (1961), Whitney and Leissa (1969) et Whitney (1969a) (voir l'Encadré 1.1 sur les différents types de plaque). Une justification rigoureuse a été proposée par Ciarlet and Destuynder (1979). Enfin, une méthode générale pour homogénéiser des plaques périodiques dans le plan et de forme quelconque a été proposée par Caillerie (1984) puis par Kohn and Vogelius (1984). Tous ces travaux reposent sur une hypothèse fondamentale de localisation : la partie plane du champ de déformation tridimensionnel est directement proportionnelle (en moyenne pour les plaques périodiques) aux variables de déformation généralisée de Love-Kirchhoff, $\mathbf{e}$ et $\boldsymbol{\chi}$: $\varepsilon^{\text{loc}}_{\alpha\beta} = \mathrm{e}_{\alpha\beta} + x_3\chi_{\alpha\beta}$. Dans ses travaux, Caillerie (1984) fait appel aux développements asymptotiques en fonction du petit paramètre h/L. L'intérêt des développements asymptotiques est qu'ils permettent de saisir quantitativement la hiérarchie entre les différents phénomènes mécaniques et qu'ils sont bien posés mathématiquement. En particulier, Caillerie montre que le modèle de plaque de Love-Kirchhoff est exactement le premier ordre du développement. Ainsi, il confirme la séparation d'échelle déjà mise en avant au paragraphe précédent entre flèche de flexion et de cisaillement et donne une assise rigoureuse au modèle de Love-Kirchhoff. Ce résultat montre aussi qu'il faut aller au moins à l'ordre deux pour faire ressortir les effets de l'effort tranchant dont on doit tenir compte lorsque l'élancement n'est pas suffisant.

1.3 Les plaques épaisses

Le modèle présenté en Section 1.1 qui fait apparaître les variables de cisaillement est aussi couramment appelé modèle de Reissner-Mindlin (Reissner, 1945; Mindlin, 1951). D'une part, c'est un modèle qui est apprécié par ceux qui le mettent en œuvre car il donne des conditions aux limites plus naturelles que celles du modèle de Love-Kirchhoff et qui, comme on a pu le voir, peut s'obtenir très simplement (d'où l'appellation parfois rencontrée de théorie "naturelle" de Reissner-Mindlin). Mais il est aussi controversé parce qu'il ne dérive pas du deuxième ordre des développements asymptotiques. En effet, le second ordre et les ordres supérieurs des développements asymptotiques ont été déterminés par Lewinski (1991c,b,a). Il apparaît que chaque ordre du développement est un modèle de la forme Love-Kirchhoff dont les chargements dépendent de l'ordre précédent. Ainsi, des champs

La plaque homogène : La plaque la plus simple est la plaque homogène, constituée d'un seul et même matériau. Un exemple typique est une tôle d'acier.

La plaque stratifiée : Pour ces plaques, les propriétés du matériau constitutif varient en fonction de l'épaisseur. Elles sont réalisées par l'empilement d'un certain nombre de couches de matériau. Par exemple, le contreplaqué est un stratifié. Les empilements qui font l'objet de beaucoup d'attention sont les stratifiés de matériaux composites. Il sont constitués de couches nommées plis. Chaque pli est homogène et est constitué d'un composite fibré unidirectionnel, tel que la fibre de carbone ou de verre imprégnée de résine époxyde, dont l'orientation varie par rapport au reste de l'empilement. Comme le comportement du matériau varie brusquement entre chaque couche, on observe des concentrations de contraintes localisées, en particulier sur les bords du stratifié, qui sont liées à des effets de cisaillement interlaminaire et qui nécessitent des modèles de plaque élaborés.

La plaque fonctionnellement graduée : La plaque fonctionnellement graduée (*functionnally graded plate*) est la version continue de la plaque stratifiée. Plus précisément, grâce à de nouveaux procédés, il est possible de faire varier presque continuement dans l'épaisseur les propriétés du matériau constitutif. Ce nouveau concept est une façon de répondre aux difficultés soulevées par les concentrations de contraintes présentées par les plaques stratifiées.

La plaque périodique : Ce sont les plaques dont le matériaux constitutif varie à la fois dans l'épaisseur, mais aussi dans le plan. Les tôles gaufrées, le bardage sont des plaques périodiques. En Génie Civil, les dalles orthotropes de ponts suspendus et les dalles caissonnées en béton sont aussi des plaques périodiques.

Le panneau sandwich Les panneaux sandwichs à âme périodique tels que le nid d'abeilles sont les plaques périodiques pour lesquelles on ajoute l'hypothèse que les peaux sont homogènes et assez rigides par rapport à l'âme hétérogène. Leur présentation est détaillée au Chapitre 2.

Encadré 1.1: Les différents types de plaques

dépendant directement des variables $\boldsymbol{Q}$ ou $\boldsymbol{\gamma}$ n'apparaissent à aucun moment.

Cet obstacle fondamental entre modèle naturel et développements asymptotiques a donné lieu indirectement à une très vaste littérature. Principalement deux angles d'attaque ont été proposés.

Le premier consiste à revoir la façon dont on passe à la limite pour un faible élancement du modèle 3D vers un modèle de plaque. On y retrouve les travaux sur la $\Gamma-$convergence dans la lignée des travaux de Ciarlet and Destuynder (1979) ainsi que ceux sur la méthode variationelle asymptotique (*variational asymptotic method*) qui ont abouti aux travaux de Yu et al. (2002b). On retiendra aussi les travaux de Miara and Podio-Guidugli (2006) ainsi que ceux de Berdichevsky (2010) où une hiérarchie est établie dans la loi de comportement tridimensionnelle de la plaque afin de faire ressortir (ou non) un modèle de plaque de Reissner-Mindlin, dans le cas homogène pour Miara and Podio-Guidugli (2006) et dans le cas d'un panneau sandwich pour Berdichevsky (2010). L'intérêt de tout ces travaux est qu'ils montrent que la façon dont on passe à la limite détermine de façon critique le modèle qu'on obtient au final. De plus, ils mettent en avant de façon fine les ordres de grandeurs entre les différentes échelles caractéristiques (rayon de courbure, épaisseur, longueur d'onde... dans le cas des coques). Cependant, l'ingénieur n'a pas le choix du passage à la limite. Ainsi les modèles obtenus ne peuvent pas être appliqués directement.

Le second angle d'attaque consiste à trouver le champ de localisation associé à Q_α ou γ_α le plus adapté dans telle ou telle configuration. Ces approches sont nommées approches axiomatiques (ou constructives) car elles se basent sur des hypothèses arbitraires. On propose de faire une revue synthétique de ces modèles.

Dans le cas de la plaque homogène, Reissner (1945) suggère une distribution des contraintes de cisaillement transverse associées à l'effort tranchant. Cette distribution est parabolique dans l'épaisseur de la plaque. Malheureusement, si cela semble vrai dans le cas de la plaque homogène, le calcul de certaines solutions exactes (Pagano, 1970a) montre que dans le cas des stratifiés, la distribution des contraintes dans l'épaisseur est beaucoup plus complexe. Ainsi pour les stratifiés, beaucoup de propositions ont été faites. La plus simple, mais aussi la plus grossière est de supposer que les déformations de cisaillement transverse $\varepsilon_{\alpha 3}$ sont uniformes dans l'épaisseur (First Order Shear Deformation Theory). L'inconvénient majeur de ce choix est qu'il impose des contraintes de cisaillement transverse discontinues et très éloignées de la réalité. Par ailleurs, cette vision de l'effet de l'effort tranchant sur la plaque mène à un ensemble de confusions que l'Encadré 1.2 tente d'éclaircir. Sans prendre de précautions, on aboutit toujours à des champs de contraintes discontinus comme l'indique Reddy (1989). Afin d'améliorer les modèles de plaque stratifiée, des modèles souvent rassemblés sous le nom de théories Zig-Zag ont été proposés. Une revue détaillée de ces modèles est proposée par Carrera (2003a). Le travail fondateur de cette approche est celui d'Ambartsumian (1969). Il consiste à donner une forme polynomiale à la distribution de contraintes en cisaillement transverse dans chaque couche, à laquelle on ajoute une fonction d'ensemble couvrant toute l'épaisseur.

On obtient ainsi une fonction dépendant d'un grand nombre de paramètres qu'on identifie grâce aux conditions de continuité des contraintes et des déplacements aux interfaces. De nombreuses propositions pour la fonction d'ensemble ont été faites : linéaire, quadratique (Whitney, 1969b), cubique (Ambartsumian, 1969; Reddy, 1984), sinusoïdale (Touratier, 1991), Zig-Zag (Murakami, 1986). Outre le fait que ces modèles sont fondés essentiellement sur le choix arbitraire de la fonction d'ensemble, leur limitation est qu'à chaque fois ils sont adaptés à des configurations spécifiques du stratifié.

La raideur à l'effort tranchant dans les plaques $\mathsf{F}_{\alpha\beta}$ est très souvent confondue avec la raideur en cisaillement transverse (transverse shear stiffness), $\mathsf{C}_{\alpha\beta} = \mathcal{C}_{\alpha3\beta3}$ où $\widetilde{\boldsymbol{\mathcal{C}}}$ est le tenseur d'ordre quatre en dimension trois des raideurs élastiques en trois dimensions.
Il se trouve en effet que dans le cas des plaques stratifiées, la déformation générée par l'effort tranchant est toujours un cisaillement transverse $\varepsilon_{\alpha3}$. Ainsi la raideur en cisaillement transverse joue un rôle crucial dans l'estimation de la raideur à l'effort tranchant.
La confusion entre ces deux raideurs vient de l'hypothèse erronée que le cisaillement transverse est uniforme dans l'épaisseur. En effet, pour une plaque homogène isotrope, supposer $\varepsilon_{\alpha3}^{\text{loc}} = \gamma_\alpha$ mène à : $\boldsymbol{Q} = h\mathbf{C} \cdot \boldsymbol{\gamma}$ où h est l'épaisseur de la plaque. Avec cette écriture, tout se passe comme si la contrainte de cisaillement transverse s'écrivait $\sigma_{\alpha3}^{\text{loc}} = Q_\alpha/h$ et était reliée directement à $\varepsilon_{\alpha3}^{\text{loc}}$ par la raideur en cisaillement transverse. Ainsi dans beaucoup de travaux, estimer le comportement d'une plaque à l'effort tranchant consiste à trouver un module de cisaillement transverse effectif $\mathbf{C}^{\text{eff}}$ le plus adapté pour qu'au final on puisse écrire directement $\boldsymbol{Q} = h\mathbf{C}^{\text{eff}} \cdot \boldsymbol{\gamma}$. Comme $\mathbf{C}^{\text{eff}}$ est souvent notablement différent de $\mathbf{C}$ on définit alors un coefficient correcteur en cisaillement $k_\alpha = \mathsf{C}_{\alpha\alpha}^{\text{eff}}/\mathsf{C}_{\alpha\alpha}$ (ici sans sommation et dans le cas où $\mathbf{C}$ est diagonale) pour qu'on puisse toujours écrire $Q_\alpha = k_\alpha \mathsf{C}_{\alpha\alpha} h\gamma_\alpha$ et faire comme si les déformations de cisaillement étaient uniformes dans l'épaisseur.
Ainsi, plutôt que de parler de raideur à l'effort tranchant, certains préfèrent utiliser le terme de raideur en cisaillement transverse de la plaque définie comme $\mathbf{C}^{\text{eff}} = \mathbf{F}/h$. Dans ce travail, les effets de l'effort tranchant sont vus comme un phénomène en soit et non comme une déformation uniforme en cisaillement transverse, corrigée. On parlera donc de raideur à l'effort tranchant, la raideur en cisaillement transverse étant une propriété locale du matériau constitutif.
Pour ajouter à la confusion, il se trouve que dans le cas des panneaux sandwichs homogènes avec des peaux minces, le cisaillement est effectivement uniforme dans l'âme et il n'y a plus de correction à faire. C'est le cadre d'étude du Chapitre 3. Dans ce chapitre, exceptionnellement, on parle indifféremment de raideur à l'effort tranchant et de raideur en cisaillement transverse pour respecter les conventions utilisées dans le dimensionnement des panneaux sandwichs.

Encadré 1.2: Cisaillement transverse et raideur à l'effort tranchant

Dans le cas des plaques périodiques sans autre hypothèse, les difficultés sont beaucoup plus considérables. Aujourd'hui, il n'existe pas de méthode permettant de construire les champs localisés dépendant directement des variables $\boldsymbol{Q}$ ou $\boldsymbol{\gamma}$. On n'est même pas certain que le modèle de Reissner-Mindlin soit le bon. Il est donc nécessaire de passer par la résolution du second ordre des développements asymptotiques qui fait appel à un modèle de plaque beaucoup plus complexe que celui de Reissner-Mindlin. On relèvera tout de même les travaux de Isaksson et al. (2007) et de Cec-

chi and Sab (2007) qui proposent une extension aux plaques périodiques des travaux de Whitney (1972) pour la plaque stratifiée. Mais ces travaux supposent que le comportement de la plaque suit un modèle de Reissner-Mindlin et sont intimement liés à l'hypothèse de flexion cylindrique.

Dans le cas des panneaux sandwichs, le fait d'avoir des peaux raides permet d'être un peu plus explicite sur les effets de l'effort tranchant dans la plaque. Une approche simplifiée de cette condition nommée ici hypothèse de contraste entre peaux et âme est abordée au Chapitre 2 et une étude bibliographique des modèles existants est fournie au Chapitre 3.

Ces efforts pour déterminer la localisation des variables d'effort tranchant sont entièrement justifiés pour plusieurs raisons. En premier lieu, même si on a clairement indiqué que la flèche de cisaillement est négligeable pour les plaques homogènes, il existe des plaques pour lesquelles cette flèche peut devenir comparable voire prépondérante : ce sont les plaques stratifiées dont les couches ont des raideurs extrêmement différentes et plus particulièrement les panneaux sandwichs qui seront introduits dans le prochain chapitre. En second lieu, même si la flèche de cisaillement reste négligeable, il est crucial d'avoir une estimation raisonnable voire précise de l'état de contrainte généré par l'effort tranchant afin de pouvoir calculer la résistance de la plaque. Cette question est particulièrement importante dans le cas des composites fibrés et stratifiés pour lesquels il existe des concentrations de contraintes interlaminaires liées à l'effort tranchant ainsi que dans le cas des panneaux sandwichs pour lesquels la rupture due à l'effort tranchant est souvent dimensionnante.

1.4 Conclusion

Comme on a pu le voir, il existe aujourd'hui un modèle de plaque bien fondé théoriquement : le modèle de Love-Kirchhoff. Contrairement au modèle de Reissner-Mindlin, ce modèle ne prend pas en compte les effets de l'effort tranchant sur la plaque. Pourtant, même si l'effort tranchant a un effet généralement négligeable sur la flèche, il est crucial de connaître l'état de contraintes qu'il génère localement dans la plaque afin d'estimer sa résistance. Ainsi un grand nombre de travaux portant chacun sur un type particulier de plaque a été écrit pour modéliser cet effet. D'une certaine façon, tous ces modèles sont confrontés au fait que le modèle de Reissner-Mindlin ne résulte pas du deuxième ordre des développements asymptotiques. A chaque fois, un particularisme apparaît pour simplifier l'approche et aboutir à un modèle de Reissner-Mindlin, que ce soit la configuration de la plaque (flexion cylindrique) ou des symétries du matériau constitutif. Aux Chapitres 4 et 5, on propose une approche qui couvre l'ensemble des types de plaque en élaborant un modèle plus riche basé sur les travaux de Reissner (1945). Avant cela et pour motiver cet approfondissement sur l'effet de l'effort tranchant dans les plaques, une présentation de l'objet d'étude de ce travail, les panneaux sandwichs à âme pliée en module à chevrons, est effectuée au chapitre qui suit, puis les limitations des méthodes existantes sont montrées au Chapitre 3

CHAPITRE

2

Cas d'étude : Les panneaux sandwich à âme pliée

La motivation originelle de ce travail est l'étude d'un nouveau type d'âme de panneau sandwich : le module à chevrons. En effet le marché des panneaux sandwichs est un marché encore jeune et en mutation dans lequel il existe des opportunités d'innovation. En particulier les panneaux sandwichs offrent des possibilités d'économie de matière dans l'habitat qu'il est tout a fait d'actualité de considérer. Étudier un nouveau type d'âme de panneau sandwich nécessite donc une bonne compréhension de ce marché ainsi que des questions scientifiques sous-jacentes.

Dans ce chapitre, on propose tout d'abord une présentation des pliages structurels périodiques en Section 2.1. En vue de leur utilisation comme âme de panneau sandwich, une introduction à ces panneaux et leur marché est proposée en Section 2.2. Cette analyse mettra en évidence que ce marché est essentiellement structuré autour du comportement mécanique des panneaux sandwichs. Plus particulièrement, une analyse mécanique simplifiée montre que l'âme joue un rôle essentiel dans la résistance du panneau sandwich à l'effort tranchant. Finalement, en gardant en mémoire les contraintes posées par le marché des panneaux sandwichs, une revue des procédés technologiques existants est effectuée en Section 2.3.

2.1 Les pliages structurels périodiques

Les pliages structurels périodiques sont des pliages périodiques qui donnent un volume à la feuille initialement plane. Ainsi la feuille présente un relief qui peut être exploité pour ses propriétés cinématiques ou structurelles. Un exemple simple est le soufflet d'un accordéon qui permet les amples mouvement du musicien tout en servant de réserve d'air à débit contrôlé.

Il existe un très grand nombre de pliages de ce type. On donne ici quelques éléments pour les distinguer puis on indiquera quelques applications envisageables pour le plus connu d'entre eux, le module à chevrons.

2.1.1 Les différent types de pliages structurels périodiques

Les pliages structurels périodiques sont aussi nommés tessellations (pavages) dans le vocabulaire des origamistes (plieurs de papier). Ils font appel à des motifs dont l'origine est très ancienne et sont rattachés aux pliages traditionnels en origami. Par ailleurs, ces motifs sont aussi très utilisés par les plisseurs de tissus (Voir les Ateliers Lognon à Paris). Ceux-ci utilisent des moules en carton (Figure 2.1) pour étuver des tissus utilisés dans la haute couture (Figure 2.2).

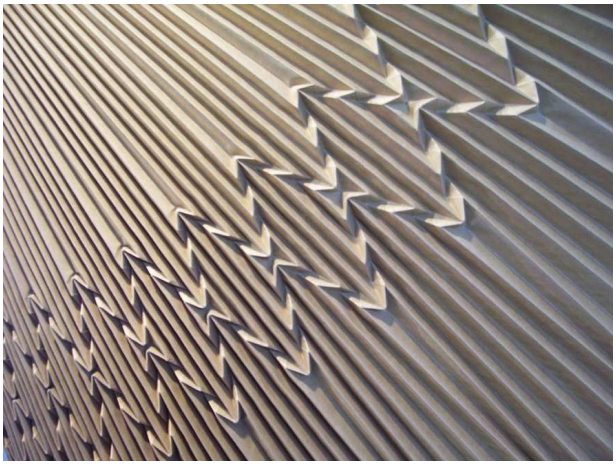

Figure 2.1 – Un moule utilisé pour le plissage des tissus (Sid, 2009)

Figure 2.2 – Une robe réalisée avec un tissu plissé (Lognon, 2010)

Bien qu'il semble y avoir une très grande variété de motifs possibles, les origamis doivent respecter certaines règles géométriques. En effet, il est bien connu qu'une feuille de papier peut être assimilée à une surface développable car elle est pratiquement inextensible dans son plan en comparaison de sa faible raideur en flexion (Cerda and Mahadevan, 2005). Ainsi, lorsqu'on plie une feuille, on ne fait qu'introduire des singularités de courbure localisées au niveau du pli. La surface engendrée demeure une surface développable. On dit alors que la feuille est isométrique au plan. Le fait de se limiter au pli et de s'interdire toute coupure de la feuille n'est donc pas sans contrainte. Il existe un certain nombre de résultats formalisant les conditions de pliabilité. Dans le cas de pliages à plat, quelques théorèmes fixant des règles de pliabilité sont rappelés en Encadré 2.1. Ces conditions locales de refermeture à chaque intersection de plis ne sont pas suffisantes pour garantir la refermeture de l'ensemble de la feuille. En réalité, savoir s'il est possible de replier une feuille en partant d'un dessin des plis à plat (crease pattern) vérifiant les conditions locales de refermeture est un problème ouvert (Demaine and Demaine, 2001). Plus récemment dans cette thématique, Tachi (2009) s'est intéressé à la cinématique d'ensemble de pliages complexes. Dans le cas des pliages tridimensionnels, on rappellera les travaux de Duncan and Duncan (1982) sur la cinématique des plis courbes, illustrant la nécessité d'employer la géométrie différentielle pour décrire correctement

Théorème de Maekawa : Lorsqu'on déplie un origami, on observe des plis "montagne" et des plis "vallée". Dans le cas des pliages plans, à l'intersection de différents plis (un sommet), la différence entre le nombre de plis montagne et de plis vallée vaut toujours 2.

Théorème de Kawasaki Kawasaki (1989) : Soit la suite des angles $a_1, a_2, ..., a_{2n}$ autour d'un sommet (il y a toujours un nombre pair d'angles autour d'un sommet). L'addition d'un angle sur deux est égale à π :

$$a_1 + a_3 + \cdots + a_{2n-1} = \pi \quad \text{ou} \quad a_2 + a_4 + \cdots + a_{2n} = \pi$$

Encadré 2.1: Théorèmes d'origami

les déformations acceptables par pliage. Enfin, des techniques systématiques pour générer de tels motifs ont été proposées par Kling (1997, 2005) et sont présentées en Figure 2.3. Parmi ces nombreux motifs, le plus connu de tous est le *module à chevrons* (*chevron pattern*). Ce pliage est aussi connu sous le nom de *Miura-Ori* (littéralement : origami de Miura, en hommage à un de ses fervents promoteurs, Koryo Miura) ainsi que *herringbone-pleating* et enfin *Zeta-Core* (nom donné au pliage par Miura lui-même (Miura, 1972)).

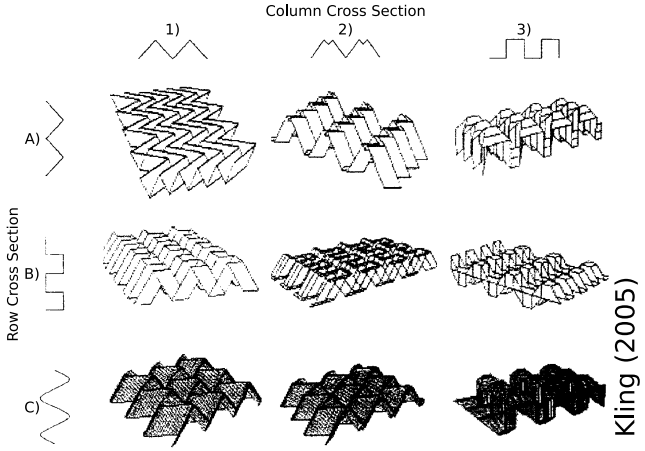

Figure 2.3 – Motif générés par la théorie de Kling

Le module à chevrons est un motif extrêmement simple, dont la maille élémentaire est constituée de quatre parallélogrammes identiques (Figure 2.4). Le paramétrage complet du motif est donné au Chapitre 3. Un des compétiteurs du module à chevrons envisagé sérieusement est le motif nommé Matted (Figure 2.5). Ce motif est légèrement plus complexe et semblerait offrir une plus grande résistance. Cependant, notre cadre d'étude se restreindra au module à chevrons qui est le plus simple à modéliser.

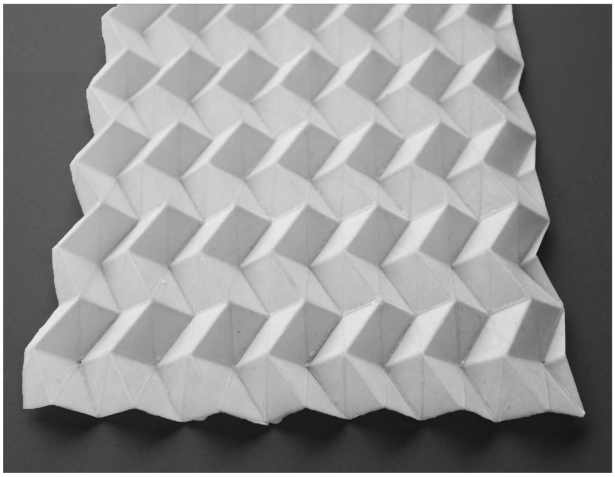

Figure 2.4 – Le module à chevrons

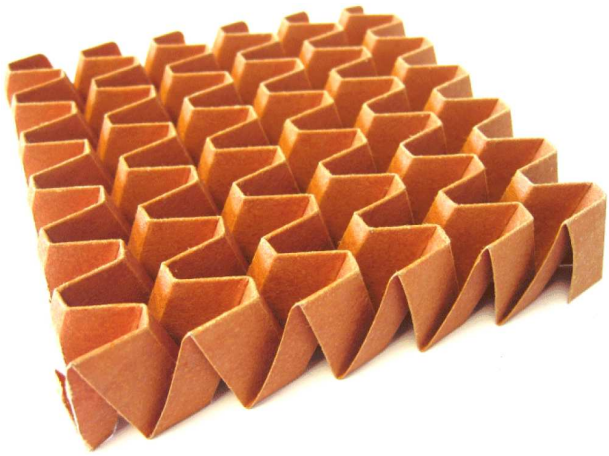

Figure 2.5 – Le motif Matted (Heimbs, 2009)

2.1.2 Les applications possibles

On peut recenser un nombre important d'applications possibles pour ces motifs. En voici une liste non exhaustive pour le module à chevrons.

- *Absorbeur de chocs* : des études montrent que le module à chevrons présente de bonnes caractéristiques pour être utilisé comme absorbeur de chocs (Basily and Elsayed, 2004b). On peut donc envisager de l'employer dans les emballages ou comme absorbeur de choc pour le parachutage de matériel.
- *Échangeur double flux* : comme le module à chevrons est une feuille sans coupure, il sépare deux domaines bien définis. Il est possible de faire circuler séparément deux fluides caloporteurs à contre courant (Figure 2.6). Ainsi le module à chevrons est un bon candidat pour des échangeur double-flux efficaces et économes à fabriquer. Pour obtenir de bons échangeurs de chaleur, il faut être capable non seulement de concentrer une grande surface dans un petit volume, mais aussi de bien mélanger chaque fluide au cours de l'échange. Le module à chevrons présente une grande surface spécifique et sa forme ondulée facilite la création de tourbillons ce qui lui confère de bonnes capacités d'échange. Les travaux de Zhang et al. (2004) sur un motif apparenté au module à chevrons illustrent ce potentiel.
- *Revêtement* : le relief donné à une feuille métallique par le module à chevrons lui donne une plus grande inertie dans les deux directions principales de flexion. On peut donc envisager des applications similaires à la tôle ondulée et au bardage. De plus, les qualités esthétiques et de formabilité du module à chevrons peuvent en faire un matériau apprécié des architectes et des designers.
- *Âme de panneau sandwich* : C'est cette application qui fait l'objet de ce travail. Une présentation détaillée des panneaux sandwichs est l'objet de la section qui suit.

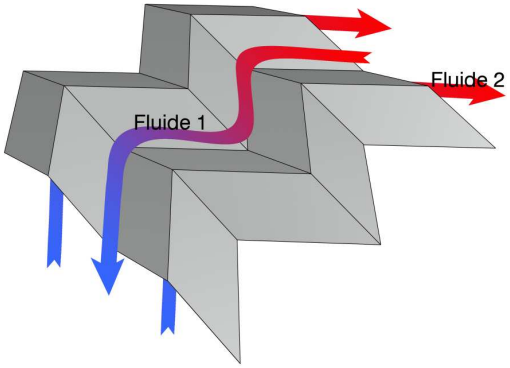

Figure 2.6 – Le fonctionnement en échangeur double flux du module à chevrons

On peut constater que la simple maîtrise d'un procédé de fabrication du motif présente déjà un intérêt à moyen terme. Il est clair que ce motif n'est pas une solution techniquement optimale pour toutes ces applications. Cependant, si le coût de fabrication de ce produit intermédiaire est très modique, il pourrait trouver des débouchés dans des domaines inattendus. Comme on souhaite utiliser le module à chevrons comme âme de panneau sandwich, on propose donc d'analyser les contraintes de ce marché.

2.2 Le marché des panneaux sandwichs et ses exigences

L'idée de prendre en sandwich un matériau léger et peu résistant entre deux couches d'un matériau noble afin d'obtenir une plaque plus résistante et plus raide en flexion à poids donné est assez ancienne. Certains la font remonter à Léonard de Vinci, d'autres au pont tubulaire sur la rivière Conwy au Royaume-Uni de Sir W. Fairbairn 1849 (Allen, 1969) et enfin certains voient dans la structure poreuse des os du crâne un exemple intemporel (Thompson, 1917; Gibson and Ashby, 1988). Aujourd'hui ce concept multiforme peut être regroupé sous la notion de panneau sandwich. Les deux couches de matériau noble sont généralement assez minces et sont appelées les peaux (skins). La couche "tendre" est appelée âme (core) en référence à l'âme des poutres profilées en I (Figure 2.7). Il est communément admis que cet agencement de la matière est optimal pour maximiser la raideur en flexion d'une plaque, à poids et gabarit donné (Laszczyk, 2010).

Le premier champ d'application dans lequel la question du poids s'est posée sérieusement est l'aéronautique et la première application industrielle reconnue est l'utilisation de panneaux sandwichs composés de contreplaqué pour les peaux et de balsa pour l'âme dans le fuselage d'un avion de combat Britannique lors de la seconde Guerre Mondiale, le De Havilland Mosquito. Aujourd'hui, les panneaux sandwichs sont des structures qui se retrouvent dans de nombreuses applications. Le plus répandu des panneaux sandwichs est le carton ondulé (Figure 2.8) qui consiste à coller entre deux feuilles de papier kraft, une feuille ondulée en guise d'âme. Les panneaux sandwichs sont aussi

répandus dans la construction comme panneaux d'isolation (Figure 2.9), éléments de cloisons et de mobilier (Portes Isoplanes). Enfin, leur excellente capacité structurelle rapportée à leur poids en font un matériau roi dans l'aéronautique et l'aérospatiale (Figure 2.10).

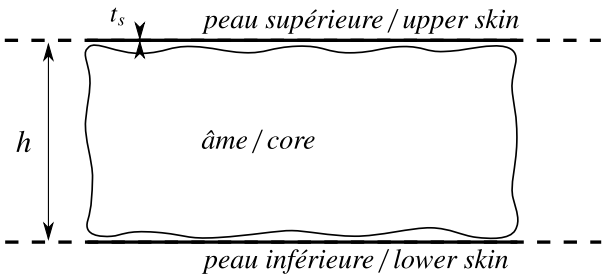

Figure 2.7 – Modèle de tri-couche à peaux minces.

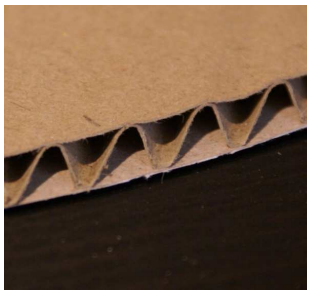

Figure 2.8 – Du carton ondulé double face

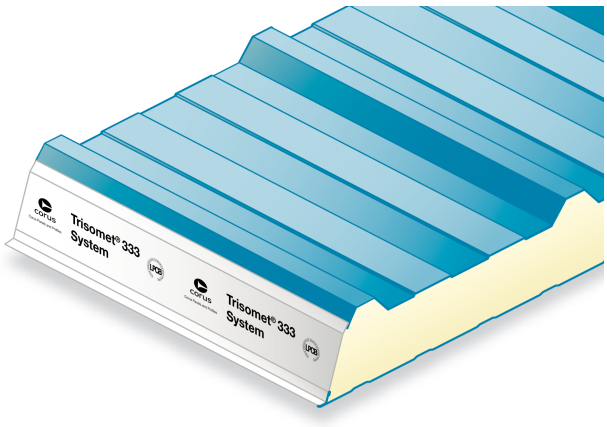

Figure 2.9 – Un panneau isolant formé de peaux en acier et d'une âme en polyuréthane (Corus, 2010)

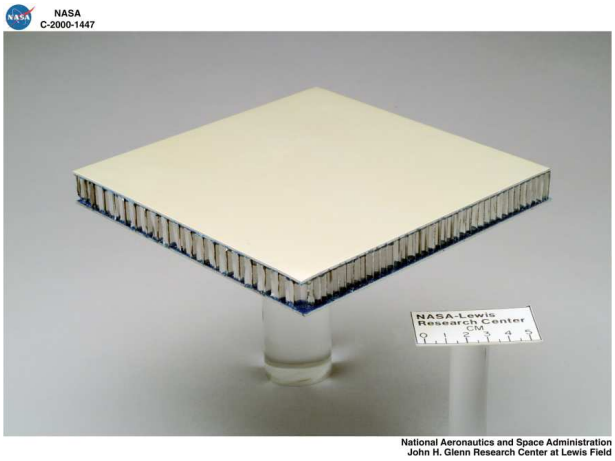

Figure 2.10 – Un panneau sandwich de très haute qualité structurelle en nid d'abeilles aluminium et peaux en aluminium (Glenn, 2000)

2.2.1 Le marché des panneaux sandwichs aujourd'hui

Comme on l'a déjà indiqué, c'est l'aéronautique qui a été la première à pousser les recherches sur ce sujet. En effet, actuellement on estime le coût d'un excès de poids à la conception sur la durée de vie complète d'un avion civil à plus de 1000€/kg. Aujourd'hui, le spectre d'application des panneaux sandwichs s'est considérablement élargi. Ainsi, si on souhaite identifier les applications pertinentes pour un nouveau type d'âme il est nécessaire de connaître la structure des marchés sous-jacents. Ceux-ci s'organisent essentiellement autour d'un arbitrage très sévère entre le coût de

fabrication et la capacité structurelle. Les panneaux sandwichs à hautes capacité structurelle se retrouvent dans l'aérospatiale. *A contrario*, on peut chercher à minimiser le plus possible le coût en gardant des capacités structurelles convenables. Le carton ondulé illustre un tel compromis.

La capacité structurelle rapportée au coût du produit final s'articule autour de trois critères. Le premier est le choix du matériau des peaux et de l'âme. Ce choix varie des métaux et des matériaux fibrés (fibre de carbone, de verre, d'aramide), pour les plus onéreux, aux plastiques thermoformables (polypropylène par ex.) et les différents types de papier, pour les moins chers. On notera aussi l'emploi déjà évoqué du balsa et du bois (dans les portes isoplanes par exemple) comme matériau noble ainsi que les mousses polymères, telles que le polyuréthane, prises en sandwich avec des tôles d'acier dans les panneaux isolants utilisés dans les hangars industriels. D'une manière plus générale et si l'on souhaite avoir une approche systématique, on peut se référer aux travaux d'Ashby sur les stratégies de choix d'un matériau (Ashby, 2000). Dans le cas présent, les rapports E/ρ, $E^{1/3}/\rho$, et σ^0/ρ face au prix jouent un rôle déterminant dans ce choix. E est le module d'Young, σ^0 la résistance ultime à la traction, ρ la masse volumique.

Le second critère est bien connu, c'est la taille du marché et les rendements d'échelle. En effet, moyennant un investissement initial conséquent, il est envisageable de produire rapidement un produit de qualité. La viabilité économique du produit réside donc sur la possibilité d'amortir rapidement l'investissement et donc sur la taille du marché accessible. Ce raisonnement fonctionne pour le carton ondulé qui a des capacités structurelles assez remarquables pour un coût très modique car la taille du marché est considérable. Dans le cas du nid d'abeilles en aluminium destiné à l'aérospatiale, la taille du marché mondial est tellement petite qu'elle ne permet pas d'amortir un investissement dans une machine industrielle de l'ordre de 500k€ sur 5 ans. Même dans ce cas plus de 50% du prix de fabrication serait dédié à l'amortissement de la machine ce qui est un frein considérable à l'entrée de nouveaux acteur sur le marché (étude réalisée à titre privé par des étudiants de master à l'université Paris Dauphine).

Le troisième critère est le choix de la géométrie d'âme, intimement lié à la cadence de fabrication accessible et au choix du matériau. Outre un remplissage complet entre les peaux avec une mousse ou du balsa, de nombreuses formes structurées ont été utilisées. La plus connue est le nid d'abeille, mais de nombreux types de gaufrage ont aussi été produits (voir Miura (1972) par exemple). Une mousse est très facile à injecter entre deux peaux alors que produire une forme structurée est inévitablement plus délicat. Par exemple, les procédés utilisés dans l'aérospatiale avec les nid d'abeilles métalliques peuvent être presque qualifiés d'artisanaux : procédé de fabrication du nid d'abeilles par collage feuille par feuille, table d'expansion du nid d'abeilles etc., ce qui a une incidence directe sur le coût de fabrication. Ainsi une des sources principales d'innovation dans le domaine réside dans la recherche de nouvelles géométries d'âme ainsi que des procédés de fabrication moins onéreux. De très nombreuse propositions ont été faites en variant les matériaux, les

géométries, etc. Deux solutions se démarquent aujourd'hui. D'une part, les âmes en treillis ("truss core") font l'objet recherches financées en partie par le ministère de la défense américain pour des raisons balistiques (Wicks and Hutchinson, 2001; Wadley, 2002; Cote et al., 2007; Doherty et al., 2009). Ces géométries sont probablement celles qui offrent la plus grande résistance à l'effort tranchant à poids fixé, mais elles restent pour l'instant difficiles à produire. D'autre part, les âmes pliées présentent la possibilité d'être fabriquées en continu à partir de techniques de pliage ce qui pourrait leur donner un avantage concurrentiel par rapport au nid d'abeilles.

Ainsi, comme on peut le voir, les panneaux sandwichs sont omniprésents dans la vie courante. C'est une technologie qui est relativement jeune et qui bénéficie encore d'un processus de démocratisation : la baisse régulière des coûts de fabrication permet l'accès à de nouveaux marchés sous réserve de se plier au compromis capacité structurelle/prix de fabrication imposé par ceux-ci. Ce processus peut offrir des opportunités à de nouveaux matériaux d'autant plus que les marchés eux-mêmes sont en forte évolution. En effet, outre le raisonnement comptable sur l'économie de matière offerte par les panneaux sandwichs, la question d'une utilisation raisonnée des ressources est devenue un enjeux de société qui nécessairement ouvre la voie à de nouvelles applications.

2.2.2 Les enjeux structurels des panneaux sandwichs

Les panneaux sandwichs ont donc un comportement structurel bien meilleur que celui d'une plaque massive. La contrepartie de cette amélioration est une complexification importante du comportement mécanique de ces objets comme on l'a déjà évoqué au chapitre précédent. Étant donné que la capacité structurelle est un élément déterminant pour les applications utilisant des panneaux sandwichs, la connaissance et la prédiction du comportement d'un panneau est un enjeux important. On propose ici une introduction au comportement mécanique simplifié des panneaux sandwichs couramment utilisé dans leurs applications.

En effet, même si on a vu que le comportement d'une plaque périodique hétérogène est aujourd'hui un problème ouvert, le fait que les peaux soient beaucoup plus raides que l'âme permet une décomposition des rôles mécaniques de l'âme et des peaux. Cette décomposition n'est possible qu'au prix d'une hypothèse de contraste qui n'est pas toujours formalisée. Une exploration quantitative de cette question sera effectuée au Chapitre 6 et sera appliquée aux panneaux sandwichs à âme en module à chevrons au Chapitre 7. Pour l'instant, on accepte cette hypothèse sans justification.

Dans le cadre de l'hypothèse de contraste, la raideur et la résistance de la plaque en flexion sont assurées essentiellement par les peaux. En effet la mise en flexion d'un panneau sandwich génère un effort de traction/compression dans les peaux alors que l'âme, étant plus souple, n'est soumise pratiquement à aucun effort (Figure 2.11). La déformation générée par l'effort tranchant est, quant à elle, liée à la mise en cisaillement de l'âme dans toute son épaisseur. Ainsi la raideur et la résistance à l'effort tranchant sont assurées essentiellement par l'âme (Figure 2.12).

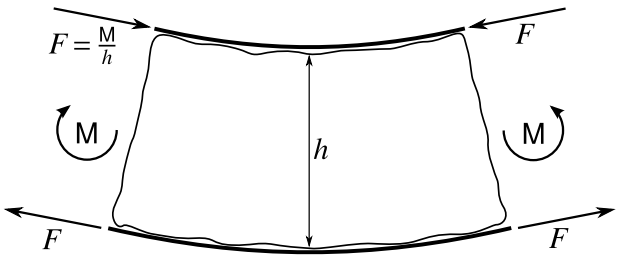

Figure 2.11 – Effet de la flexion sur les peaux

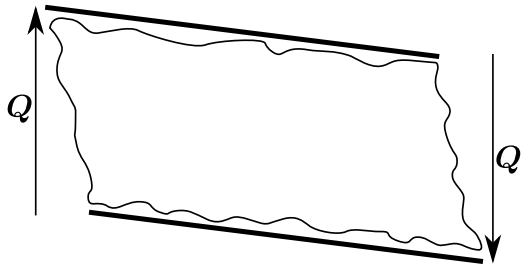

Figure 2.12 – Effet de l'effort tranchant sur l'âme

Puisqu'on cherche à comparer le module à chevrons utilisé comme âme de panneau sandwich, c'est l'étude de la raideur et de la résistance à l'effort tranchant qui sont pertinentes. Comme on l'a déjà indiqué, la flèche de cisaillement peut devenir prépondérante dans le cas des panneaux sandwichs. Mais plus encore, lorsqu'on s'intéresse à la résistance, il est absolument nécessaire de connaître précisément les efforts locaux générés par l'effort tranchant.

En effet, pour la plupart des chargements conventionnels, la ruine d'un panneau sandwich se produit par instabilité élastique. Le nombre de types de ruine observé est assez grand, allant du flambement d'ensemble au micro-voilement des facettes qui constituent l'âme. A titre d'illustration, une étude détaillée dans le cas de panneaux sandwichs à âme en nid d'abeilles est proposée par Petras and Sutcliffe (1999) mais aussi par Rammerstorfer et al. (2006). Pour le comportement en grande transformations du nid d'abeilles seul on pourra aussi se référer aux travaux de Wierzbicki (1983) et Mohr and Doyoyo (2004). Cette observation mène à deux conclusions. La première est qu'il est essentiel d'avoir une connaissance détaillée et suffisamment exacte du comportement élastique pour estimer correctement le point de bifurcation. La seconde conclusion est que la qualité géométrique de l'âme qui est produite est cruciale pour obtenir des performance structurelles acceptables. Ainsi, la résistance d'une géométrie donnée dépend fondamentalement du procédé qui a été utilisé pour la produire. Cette observation explique donc l'arbitrage sévère entre prix et capacité structurelle qui fait la spécificité du marché des panneaux sandwichs. Une revue des procédés de fabrication du module à chevrons existants s'avère donc nécessaire.

2.3 Comment fabriquer des âmes pliées

Comme nous l'avons montré en Section 2.2.1, il existe un compromis entre le coût de fabrication et la capacité structurelle du motif. Ainsi, soit on vise un marché petit et ayant de fortes attentes structurelles avec un procédé quasi artisanal ; soit on vise un marché très grand, pour lequel on doit être capable de fournir à haute cadence avec des rendements d'échelles conséquents (auxquels s'ajoute un coût d'entrée élevé). Jusqu'à récemment la fabrication des âmes pliées a posé

trop de problèmes soit du côté de la qualité structurelle soit du côté de la vitesse de fabrication pour qu'elles s'imposent vraiment comme le matériau d'avenir pour les âmes de panneau sandwich. En effet, le module à chevrons a beau être un pliage, il n'est pas du tout évident de le produire à l'échelle industrielle.

A priori on peut envisager deux approches pour fabriquer en continu le module à chevrons. La première serait de le produire uniquement par des techniques de pliage. L'avantage de cette approche est que le pliage est fondamentalement peu coûteux en énergie et n'endommage le matériau que sur une surface limitée à la zone de pli. On s'attendrait donc à avoir un produit fini de bonne qualité avec une telle méthode. Malheureusement une telle approche est impossible au premier abord. La raison principale à cela est qu'on ne peut produire le module à chevrons en faisant une suite simple de pli élémentaires mais qu'il faut imposer sa forme "d'un seul coup" à la feuille (on parle de pli complexe). Une deuxième approche viserait à estamper directement la feuille à mettre en forme (pressage entre deux outils gaufrés). De nouveau, une telle approche n'est pas applicable. Pour avoir une capacité structurelle raisonnable, le matériau ne doit pas être trop endommagé au cours du procédé. Or les géométries qui présentent un intérêt structurel ont un relief tel qu'il faudrait étirer la feuille dans son plan d'un facteur trois ou quatre.

On se propose ici de donner un état de l'art non exhaustif tournant autour de cette thématique qui est à la fois ancienne et a connu plusieurs foyers d'innovation.

2.3.1 Quelques exemples anciens

Il existe un corpus assez ancien de brevets portant sur une très grande variété de gaufrage du papier, remontant sans problème à la seconde moitié du XIX^{ème} siècle. Une première phase de développements technologiques autour des âmes pliées a démarré dans les années 50 en même temps que l'on s'intéressait de plus près au nid d'abeilles (Kelsey et al., 1958). Ainsi le premier brevet portant sur l'usage du module à chevrons comme âme de panneau sandwich est à ma connaissance celui déposé par Rapp (1960) illustré Figure 2.13. Cependant il n'est pas exclu qu'il y ait des antériorités car à la même époque, il existait déjà des tentatives de production du module à chevrons. Ainsi Hochfeld (1959) propose un procédé itératif présenté Figure 2.14. Il est rapidement suivi par Gewiss qui fera deux propositions de machine. Une première machine "pas à pas" (Gewiss, 1960, 1969b,a, 1976) illustrée Figure 2.15, puis une seconde machine permettant probablement une production presque continue du module à chevrons (Gewiss, 1968, 1977). Cette analyse ne se base que sur les brevets publiés. Il est donc difficile de donner une raison précise sur l'absence de généralisation des âmes pliées dans l'industrie à cette époque. Ceci étant dit, vu la complexité des machines proposées et le fait qu'elles présentent des mécanismes plus ou moins itératifs laisse à penser que leurs cadences n'étaient pas suffisantes.

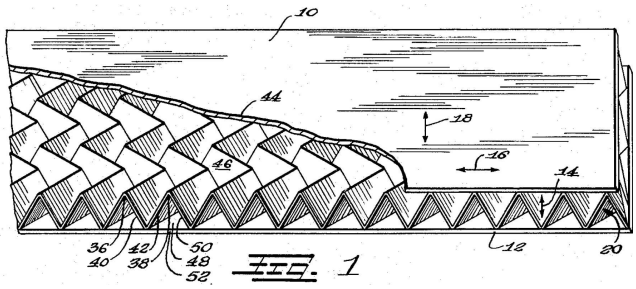

Figure 2.13 – Brevet sur le concept de panneau sandwich incluant le module à chevrons (Rapp, 1960).

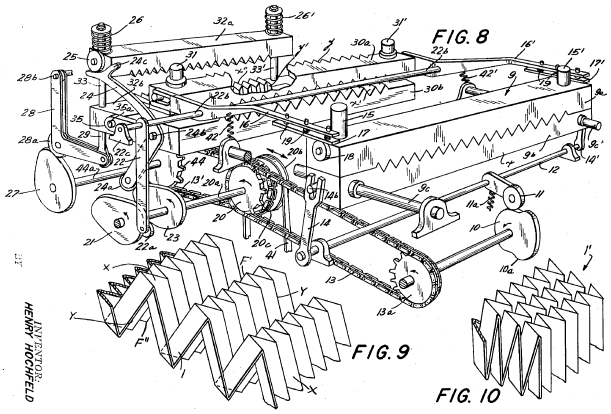

Figure 2.14 – Machine itérative proposée par Hochfeld (1959)

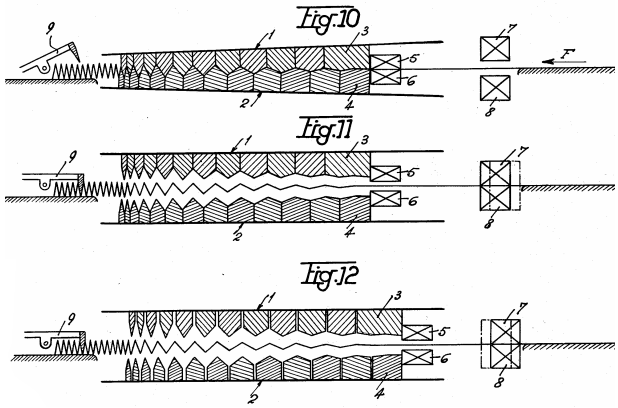

Figure 2.15 – Machine itérative proposée par Gewiss (1976)

2.3.2 Koryo Miura

Parallèlement à ces développements en Europe et aux États-Unis, le sujet émerge aussi au Japon avec Miura qui est aujourd'hui Professeur émérite à l'université de Tokyo et s'est intéressé essentiellement à l'aérospatiale. Il a été le premier à formaliser l'étude du module à chevron. Il a en particulier calculé analytiquement la borne supérieure de la raideur transverse du module à chevrons (Miura, 1972) (voir Chapitre 3). En ce qui concerne la fabrication du module à chevrons, bien que conscient des difficultés il ne semble pas que Miura se soit penché de manière approfondie sur la question. Deux approches sont proposées dans ses travaux. Une première proposition (Miura, 1972) consiste à directement estamper le motif, avec les limitations que l'on a indiquées. Le résultat est présenté Figure 2.16. En regardant de près on peut constater que la géométrie du motif est assez approximative ce qui ne laisse pas présager de capacités structurelles suffisantes. Une deuxième proposition (Miura, 1980) consiste à mouler le motif avec un polymère (Figure 2.17). Malheureusement le moulage ne se prête pas du tout à une production en continu. Il semble que Miura n'a pas persévéré sur l'emploi du module à chevrons comme âme de panneau sandwich mais qu'il se soit intéressé par la suite à ses propriétés cinématiques. Ces propriétés ne seront pas détaillées ici. On indiquera seulement que le module à chevrons a inspiré la cinématique de déploiement de panneaux solaires ainsi qu'une nouvelle technique pour plier les cartes (Miura, 1994).

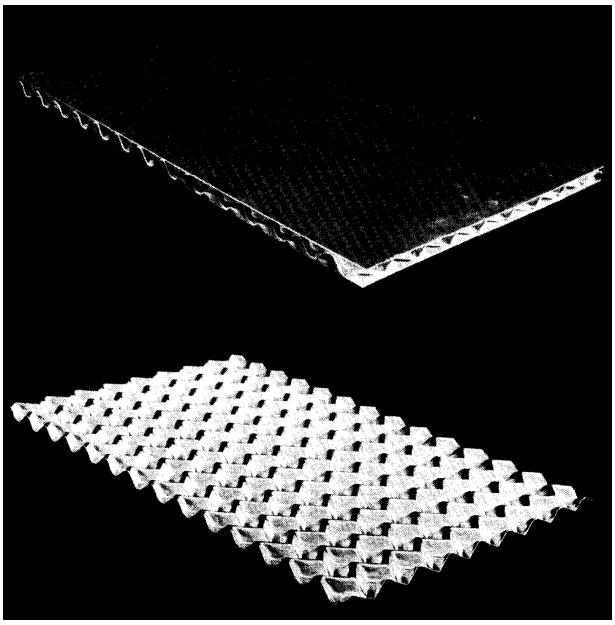

Figure 2.16 – Un panneau sandwich incluant le module à chevrons présenté par Miura (1972)

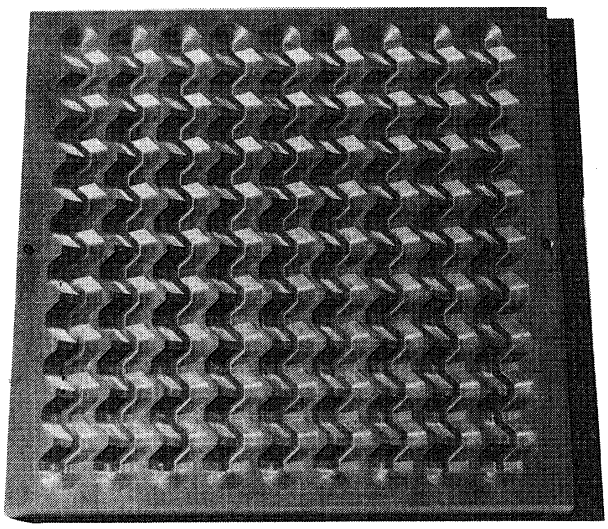

Figure 2.17 – Moule utilisé par Miura pour réaliser le module à chevrons (Miura, 1980)

2.3.3 Université de Kazan

Selon toute vraisemblance, l'université de Kazan (Russie) a travaillé dans le courant des années 70 sur le module à chevrons. Malheureusement il existe très peu de documentation d'époque à ce sujet. Certains auteurs (Nguyen et al., 2005a; Kintscher et al., 2007) indiquent qu'il a été envisagé d'utiliser le module à chevrons dans l'aéronautique mais aussi dans l'industrie pétrolière pour des raisons acoustiques. Plus récemment on trouve des articles publiés dans la revue Russian Aeronautics avec une orientation essentiellement technologique (Khaliulin, 1999, 2005; Khaliulin et al., 2005; Khaliulin and Batrakov, 2005, 2006; Zakirov and Alekseyev, 2005; Zakirov et al., 2006, 2008; Kayumov et al., 2007; Movchan, 2007). De plus de nombreux brevets ont été déposés en collaboration avec Airbus Deutschland (Akishev et al., 2005b,a; Akishev and Zakirov, 2005b,d,a,e,c).

Le procédé étudié à l'université de Kazan utilise des techniques d'hydroformage avec des moules déformables pour accompagner la refermeture du module à chevrons lors de sa mise en forme par pliage (Figure 2.18). Ce procédé permet en particulier de mettre en forme des composites à fibres de carbone, préimprégnés de résine époxy, connus pour être particulièrement difficiles à plier (très fort retour élastique). Cependant, la précision de réalisation est limitée par la qualité du moule déformable utilisé et il s'agit de nouveau d'un procédé à la pièce.

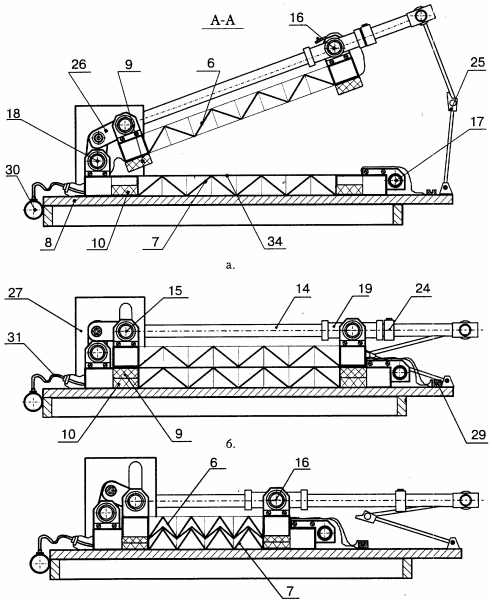

Figure 2.18 – Hydroformage avec moule déformable (Akishev et al., 2005a)

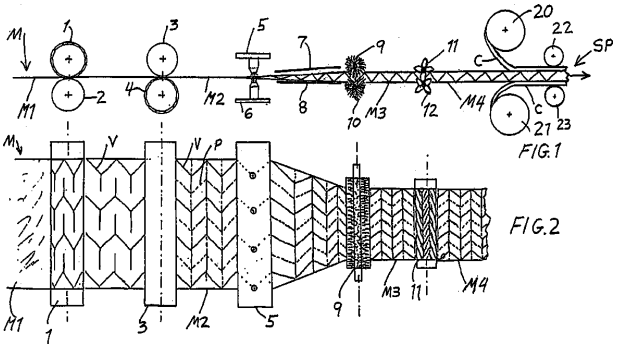

Figure 2.19 – Exemple d'emploi des panneaux produits par Foldcore (Kehrle, 2004)

2.3.4 Foldcore

L'entreprise Foldcore est une spin-off de l'université de Stuttgart dirigée par Dr-ing. Reiner Kehrle. Elle dispose d'une machine brevetée (Kehrle, 2004, 2009, 2010) présentée en Figure 2.19, permettant de produire en continu différents motifs d'âmes pliées. Le procédé consiste à effectuer un estampage léger du motif, voire de réaliser de légères incisions avec des outils rotatifs, pour amorcer le repliement. Ensuite, la refermeture est forcée dans le plan du motif avec éventuellement un chauffage (dans le cas des plastiques thermoformables). Les matériaux employés vont du papier aux métaux en passant par les plastiques thermoformables et le Nomex®. Le Nomex® est un papier de fibres d'aramides très couramment utilisé pour fabriquer des nid d'abeilles dans l'aviation civile. C'est une marque déposée par DuPont. Contrairement à la technologie développée à Kazan, il n'est probablement pas possible de mettre en forme des fibres de carbone préimprégnées. Enfin, il ne semble pas y avoir de limitation intrinsèque de cadence. Foldcore est aujourd'hui une des entreprises les plus avancées autour de ces technologies.

2.3.5 Le programme Celpact

Le programme CELPACT (Cellular Structures for Impact Performance) rassemble partenaires industriels et scientifiques autour de l'étude de nouvelles structures sandwich. C'est un programme subventionné par la Commission Européenne à travers l'organisme European Aeronautics Science Network (N°AST5-CT-26-031038).

Le programme vise à étudier quantitativement des solutions concurrentes du nid d'abeilles (Herrmann et al., 2005). Le nid d'abeilles en Nomex® est en effet considéré comme trop cher à fabriquer. De plus, comme les cellules du nid d'abeilles sont fermées, un nouveau type de dommage caché est apparu. L'enchaînement des décollages et atterrissages provoque l'accumulation de condensation dans les cellules. L'eau finit par faire moisir le nid d'abeilles ce qui provoque des délaminages intempestifs. Ces deux raisons principales poussent donc à considérer de nouvelles structures dont les âmes pliées car elles sont ventilables (voir remarque sur l'application en échangeur de chaleur du module à chevrons, Section 2.1.2).

Le partenaire industriel moteur est EADS, représenté par Airbus Deutschland qui possède la propriété industrielle de la technologie développée à Kazan, mais on y retrouve aussi l'entreprise Foldcore. L'objectif est de comparer les capacités structurelles des deux types de produits et plus particulièrement la résistance aux chocs.

Du point de vue scientifique le programme regroupe sept institutions. On retiendra EADS Innovation Works, le Deutsches Zentrum für Luft und Raumfahrt et le LMT de l'ENS Cachan car ils ont travaillé de plus près sur les âmes pliées. Un certain nombre de publications sont sorties récemment et d'autres sont probablement à venir. L'orientation globale de ces travaux est de mettre en place des

techniques de simulation numérique reproduisant le plus fidèlement le comportement des âmes pliées et du nid d'abeilles en incluant les non-linéarités de toutes origines ainsi que des comportements endommageants pour fitter au mieux les courbes expérimentales. ("virtual materials" : (Heimbs et al., 2006, 2007, 2010; Heimbs, 2009; Nguyen et al., 2005a; Kintscher et al., 2007; Fischer et al., 2009; Baranger et al., 2010)). Mise à part l'étude de la résistance aux impacts, ces travaux très utiles pour la conception de ces nouveaux panneaux sandwichs s'intéressent tous à l'âme prise isolément, sans tenir compte de possibles interactions avec les peaux.

2.3.6 Rutgers University

L'université de Rutgers dans le New Jersey aux Etats-Unis travaille aussi indépendamment sur le sujet. Initialement une équipe formée par Basily, Elsayed et Kling a collaboré autour de la conception d'une machine brevetée Basily et al. (2006); Basily and Elsayed (2007) produisant en continu les âmes pliées. Basily and Elsayed ont travaillé sur la réalisation de la machine qui met en forme du papier et des métaux (Figure 2.20). Cependant, il semblerait que le produit finit soit de moins bonne qualité structurelle que celui proposé par Foldcore et que le procédé ne s'applique ni au Nomex®, ni aux fibres de carbone. Les applications citées sont d'ailleurs le packaging, les absorbeurs de chocs (Figure 2.21) et les échangeurs de chaleur (Figure 2.22), (Basily and Elsayed, 2004a,b; El-Sawi et al., 2010).

De son côté, Kling a travaillé sur la génération de motifs pliable présentée en Section 2.1.1 Kling (2005) et a créé sa société Folded Structures portant sur ces thématiques.

Figure 2.20 – La machine développée à l'université de Rutgers (Basily and Elsayed, 2004a)

Figure 2.21 – Étude sur les capacité d'absorption des chocs réalisée par Basily and Elsayed (2004b)

Figure 2.22 – Les panneaux solaires thermiques développés à l'université de Rutgers (El-Sawi et al., 2010)

2.4 Discussion

Comme on peut le voir, l'intérêt pour le module à chevrons et plus généralement les âmes pliées est assez ancien et a connu plusieurs foyers d'innovation (France, Japon, Russie, États-Unis). Ce constat impose immédiatement de s'interroger sur la raison pour laquelle ce type d'âme ne s'est pas répandu largement. En premier lieu, il n'est pas évident *a priori* de savoir si le module à chevrons est plus performant d'un point de vue structurel. En effet, la plupart des essais ont eu lieu avec des méthodes de fabrication relativement artisanales et on ne peut savoir si c'est un manque de qualité dans la réalisation ou un problème inhérent à la géométrie du motif qui fait que ces expériences n'ont pas été concluantes. En second lieu, il peut tout simplement s'agir d'un problème de marché. Dans le cas d'une application de masse, il y a un coût d'entrée conséquent, qui n'a peut être pas été surmonté jusqu'ici. Dans le cas de marchés de niche, peut être que les investissements requis pour obtenir un produit de meilleure qualité structurelle sont trop grands en proportion des ventes potentielles.

Aujourd'hui, ce constat semble remis en cause puisqu'un industriel de taille (EADS) s'intéresse à ce motif. De plus, comme on l'a déjà évoqué, la démocratisation des panneaux sandwichs permet d'imaginer qu'il va apparaître de nouveaux marchés dans lesquel les âmes pliées seront pertinentes. On pense en premier lieu au domaine de la construction où les exigence en matière structurelle sont moins grandes que l'aéronautique mais où les surfaces à produire peuvent très rapidement devenir grandes.

D'un point de vue scientifique, les âmes pliées sont un sujet qui a été essentiellement porté par les industriels et les ingénieurs. Ainsi, aujourd'hui l'ensemble des connaissances reste de l'ordre technologique et peu formalisé, bien que des travaux d'une qualité certaine commencent à émerger. Comme on l'a indiqué, l'évaluation d'une âme de panneau sandwich passe par la maîtrise de son comportement au cisaillement. On se propose donc d'utiliser pour le module à chevrons la toute

première méthode proposée pour estimer la raideur en cisaillement d'un panneau sandwich avec du nid d'abeilles dans le chapitre qui suit (Kelsey et al., 1958).

CHAPTER

3

Transverse shear stiffness of a chevron folded core used in sandwich construction

Dans ce chapitre, on applique la méthode de Kelsey et al. (1958) pour calculer des bornes encadrant la raideur en cisaillement transverse de l'âme d'un panneau sandwich. C'est l'occasion d'introduire un paramétrage précis du module à chevrons et d'étudier ses symétries. Ensuite, des bornes analytiques sont déterminées en supposant que les champs de contraintes et de déformation sont constants dans chaque facette du module à chevrons. Ces bornes conduisent à certaines solutions exactes mais restent insuffisantes pour estimer la raideur à l'effort tranchant dans les cas pratiques. Une validation des bornes analytiques est effectuée par un calcul éléments finis. Même si les bornes obtenues par ce calcul sont plus étroites que les bornes analytiques, dans les cas pratiques elles restent largement insuffisantes pour estimer précisément la flèche de cisaillement. On aura donc besoin d'une méthode plus élaborée pour calculer la raideur à l'effort tranchant.

Un résultat secondaire de ce travail est qu'il existe des configurations où la raideur totale à l'effort trachant $(\mathsf{F}_{11} + \mathsf{F}_{22})$ *du module à chevrons peut être de 40% supérieure à celle du nid d'abeilles. De plus, même si le module à chevrons est généralement orthotrope (les deux directions principales d'effort tranchant n'ont pas la même raideur), il existe un ensemble continu de configurations géométriques pour lesquelles il devient isotrope pour cette raideur.*

Ce chapitre a été publié dans la revue International Journal of Solids and Structures sous la référence Lebée and Sab (2010d).

Abstract

Using Kelsey, Gellatly, and Clark (1958) unit load method, upper and lower bounds for the effective transverse shear moduli of a chevron folded core used in sandwich construction are analytically derived and compared to finite element computations. We found that these bounds are generally loose and that in some cases chevron folded cores are 40% stiffer than honeycomb-like cores.

3.1 Introduction

Sandwich panels made of two thin skins separated by a thick periodic core structure are commonly used in many engineering applications. They offer a good compromise between strength and weight which is especially important in aeronautics.

When bending the sandwich panel, the skins are subjected to in-plane traction and compression whereas the core is subjected to transverse shear. Many constituents can be used as core materials. Balsa glued between stiffer pieces of wood was one of the first attempts to make a sandwich panel. Nowadays, organic compound foams (such as polyurethane foam) used with metallic skins are widespread in buildings as insulating panels. Phenolic paper honeycomb is extensively used in aeronautic structures.

Recently, new types of promising cores have emerged. Truss core panels using new welding techniques are raising interest because of their strength (Wicks and Hutchinson, 2001; Wadley, 2002; Cote et al., 2007). Folded cores are promising because of new production means (Basily and Elsayed, 2004b; Nguyen et al., 2005a; Heimbs et al., 2006; Kintscher et al., 2007). Among them, the chevron folded core was probably the first to be manufactured (Figure 3.1).

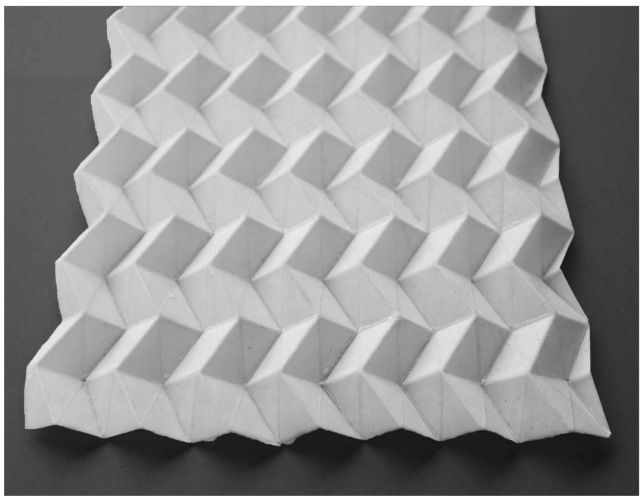

Figure 3.1: Chevron folded paper

It seems that chevron folded core manufacturing was first considered at the beginning of the 20^{th} century. Later, the pattern was under investigation in Kazan University. More recently, continuous production and several new techniques have emerged (Kling, 2005; Basily et al., 2006; Basily and Elsayed, 2004b; Kehrle, 2004).The strength of chevron folded cores has been experimentally investigated by Basily and Elsayed (2004b), Kintscher et al. (2007) and Nguyen et al. (2005a) and it has been numerically simulated by Nguyen et al. (2005a), Heimbs et al. (2006) and Heimbs (2009). Moreover, their transverse shear stiffness has been experimentally investigated by Kintscher et al.

(2007) but, to the authors knowledge, no theoretical work has been done yet [1].

The aim of this paper is to derive bounds for the transverse shear stiffness of chevron folded cores. Kelsey et al. (1958) first suggested a method for deriving such bounds for honeycomb-like cores. One may refer also to Gibson and Ashby (1988) for a detailed description of this method. Since then, many honeycomb geometries have been assessed (Hohe and Becker, 2002; Xu et al., 2001). New homogenization methods have been suggested. For instance, Hohe (2003) suggested the application of *ad hoc* boundary conditions reproducing transverse strain loading $\varepsilon_{\alpha 3}$ to a unit cell of the sandwich panel, including the skins, so that the interaction between the core and the skins was taken into account. Chen and Davalos (2005) suggested a semi-analytical approach in order to refine Kelsey et al. (1958) analysis close to the skins.

Yet, as a first attempt to determine the transverse shear stiffness of folded chevron, it seems relevant to use Kelsey et al. (1958) approach. Even if only bounds will be derived, it offers a quick and comprehensive view of chevron pattern stiffness, enables us to look for most efficient configurations and leads to exact solutions when bounds are equal.

The paper is organized as follows: Section 3.2 is devoted to the geometric description of the chevron pattern and the suggested analytical bounds are derived in Section 3.3. In order to assess the validity of these bounds, a finite element analysis on a representative unit cell is performed in Section 3.4. The final section gives an insight into future works.

3.2 The chevron pattern homogenized as Reissner-Mindlin plate model

Like honeycomb, the chevron pattern is periodic in the in-plane directions. Four identical parallelogram - shape faces are necessary to generate the whole pattern by periodicity along the $\widetilde{\boldsymbol{e}}_1$ vector (period $2a$) and the $\widetilde{\boldsymbol{e}}_2$ [2] vector (period $2s$) where $\mathcal{M} = (A, \widetilde{\boldsymbol{e}}_1, \widetilde{\boldsymbol{e}}_2, \widetilde{\boldsymbol{e}}_3)$ is the main coordinate system. Figure 3.2-a shows these faces: Face 1= $ABCD$, Face 2= $D'CBA'$, Face 3= $A'''B''CD'$ and Face 4 = $DCB''A''$.

Table 3.1 gives the vertices' coordinates in terms of four geometric parameters: a, s, v and t_c where v is a horizontal offset parameter ($v = 0$ when B is aligned with A and A') and t_c is the pattern height.

Actually, several parameter sets have been suggested for the geometric description of the chevron pattern (Basily and Elsayed, 2004b; Zakirov et al., 2008). Among them, the set a_0, b_0, δ, ζ fully determines the geometry and the position of Face 1. Face 1 is a parallelogram (a_0 and b_0 are the side

1. A la date de rédaction de cet article, les travaux de Miura (1972) m'étaient inconnus
2. D'une manière générale, dans ce mémoire les tenseurs sont en dimension 2 et 3. Comme les plaques font appel à de nombreuses variables en dimension 2, lorsqu'on manipule une variable en dimension 3 on l'indique par un $\widetilde{\bullet}$

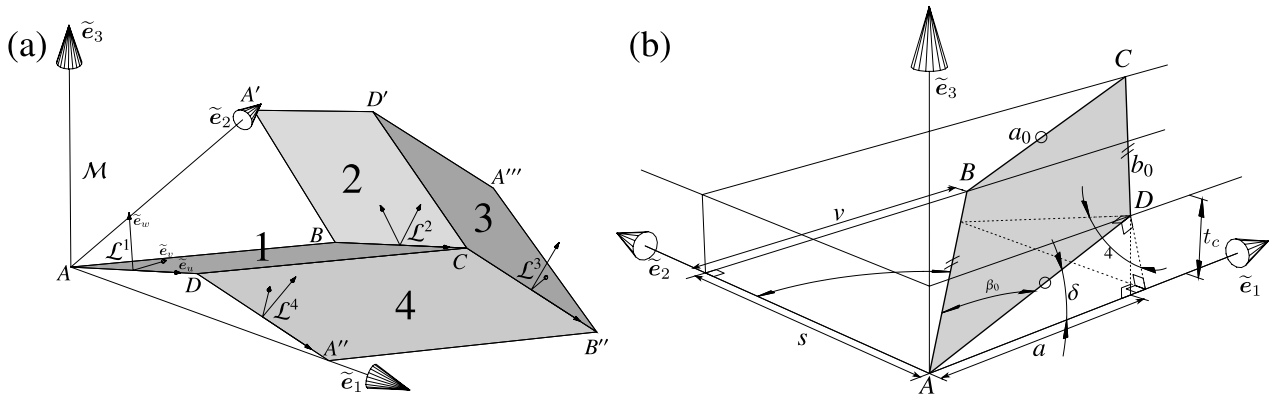

Figure 3.2: The four elementary faces of the pattern (a) and Face 1 orientation (b)

Vertex	A	B	C	D	A'	D'	A''	B''	A'''
x_1	0	v	$a+v$	a	0	a	$2a$	$2a+v$	$2a$
x_2	0	s	s	0	$2s$	$2s$	0	s	$2s$
x_3	0	0	t_c	t_c	0	t_c	0	0	0

Table 3.1: Vertices' coordinates

lengths) which is tilted by angles δ and ζ with respect to the main coordinate system, as shown in Figure 3.2-b:

- δ is the *member angle* by analogy with truss beams: cutting the chevron pattern by the $(A, \widetilde{\boldsymbol{e}}_1, \widetilde{\boldsymbol{e}}_3)$ plane gives a zigzag shape similar to that of a Warren-type truss beam.
- ζ is the *closure angle* equal to the half angle between Face 1 and Face 2 along the BC edge. For $\zeta = 0$, the pattern is completely folded and for $\zeta = \pi/2$, the pattern is prismatic.
- $\beta_0 = \arctan\left(\frac{\tan\delta}{\cos\zeta}\right)$ is DAB angle
- $\alpha = \arctan\left(\frac{1}{\tan\zeta\sin\delta}\right)$ is $A'AB$ angle

We have:

$$\begin{aligned} a &= a_0\cos\delta, \\ s &= b_0\cos\alpha, \\ v &= b_0\sin\alpha, \\ t_c &= a_0\sin\delta. \end{aligned}$$

Figure 3.3 shows the unit cell for several values of ζ, δ with $a_0/b_0 = 1$.

The chevron pattern has actually three major symmetries. When used as a core between two isotropic skins, these symmetries lead to several simplifications in the Reissner-Mindlin plate constitutive law (Reissner, 1985). The fully coupled constitutive law can be summarized as follows:

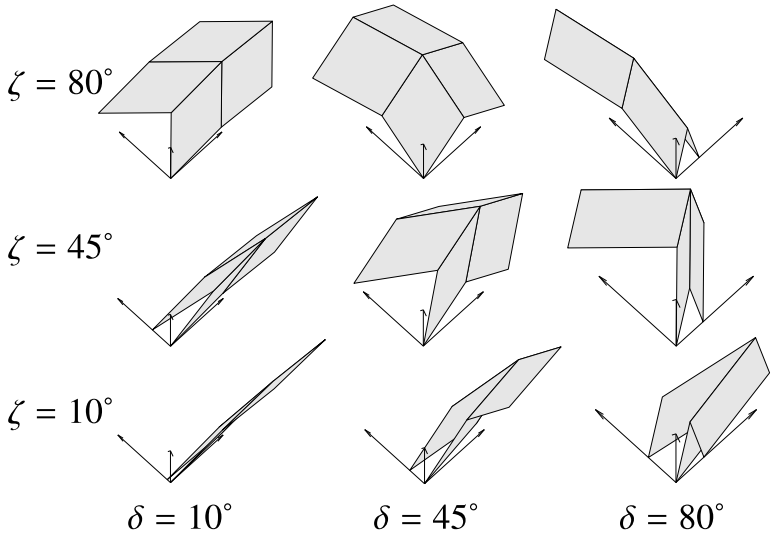

Figure 3.3: Chevron Pattern configurations for several δ and ζ angles and $a_0/b_0 = 1$

$$\begin{pmatrix} \mathsf{N}_{11} \\ \mathsf{N}_{22} \\ \mathsf{N}_{12} \\ \hline \mathsf{M}_{11} \\ \mathsf{M}_{22} \\ \mathsf{M}_{12} \\ \hline Q_1 \\ Q_2 \end{pmatrix} = \left(\begin{array}{ccc|ccc|cc} \mathcal{A}_{11} & \mathcal{A}_{12} & \mathcal{A}_{13} & \mathcal{B}_{11} & \mathcal{B}_{21} & \mathcal{B}_{31} & \mathsf{K}_{11} & \mathsf{K}_{12} \\ \mathcal{A}_{12} & \mathcal{A}_{22} & \mathcal{A}_{23} & \mathcal{B}_{12} & \mathcal{B}_{22} & \mathcal{B}_{32} & \mathsf{K}_{21} & \mathsf{K}_{22} \\ \mathcal{A}_{13} & \mathcal{A}_{23} & \mathcal{A}_{33} & \mathcal{B}_{13} & \mathcal{B}_{23} & \mathcal{B}_{33} & \mathsf{K}_{31} & \mathsf{K}_{32} \\ \hline \mathcal{B}_{11} & \mathcal{B}_{12} & \mathcal{B}_{13} & \mathcal{D}_{11} & \mathcal{D}_{12} & \mathcal{D}_{13} & \mathsf{L}_{41} & \mathsf{L}_{42} \\ \mathcal{B}_{21} & \mathcal{B}_{22} & \mathcal{B}_{23} & \mathcal{D}_{12} & \mathcal{D}_{22} & \mathcal{D}_{23} & \mathsf{L}_{51} & \mathsf{L}_{52} \\ \mathcal{B}_{31} & \mathcal{B}_{32} & \mathcal{B}_{33} & \mathcal{D}_{13} & \mathcal{D}_{23} & \mathcal{D}_{33} & \mathsf{L}_{61} & \mathsf{L}_{62} \\ \hline \mathsf{K}_{11} & \mathsf{K}_{21} & \mathsf{K}_{31} & \mathsf{L}_{41} & \mathsf{L}_{51} & \mathsf{L}_{61} & \mathsf{F}_{11} & \mathsf{F}_{12} \\ \mathsf{K}_{12} & \mathsf{K}_{22} & \mathsf{K}_{32} & \mathsf{L}_{42} & \mathsf{L}_{52} & \mathsf{L}_{62} & \mathsf{F}_{12} & \mathsf{F}_{22} \end{array}\right) \cdot \begin{pmatrix} \mathsf{e}_{11} \\ \mathsf{e}_{22} \\ 2\mathsf{e}_{12} \\ \hline \chi_{11} \\ \chi_{22} \\ 2\chi_{12} \\ \hline \gamma_1 \\ \gamma_2 \end{pmatrix} \tag{3.1}$$

where $\mathsf{N}_{\alpha\beta}$ are the membrane generalized stress components, $\mathsf{M}_{\alpha\beta}$ are the bending moment components, Q_α are the shear forces, $\mathsf{e}_{\alpha\beta}$ are the in-plane strains, $\chi_{\alpha\beta}$ are the curvatures and γ_α are the out-of-plane shear strains. Generalized strains are illustrated on Fig. 3.4. $\mathcal{A}_{ij}$, $\mathcal{B}_{ij}$ and $\mathcal{D}_{ij}$ are the usual Love-Kirchhoff plate stiffnesses. $\mathsf{F}_{\alpha\beta}$ is the usual Reissner shear stiffness. $\mathsf{K}_{\alpha i}$ and $\mathsf{L}_{\alpha i}$ are a possible couplings between ($\mathsf{N}_{\alpha\beta}$, $\mathsf{M}_{\alpha\beta}$) and Q_α.

Due to the rotational symmetry $\mathcal{S}$ of axis $(S, \widetilde{\boldsymbol{e}}_3)$, shown in Figure 3.5-a, we have $\mathsf{K}_{\alpha i} = \mathsf{L}_{\alpha i} = 0$. Figure 3.5-b shows the central symmetry $\mathcal{R}$ with respect to the center point of Face 1, R. This symmetry uncouples membrane stresses and flexural stresses: $\mathcal{B}_{ij} = 0$ (similar to mirror symmetry for laminates). Figure 3.5-c shows the symmetry $\mathcal{N}$ with respect to the $(B, \widetilde{\boldsymbol{e}}_1, \widetilde{\boldsymbol{e}}_3)$ plane. This symmetry sets $\mathcal{A}_{13} = \mathcal{A}_{23} = \mathcal{D}_{13} = \mathcal{D}_{23} = \mathsf{F}_{12} = 0$. Thus, it uncouples transverse shear stresses.

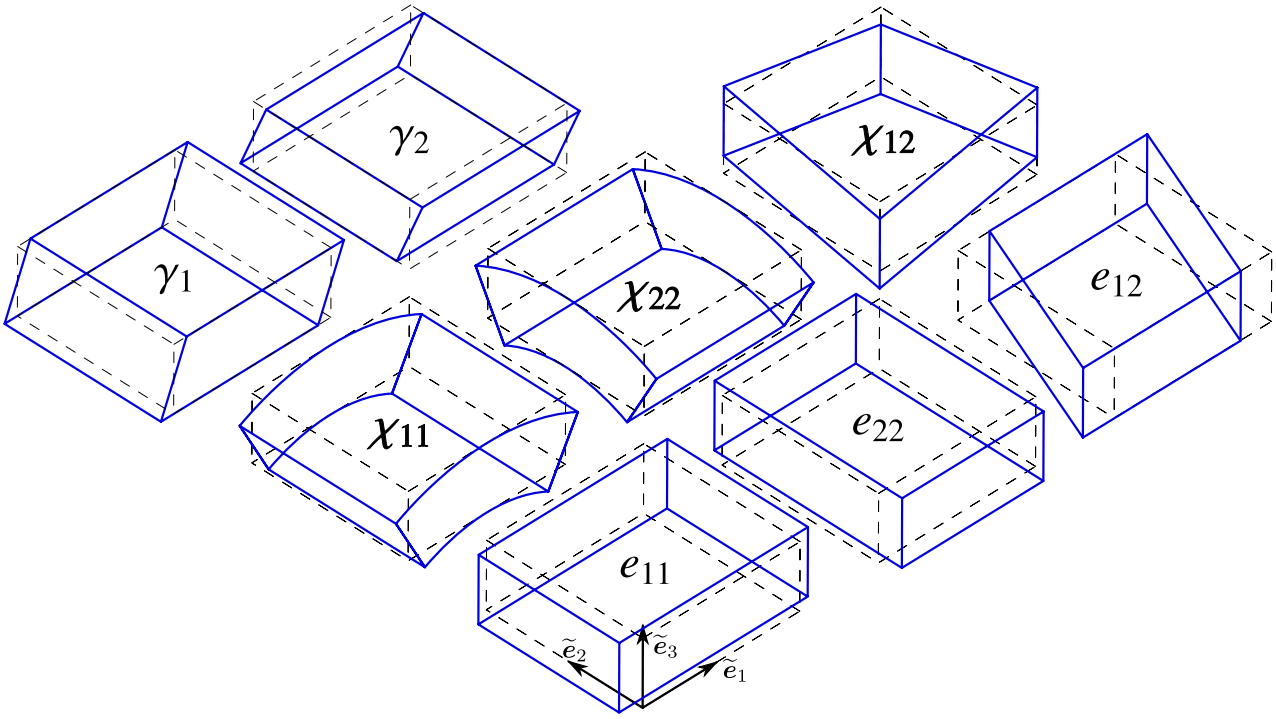

Figure 3.4: Reissner-Mindlin generalized strains

Taking into account all uncouplings leads to the following constitutive law [3]:

$$\left(\begin{array}{c} \mathsf{N}_{11} \\ \mathsf{N}_{22} \\ \mathsf{N}_{12} \\ \hline \mathsf{M}_{11} \\ \mathsf{M}_{22} \\ \mathsf{M}_{12} \\ \hline Q_1 \\ Q_2 \end{array}\right) = \left(\begin{array}{ccc|ccc|cc} \mathcal{A}_{11} & \mathcal{A}_{12} & 0 & 0 & 0 & 0 & 0 & 0 \\ \mathcal{A}_{12} & \mathcal{A}_{22} & 0 & 0 & 0 & 0 & 0 & 0 \\ 0 & 0 & \mathcal{A}_{33} & 0 & 0 & 0 & 0 & 0 \\ \hline 0 & 0 & 0 & \mathcal{D}_{11} & \mathcal{D}_{12} & 0 & 0 & 0 \\ 0 & 0 & 0 & \mathcal{D}_{12} & \mathcal{D}_{22} & 0 & 0 & 0 \\ 0 & 0 & 0 & 0 & 0 & \mathcal{D}_{33} & 0 & 0 \\ \hline 0 & 0 & 0 & 0 & 0 & 0 & \mathsf{F}_{11} & 0 \\ 0 & 0 & 0 & 0 & 0 & 0 & 0 & \mathsf{F}_{22} \end{array}\right) \cdot \left(\begin{array}{c} \mathsf{e}_{11} \\ \mathsf{e}_{22} \\ 2\mathsf{e}_{12} \\ \hline \chi_{11} \\ \chi_{22} \\ 2\chi_{12} \\ \hline \gamma_1 \\ \gamma_2 \end{array}\right) \tag{3.2}$$

The symmetries described above are respectively associated with the following matrices in the reference frame $(\widetilde{e}_1, \widetilde{e}_2, \widetilde{e}_3)$:

$$\widetilde{\mathsf{P}}^{\mathcal{R}} = \begin{pmatrix} -1 & 0 & 0 \\ 0 & -1 & 0 \\ 0 & 0 & -1 \end{pmatrix}, \quad \widetilde{\mathsf{P}}^{\mathcal{N}} = \begin{pmatrix} 1 & 0 & 0 \\ 0 & -1 & 0 \\ 0 & 0 & 1 \end{pmatrix}, \quad \widetilde{\mathsf{P}}^{\mathcal{S}} = \begin{pmatrix} -1 & 0 & 0 \\ 0 & -1 & 0 \\ 0 & 0 & 1 \end{pmatrix}. \tag{3.3}$$

3. Ces découplages sont justifiés en détail en Section 4.A.1

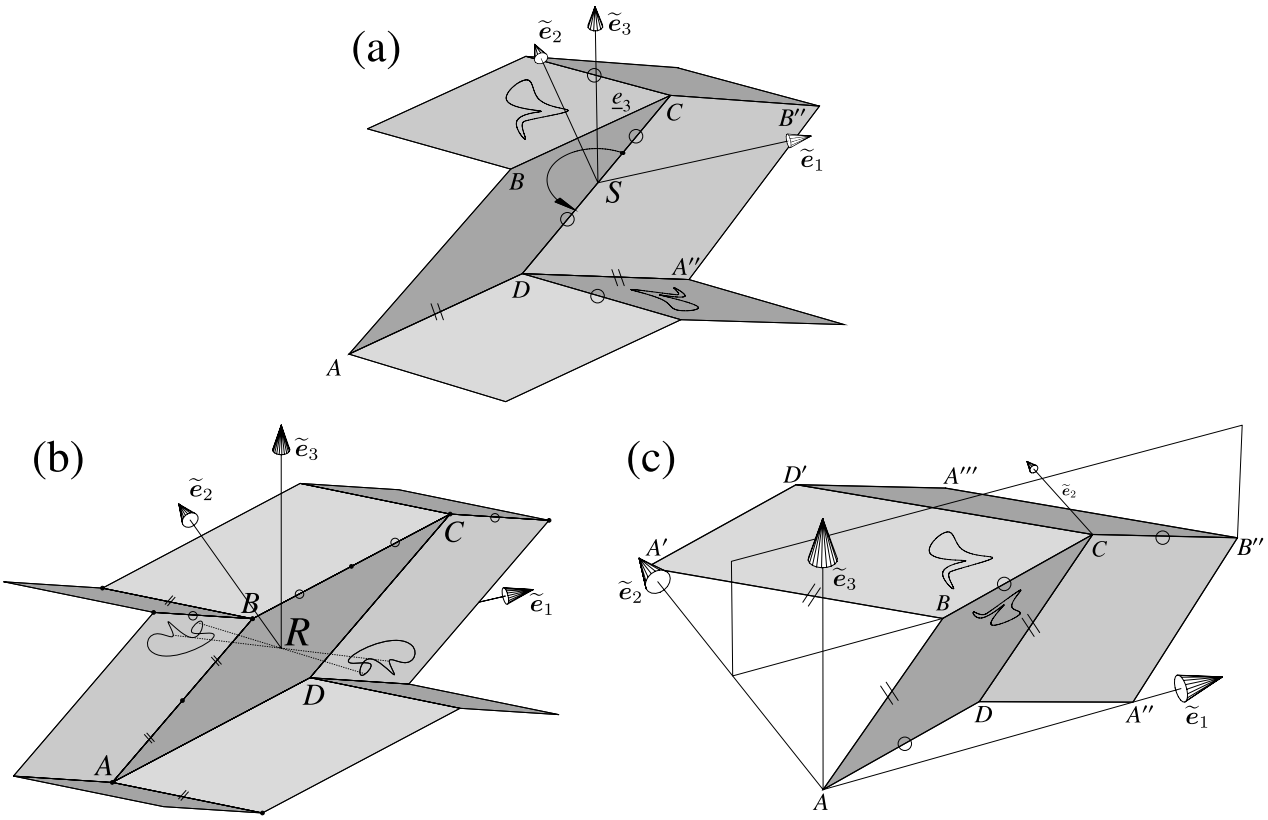

Figure 3.5: Rotational symmetry with respect to $(S, \widetilde{e}_3)$ (a). Central symmetry with respect to point R (b). Symmetry with respect to $(B, \widetilde{e}_1, \widetilde{e}_3)$ plane (c)

It is useful to introduce a local basis $\mathcal{L}^k = (\widetilde{\boldsymbol{e}}_u^k, \widetilde{\boldsymbol{e}}_v^k, \widetilde{\boldsymbol{e}}_w^k)$ associated to Face k ($k = 1, 2, 3, 4$) as shown in Figure 3.2. For Face 1, vector $\widetilde{\boldsymbol{e}}_u^1$ is along the AD edge, $\widetilde{\boldsymbol{e}}_w^1$ is normal to the face with $\widetilde{\boldsymbol{e}}_w^1 \cdot \widetilde{\boldsymbol{e}}_3 > 0$ and $\widetilde{\boldsymbol{e}}_v^1$ is such that $\mathcal{L}^1$ is direct. Thus, the components of $(\widetilde{\boldsymbol{e}}_u^1, \widetilde{\boldsymbol{e}}_v^1, \widetilde{\boldsymbol{e}}_w^1)$ in the $(\widetilde{\boldsymbol{e}}_1, \widetilde{\boldsymbol{e}}_2, \widetilde{\boldsymbol{e}}_3)$ basis are given by:

$$(\widetilde{\boldsymbol{e}}_u^1, \widetilde{\boldsymbol{e}}_v^1, \widetilde{\boldsymbol{e}}_w^1) = \widetilde{\mathsf{P}}^{\mathcal{L}^1} = \begin{pmatrix} \cos\delta & \sin\zeta\cos\delta & -\sin\delta\sin\zeta \\ 0 & \sin\zeta & \cos\zeta \\ \sin\delta & -\cos\delta\cos\zeta & \cos\delta\sin\zeta \end{pmatrix}_{(\widetilde{\boldsymbol{e}}_1, \widetilde{\boldsymbol{e}}_2, \widetilde{\boldsymbol{e}}_3)} . \tag{3.4}$$

Moreover, the symmetry matrices enables the determination of the components of the other local basis $\mathcal{L}^2$, $\mathcal{L}^3$ and $\mathcal{L}^4$:

$$(\widetilde{\boldsymbol{e}}_u^2, \widetilde{\boldsymbol{e}}_v^2, \widetilde{\boldsymbol{e}}_w^2) = \widetilde{\mathsf{P}}^{\mathcal{N}} : \widetilde{\mathsf{P}}^{\mathcal{L}^1} : \widetilde{\mathsf{P}}^{\mathcal{N}} = \widetilde{\mathsf{P}}^{\mathcal{L}^2} = \begin{pmatrix} \cos\delta & -\sin\zeta\cos\delta & -\sin\delta\sin\zeta \\ 0 & \sin\zeta & -\cos\zeta \\ \sin\delta & \cos\delta\cos\zeta & \cos\delta\sin\zeta \end{pmatrix}_{(\widetilde{\boldsymbol{e}}_1, \widetilde{\boldsymbol{e}}_2, \widetilde{\boldsymbol{e}}_3)} \tag{3.5}$$

$$(\widetilde{\boldsymbol{e}}_u^3, \widetilde{\boldsymbol{e}}_v^3, \widetilde{\boldsymbol{e}}_w^3) = \widetilde{\mathsf{P}}^{\mathcal{S}} : \widetilde{\mathsf{P}}^{\mathcal{N}} : \widetilde{\mathsf{P}}^{\mathcal{L}^1} : \widetilde{\mathsf{P}}^{\mathcal{N}} : \widetilde{\mathsf{P}}^{\mathcal{S}} = \widetilde{\mathsf{P}}^{\mathcal{L}^3} = \begin{pmatrix} \cos\delta & -\sin\zeta\cos\delta & \sin\delta\sin\zeta \\ 0 & \sin\zeta & \cos\zeta \\ -\sin\delta & -\cos\delta\cos\zeta & \cos\delta\sin\zeta \end{pmatrix}_{(\widetilde{\boldsymbol{e}}_1, \widetilde{\boldsymbol{e}}_2, \widetilde{\boldsymbol{e}}_3)} \tag{3.6}$$

$$(\widetilde{\boldsymbol{e}}_u^4, \widetilde{\boldsymbol{e}}_v^4, \widetilde{\boldsymbol{e}}_w^4) = \widetilde{\mathsf{P}}^{\mathcal{S}} : \widetilde{\mathsf{P}}^{\mathcal{L}^1} : \widetilde{\mathsf{P}}^{\mathcal{S}} = \widetilde{\mathsf{P}}^{\mathcal{L}^4} = \begin{pmatrix} \cos\delta & \sin\zeta\cos\delta & \sin\delta\sin\zeta \\ 0 & \sin\zeta & -\cos\zeta \\ -\sin\delta & \cos\delta\cos\zeta & \cos\delta\sin\zeta \end{pmatrix}_{(\widetilde{\boldsymbol{e}}_1, \widetilde{\boldsymbol{e}}_2, \widetilde{\boldsymbol{e}}_3)} \tag{3.7}$$

In sandwich panels, the membrane and flexural moduli are usually derived assuming that the core structure does not contribute to the overall stiffness. It is also assumed for transverse shear stiffness that $\mathsf{F}_{\alpha\beta} = h\mathsf{C}^{\text{eff}}_{\alpha\beta}$ where $\mathbf{C}^{\text{eff}}$ is the effective shear stiffness of the core. Finally, regarding shear behavior, there are only two transverse shear moduli to determine: $\mathsf{C}^{\text{eff}}_{11}$ and $\mathsf{C}^{\text{eff}}_{22}$.

3.3 Analytical bounds

According to the approach of Kelsey et al. (1958), the minimum potential energy theorem is used to derive upper bounds for the effective transverse shear modulus in the $\alpha-$ direction, $\mathsf{C}^{\text{eff}}_{\alpha\alpha}$. A uniform horizontal displacement $t_c\gamma_{\alpha 3}$ in the $\alpha-$direction is imposed on the top face of the core material while its lower face is fixed. Here, $\alpha = 1, 2$ are the in-plane directions, $\gamma_{\alpha 3}$ is the out-of-plane shear strain in the $\alpha-$direction and t_c is the height of the core. Then, the normalized strain energy of any trial strain field which is piecewise uniform in the core walls and compatible with the kinematic boundary conditions provides an upper bound for $\mathsf{C}^{\text{eff}}_{\alpha\alpha}$, noted $\mathsf{C}^{K+}_{\alpha\alpha}$. Similarly, the minimum complementary energy theorem is used for deriving lower bounds for $\mathsf{C}^{\text{eff}}_{\alpha\alpha}$. A uniform

horizontal stress load $\tau_{\alpha 3}$ (respectively, $-\tau_{\alpha 3}$) is applied in the $\alpha-$direction to the upper (respectively, lower) face of the core material. Then, the normalized stress energy of any piecewise uniform trial stress field which is statically compatible with the boundary conditions provides a lower bound for $C^{\text{eff}}_{\alpha\alpha}$, noted $C^{K-}_{\alpha\alpha}$.

3.3.1 Lower bounds

A uniformly distributed horizontal force per unit length, $\widetilde{\boldsymbol{f}}^{\pm}$, is applied to the upper $(-)$ and lower edges $(+)$ of the pattern. Figure 3.6-a shows $\widetilde{\boldsymbol{f}}^{\pm}$ for transverse shear loading in Direction 1, τ_1:

$$\widetilde{\boldsymbol{f}}^{\pm} = \pm 2 \frac{a\, s}{b_0} \tau_1 \widetilde{\boldsymbol{e}}_1 \ , \tag{3.8}$$

and Figure 3.6-b shows $\widetilde{\boldsymbol{f}}^{\pm}$ for transverse shear loading in Direction 2, τ_2:

$$\widetilde{\boldsymbol{f}}^{\pm} = \pm 2 \frac{a\, s}{b_0} \tau_2 \widetilde{\boldsymbol{e}}_2 . \tag{3.9}$$

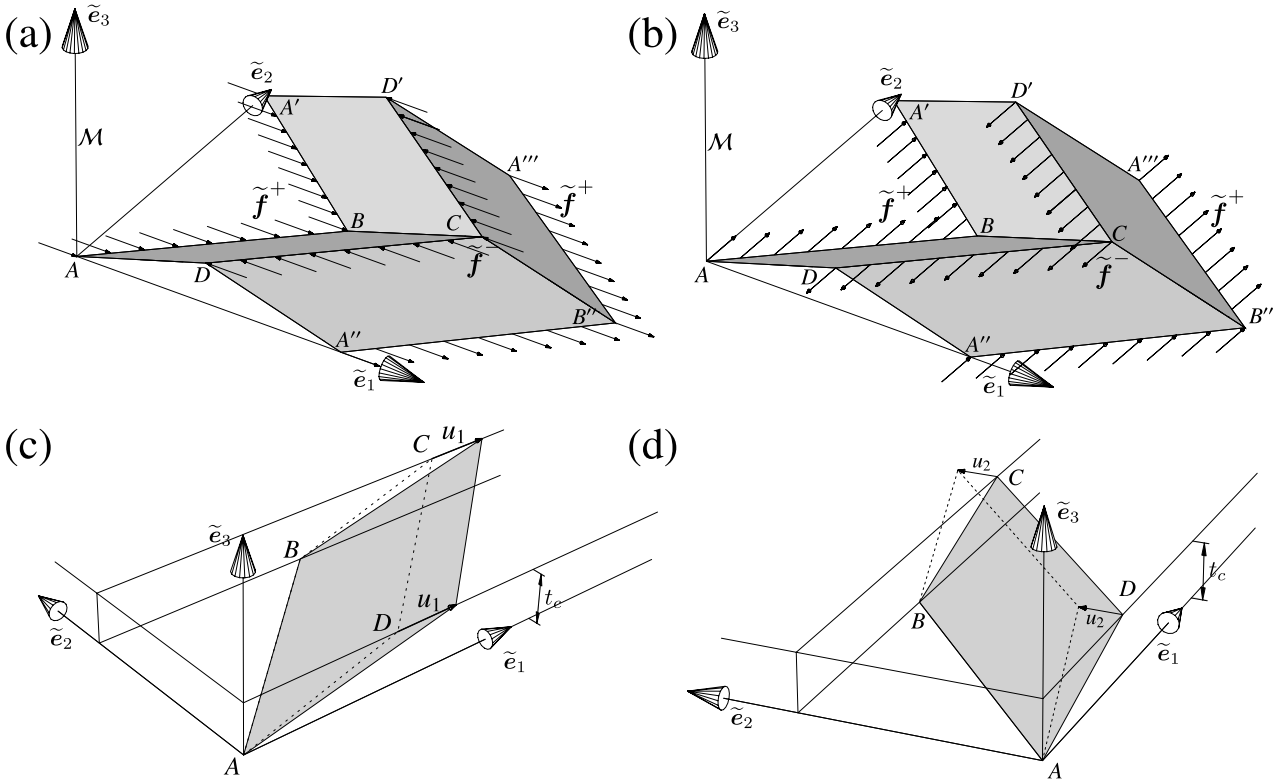

Figure 3.6: Stress load in Direction 1: (a) and in Direction 2: (b). Face 1 displacement in Direction 1: (c) and in Direction 2: (d)

Piecewise uniform plane stress is assumed for each face. Hence, the stress of Face 1 writes:

$$\widetilde{\boldsymbol{\sigma}}^1 = \sigma^1_{uu}\widetilde{\boldsymbol{e}}^1_u \otimes \widetilde{\boldsymbol{e}}^1_u + \sigma^1_{vv}\widetilde{\boldsymbol{e}}^1_v \otimes \widetilde{\boldsymbol{e}}^1_v + \sigma^1_{uv}\left(\widetilde{\boldsymbol{e}}^1_u \otimes \widetilde{\boldsymbol{e}}^1_v + \widetilde{\boldsymbol{e}}^1_v \otimes \widetilde{\boldsymbol{e}}^1_u\right) \tag{3.10}$$

where $\otimes$ is the dyadic product of two vectors and σ^1_{uu}, σ^1_{vv}, σ^1_{uv} are three unknowns to be determined. Thanks to $\mathcal{N}$ and $\mathcal{S}$ symmetries of the pattern and the considered loadings, it is possible to express the stress $\widetilde{\boldsymbol{\sigma}}^k$ of Face k, $k = 2, 3, 4$, in terms of $\widetilde{\boldsymbol{\sigma}}^1$. Indeed, the following relations are easily derived:

$$\widetilde{\boldsymbol{\sigma}}^2 = \epsilon\,\widetilde{\mathbf{P}}^{\mathcal{N}} : \widetilde{\boldsymbol{\sigma}}^1 : \widetilde{\mathbf{P}}^{\mathcal{N}}, \qquad \widetilde{\boldsymbol{\sigma}}^4 = -\widetilde{\mathbf{P}}^{\mathcal{S}} : \widetilde{\boldsymbol{\sigma}}^1 : \widetilde{\mathbf{P}}^{\mathcal{S}}, \qquad \widetilde{\boldsymbol{\sigma}}^3 = \epsilon\,\widetilde{\mathbf{P}}^{\mathcal{N}} : \widetilde{\boldsymbol{\sigma}}^4 : \widetilde{\mathbf{P}}^{\mathcal{N}}, \tag{3.11}$$

where $\epsilon = 1$ for loading in Direction 1 and $\epsilon = -1$ for loading in Direction 2.

The equilibrium condition at edge AD (or edge BC) is written as:

$$\widetilde{\boldsymbol{\sigma}}^1 \cdot \widetilde{\boldsymbol{e}}^1_v + \widetilde{\boldsymbol{\sigma}}^2 \cdot \left(-\widetilde{\boldsymbol{e}}^2_v\right) = \widetilde{\mathbf{0}} \tag{3.12}$$

Similarly, the equilibrium condition at edge CD (or edge AB) writes:

$$-t_f\left(\widetilde{\boldsymbol{\sigma}}^1 \cdot \widetilde{\boldsymbol{n}}^1 + \widetilde{\boldsymbol{\sigma}}^4 \cdot \widetilde{\boldsymbol{n}}^4\right) + \widetilde{\boldsymbol{f}}^+ = 0 \tag{3.13}$$

where t_f is the faces' thickness and $\widetilde{\boldsymbol{n}}^k$ is the outer normal of Face $k = 1, 4$ along CD ($\widetilde{\boldsymbol{n}}^k$ belongs to Face k plane):

$$\widetilde{\boldsymbol{n}}^1 = -\sin\beta_0\widetilde{\boldsymbol{e}}^1_u + \cos\beta_0\widetilde{\boldsymbol{e}}^1_v \qquad \widetilde{\boldsymbol{n}}^4 = \sin\beta_0\widetilde{\boldsymbol{e}}^4_u - \cos\beta_0\widetilde{\boldsymbol{e}}^4_v \tag{3.14}$$

The six (non independent) linear equations (3.12-3.13) uniquely determine the three unknowns σ^1_{uu}, σ^1_{vv}, σ^1_{uv}. The solution is:

loading in Direction 1:	loading in Direction 2:
$\sigma^1_{uu} = -\frac{a_0\tau_1}{t_f}\sin\zeta$	$\sigma^1_{uu} = -\frac{a_0\tau_2}{t_f}\left(\frac{1}{\tan\delta} - \tan\delta\right)\cos\zeta\cos\delta$
$\sigma^1_{vv} = 0$	$\sigma^1_{vv} = 0$
$\sigma^1_{uv} = 0$	$\sigma^1_{uv} = -\frac{a_0\tau_2}{t_f}\cos\delta$

The faces' constitutive material is assumed to be isotropic[4]. Hence, the total stress energy of the unit cell is given by:

$$V^*_{int} = 2\sin\beta_0 b_0 a_0 t_f\left(\frac{2(1+\nu_m)}{E_m}(\sigma^1_{uv})^2 + \frac{1}{E_m}(\sigma^1_{uu})^2\right) \tag{3.15}$$

where E_m and ν_m are the constitutive material Young modulus and Poisson's ratio. The stress energy

4. This is the case for metallic cores and for Nomex paper core. For CFRP cores, anisotropy has to be introduced.

of the effective core material subjected to the transverse shear stress τ_α in the direction α is:

$$V^*_{ext} = 2at_c s \frac{\tau_\alpha^2}{\mathsf{C}^{\text{eff}}_{\alpha\alpha}}. \tag{3.16}$$

The theorem of the complementary energy states that $V^*_{ext} \leq V^*_{int}$. Inserting the expressions of σ^1_{uu} and σ^1_{uv} into (3.15) gives the lower bounds:

$$\begin{aligned}
\mathsf{C}^{\text{eff}}_{11} &\geq \mathsf{C}^{K-}_{11} = \tfrac{t_f}{a_0} E_m \ \tfrac{\sin\delta\cos\delta}{\sin\zeta}, \\
\mathsf{C}^{\text{eff}}_{22} &\geq \mathsf{C}^{K-}_{22} = \tfrac{t_f}{a_0} E_m \ \tfrac{\sin\delta}{\cos\delta} \ \frac{\sin\zeta}{2(1+\nu_m)+\left(\frac{1}{\tan\delta}-\tan\delta\right)^2\cos^2\zeta}.
\end{aligned}$$

It is more convenient to use the following normalization:

$$\mathcal{E}_\alpha = \frac{\mathsf{C}^{\text{eff}}_{\alpha\alpha}}{\rho G_m} \tag{3.17}$$

where ρ is the core relative density, G_m is the solid shear modulus and $\mathcal{E}_\alpha$ is the normalized transverse shear modulus in direction α. For chevron cores, ρ is given by:

$$\rho = \frac{t_f}{a_0 \sin\zeta \sin\delta \cos\delta}. \tag{3.18}$$

Hence, we have:

$$\begin{aligned}
\mathcal{E}_1 &\geq \mathcal{E}_1^- = 2(1+\nu_m) \ \sin^2\delta\cos^2\delta, \\
\mathcal{E}_2 &\geq \mathcal{E}_2^- = 2(1+\nu_m) \ \frac{\sin^2\delta\sin^2\zeta}{2(1+\nu_m)+\left(\frac{1}{\tan\delta}-\tan\delta\right)^2\cos^2\zeta}.
\end{aligned}$$

3.3.2 Upper bounds

In order to derive an upper bound for the transverse shear modulus $G_{\alpha 3}$, a relative horizontal displacement, $\gamma_\alpha t_c$, between the top and the bottom of the chevron pattern is prescribed in the direction α as shown in Figure 3.6-(c,d). The corresponding overall transformation is:

$$\widetilde{\mathsf{F}} = \widetilde{\boldsymbol{\delta}} + \gamma_\alpha \widetilde{\boldsymbol{e}}_\alpha \otimes \widetilde{\boldsymbol{e}}_3 \tag{3.19}$$

where $\widetilde{\boldsymbol{\delta}}$ is the unit second order tensor.

The in-plane components of the uniform Green-Lagrange strain tensor of Face 1 with respect to the $(\widetilde{\boldsymbol{e}}^1_u, \widetilde{\boldsymbol{e}}^1_v)$ local basis are given by:

$$\mathsf{e}^1_{\lambda\mu} = \frac{1}{2}\left(\widetilde{\boldsymbol{e}}^{1*}_\lambda \cdot \widetilde{\boldsymbol{e}}^{1*}_\mu - \delta_{\lambda\mu}\right) \qquad \lambda,\mu = u,v, \tag{3.20}$$

where $\widetilde{\boldsymbol{e}}_\lambda^{1*} = \widetilde{\mathbf{F}} \cdot \widetilde{\boldsymbol{e}}_\lambda^1$, and $\delta_{\lambda\mu}$ is the Krönecker symbol. Neglecting the second order terms in γ_α leads to the following linearized in-plane strain components:

loading in Direction 1:	loading in Direction 2:
$\varepsilon_{uu}^1 = \gamma_1 \sin\delta\cos\delta$	$\varepsilon_{uu}^1 = 0$
$\varepsilon_{vv}^1 = -\gamma_1 \sin\delta\cos\delta\cos^2\zeta$	$\varepsilon_{vv}^1 = -\gamma_2 \cos\zeta\sin\zeta\cos\delta$
$\varepsilon_{uv}^1 = -\frac{\gamma_1}{2}\cos 2\delta\cos\zeta$	$\varepsilon_{uv}^1 = \frac{\gamma_2}{2}\sin\zeta\sin\delta$

Piecewise uniform plane stress is assumed in each face. Therefore, the strain energy density of Face 1 is given by:

$$w = \frac{1}{2}\left(\frac{E_m}{1+\nu_m}\left((\varepsilon_{uu}^1)^2 + (\varepsilon_{vv}^1)^2 + 2(\varepsilon_{uv}^1)^2\right) + \frac{\nu_m E_m}{1-\nu_m^2}\left(\varepsilon_{uu}^1 + \varepsilon_{vv}^1\right)^2\right). \tag{3.21}$$

The total strain energy stored in the unit cell is:

$$V_{int} = 2\sin\beta_0 b_0 a_0 t_f w. \tag{3.22}$$

The strain energy stored in the effective core material is:

$$V_{ext} = 2at_c s\mathsf{C}_{\alpha\alpha}^{\text{eff}}\gamma_\alpha^2. \tag{3.23}$$

According to the potential energy theorem, we have $V_{ext} \leq V_{int}$. Hence, the following upper bounds for the normalized transverse shear moduli are obtained:

$$\mathcal{E}_1 \leq \mathcal{E}_1^+ = \tfrac{2}{1-\nu_m}\sin^2\delta\cos^2\delta\sin^4\zeta + \cos^2\zeta$$
$$\mathcal{E}_2 \leq \mathcal{E}_2^+ = \left(\tfrac{2}{1-\nu_m}\cos^2\delta\cos^2\zeta + \sin^2\delta\right)\sin^2\zeta$$

3.3.3 Results

As expected, for both directions, we have:

$$0 < \mathcal{E}_\alpha^- \leq \mathcal{E}_\alpha^+ < 1$$

where $\mathcal{E} = 1$ corresponds to the Voigt upper bound and $\mathcal{E} = 0$ corresponds to the Reuss lower bound. It should be emphasized that the derived bounds are independent of the shape ratio a_0/b_0. They are only functions of ν_m and the angles ζ and δ.

Figure 3.7-(a,b) shows the normalized lower and upper bounds in Direction 1 as functions of δ and ζ for $\nu_m = 0.4$. It is possible to give a simple interpretation for the lower bound $\mathcal{E}_1^-$. The corresponding trial stress has only one non-zero component: σ_{uu}. All the faces are subjected to

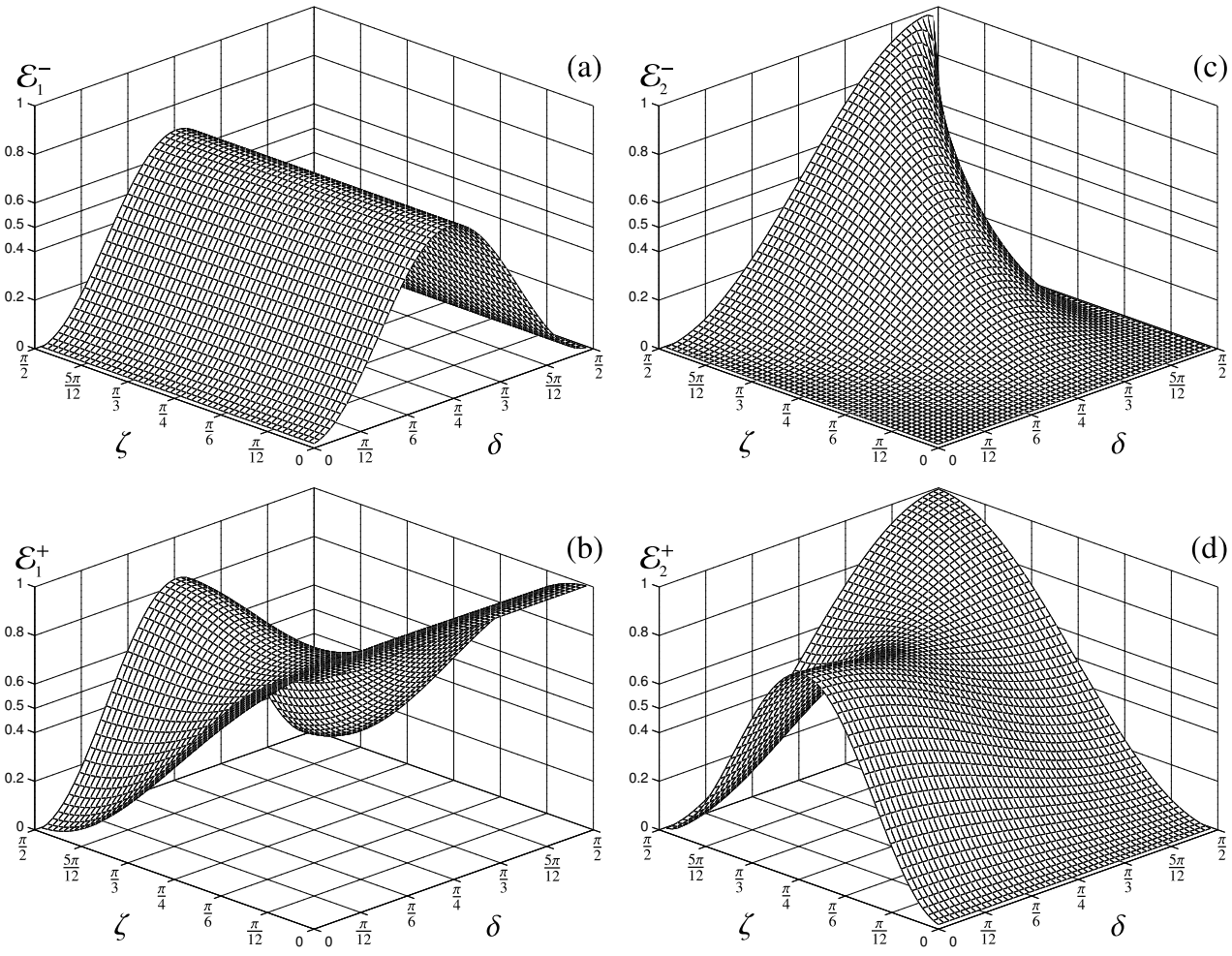

Figure 3.7: Analytical bounds $\mathcal{E}$ for both directions as the function of ζ and δ for $\nu_m = 0.4$ and $a_0/b_0 = 1$

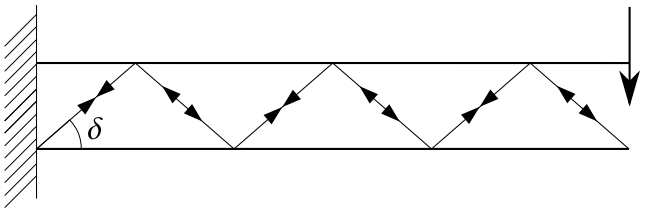

Figure 3.8: Warren truss beam

uni-axial traction and compression in the $\widetilde{e}_u$ direction. This structural behavior can be compared to Warren truss beams (Figure 3.8) where members are under alternative traction and compression. Hence, it is not surprising that the lower bound depends only on the member angle δ and is maximum for $\delta = \pi/4$ as for Warren truss beams. For most values of ζ and δ, $\mathcal{E}_1^-$ and $\mathcal{E}_1^+$ are not equal. However, for $\delta = \pi/4$ and $\cos^2\zeta = \nu_m$, they are coincident ($\mathcal{E}_1^- = \mathcal{E}_1^+ = \frac{1+\nu_m}{2}$). This means that, for this geometric configuration, the piecewise uniform trial strain and stress fields are the exact solutions for the transverse shear loading in Direction 1.

Figure 3.7-(c,d) shows the normalized lower and upper bounds in Direction 2. The trial stress field associated to $\mathcal{E}_2^-$ is mainly in-plane shear of the core walls as is the case for a honeycomb-like core. For $\zeta = \pi/2$, the pattern is prismatic and both bounds are equal to $\sin^2\delta$ which is an exact value for $\mathcal{E}_2$. Actually, prismatic cores are not used much in sandwich panels because they are not resistant enough. When decreasing ζ from $\pi/2$, the prismatic pattern becomes wavy and this waviness increases the faces' buckling strength under transverse shear loading in Direction 1.

3.4 Finite element bounds

The analytical bounds suggested in the previous section are based on the piecewise uniform stress or strain assumption. In order to assess the validity of this assumption, a Finite Element analysis is conducted. The resulting numerical bounds will be compared to the analytical bounds.

3.4.1 The finite element model

The computation of the transverse shear moduli for both directions and both loading cases (stress and displacement) has been performed within the linear elasticity framework. The unit cell of Figure 3.2 is chosen as a representative volume element.

Since faces are very thin, Kirchhoff shell elements are used. Four elements of the ABAQUS software (triangles P1 (STRI3), triangles P2 (STRI65), quadrangles P1 (S4R5) and quadrangles P2 (S8R5)) were tested and compared through a convergence analysis (ABAQUS, 2007b). Element S4R5 with a 441 node mesh gives accurate results for a low computation cost.

Boundary conditions involve both nodal displacements $\widetilde{\boldsymbol{U}}$ and rotations $\widetilde{\boldsymbol{\theta}}$. For instance, $\widetilde{\boldsymbol{U}}^{ABA'}$ and $\widetilde{\boldsymbol{\theta}}^{ABA'}$ refer respectively to nodal displacements and rotations along the edges AB and BA'.

Periodicity conditions in Direction 1 and 2 have to be applied: ABA' matches $A''B''A'''$ and ADA'' matches $A'D'A'''$. As mentioned before, thanks to the symmetries of the unit cell there is no in-plane overall strain when applying transverse shear loading. Hence, the following periodicity conditions are prescribed:

$$\widetilde{\boldsymbol{U}}^{ABA'} = \widetilde{\boldsymbol{U}}^{A''B''A'''}, \qquad \widetilde{\boldsymbol{\theta}}^{ABA'} = \widetilde{\boldsymbol{\theta}}^{A''B''A'''},$$

$$\widetilde{\boldsymbol{U}}^{ADA''} = \widetilde{\boldsymbol{U}}^{A'D'A'''}, \qquad \widetilde{\boldsymbol{\theta}}^{ADA''} = \widetilde{\boldsymbol{\theta}}^{A'D'A'''}.$$

The reader is referred to Sab (1996); Pradel and Sab (1998); Laroussi et al. (2002); Lachihab and Sab (2005); Florence and Sab (2006) for more details on periodic boundary conditions involving both nodal displacements and nodal rotations.

For the upper (respectively, lower) bound, the prescribed displacements (respectively, forces per unit length) are applied to the AB, BA', DC, CD', $A''B''$, $B''A'''$ edges. For the lower bound case, node A displacements and rotations are set to zero to prevent rigid motion.

Few detailed chevron folded core geometries are available in the open literature. Similar to Nguyen et al. (2005a), the following geometric parameters are investigated with $E_m = 3GPa$ and $\nu_m = 0.4$: $a_0 = 30\ mm$, $b_0 \in [20\ mm, 60\ mm]$, $t_f = 0.1mm$, $\delta = 72°$, $\zeta = 34°$. The analytical normalized bounds for these configurations are:

$$0.23 < \mathcal{E}_1 < 0.71,$$
$$0.09 < \mathcal{E}_2 < 0.35.$$

Figure 3.9-(a,b,c) shows the stresses in the unit cell when submitted to the stress loading τ_1 for the case $a_0 = b_0 = 30mm$. At first sight, it is clear that the stresses are almost piecewise uniform in each face which is consistent with the assumption made for the analytical derivation of the lower bounds. Also, the stress distribution complies to the symmetries described in section 3.2. As expected, the main component is σ_{uu} as predicted by the Warren truss beam analogy.

Figure 3.9-(d,e,f) shows the strains in the unit cell when submitted to the strain loading γ_1. Again, strains are approximately piecewise uniform in each face. Analytical estimations are $\frac{\varepsilon_{uu}}{\gamma_1} \approx 0.29$, $\frac{\varepsilon_{vv}}{\gamma_1} \approx 0.20$, $\frac{\varepsilon_{uv}}{\gamma_1} \approx 0.40$. FE fields seems consistent with this prediction.

Similar observations were made for the stress loading τ_2 and the strain loading γ_2 in Direction 2.

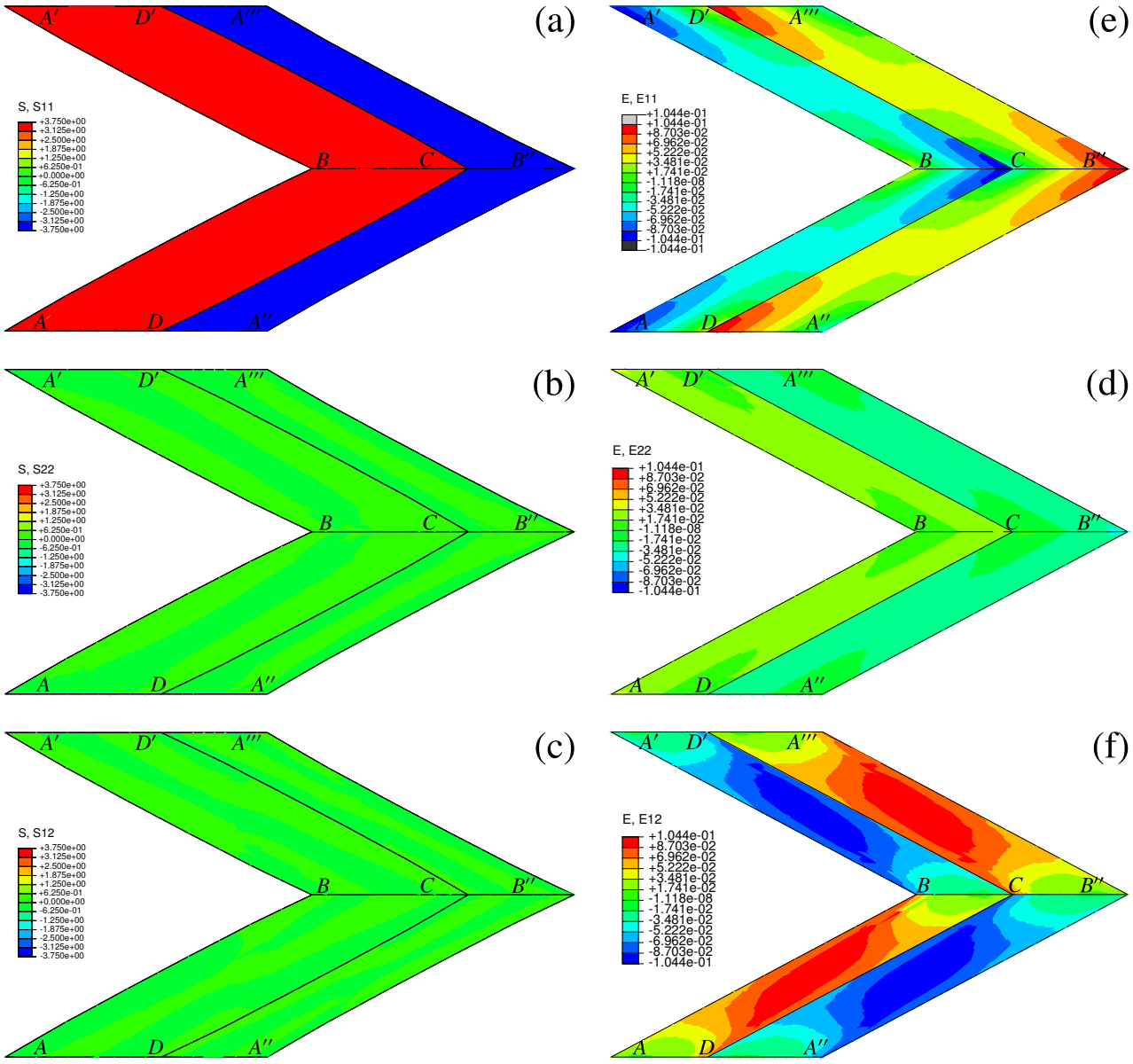

Figure 3.9: Membrane stresses for τ_1 load, $\delta = 72°$, $\zeta = 34°$ ((a): σ_{uu}, (b): σ_{vv}, (c): σ_{uv}) and membrane strains for γ_1 load, $\delta = 72°$, $\zeta = 34°$ ((d): ε_{uu}, (e): ε_{vv}, (f): ε_{uv})

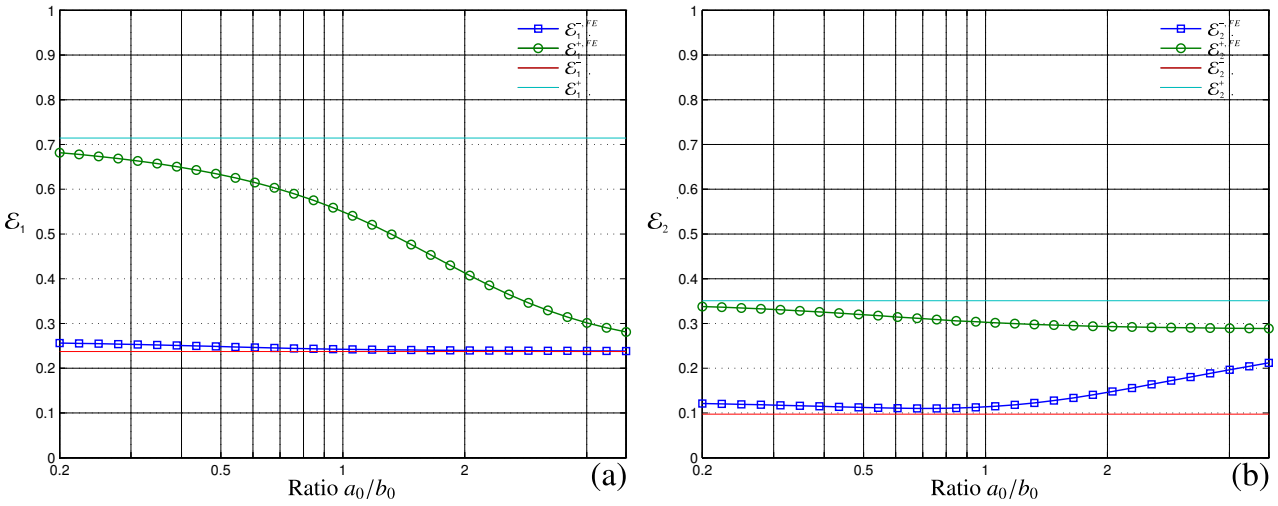

Figure 3.10: Bounds versus a_0/b_0 for $\delta = 72°$, $\zeta = 34°$ and $\nu_m = 0.4$ in both directions

3.4.2 Results

FE analysis has been performed also for several values of the shape ratio a_0/b_0 and for both loading directions. Results are shown on Figure 3.10-(a,b).

For all shape ratios, the expected hierarchy between bounds is observed:

$$\mathcal{E}_\alpha^- < \mathcal{E}_\alpha^{-,\,FE} < \mathcal{E}_\alpha^{+,\,FE} < \mathcal{E}_\alpha^+. \tag{3.24}$$

For Direction 1, on the one hand, the FE lower bound is really close to the analytical lower bound whatever the shape ratio is. This good agreement is consistent with the good uniformity of the stresses shown in Figure 3.9-(a,b,c). On the other hand, the FE upper bound is dependent on the shape ratio. In fact, the computed strain fields are not perfectly piecewise uniform in this case. Figure 3.9-(d,e,f). Moreover, it should be emphasized that the numerical FE bounds for Direction 1 cover all the range between the analytical upper and lower bounds as the shape ratio varies. For Direction 2, it is the lower bound which presents less uniform FE fields and is more sensitive to shape ratio. As expected, when the actual fields are almost piecewise uniform, then the analytical and numerical bounds are consistent.

One important conclusion of this study is that both FE and analytical bounds are loose for practical values of the shape ratio ($a_0/b_0 \in [0.5, 1.5]$). This means that the effective transverse shear moduli of the considered chevron pattern ($\delta = 72°$, $\zeta = 34°$) are sensitive to the the skin effect. According to Kelsey et al. (1958), this is due to the lack of consideration of the interaction between the skins and the core of the sandwich panel. Moreover, they indicate that the upper bound is relevant for sandwich panels with thick skins while the lower bound is relevant for thin skins.

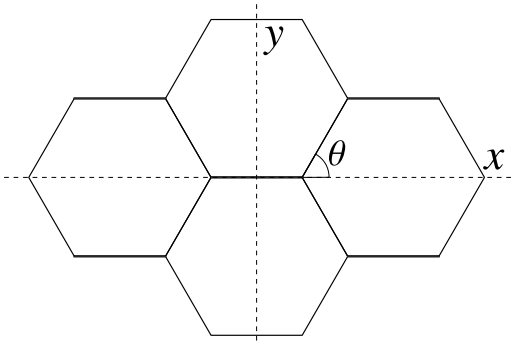

Figure 3.11: Honeycomb angle

3.4.3 Comparison with honeycomb

It is of interest to compare honeycomb geometries with chevron pattern.

For a regular honeycomb core with the same wall thickness, the use of piecewise uniform strain and stress in the core walls gives equal lower and upper bounds:

$$\mathcal{E}_1 = \mathcal{E}_2 = 0.5.$$

The normalized upper bounds for hexagonal honeycomb with a double wall in the glueing area are (Kelsey et al. (1958)):

$$\mathcal{E}_1^+ = \frac{1+\cos^2\theta}{2}, \qquad \mathcal{E}_2^+ = \frac{\sin^2\theta}{2}, \tag{3.25}$$

where the angle θ is a design parameter shown in Figure 3.11. In order to compare chevron pattern to honeycomb, the sum $\Sigma = \mathcal{E}_1 + \mathcal{E}_2$ can be considered. Its upper bound for all honeycomb geometries is $\Sigma^+ = 1$ (Xu et al., 2001). However, for chevron pattern, it is:

$$\Sigma^+ = \left(\frac{2}{1-\nu_m}\cos^2\delta\sin^2\zeta + 1\right)\left(1-\cos^2\delta\sin^2\zeta\right) \tag{3.26}$$

which reaches the maximum value:

$$\frac{(3-\nu_m)^2}{8(1-\nu_m)} \tag{3.27}$$

for

$$\cos^2\delta\sin^2\zeta = \frac{1+\nu_m}{4}. \tag{3.28}$$

Figure 3.12-(a) shows Σ^+ as the function of ζ and δ for $\nu_m = 0.4$, and the continuous set of (ζ, δ) for which Σ^+ reaches its maximum value. On Figure 3.13 the maximum value of Σ^+ versus ν_m is plotted. Thus, considering Σ^+, the chevron pattern can potentially outperform honeycomb by $\simeq 40\%$ for usual values of ν_m.

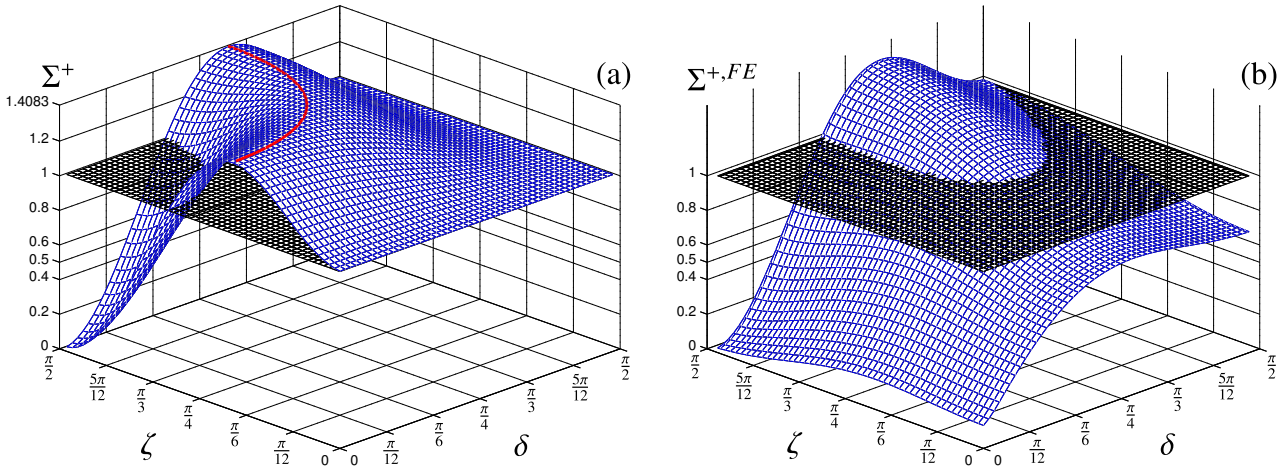

Figure 3.12: Σ^{+} and $\Sigma^{+,FE}$ as the function of ζ and δ for $\nu_m = 0.4$ and $a_0/b_0 = 1$

In Figure 3.12-(b) the FE computed sum of upper bounds $\Sigma^{+,FE}$ is plotted for $a_0/b_0 = 1$. As expected FE upper bounds are lower than analytical upper bounds. The domain where chevron pattern outperforms honeycomb geometries ($\Sigma^{+,FE} > 1$) is smaller but still includes geometries that can be manufactured. Yet, $\Sigma^{+,FE} \simeq 0.65$ for the geometry considered in Nguyen et al. (2005a).

3.5 Discussion

The main reason for the gap observed between bounds, even with FE computations, is the lack of knowledge on the actual effect of shear forces on plates. Since Reissner (1945) we know that local transverse shear is parabolic through the thickness in a homogeneous plate. However, when considering anisotropic laminated plates, it is difficult to approximate the actual transverse shear stress distribution. To overcome this difficulty, Mindlin (1951) suggested to introduce shear correction factors, which improved the accuracy of the deflection prediction but did not provided the actual transverse shear stress distribution. Numerous proposals have been made to improve stress estimation and were reviewed by Reddy (1989) and Carrera (2002). This issue becomes critical when considering heterogeneous periodic plates such as honeycomb and chevron pattern sandwich panels.

Most of the approaches suggested for sandwich panels rely on the following steps. First, the heterogeneous core is homogenized, and replaced with an equivalent homogeneous layer. Second, the First Order Shear Deformation Theory (FOSDT) is applied to derive the transverse shear stiffness of the obtained laminated plate. To do this, the transverse shear strain is assumed uniform through the thickness. Two difficulties arise from this two step method.

Firstly, the actual boundary conditions replacing the effect of the skins on the core are unknown.

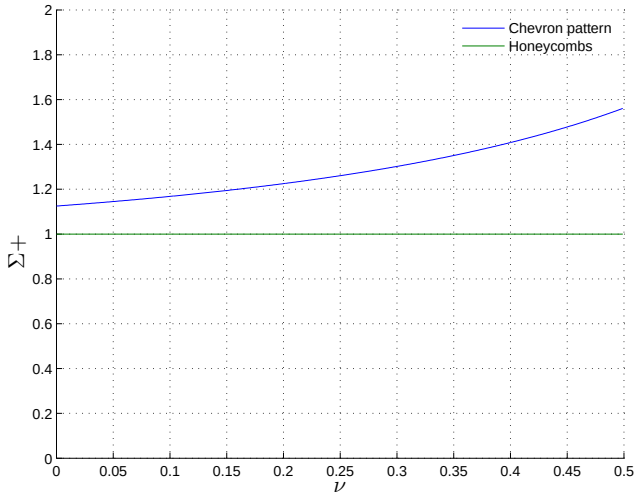

Figure 3.13: Maximum value of Σ^+ for honeycombs and chevron pattern versus Poisson's ratio, ν_m

Imposing uniform displacements or uniform forces gives bounds for the homogenized constitutive behavior of the heterogeneous core. As it is illustrated in this paper, these bounds may be loose. This is the main drawback of the two step approach.

Secondly, as previously mentioned, the application of FOSDT necessitates the computation of shear correction factors. However shear correction factors depend on the ply configuration. In the case of heterogeneous plates, the concept of shear correction factor is even more fuzzy. The work of Buannic et al. (2003) points out limitations of the shear correction factor approach.

One way has been suggested to overcome these difficulties in the case of honeycomb sandwich panels. It consists in refining the analysis on the connection between the skins and the core, as suggested by Hohe and Becker (2001) and Chen and Davalos (2005). In these papers the incompatibility between the skins and the core average displacement is treated as an edge effect relatively to the ratio between the cell width and the core thickness. Following a completely different path, Lebée and Sab (2010b) suggested a model which enables the consideration of such incompatibilities and edge effects in more general configurations. Yet this kind of approach is relevant only for honeycombs. Unlike honeycombs, the chevron pattern has no scale separation between the cell width and the core thickness.

A second way to improve the estimation of the transverse shear stiffness is to reconsider globally the effect of shear forces on the sandwich panel. This was done by Hohe (2003) and Cecchi and Sab (2007) among others. Hohe (2003), followed by Pahr and Rammerstorfer (2006), presented a direct homogenization scheme assuming *ad hoc* boundary conditions on the representative volume element, including skins. When including skins, Hohe (2003) overcomes the difficulty of choosing the actual boundary conditions that should be used in the two step method. However, applying this method to a homogeneous plate leads to a uniform stress distribution which contradicts Reissner

(1945)'s prediction and overestimates transverse shear stiffness (hG instead of $5/6hG$). The reason why Hohe (2003) method is efficient for sandwich panels comes from a contrast assumption. In sandwich panels, the core is allways much more compliant than the skins. In this specific case it is possible to assume a uniform distribution of shear strains through the core thickness. Yet, in practical applications, the contrast assumption is not always fullfilled which limits the validity of this method. Another proposal, made by Cecchi and Sab (2007) (as well as, Cecchi and Sab (2004); Nguyen et al. (2005b); Cecchi and Sab (2007); Nguyen et al. (2007, 2008a)), is based on Whitney (1972) work on the derivation of shear correction factors for laminates. This seminal work is extended to heterogeneous plates thanks to an energetic equivalence. It consists in using the Reissner-Mindlin equilibrium equation $\mathsf{M}_{\alpha\beta,\beta} = Q_\alpha$ in the cylindrical bending case in order to derive the actual 3D stress field generated by shear forces. This method does not make an *a priori* assumption on transverse shear strain or stress. It is currently under investigation for application to sandwich panels.

3.6 Conclusion

For an out-of-plane loaded sandwich panel with stiff skins (0.6 mm of CFRP for instance), small slenderness ratio (10 for example) and usual chevron folded core thickness (0.1 mm of impregnated aramid paper), the deflection is almost proportional to the effective transverse shear moduli of the chevron folded core. In this paper, Kelsey et al. (1958) approach has been used to derive analytical and numerical upper bounds for these moduli. For some pattern geometries, the exact fields have been obtained. Moreover, it has been shown that for some geometries, the chevron folded cores are stiffer than honeycomb-like cores (lower bounds for the chevron core are higher than upper bounds for honeycombs). Finally, this work sets the path for the derivation of analytical bounds for other folded core geometries such as the M-type core (Heimbs et al., 2007).

However, the bounds obtained for the already existing pattern geometries (Nguyen et al., 2005a), $\delta = 72°$, $\zeta = 34°$, are too loose (more than 100% discrepancy). Kelsey et al. (1958) already discussed this difficulty in the context of honeycomb core structures, but it is even more pronounced in the case of chevron structures.

In the case of honeycomb-like cores, the discrepancy between bounds has been identified as a skin effect (Hohe and Becker, 2001; Xu and Qiao, 2002; Chen and Davalos, 2005) and correlated to the ratio between the cell width and the core thickness. In the case of chevron folded core, the large discrepancy between the bounds has still no explanation and necessitates more refined models able to take into account the interaction between the skins and the core.

CHAPTER

4

A full bending gradient plate theory for thick plates Part I:Theory

Comme on a pu le voir au Chapter 1, déterminer la raideur à l'effort tranchant d'une plaque est un problème qui pose beaucoup de difficultés en raison d'une différence notable entre le modèle naturel de plaque et le second ordre des développements asymptotiques. De plus, dans le cas du module à chevrons, il apparaît clairement que la méthode traditionnelle pour estimer cette raideur est insuffisante. Le besoin d'une methode de portée générale se fait donc sentir. Dans ce chapitre on propose donc de revisiter l'approche choisie par Reissner (1945) pour déterminer les contraintes de cisaillement transverse dans le cas d'une plaque homogène. On se place ici dans le cas plus général des plaques dont les propriétés sont invariantes dans leur plan (stratifiées et fonctionnellement graduées). On en tire une nouvelle théorie de plaque dans laquelle l'effort tranchant est remplacé par le gradient du moment de flexion. Cette nouvelle théorie nommée théorie de gradient du moment ne peut pas être réduite au modèle de Reissner-Mindlin. Cependant, dans certains cas elle est dégénérée en un modèle de Reissner-Mindlin. C'est le cas des plaques homogènes. L'extension au cas des plaques périodiques sera faite au Chapitre 6 après une application de la théorie de gradient du moment à la flexion cylindrique de plaques stratifiées.

Ce chapitre est la première partie d'un article en deux parties soumis le 19/07/2010.

Abstract

This is the first part of a two-part paper dedicated to a new plate theory for out-of-plane loaded thick plates where the static unknowns are those of the Love-Kirchhoff theory (3 in-plane stresses and 3 bending moments), to which six components are added representing the gradient of the bending moment. The new theory, called the Bending-Gradient plate theory is described in the present paper. It is an extension to arbitrary multilayered plates of the Reissner-Mindlin plate theory which appears as a special case of the Bending-Gradient plate theory when the plate is homogeneous. However,

we demonstrate also that, in the general case, the Bending-Gradient model cannot be reduced to a Reissner-Mindlin model. In part two (Lebée and Sab, 2010a), the Bending-Gradient theory is applied to multilayered plates and its predictions are compared to those of the Reissner-Mindlin theory and to full 3D Pagano's exact solutions. The main conclusion of the second part is that the Bending-Gradient gives good predictions of both deflection and shear stress distributions in any material configuration. Moreover, under some symmetry conditions, the Bending-Gradient model coincides with the second-order approximation of the exact solution as the slenderness ratio L/h goes to infinity.

4.1 Introduction

Laminated composite plates are widely used in engineering applications, especially in aeronautics. They offer excellent stiffness and strength performance for a low density. However, as fiber reinforced composites are very anisotropic materials, the overall plate properties of these laminates has been really difficult to capture. Because of a strong demand from industry for reliable models, many suggestions have been made.

Let us recall some essential requirements for such a model. The main goal is to simplify a computationally heavy 3D model into a 2D plate model without losing local 3D fields' accuracy. One would expect:

1. Good estimation of macroscopic deflection,
2. No limitation on local material symmetries,
3. A plate theory which is easy to implement with standard finite element tools,
4. Good relocalization of 3D fields in order to estimate local stresses.

The simplest and most widely-used theory is the Love-Kirchhoff plate model. This model is easy to implement and gives good estimates for in-plane stress components (far from the edges of the plate) and neglects the contribution of out-of-plane stress components to the stress energy. However, when the plate slenderness ratio L/h (h is the plate thickness and L the span) is not large enough, out-of-plane stresses have an increasing influence on the plate deflection. This phenomenon becomes sensitive when $L/h < 10$ for an isotropic plate and $L/h < 40$ for classical carbon fiber reinforced laminated plates and cannot be neglected for conventional use of composite laminates.

In recent decades many suggestions have been made to improve both deflection estimation and field localization for highly heterogeneous laminates. Reddy (1989), Noor and Malik (2000) and Carrera (2002) provided detailed reviews for these models. Two main approaches can be found: asymptotic approaches and axiomatic approaches. The first one is mainly based on the fact that h/L is a small parameter. Using asymptotic expansions in the small parameter h/L (Caillerie, 1984;

Lewinski, 1991c,b,a), it is found that the Love-Kirchhoff kinematic is actually the first order of the expansion. However, higher-order terms yield only intricated "Love-Kirchhoff" plate equations and no simple model to implement. This difficulty is illustrated in (Boutin, 1996) for 3D periodic composites and in Buannic and Cartraud (2001a,b) for periodic beams. Another asymptotic method is based on the so-called Variational Asymptotic Method (VAM) applied to plates by Yu et al. (2002b,a). The strength of this approach is that it does not make more assumption than having h/L small and, according to its authors, it could be applied also to any non-linearities. However, this method does not seem simple to implement in conventional finite element code.

The second main approach is based on assuming *ad hoc* displacement or stress 3D fields and often referred to as axiomatic approach. One of the assets of these approaches is that they seem easier to implement in finite element codes. These models can be "Equivalent Single Layer" or "layerwise".

Equivalent single layer models treat the whole laminate as an equivalent homogeneous plate. Stress or displacement approaches have been suggested. Reissner (1945) was the first one who suggested a stress approach for homogeneous and isotropic plates. His approach will be detailled further in the present work. Reissner's transverse shear stress field is a parabolic distribution through the thickness. However, experiments and some exact solutions (Pagano, 1969, 1970a,b) when considering composite laminates, revealed that shear stress distributions are much more distorted than that. At the same time, numerous displacement approaches were suggested. The roughest suggestion for taking into account transverse shear strains, $\varepsilon_{\alpha 3}$, is assuming that $\varepsilon_{\alpha 3}$ is uniform through the thickness (First Order Shear Deformation Theory). Yet, it leads to too stiff shear behavior and necessitates the introduction of shear correction factors (Mindlin (1951) and Whitney (1972)). Above all, this assumption enforces a discontinuous shear stress $\sigma_{\alpha 3}$ through the thickness. Other models have been designed (Reddy, 1984; Touratier, 1991; Vidal and Polit, 2008) to remove the use of shear correction factors, but they did not lead to continuous $\sigma_{\alpha 3}$, as indicated by Reddy (1989). The most refined Equivalent Single Layers models, which finally led to continuous shear stress are zigzag models (Ambartsumian, 1969; Whitney, 1969b; Carrera, 2003a). However, these models are restricted to some specific configurations (symmetry of the plate and material constitutive equation).

The difficulties encountered with transverse stress fields instigated the consideration of enriched models: layerwise models. In these models, all plate degrees of freedom are introduced in each layer of the laminate. Continuity conditions are enforced between layers. In this area, most of the improvements have been focused on refining the local displacement field. The reader can refer to Reddy (1989) and Carrera (2002) for detailed reviews. It should be noted that a static approach has also been considered for layerwise models. Based on the variational formulation from Pagano (1978), it treats each layer as a Reissner-Mindlin plate and enforces stress continuity conditions (Naciri et al., 1998; Diaz Diaz et al., 2001; Hadj-Ahmed et al., 2001; Caron et al., 2006; Diaz Diaz

et al., 2007; Dallot and Sab, 2008). Both stress and displacement layerwise models lead to correct estimates of local 3D fields. However their main drawback is that they involve many more degrees of freedom (proportional to the number of layers) than Equivalent Single Layer models.

Based on Reissner (1945) paper, the purpose of this work is to suggest an Equivalent Single Layer higher-order plate theory which gives an accurate enough estimate of transverse shear stresses in the linear elasticity framework. For this, we are motivated by two observations. The first one is that Love-Kirchhoff strain fields have clearly been identified as good first-order approximation for slender plates thanks to asymptotic expansion approaches. Thus, it would be inconsistent to refine in-plane fields further without introducing correct estimation of transverse fields. The second one is that the 3D equilibrium plays a critical role in the estimation of transverse shear stress in all the existing approaches. For instance, Whitney (1972) introduced 3D equilibrium in order to compute shear correction factors and more recently, when benchmarking several plate models, Noor and Malik (2000) used the 3D equilibrium to estimate shear stresses. We show in this paper that revisiting the use of 3D equilibrium in order to derive transverse shear stress as Reissner (1945) did for homogeneous plates leads to a full bending gradient plate theory. The Reissner-Mindlin theory will appear as a special case of the new Bending-Gradient theory when the plate is homogeneous.

The paper is organized as follows. In Section 4.2 notations are introduced. In Section 4.3 we recall briefly the full 3D elastic problem for a clamped plate and, in Section 4.4, how it is possible to derive plate equilibrium equations without any assumption on microscopic fields and how Reissner derived his shear stress distribution. Then we demonstrate in Section 4.5.1 that applying Reissner's approach for deriving transverse shear stress to a composite laminate involves more static shear degrees of freedom (DOF) than the usual shear forces $\boldsymbol{Q}$. The mechanical meaning of these new DOF is presented and compatible fields are identified in Section 4.5.2. The constitutive equation for the bending gradient is derived in Section 4.5.3 which leads to the formulation of a complete plate theory. Finally, in Section 4.6, it is demonstrated that for the special case of homogeneous plates, the Reissner-Mindlin and the Bending-Gradient plate theory are identical. Thus a means to quantitatively compare both theories is provided and applied to conventional laminates.

4.2 Notations

Vectors and higher-order tensors are boldfaced and different typefaces are used for each order: vectors are slanted: $\boldsymbol{T}$, $\boldsymbol{u}$. Second order tensors are sans serif: M, e. Third order tensors are in typewriter style: $\mathtt{\Phi}$, $\mathtt{\Gamma}$. Fourth order tensors are in calligraphic style $\mathcal{D}$, $\mathcal{c}$. Sixth order tensors are double stroked $\mathbb{F}$, $\mathbb{W}$.

When dealing with plates, both 2-dimensional (2D) and 3D tensors are used. Thus, $\widetilde{\boldsymbol{T}}$ denotes a 3D vector and $\boldsymbol{T}$ denotes a 2D vector or the in-plane part of $\widetilde{\boldsymbol{T}}$. The same notation is used for higher-

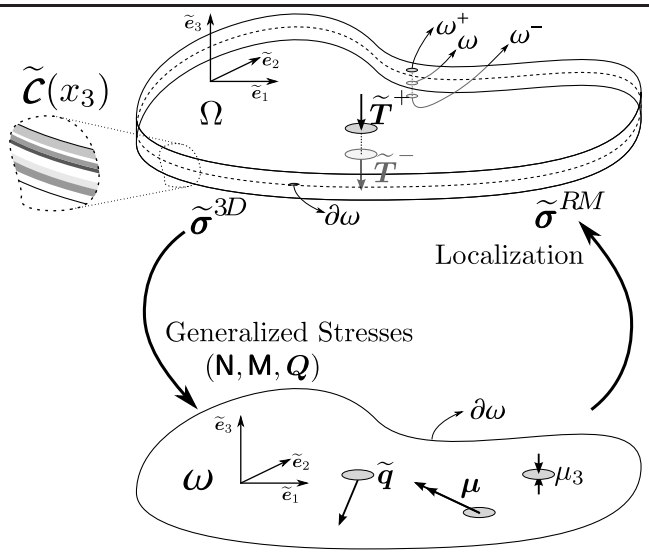

Figure 4.1: The Plate Configuration

order tensors: $\widetilde{\boldsymbol{\sigma}}$ is the 3D second-order stress tensor while $\boldsymbol{\sigma}$ is its in-plane part. When dealing with tensor components, the indexes specify the dimension: a_{ij} denotes the 3D tensor $\widetilde{\mathbf{a}}$ with Latin index $i, j, k.. = 1, 2, 3$ and $\mathsf{a}_{\alpha\beta}$ denotes the 2D $\mathbf{a}$ tensor with Greek indexes $\alpha, \beta, \gamma.. = 1, 2$. $\widetilde{\boldsymbol{\mathcal{C}}} = \mathcal{C}_{ijkl}$ is the fourth-order 3D elasticity stiffness tensor. $\widetilde{\boldsymbol{\mathcal{S}}} = \mathcal{S}_{ijkl} = \widetilde{\boldsymbol{\mathcal{C}}}^{-1}$ is the fourth-order 3D elasticity compliance tensor while $\boldsymbol{c} = c_{\alpha\beta\gamma\delta}$ denotes the plane-stress elasticity tensor. $\boldsymbol{c}$ is not the in-plane part of $\widetilde{\boldsymbol{\mathcal{C}}}$ but it is the inverse of the in-plane part of $\widetilde{\boldsymbol{\mathcal{S}}}$: $\boldsymbol{c} = \boldsymbol{\mathcal{S}}^{-1}$. The identity for in-plane elasticity is $i_{\alpha\beta\gamma\delta} = \frac{1}{2}\left(\delta_{\alpha\gamma}\delta_{\beta\delta} + \delta_{\alpha\delta}\delta_{\beta\gamma}\right)$, where $\delta_{\alpha\beta}$ is Kronecker symbol ($\delta_{\alpha\beta} = 1$ if $\alpha = \beta$, $\delta_{\alpha\beta} = 0$ otherwise).

The transpose operation ${}^t\bullet$ is applied to any order tensors as follows: $\left({}^tA\right)_{\alpha\beta\ldots\psi\omega} = A_{\omega\psi\ldots\beta\alpha}$.

Three contraction products are defined, the usual dot product ($\widetilde{\boldsymbol{a}} \cdot \widetilde{\boldsymbol{b}} = a_i b_i$), the double contraction product ($\widetilde{\mathbf{a}} : \widetilde{\mathbf{b}} = \mathsf{a}_{ij}\mathsf{b}_{ji}$) and a triple contraction product ($\mathbf{A} \therefore \mathbf{B} = \mathtt{A}_{\alpha\beta\gamma}\mathtt{B}_{\gamma\beta\alpha}$). In these definitions Einstein's notation on repeated indexes is used. It should be noticed that closest indexes are summed together in contraction products. Thus, $\boldsymbol{\Phi} \cdot \boldsymbol{n} = \Phi_{\alpha\beta\gamma} n_\gamma$ is different from $\boldsymbol{n} \cdot \boldsymbol{\Phi} = n_\alpha \Phi_{\alpha\beta\gamma}$. The reader might easily check that $\boldsymbol{i} : \boldsymbol{i} = \boldsymbol{i}$, $\boldsymbol{i} \therefore \boldsymbol{i} = 3/2\,\boldsymbol{\delta}$ and that $\boldsymbol{i} \cdot \boldsymbol{i} = i_{\alpha\beta\gamma\delta} i_{\delta\epsilon\zeta\eta}$ is a sixth-order tensor. We recall also that resp. $\boldsymbol{a} \cdot \boldsymbol{b}$, ${}^t\mathbf{a} : \mathbf{b}$ and ${}^t\mathbf{a} \therefore \mathbf{b}$ define inner products and associated norms on $\mathbb{R}^2$, $\left(\mathbb{R}^2\right)^2$ and $\left(\mathbb{R}^2\right)^3$, respectively.

The derivation operator $\widetilde{\boldsymbol{\nabla}}$ is also formally represented as a vector: $\widetilde{\mathbf{a}} \cdot \widetilde{\boldsymbol{\nabla}} = \mathsf{a}_{ij}\nabla_j = \mathsf{a}_{ij,j}$ is the divergence and $\widetilde{\mathbf{a}} \otimes \widetilde{\boldsymbol{\nabla}} = \mathsf{a}_{ij}\nabla_k = \mathsf{a}_{ij,k}$ is the gradient. Here $\otimes$ is the dyadic product.

Finally, the integration through the thickness is noted $\langle\bullet\rangle$: $\int_{-\frac{h}{2}}^{\frac{h}{2}} f(x_3)dx_3 = \langle f \rangle$.

4.3 The 3D model

We consider a linear elastic plate of thickness h occupying the 3D domain $\Omega = \omega \times]-h/2, h/2[$, where $\omega \subset \mathbb{R}^2$ is the mid-plane of the plate (Figure 4.1). Cartesian coordinates (x_1, x_2, x_3) in the reference frame $(\widetilde{\boldsymbol{e}}_1, \widetilde{\boldsymbol{e}}_2, \widetilde{\boldsymbol{e}}_3)$ are used. The constitutive material is assumed to be invariant with respect to translations in the (x_1, x_2) plane. Hence, the stiffness tensor $\widetilde{\boldsymbol{\mathcal{C}}}$ is a function of x_3 only. The plate is loaded on its upper and lower faces $\omega^{\pm} = \omega \times \{\pm h/2\}$ with the distributed force $\widetilde{\boldsymbol{T}}^{\pm}$. There are no body forces and the plate is clamped on its lateral edge, $\partial\omega \times] - h/2, h/2[$ where $\partial\omega$ is the edge of ω.

The 3D problem $\mathcal{P}^{3D}$ is summarized as follows:

$$\mathcal{P}^{3D} \begin{cases} \widetilde{\boldsymbol{\sigma}} \cdot \widetilde{\boldsymbol{\nabla}} = 0 \quad \text{on } \Omega. & \text{(4.1a)} \\ \widetilde{\boldsymbol{\sigma}} = \widetilde{\boldsymbol{\mathcal{C}}}(x_3) : \widetilde{\boldsymbol{\varepsilon}} \quad \text{on } \Omega. & \text{(4.1b)} \\ \widetilde{\boldsymbol{\sigma}} \cdot \widetilde{\boldsymbol{e}}_3 = \widetilde{\boldsymbol{T}}^{\pm} \quad \text{on } \omega^{\pm}. & \text{(4.1c)} \\ \widetilde{\boldsymbol{\varepsilon}} = \dfrac{1}{2}\left(\widetilde{\boldsymbol{\nabla}} \otimes \widetilde{\boldsymbol{u}} + \widetilde{\boldsymbol{u}} \otimes \widetilde{\boldsymbol{\nabla}}\right) \quad \text{on } \Omega. & \text{(4.1d)} \\ \widetilde{\boldsymbol{u}} = 0 \quad \text{on } \partial\omega \times] - h/2, h/2[. & \text{(4.1e)} \end{cases}$$

where $\widetilde{\boldsymbol{u}}$ is the 3D displacement vector field, $\widetilde{\boldsymbol{\varepsilon}}$ is the strain tensor field and $\widetilde{\boldsymbol{\sigma}}$ is the stress tensor field. It is useful to recall the variational approach for the problem $\mathcal{P}^{3D}$. The sets of statically compatible stress fields SC^{3D} and kinematically compatible strain fields KC^{3D} are introduced. SC^{3D} is the set of stress fields $\widetilde{\boldsymbol{\sigma}}$ which comply with equilibrium equation (4.1a) and boundary condition on the upper and lower faces of the plate (4.1c). KC^{3D} is the set of strain fields $\widetilde{\boldsymbol{\varepsilon}}$ which derive from a continuous displacement field $\widetilde{\boldsymbol{u}}$ (Equation 4.1d) and comply with boundary condition on the edge of the plate (4.1e).

The strain and stress energy density w^{3D} and w^{*3D} are respectively given by:

$$w^{3D}\left(\widetilde{\boldsymbol{\varepsilon}}\right) = \frac{1}{2}\widetilde{\boldsymbol{\varepsilon}} : \widetilde{\boldsymbol{\mathcal{C}}} : \widetilde{\boldsymbol{\varepsilon}}, \qquad w^{*3D}\left(\widetilde{\boldsymbol{\sigma}}\right) = \frac{1}{2}\widetilde{\boldsymbol{\sigma}} : \widetilde{\boldsymbol{\mathcal{S}}} : \widetilde{\boldsymbol{\sigma}} \tag{4.2}$$

They are related by the following Legendre-Fenchel transform:

$$w^{*3D}\left(\widetilde{\boldsymbol{\sigma}}\right) = \sup_{\widetilde{\boldsymbol{\varepsilon}}} \left\{\widetilde{\boldsymbol{\sigma}} : \widetilde{\boldsymbol{\varepsilon}} - w^{3D}\left(\widetilde{\boldsymbol{\varepsilon}}\right)\right\} \tag{4.3}$$

The kinematic variational approach states that the strain solution $\widetilde{\boldsymbol{\varepsilon}}^{3D}$ of $\mathcal{P}^{3D}$ is the one that minimizes P^{3D} among all kinematically compatible strain fields:

$$P^{3D}\left(\widetilde{\boldsymbol{\varepsilon}}^{3D}\right) = \min_{\widetilde{\boldsymbol{\varepsilon}} \in KC^{3D}} \left\{P^{3D}\left(\widetilde{\boldsymbol{\varepsilon}}\right)\right\} \tag{4.4}$$

where P^{3D} is the potential energy given by:

$$P^{3D}\left(\widetilde{\boldsymbol{\varepsilon}}\right)=\int_{\Omega}w^{3D}\left(\widetilde{\boldsymbol{\varepsilon}}\right)d\Omega-\int_{\omega}\widetilde{\boldsymbol{T}}^{+}\cdot\widetilde{\boldsymbol{u}}^{+}+\widetilde{\boldsymbol{T}}^{-}\cdot\widetilde{\boldsymbol{u}}^{-}d\omega \tag{4.5}$$

and $\widetilde{\boldsymbol{u}}^{\pm}=\widetilde{\boldsymbol{u}}(x_1,x_2,\pm h/2)$ are the 3D displacement fields on the upper and lower faces of the plate.

The static variational approach states that the stress solution $\widetilde{\boldsymbol{\sigma}}^{3D}$ of $\mathcal{P}^{3D}$ is the one that minimizes P^{*3D} among all statically compatible stress fields:

$$P^{*3D}\left(\widetilde{\boldsymbol{\sigma}}^{3D}\right)=\min_{\widetilde{\boldsymbol{\sigma}}\in SC^{3D}}\left\{P^{*3D}\left(\widetilde{\boldsymbol{\sigma}}\right)\right\} \tag{4.6}$$

where P^{*3D} is the complementary potential energy given by:

$$P^{*3D}\left(\widetilde{\boldsymbol{\sigma}}\right)=\int_{\Omega}w^{*3D}\left(\widetilde{\boldsymbol{\sigma}}\right)d\Omega \tag{4.7}$$

Moreover, the following relation holds for the solution:

$$P^{3D}\left(\widetilde{\boldsymbol{\varepsilon}}^{3D}\right)=-P^{*3D}\left(\widetilde{\boldsymbol{\sigma}}^{3D}\right)\Leftrightarrow V_{ext}^{3D}=V_{int}^{3D} \tag{4.8}$$

where the external work is:

$$V_{ext}^{3D}=\int_{\omega}\widetilde{\boldsymbol{T}}^{+}\cdot\widetilde{\boldsymbol{u}}^{3D+}+\widetilde{\boldsymbol{T}}^{-}\cdot\widetilde{\boldsymbol{u}}^{3D-}d\omega, \tag{4.9}$$

and the internal work is:

$$V_{int}^{3D}=\int_{\Omega}\widetilde{\boldsymbol{\sigma}}^{3D}:\widetilde{\boldsymbol{\varepsilon}}^{3D}d\Omega. \tag{4.10}$$

4.4 Revisiting the Reissner-Mindlin plate theory

4.4.1 Reissner-Mindlin statically compatible fields

This section recalls shortly the procedure for the derivation of Reissner-Mindlin equilibrium equations (Reissner, 1945; Mindlin, 1951; Caron and Sab, 2001; Nguyen et al., 2005b).

The generalized Reissner-Mindlin stresses associated to the 3D stress field $\widetilde{\boldsymbol{\sigma}}$ are:

$$\begin{cases}\mathsf{N}_{\alpha\beta}\left(x_1,x_2\right)=\langle\sigma_{\alpha\beta}\rangle & \text{(4.11a)}\\ \mathsf{M}_{\alpha\beta}\left(x_1,x_2\right)=\langle x_3\sigma_{\alpha\beta}\rangle & \text{(4.11b)}\\ Q_{\alpha}\left(x_1,x_2\right)=\langle\sigma_{\alpha3}\rangle & \text{(4.11c)}\end{cases}$$

where N is the membrane stress, M the bending moment, and $\boldsymbol{Q}$ the shear forces.

Reissner-Mindlin equilibrium equations are obtained by integrating equations (4.1a) and $x_3\times$(4.1a) with respect to x_3 leading to:

$$\begin{cases} \langle\sigma_{\alpha\beta,\beta}\rangle + [\sigma_{\alpha 3}]_{-h/2}^{h/2} = 0 \\ \langle\sigma_{\alpha 3,\alpha}\rangle + [\sigma_{33}]_{-h/2}^{h/2} = 0 \\ \langle x_3\sigma_{\alpha\beta,\beta}\rangle - \langle\sigma_{\alpha 3}\rangle + [x_3\sigma_{\alpha 3}]_{-h/2}^{h/2} = 0 \end{cases}$$

Using boundary conditions (4.1c) yields:

$$\begin{cases} \mathsf{N}_{\alpha\beta,\beta} + p_\alpha = 0 & \text{(4.12a)} \\ Q_{\alpha,\alpha} + p_3 = 0 & \text{(4.12b)} \\ \mathsf{M}_{\alpha\beta,\beta} - Q_\alpha + \mu_\alpha = 0 & \text{(4.12c)} \end{cases}$$

where $p_i = T_i^+ + T_i^-$ are symmetric loadings per unit surface and $\mu_i = \frac{h}{2}(T_i^+ - T_i^-)$ are skew-symmetric loadings per unit surface. More precisely, $\boldsymbol{p} = (p_\alpha)$ are membrane loadings per unit surface, p_3 is the out-of-plane loading per unit surface, $\boldsymbol{\mu} = (\mu_\alpha)$ are couples per unit surface and μ_3 is the transverse bulk loading.

Since in-plane loadings ($\boldsymbol{p}$, $\boldsymbol{\mu}$) and out-of-plane loadings (p_3, μ_3) are not of the same order in the asymptotic analysis of the plate as h/L goes to 0 (see Lewinski (1991c)), and for the sake of simplicity, we focus only on the out-of-plane loading p_3 ($p_\alpha = \mu_i = 0$).

Finally, for clamped plates, $\mathcal{SC}^{RM}$ is the set of statically compatible $(\mathbf{N}, \mathbf{M}, \boldsymbol{Q})$ fields defined by:

$$(\mathbf{N}, \mathbf{M}, \boldsymbol{Q}) \in \mathcal{SC}^{RM} \Leftrightarrow \begin{cases} \mathbf{N}\cdot\boldsymbol{\nabla} = \mathbf{0} \text{ on } \omega & \text{(4.13a)} \\ \mathbf{M}\cdot\boldsymbol{\nabla} - \boldsymbol{Q} = \mathbf{0} \text{ on } \omega & \text{(4.13b)} \\ \boldsymbol{Q}\cdot\boldsymbol{\nabla} + q_3 = 0 \text{ on } \omega & \text{(4.13c)} \end{cases}$$

4.4.2 Localization

The second step of the static approach consists in deriving the stress energy per unit surface $w^{*RM}(\mathbf{N}, \mathbf{M}, \boldsymbol{Q})$ from the 3D model. Then, the solution for the Reissner-Mindlin model is obtained by minimizing the complementary potential energy $P^{*RM} = \int_\omega w^{*RM} d\omega$ over all $(\mathbf{N}, \mathbf{M}, \boldsymbol{Q})$ in $\mathcal{SC}^{RM}$.

As in many homogenization procedures, the derivation of w^{*RM} is based on an approximation scheme for the real 3D stress fields in terms of the generalized plate stress fields:

$$\widetilde{\boldsymbol{\sigma}}^{RM}(x_1, x_2, x_3) = \widetilde{\boldsymbol{\sigma}}^{(\mathsf{N})}(x_1, x_2, x_3) + \widetilde{\boldsymbol{\sigma}}^{(\mathsf{M})}(x_1, x_2, x_3) + \widetilde{\boldsymbol{\sigma}}^{(Q)}(x_1, x_2, x_3)$$

where $\widetilde{\boldsymbol{\sigma}}^{(\mathsf{N})}$, $\widetilde{\boldsymbol{\sigma}}^{(\mathsf{M})}$, and $\widetilde{\boldsymbol{\sigma}}^{(Q)}$ are 3D stress fields generated by $\mathbf{N}$, $\mathbf{M}$ and $\boldsymbol{Q}$ as follows:

$$\begin{cases} \sigma_{ij}^{(\mathsf{N})} = s_{ij\alpha\beta}^{(\mathsf{N})}(x_3)\mathsf{N}_{\alpha\beta}(x_1,x_2) & \text{(4.14a)} \\ \sigma_{ij}^{(\mathsf{M})} = s_{ij\alpha\beta}^{(\mathsf{M})}(x_3)\mathsf{M}_{\alpha\beta}(x_1,x_2) & \text{(4.14b)} \\ \sigma_{ij}^{(Q)} = s_{ij\alpha}^{(Q)}(x_3)Q_{\alpha}(x_1,x_2) & \text{(4.14c)} \end{cases}$$

where $s_{ij\alpha\beta}^{(\mathsf{N})}(x_3)$, $s_{ij\alpha\beta}^{(\mathsf{M})}(x_3)$ and $s_{ij\alpha}^{(Q)}(x_3)$ are localization tensors depending only on the x_3 coordinate. This can be rewritten using contraction products as:

$$\widetilde{\boldsymbol{\sigma}}^{RM} = \widetilde{\boldsymbol{s}}^{(\mathsf{N})} : \mathbf{N} + \widetilde{\boldsymbol{s}}^{(\mathsf{M})} : \mathbf{M} + \widetilde{\boldsymbol{s}}^{(Q)} \cdot \boldsymbol{Q}$$

Once this approximation of stress fields is set, the stress potential energy density $w^{*RM}(\mathbf{N},\mathbf{M},\boldsymbol{Q})$ is defined simply as the quadratic form:

$$w^{*RM}(\mathbf{N}(x_1,x_2),\mathbf{M}(x_1,x_2),\boldsymbol{Q}(x_1,x_2)) = \frac{1}{2}\left\langle \widetilde{\boldsymbol{\sigma}}^{RM}(x_1,x_2,x_3) : \widetilde{\boldsymbol{\mathcal{S}}}(x_3) : \widetilde{\boldsymbol{\sigma}}^{RM}(x_1,x_2,x_3) \right\rangle \quad (4.15)$$

Hence, a consistent choice for $\widetilde{\boldsymbol{s}}^{(\mathsf{N})}$, $\widetilde{\boldsymbol{s}}^{(\mathsf{M})}$ and $\widetilde{\boldsymbol{s}}^{(Q)}$ is critical.

4.4.2.1 Love-Kirchhoff fields

The derivation of $\widetilde{\boldsymbol{s}}^{(\mathsf{N})}$ and $\widetilde{\boldsymbol{s}}^{(\mathsf{M})}$ is based on the Love-Kirchhoff plate theory. According to this theory, plane-stress is assumed and the in-plane part of the strain is linear in x_3:

$$\boldsymbol{\varepsilon}^{LK} = \mathbf{e} + x_3\boldsymbol{\chi} \quad (4.16)$$

where $\mathbf{e}$ is the membrane strain and $\boldsymbol{\chi}$ the curvature. We draw the reader's attention to the fact that strain components ε_{i3} are not null in the general case.

Membrane stress $\mathbf{N}$ and bending moments $\mathbf{M}$ are linearly dependent on $\mathbf{e}$ and $\boldsymbol{\chi}$:

$$\begin{cases} \mathbf{N} = \boldsymbol{\mathcal{A}} : \mathbf{e} + \boldsymbol{\mathcal{B}} : \boldsymbol{\chi} & \text{(4.17a)} \\ \mathbf{M} = {}^t\boldsymbol{\mathcal{B}} : \mathbf{e} + \boldsymbol{\mathcal{D}} : \boldsymbol{\chi} & \text{(4.17b)} \end{cases}$$

with:

$$(\boldsymbol{\mathcal{A}},\boldsymbol{\mathcal{B}},\boldsymbol{\mathcal{D}}) = \left\langle \left(1, x_3, x_3^2\right) \boldsymbol{c}(x_3) \right\rangle \quad (4.18)$$

Using 3D constitutive equation under plane-stress assumption, Love-Kirchhoff constitutive equation (4.17) and in-plane strains definition (4.16), it is possible to express Love-Kirchhoff stress

fields as functions of $\mathbf{N}$ and $\mathbf{M}$:

$$\begin{cases} \boldsymbol{\sigma}^{(\mathsf{N})}(x_1,x_2,x_3) = \boldsymbol{c}(x_3) : \left(\boldsymbol{a} + x_3\, {}^t\boldsymbol{b}\right) : \mathbf{N}(x_1,x_2) \quad \text{and } \sigma^{(\mathsf{N})}_{i3} = 0 & \text{(4.19a)} \\ \boldsymbol{\sigma}^{(\mathsf{M})}(x_1,x_2,x_3) = \boldsymbol{c}(x_3) : (\boldsymbol{b} + x_3\, \boldsymbol{d}) : \mathbf{M}(x_1,x_2) \quad \text{and } \sigma^{(\mathsf{M})}_{i3} = 0 & \text{(4.19b)} \end{cases}$$

where $\boldsymbol{a}$, $\boldsymbol{b}$ and $\boldsymbol{d}$ are the reciprocal compliance tensors of the constitutive equation (4.17):

$$\begin{cases} \mathbf{e} = \boldsymbol{a} : \mathbf{N} + \boldsymbol{b} : \mathbf{M} & \text{(4.20a)} \\ \boldsymbol{\chi} = {}^t\boldsymbol{b} : \mathbf{N} + \boldsymbol{d} : \mathbf{M} & \text{(4.20b)} \end{cases}$$

Hence, for a homogeneous plate, Love-Kirchhoff stress fields are given by:

$$\begin{cases} \boldsymbol{\sigma}^{(\mathsf{N})}(x_1,x_2,x_3) = \dfrac{1}{h}\mathbf{N}(x_1,x_2) \quad \text{and } \sigma^{(\mathsf{N})}_{i3} = 0 & \text{(4.21a)} \\ \boldsymbol{\sigma}^{(\mathsf{M})}(x_1,x_2,x_3) = \dfrac{12x_3}{h^3}\mathbf{M}(x_1,x_2) \quad \text{and } \sigma^{(\mathsf{M})}_{i3} = 0 & \text{(4.21b)} \end{cases}$$

4.4.2.2 Shear fields for a homogeneous plate

Let us recall the approach from Reissner (1945) for deriving $\widetilde{\boldsymbol{\sigma}}^{(Q)}$ in the case of a homogeneous monoclinic [1] plate.

The main idea of the method is to recall that the shear forces are related to the bending moment through the plate equilibrium (4.13b). In the previous section, 3D fields generated by a (x_1,x_2)-invariant bending moment have been derived (Equation 4.21). If $\mathbf{M}$ is invariant, we have $\widetilde{\boldsymbol{\sigma}}^{(\mathsf{M})} \cdot \widetilde{\boldsymbol{\nabla}} = \widetilde{\mathbf{0}}$. However, if $\mathbf{M}$ is function of x_1 and x_2, $\widetilde{\boldsymbol{\sigma}}^{(\mathsf{M})}$ field is no more equilibrated and it comes directly: $\boldsymbol{\sigma}^{(\mathsf{M})} \cdot \boldsymbol{\nabla} = \frac{12x_3}{h^3}(\mathbf{M}\cdot\boldsymbol{\nabla}) = \frac{12x_3}{h^3}\boldsymbol{Q}$. $\boldsymbol{f}^{(Q)} = \frac{12x_3}{h^3}\boldsymbol{Q}$ appears as the volume load generated by the bending moment variations and is directly proportional to shear forces. Then $\widetilde{\boldsymbol{\sigma}}^{(Q)}$ is defined as the unique (x_1,x_2)-invariant stress field which balances $\boldsymbol{f}^{(Q)}$. This leads to the following auxiliary problem:

$$\begin{cases} \widetilde{\boldsymbol{\sigma}}^{(Q)} \cdot \widetilde{\boldsymbol{\nabla}} + 12x_3\dfrac{\widetilde{\boldsymbol{Q}}}{h^3} = \widetilde{\mathbf{0}}, \text{ where } Q_3 = 0 & \text{(4.22a)} \\ \widetilde{\boldsymbol{\sigma}}^{(Q)} \cdot \widetilde{\boldsymbol{e}}_3 = \widetilde{\mathbf{0}} \quad \text{for} \quad x_3 = \pm h/2 & \text{(4.22b)} \end{cases}$$

The (x_1,x_2)-invariant solution of this problem is:

$$\sigma^{(Q)}_{\alpha 3} = -\int_{-\frac{h}{2}}^{x_3} 12z\frac{Q_\alpha}{h^3}dz = \frac{6}{h^3}\left(\frac{h^2}{4} - x_3^2\right)Q_\alpha, \quad \sigma^{(Q)}_{\alpha\beta} = 0 \quad \text{and} \quad \sigma^{(Q)}_{33} = 0$$

This is the original shear stress field derived by Reissner.

1. The constitutive material is symmetric with respect to (x_1,x_2) plane. This assumption could be released but would compromise the simplicity of the presentation.

4.4.2.3 Extension to laminates under cylindrical bending

When considering laminated plates, the approach described above does not work any more, because it is not possible to bring out shear forces in $(\widetilde{\boldsymbol{\sigma}}^{(\mathsf{M})} \cdot \widetilde{\boldsymbol{\nabla}})$. Whitney (1972) overcame this difficulty assuming the plate is under cylindrical bending. This is equivalent to assuming: $\boldsymbol{Q}_1 = \mathbf{M}_{11,1}$, $\boldsymbol{Q}_2 = \mathbf{M}_{12,1}$, $\mathbf{e}_{22} = 0$ and $\boldsymbol{\chi}_{22} = 0$.

Whitney's approach for deriving shear correction factors is still implemented in ABAQUS (2007a) under additional assumptions. Compared to exact solutions for cylindrical bending (Pagano, 1969, 1970b), this method gives good approximation for overall deflection and shear stresses in laminated plates. Eventually, it has also been generalized to functionally graded materials (Nguyen et al., 2007, 2008a) and heterogeneous plates (Cecchi and Sab, 2002, 2007) and (Lebée and Sab, 2010c,d). However, how shear stress should be extended for more complex loadings than cylindrical bending (especially involving torsion) is still an issue.

4.5 The Bending-Gradient plate theory

4.5.1 Stress field generated by a linear variation of the bending moment

Since with laminated plates it is not possible to bring out shear force with Reissner's approach, we suggest considering a more general shear variable, the full bending gradient: $\mathbf{R} = \mathbf{M} \otimes \boldsymbol{\nabla}$. This will release the cylindrical bending assumption for laminated plates. In the following, we resume Section 4.4.2.2 procedure for deriving shear fields in the case of laminated plates.

We have $\widetilde{\boldsymbol{\sigma}}^{(\mathsf{M})} \cdot \widetilde{\boldsymbol{\nabla}} = 0$ if $\mathbf{M}$ is (x_1, x_2)-invariant. When $\mathbf{M}$ is function of x_1 and x_2, we have:

$$\widetilde{\boldsymbol{\sigma}}^{(\mathsf{M})} \cdot \widetilde{\boldsymbol{\nabla}} = s^{(\mathsf{M})}_{ij\beta\alpha}(x_3)\mathsf{M}_{\alpha\beta}(x_1,x_2)\nabla_j = s^{(\mathsf{M})}_{ij\beta\alpha}\mathsf{M}_{\alpha\beta,\gamma}\delta_{j\gamma} = s^{(\mathsf{M})}_{i\gamma\beta\alpha}\mathsf{R}_{\alpha\beta\gamma}$$

Again $f^{(\mathsf{R})}_i = s^{(\mathsf{M})}_{i\gamma\beta\alpha}\mathsf{R}_{\alpha\beta\gamma}$ is the force per unit volume generated by first order variations of the bending moment $\mathbf{R}$. $\mathsf{R}_{\alpha\beta\gamma}$ is a third-order tensor which respects $\mathsf{M}_{\alpha\beta}$ symmetries ($\mathsf{R}_{\alpha\beta\gamma} = \mathsf{R}_{\beta\alpha\gamma}$). Using $\widetilde{\boldsymbol{\sigma}}^{(\mathsf{M})}$ definition (Equation 4.19b) and assuming that each layer follows monoclinic symmetry we identify the force per unit volume as:

$$\boldsymbol{f}^{(\mathsf{R})} = \boldsymbol{c}(x_3) : (\boldsymbol{b} + x_3\,\boldsymbol{d}) \therefore \mathbf{R} \text{ and } f^{(\mathsf{R})}_3 = 0 \tag{4.23}$$

Then, we define $\widetilde{\boldsymbol{\sigma}}^{(\mathsf{R})}$ the 3D stress generated by a (x_1, x_2)-invariant bending gradient $\mathbf{R}$ associated to the localization tensor $s^{(\mathsf{R})}_{ij\alpha\beta\gamma}$ such as $\widetilde{\boldsymbol{\sigma}}^{(\mathsf{R})} = \widetilde{\boldsymbol{s}}^{(\mathsf{R})} \therefore \mathbf{R}$. Like in the case of homogeneous plate, this

stress field is derived through the auxiliary problem:

$$\begin{cases} \widetilde{\boldsymbol{\sigma}}^{(\mathtt{R})} \cdot \widetilde{\boldsymbol{\nabla}} + \widetilde{\boldsymbol{f}}^{(\mathtt{R})} = \widetilde{\mathbf{0}} & \text{(4.24a)} \\ \widetilde{\boldsymbol{\sigma}}^{(\mathtt{R})} \cdot \widetilde{\boldsymbol{e}}_3 = \widetilde{\mathbf{0}} \quad \text{for} \quad x_3 = \pm h/2 & \text{(4.24b)} \end{cases}$$

The (x_1, x_2)-invariant solution of this problem is easily found, leading to the explicit determination of $\widetilde{\boldsymbol{s}}^{(\mathtt{R})}$:

$$s^{(\mathtt{R})}_{\alpha 3\eta\zeta_\epsilon}(x_3) = -\int_{-\frac{h}{2}}^{x_3} c_{\alpha\eta\gamma\delta}(z)\,(b_{\delta\gamma\epsilon\zeta} + z\, d_{\delta\gamma\epsilon\zeta})\,dz\ ,\ s^{(\mathtt{R})}_{\alpha\beta\eta\zeta_\epsilon} = 0 \text{ and } s^{(\mathtt{R})}_{33\eta\zeta_\epsilon} = 0 \tag{4.25}$$

NB: The integral in the determination of $\widetilde{\boldsymbol{\sigma}}^{(\mathtt{R})}$ enforces directly the continuity of shear stress distributions and $\widetilde{\boldsymbol{s}}^{(\mathtt{R})}(-h/2) = \widetilde{\boldsymbol{s}}^{(\mathtt{R})}(h/2) = 0$ ensures the traction free boundary condition on the upper and lower faces of the plate.

We have derived a localization tensor $\widetilde{\boldsymbol{s}}^{(\mathtt{R})}$ which depends on all bending gradient components: $\mathtt{R}_{\alpha\beta\gamma} = \mathtt{M}_{\alpha\beta,\gamma}$. Accordingly we define a new approximation of stress fields involving all bending gradient components:

$$\widetilde{\boldsymbol{\sigma}}^{BG} = \widetilde{\boldsymbol{\sigma}}^{(\mathtt{N})} + \widetilde{\boldsymbol{\sigma}}^{(\mathtt{M})} + \widetilde{\boldsymbol{\sigma}}^{(\mathtt{R})}$$

and a new stress energy density identical to Definition 4.15:

$$w^{*BG}(\mathbf{N}, \mathbf{M}, \mathbf{R})$$

Actually $\widetilde{\boldsymbol{\sigma}}^{BG}$ approximation for 3D stress fields is a higher-order gradient theory, as described in Boutin (1996) for 3D continuum and Buannic and Cartraud (2001a) for periodic beams. However, to be consistent with higher-order theories, we should have taken into account the gradient of other static unknowns such as the membrane stress gradient for instance. It is the choice of the authors to limit the number of static variables only to those which have a contribution to the macroscopic equilibrium of the plate. Thus the number of unknowns remains limited and adapted to engineering applications, contrary to asymptotic expansions and other rigorous approaches in which no distinction is made between significant static unknowns.

Now it is possible to design a complete plate model.

4.5.2 Compatible fields for the full bending gradient

4.5.2.1 Bending gradient statically compatible fields

4.5.2.1.1 Generalized stress The full bending gradient $\mathbf{R}$ has six components ($\mathtt{R}_{111}$, $\mathtt{R}_{221}$, $\mathtt{R}_{121}$, $\mathtt{R}_{112}$, $\mathtt{R}_{222}$, $\mathtt{R}_{122}$) whereas $\boldsymbol{Q}$ has two components. Thus, using the full bending gradient as static unknown introduces four static unknowns which *a priori* are not related to plate equilibrium (4.13). Only $(\mathbf{N}, \mathbf{M}, \boldsymbol{Q})$ appeared in Reissner-Mindlin statically compatible fields, SC^{RM}, while integrating

	$\mathtt{R}_{111}$	$\mathtt{R}_{221}$	$\mathtt{R}_{121}$	$\mathtt{R}_{112}$	$\mathtt{R}_{222}$	$\mathtt{R}_{122}$
σ_{13}	$\left\langle s^{(\mathtt{R})}_{13111}\right\rangle = 1$	$\left\langle s^{(\mathtt{R})}_{13122}\right\rangle = 0$	$\left\langle s^{(\mathtt{R})}_{13121}\right\rangle = 0$	$\left\langle s^{(\mathtt{R})}_{13211}\right\rangle = 0$	$\left\langle s^{(\mathtt{R})}_{13222}\right\rangle = 0$	$\left\langle s^{(\mathtt{R})}_{13221}\right\rangle = 1/2$
σ_{23}	$\left\langle s^{(\mathtt{R})}_{23111}\right\rangle = 0$	$\left\langle s^{(\mathtt{R})}_{23122}\right\rangle = 0$	$\left\langle s^{(\mathtt{R})}_{23121}\right\rangle = 1/2$	$\left\langle s^{(\mathtt{R})}_{23211}\right\rangle = 0$	$\left\langle s^{(\mathtt{R})}_{23222}\right\rangle = 1$	$\left\langle s^{(\mathtt{R})}_{23221}\right\rangle = 0$

3D equilibrium equation (4.1a) through the thickness in Section 4.4.1.

Let us derive generalized stresses associated to $\widetilde{\boldsymbol{\sigma}}^{(\mathtt{R})}$. Using Equation 4.25 and integrating by parts when necessary leads to:

$$\left\langle \sigma^{(\mathtt{R})}_{\alpha\beta}\right\rangle = 0, \qquad \left\langle x_3\sigma^{(\mathtt{R})}_{\alpha\beta}\right\rangle = 0, \qquad \left\langle s^{(\mathtt{R})}_{\alpha 3\beta\gamma\delta}\right\rangle = i_{\alpha\beta\gamma\delta} \tag{4.26}$$

and we have: $\left\langle \sigma^{(\mathtt{R})}_{\alpha 3}\right\rangle = \boldsymbol{i} \therefore \mathbf{R} = \boldsymbol{Q}$. Only $\boldsymbol{Q}$ remains after integrating $\widetilde{\boldsymbol{\sigma}}^{(\mathtt{R})}$ through the thickness and the four other static unknowns are self-equilibrated stress. These stresses are analogous to bimoment and warping functions in the theory of beams under torsion from Vlasov (1961). More precisely we have:

$\mathtt{R}_{111}$ and $\mathtt{R}_{222}$ are the cylindrical bending part of shear forces Q_1 and Q_2, $\mathtt{R}_{121}$ and $\mathtt{R}_{122}$ are the torsion part of shear forces and $\mathtt{R}_{112}$ and $\mathtt{R}_{221}$ are linked to strictly self-equilibrated stresses.

4.5.2.1.2 Bending gradient equilibrium equations Two observations lead to the definition of statically compatible fields for the bending gradient SC^{BG}. The first one is that we chose $\mathbf{R}$ such as $\mathbf{M} \otimes \boldsymbol{\nabla} = \mathbf{R}$ in Section 4.5.1. The second one is that we have $\boldsymbol{Q} = \boldsymbol{i} \therefore \mathbf{R}$. Adapting SC^{RM} fields (4.13) we suggest the following definition of SC^{BG}:

$$(\mathbf{N},\mathbf{M},\mathbf{R}) \in SC^{BG} \Leftrightarrow \begin{cases} \mathbf{N}\cdot\boldsymbol{\nabla} = \mathbf{0} \text{ on } \omega & \text{(4.27a)} \\ \mathbf{M}\otimes\boldsymbol{\nabla} - \mathbf{R} = \mathbf{0} \text{ on } \omega & \text{(4.27b)} \\ \boldsymbol{i} \therefore \mathbf{R}\cdot\boldsymbol{\nabla} + p_3 = 0 \text{ on } \omega & \text{(4.27c)} \end{cases}$$

4.5.2.2 Bending gradient kinematically compatible fields

4.5.2.2.1 Dual variables Taking the derivative of $w^{*BG}(\mathbf{N},\mathbf{M},\mathbf{R})$ with respect to each static unknown leads to the following definition of dual variables:

$$\mathbf{e} = \frac{\partial w^{*BG}}{\partial \mathbf{N}}, \quad \boldsymbol{\chi} = \frac{\partial w^{*BG}}{\partial \mathbf{M}}, \quad \boldsymbol{\Gamma} = \frac{\partial w^{*BG}}{\partial \mathbf{R}} \tag{4.28}$$

where $\mathbf{e}$ is associated to membrane strains and $\boldsymbol{\chi}$ to curvatures. $\boldsymbol{\Gamma}$ is a generalized shear strain. $\boldsymbol{\Gamma}$ is a third-order 2D tensor following $\mathbf{R}$ symmetry: $\Gamma_{\beta\alpha\gamma} = \Gamma_{\alpha\beta\gamma}$.

Internal work for the bending gradient plate model is accordingly written as:

$$V_{int}^{BG} = \int_\omega \mathbf{N} : \mathbf{e} + \mathbf{M} : \boldsymbol{\chi} + {}^t\mathbf{R} \therefore \boldsymbol{\Gamma} d\omega \tag{4.29}$$

4.5.2.2.2 Dualization of bending gradient equilibrium equations Since SC^{BG} is defined, it is very classical to identify kinematically compatible fields KC^{BG} by integrating by parts the equilibrium equations (4.27) multiplied with *ad hoc* test fields $\widetilde{\boldsymbol{U}}$ and $\boldsymbol{\Phi}$, where $\widetilde{\boldsymbol{U}}(x_1, x_2)$ is a 3D vector and $\boldsymbol{\Phi}(x_1, x_2)$ a third-order 2D tensor following $\mathbf{R}$ symmetry: $\Phi_{\beta\alpha\gamma} = \Phi_{\alpha\beta\gamma}$. Detailed computation is given in Appendix 4.A.2. This leads to the weak formulation of the plate theory:

$$V_{int}^{BG} = V_{ext}^{BG}$$

where

$$V_{int}^{BG} = \int_\omega \mathbf{N} : (\boldsymbol{i} : (\boldsymbol{\nabla} \otimes \boldsymbol{U})) + \mathbf{M} : (\boldsymbol{\Phi} \cdot \boldsymbol{\nabla}) + {}^t\mathbf{R} \therefore (\boldsymbol{\Phi} + \boldsymbol{i} \cdot \boldsymbol{\nabla} U_3)\, d\omega \tag{4.30}$$

$$V_{ext}^{BG} = \int_\omega p_3 U_3 d\omega + \int_{\partial\omega} (\mathbf{N} \cdot \boldsymbol{n}) \cdot \boldsymbol{U} + \mathbf{M} : (\boldsymbol{\Phi} \cdot \boldsymbol{n}) + (\boldsymbol{i} \therefore \mathbf{R} \cdot \boldsymbol{n})\, U_3 dl \tag{4.31}$$

and $\boldsymbol{n}$ is the in-plane unit vector outwardly normal to ω.

Dual strains are identified in V_{int}^{BG} as:

$$\mathbf{e} = \boldsymbol{i} : (\boldsymbol{\nabla} \otimes \boldsymbol{U}), \quad \boldsymbol{\chi} = \boldsymbol{\Phi} \cdot \boldsymbol{\nabla}, \quad \boldsymbol{\Gamma} = \boldsymbol{\Phi} + \boldsymbol{i} \cdot \boldsymbol{\nabla} U_3 \tag{4.32}$$

where $\boldsymbol{\Phi}$ is a generalized rotation and $\mathbf{e}$ is exactly the Love-Kirchhoff membrane strain. Since we have assumed the plate is clamped, there is no external work on the edge $\partial\omega$ in V_{ext}^{BG} (Equation 4.31). This leads to the following condition on $\widetilde{\boldsymbol{U}}$ and $\boldsymbol{\Phi}$ for clamped edges:

$$\boldsymbol{\Phi} \cdot \boldsymbol{n} = \mathbf{0} \text{ on } \partial\omega, \qquad \widetilde{\boldsymbol{U}} = \widetilde{\mathbf{0}} \text{ on } \partial\omega$$

The above remarks enable us to define the set of kinematically compatible fields KC^{BG} for clamped plates:

$$(\mathbf{e}, \boldsymbol{\chi}, \boldsymbol{\Gamma}) \in KC^{BG} \Leftrightarrow \begin{cases} \mathbf{e} = \boldsymbol{i} : (\boldsymbol{\nabla} \otimes \boldsymbol{U}) \text{ on } \omega & \text{(4.33a)} \\ \boldsymbol{\chi} = \boldsymbol{\Phi} \cdot \boldsymbol{\nabla} \text{ on } \omega & \text{(4.33b)} \\ \boldsymbol{\Gamma} = \boldsymbol{\Phi} + \boldsymbol{i} \cdot \boldsymbol{\nabla} U_3 \text{ on } \omega & \text{(4.33c)} \\ \boldsymbol{\Phi} \cdot \boldsymbol{n} = \mathbf{0} \text{ on } \partial\omega & \text{(4.33d)} \\ \widetilde{\boldsymbol{U}} = \widetilde{\mathbf{0}} \text{ on } \partial\omega & \text{(4.33e)} \end{cases}$$

The set KC^{BG} has been defined previously using standard dualization techniques. In order to recover a physical meaning for $(\mathbf{e}, \boldsymbol{\chi}, \boldsymbol{\Gamma})$ we notice that, with $\boldsymbol{p} = \mathbf{0}$ and $\widetilde{\boldsymbol{\mu}} = \widetilde{\mathbf{0}}$, the 3D problem $\mathcal{P}^{3D}$ external work rewrites (Equation 4.9):

$$V_{ext}^{3D} = \int_{\omega} p_3 U_3^{3D} d\omega \tag{4.34}$$

where

$$U_3^{3D} = \frac{u_3^{3D+} + u_3^{3D-}}{2} \tag{4.35}$$

Besides we have just demonstrated for a clamped plate:

$$V_{ext}^{BG} = \int_{\omega} p_3 U_3 d\omega \tag{4.36}$$

Thus setting $U_3 = U_3^{3D}$, preserves the energetic relation between the full gradient model and the 3D problem and enables us to recover 3D displacement field $\widetilde{\boldsymbol{u}}^{3D}$. We draw the reader's attention to the fact that no assumption has been made on $\widetilde{\boldsymbol{u}}^{3D}$.

Moreover, assuming $\boldsymbol{\Gamma} = 0$ leads to $\boldsymbol{\Phi} = -\boldsymbol{i} \cdot \boldsymbol{\nabla} U_3$ and therefore $\chi_{\alpha\beta} = \Phi_{\alpha\beta\gamma}\nabla_\gamma = -U_{3,\alpha\beta}$ coincides with the Love-Kirchhoff definition of curvatures. Thus it is possible to rewrite the Bending-Gradient curvature as the sum of two terms, $\boldsymbol{\chi} = \boldsymbol{\chi}^{LK} + \boldsymbol{\Gamma} \cdot \boldsymbol{\nabla}$, the Love-Kirchhoff curvature and the contribution of the generalized shear strains $\boldsymbol{\Gamma}$.

4.5.3 Bending gradient constitutive equations

4.5.3.1 Bending gradient stress energy density

A detailed analysis dedicated to material symmetries is provided in Appendix 4.A.1. The main result is that material symmetry of the plate constituents with respect to (x_1, x_2) plane uncouples Love-Kirchhoff $(\mathbf{M}, \mathbf{N})$ and shear unknowns $(\mathbb{R})$. Since this is true for almost all laminated plates of interest, we restrict the analysis to this case. This means that the energy density can be written as the sum of two terms:

$$w^{*BG} = w^{*BG,LK}(\mathbf{N}, \mathbf{M}) + w^{*BG,\mathbb{R}}(\mathbb{R})$$

According to Definition 4.15, the shear part of the stress energy density is:

$$w^{*BG,\mathbb{R}}(\mathbb{R}) = \frac{1}{2}\int_{-\frac{h}{2}}^{\frac{h}{2}} {}^t\left(\widetilde{\boldsymbol{s}}^{(\mathbb{R})} \therefore \mathbb{R}\right) : \widetilde{\boldsymbol{\mathcal{S}}}(x_3) : \left(\widetilde{\boldsymbol{s}}^{(\mathbb{R})} \therefore \mathbb{R}\right) dx_3 = \frac{1}{2}{}^t\mathbb{R} \therefore \mathbb{f} \therefore \mathbb{R} \tag{4.37}$$

where:

$$\mathbb{f} = \left\langle {}^t\left(\widetilde{\boldsymbol{s}}^{(\mathbb{R})}\right) : \widetilde{\boldsymbol{\mathcal{S}}}(x_3) : \widetilde{\boldsymbol{s}}^{(\mathbb{R})} \right\rangle \tag{4.38}$$

Inserting $\widetilde{\boldsymbol{s}}^{(\mathbb{R})}$ (Equation 4.25) into $\mathbb{f}$ definition leads to:

$$\mathbb{f}_{\alpha\beta\gamma\delta\epsilon\zeta} = \int_{-\frac{h}{2}}^{\frac{h}{2}} 4 s^{(\mathbb{R})}_{\phi 3\gamma\beta\alpha}(x_3)\mathcal{S}_{\phi 3\psi 3}(x_3)s^{(\mathbb{R})}_{\psi 3\delta\epsilon\zeta}(x_3)dx_3 \tag{4.39}$$

which becomes:

$$\mathbb{f} = \int_{-\frac{h}{2}}^{\frac{h}{2}} \left(\int_{-\frac{h}{2}}^{x_3} \left({}^t\boldsymbol{\mathcal{b}} + z\,\boldsymbol{\mathcal{d}}\right) : \boldsymbol{c}(z)dz \right) \cdot \mathbf{S}(x_3) \cdot \left(\int_{-\frac{h}{2}}^{x_3} \boldsymbol{c}(z) : \left(\boldsymbol{\mathcal{b}} + z\,\boldsymbol{\mathcal{d}}\right) dz \right) dx_3 \tag{4.40}$$

where $\mathbf{S} = \mathsf{S}_{\alpha\beta} = 4\mathcal{S}_{\alpha 3\beta 3}$ is the out-of-plane shear compliance tensor.

The generalized shear compliance $\mathbb{f}$ is a sixth-order tensor, with two symmetries. The major symmetry: ${}^t\mathbb{f} = \mathbb{f}$ and the minor symmetries: $\mathbb{f}_{\alpha\beta\gamma\delta\epsilon\zeta} = \mathbb{f}_{\beta\alpha\gamma\delta\epsilon\zeta}$. The identity for these tensors is: $\mathbb{I}_{\alpha\beta\gamma\delta\epsilon\zeta} = i_{\alpha\beta\epsilon\zeta}\,\delta_{\gamma\delta}$. $\mathbb{f}$ definition ensures symmetry and positiveness. However, $\mathbb{f}$ is not always definite since four static degrees of freedom are self-equilibrated stress (like warping is degenerated in the torsion of a beam with a circular section). More details about $\mathbb{f}$ kernel is given in Appendix 4.A.4.

Once the stress energy density is defined, it is straightforward to derive the constitutive equation:

$$\boldsymbol{\Gamma} = \frac{\partial w^{*BG}}{\partial \mathbf{R}} = \mathbb{f} \therefore \mathbf{R} \tag{4.41}$$

4.5.3.2 Bending gradient strain energy density

The strain energy density is defined through the Legendre-Fenchel transform. Thus it necessitates the definition of $\mathbb{f}$ inverse. As indicated previously, $\mathbb{f}$ is not always definite. This is the case for a homogeneous plate. Yet it is possible to be more explicit about $\mathbb{f}$ inverse.

The generalized shear compliance $\mathbb{f}$ maps symmetric third-order tensors on its image:

$$\mathbb{f}: \quad \mathbf{R} \in \left(\mathbb{R}^2\right)^3 \longmapsto \mathbb{f} \therefore \mathbf{R} = \boldsymbol{\Gamma} \in Im\left(\mathbb{f}\right) \subseteq \left(\mathbb{R}^2\right)^3$$

In order to define an inverse for $\mathbb{f}$ we introduce the Moore-Penrose pseudo inverse $\mathbb{F}$ defined as

$$\mathbb{F} = \lim_{\kappa \to 0} \left(\mathbb{f} \therefore \mathbb{f} + \kappa \mathbb{I}\right)^{-1} \therefore \mathbb{f}$$

For instance $\left(\begin{smallmatrix} \lambda & 0 \\ 0 & 0 \end{smallmatrix}\right)$ pseudo inverse is $\left(\begin{smallmatrix} 1/\lambda & 0 \\ 0 & 0 \end{smallmatrix}\right)$. With this definition we have:

$$\mathbb{F}: \quad \boldsymbol{\Gamma} \in \left(\mathbb{R}^2\right)^3 \longmapsto \mathbb{F} \therefore \boldsymbol{\Gamma} = \mathbf{R} \in Im\left(\mathbb{F}\right) \subseteq \left(\mathbb{R}^2\right)^3$$

Hence $\mathbb{F} \therefore \mathbb{f}$ is the orthogonal projector onto $Im\left(\mathbb{F}\right)$ and $\mathbb{I} - \mathbb{f} \therefore \mathbb{F}$ is the orthogonal projector onto $Ker\left(\mathbb{F}\right)$. Defining an inverse relation for $\mathbb{f}$ imposes to restrain $\mathbb{F}$ domain to $Im\left(\mathbb{f}\right)$: $\left(\mathbb{I} - \mathbb{f} \therefore \mathbb{F}\right) \therefore$

$\mathbf{\Gamma} = \mathbf{0}$. Thus there is an internal constraint over generalized shear strains $\mathbf{\Gamma}$ when $\mathbb{f}$ is not positive definite. Finally, we have the equivalence:

$$\begin{cases} \mathbf{\Gamma} = \mathbb{f} \therefore \mathbf{R} \\ (\mathbb{I} - \mathbb{f} \therefore \mathbb{F}) \therefore \mathbf{\Gamma} = \mathbf{0} \end{cases} \Leftrightarrow \begin{cases} \mathbf{R} = \mathbb{F} \therefore \mathbf{\Gamma} + \mathbf{R}^k \\ \mathbb{F} \therefore \mathbb{f} \therefore \mathbf{R}^k = \mathbf{0} \end{cases} \tag{4.42}$$

This enables the definition of the shear part of the strain energy density, using the Legendre-Fenchel transform:

$$w^{BG,\mathbf{\Gamma}}(\mathbf{\Gamma}) = \frac{1}{2} {}^t\mathbf{\Gamma} \therefore \mathbb{F} \therefore \mathbf{\Gamma} \quad \text{for } \mathbf{\Gamma} \text{ such that} \quad (\mathbb{I} - \mathbb{f} \therefore \mathbb{F}) \therefore \mathbf{\Gamma} = \mathbf{0} \tag{4.43}$$

4.5.3.3 Summary of the Bending gradient plate model

Let us summarize all the definitions introduced for the new plate model.

The set of kinematically compatible fields is:

$$(\mathbf{e}, \boldsymbol{\chi}, \mathbf{\Gamma}) \in KC^{BG} \Leftrightarrow \begin{cases} \mathbf{e} = \boldsymbol{i} : (\boldsymbol{\nabla} \otimes \boldsymbol{U}) \text{ on } \omega & \text{(4.44a)} \\ \boldsymbol{\chi} = \mathbf{\Phi} \cdot \boldsymbol{\nabla} \text{ on } \omega & \text{(4.44b)} \\ \mathbf{\Gamma} = \mathbf{\Phi} + \boldsymbol{i} \cdot \boldsymbol{\nabla} U_3 \text{ on } \omega & \text{(4.44c)} \\ \mathbf{\Phi} \cdot \boldsymbol{n} = \mathbf{0} \text{ on } \partial\omega & \text{(4.44d)} \\ \widetilde{\boldsymbol{U}} = \widetilde{\mathbf{0}} \text{ on } \partial\omega & \text{(4.44e)} \end{cases}$$

where $\mathbf{e}$ is the conventional in-plane plate strain, $\boldsymbol{\chi}$ is the curvature, $\mathbf{\Gamma}$ is the generalized shear strain and $\mathbf{\Phi}$ is the generalized rotation. These fields are almost identical to Reissner-Mindlin kinematically compatible fields but rotation pseudo-vector is replaced by the generalized third-order rotation tensor $\mathbf{\Phi}$.

The set of statically compatible fields is

$$(\mathbf{N}, \mathbf{M}, \mathbf{R}) \in SC^{BG} \Leftrightarrow \begin{cases} \mathbf{N} \cdot \boldsymbol{\nabla} = 0 \text{ on } \omega & \text{(4.45a)} \\ \mathbf{M} \otimes \boldsymbol{\nabla} - \mathbf{R} = \mathbf{0} \text{ on } \omega & \text{(4.45b)} \\ (\boldsymbol{i} \therefore \mathbf{R}) \cdot \boldsymbol{\nabla} = -p_3 \text{ on } \omega & \text{(4.45c)} \end{cases}$$

where $\mathbf{N}$ is the membrane stress, $\mathbf{M}$ is the bending moment and $\mathbf{R}$ the gradient of the bending moment. This set of equations is almost identical to Reissner-Mindlin equations where shear forces have been replaced by the bending gradient $\mathbf{R}$.

Finally, for constitutive material following local monoclinic symmetry with respect to (x_1, x_2) plane (uncoupling between $\mathbf{R}$ and $(\mathbf{N}, \mathbf{M})$) the Bending-Gradient plate constitutive equations write

as:

$$\begin{cases} \mathbf{N} = \boldsymbol{\mathcal{A}} : \mathbf{e} + \boldsymbol{\mathcal{B}} : \boldsymbol{\chi} & \text{(4.46a)} \\ \mathbf{M} = {}^t\boldsymbol{\mathcal{B}} : \mathbf{e} + \boldsymbol{\mathcal{D}} : \boldsymbol{\chi} & \text{(4.46b)} \\ \boldsymbol{\Gamma} = \mathbb{f} \therefore \mathbb{R}, \quad \text{where} \quad (\mathbb{I} - \mathbb{f} \therefore \mathbb{F}) \therefore \boldsymbol{\Gamma} = 0 & \text{(4.46c)} \end{cases}$$

The solution of the plate model must comply with the three sets of equations (4.44, 4.45, 4.46).

We recall also variational approaches for the model: solving the static approach of Bending-Gradient consists in finding the set of statically compatible fields $(\mathbf{N}, \mathbf{M}, \mathbb{R})^{BG}$ which minimizes the complementary potential energy:

$$P^{*BG}\left((\mathbf{N}, \mathbf{M}, \mathbb{R})^{BG}\right) = \min_{(\mathbf{N}, \mathbf{M}, \mathbb{R}) \in SC^{BG}} \left\{ P^{*BG}\left(\mathbf{N}, \mathbf{M}, \mathbb{R}\right) \right\} \tag{4.47}$$

where P^{*BG}, the complementary potential energy of the bending gradient plate problem $\mathcal{P}^{BG}$ is written as:

$$P^{*BG}\left(\mathbf{N}, \mathbf{M}, \mathbb{R}\right) = \int_{\omega} w^{*BG}\left(\mathbf{N}, \mathbf{M}, \mathbb{R}\right) d\omega \tag{4.48}$$

Again, the strain potential energy of $\mathcal{P}^{BG}$ is:

$$P^{BG}(\mathbf{e}, \boldsymbol{\chi}, \boldsymbol{\Gamma}) = \int_{\omega} w^{BG}(\mathbf{e}, \boldsymbol{\chi}, \boldsymbol{\Gamma}) - p_3 U_3 d\omega \tag{4.49}$$

and solving the kinematic approach of $\mathcal{P}^{BG}$ consists in finding the set of kinematically compatible fields $(\mathbf{e}, \boldsymbol{\chi}, \boldsymbol{\Gamma})^{BG}$ which minimizes the strain potential energy under the kinematic constraint $(\mathbb{I} - \mathbb{f} \therefore \mathbb{F}) \therefore \boldsymbol{\Gamma} = \mathbf{0}$:

$$P^{BG}\left((\mathbf{e}, \boldsymbol{\chi}, \boldsymbol{\Gamma})^{BG}\right) = \min_{\substack{(\mathbf{e}, \boldsymbol{\chi}, \boldsymbol{\Gamma}) \in KC^{BG} \\ (\mathbb{I} - \mathbb{f} \therefore \mathbb{F}) \therefore \boldsymbol{\Gamma} = \mathbf{0}}} \left\{ P^{BG}\left(\mathbf{e}, \boldsymbol{\chi}, \boldsymbol{\Gamma}\right) \right\} \tag{4.50}$$

Note that the model presented in this paper for clamped plates can be extended to other boundary conditions as detailed in Appendix 4.A.3.

4.6 Bending-Gradient or Reissner-Mindlin plate model?

4.6.1 Homogeneous plate

For a homogeneous plate, we have

$$\boldsymbol{f}^{(\mathbb{R})} = \frac{12 x_3}{h^3} \boldsymbol{i} \therefore \mathbb{R} \text{ and } f_3^{(\mathbb{R})} = 0 \tag{4.51}$$

and

$$s^{(\mathbb{R})}_{\alpha 3\beta\gamma\delta}(x_3) = \frac{6}{h^3}\left(\frac{h^2}{4} - x_3^2\right) i_{\alpha\beta\gamma\delta}, \quad s^{(\mathbb{R})}_{\alpha\beta\gamma\delta\epsilon} = 0 \quad \text{and } s^{(\mathbb{R})}_{33\gamma\delta\epsilon} = 0 \tag{4.52}$$

which is exactly the same result as in Section 4.4.2.2. Moreover, the generalized shear compliance is:

$$\mathbb{f} = \frac{6}{5h}\boldsymbol{i}\cdot\mathsf{S}\cdot\boldsymbol{i} \tag{4.53}$$

and the shear stress energy is:

$$w^{*BG,\mathbf{R}}(\mathbf{R}) = \frac{1}{2}{}^t\mathbf{R} \therefore \boldsymbol{i}\cdot\frac{6}{5h}\mathsf{S}\cdot\boldsymbol{i} \therefore \mathbf{R} \tag{4.54}$$

Since $\boldsymbol{Q} = \boldsymbol{i} \therefore \mathbf{R}$, it is possible to identify there the Reissner-Mindlin stress energy density as:

$$w^{*RM,\boldsymbol{Q}}(\boldsymbol{Q}) = \frac{1}{2}{}^t\boldsymbol{Q}\cdot\frac{6}{5h}\mathsf{S}\cdot\boldsymbol{Q}$$

which leads to the constitutive equation:

$$\boldsymbol{Q} = \frac{5h}{6}\mathsf{S}^{-1}\cdot\boldsymbol{\gamma}$$

where $\boldsymbol{\gamma}$ stands here for Reissner-Mindlin plate shear strain. This is the result from Reissner (1945) which exhibits the well-known shear correction factor $k_\alpha = 5/6$. It is furthermore demonstrated in Appendix 4.A.5 that boundary conditions are also identical.

Finally, for homogeneous plates, the Reissner-Mindlin model and the Bending-Gradient model are completely identical.

4.6.2 Projection of the Bending-Gradient plate model

Since in some cases, the Bending-Gradient is turned into a Reissner-Mindlin plate model, we need a means to estimate the difference between both plate models. For this, we define the projection of the Bending-Gradient model on a Reissner-Mindlin model.

The shear forces energy density in the case of a Reissner-Mindlin plate model writes as:

$$w^{*RM,\boldsymbol{Q}}(\boldsymbol{Q}) = \frac{1}{2}{}^t\boldsymbol{Q}\cdot\mathsf{f}^{RM}\cdot\boldsymbol{Q} \tag{4.55}$$

Since $\boldsymbol{Q} = \boldsymbol{i} \therefore \mathbf{R}$, this stress energy becomes in Bending-Gradient plate model:

$$w^{*BG,\mathbf{R}}(\mathbf{R}) = \frac{1}{2}{}^t\mathbf{R} \therefore \boldsymbol{i}\cdot\mathsf{f}^{RM}\cdot\boldsymbol{i} \therefore \mathbf{R} \tag{4.56}$$

Thus a Reissner-Mindlin compliance f^{RM} is expressed in the Bending-Gradient exactly as for a

homogeneous plate (Equation (4.53)):

$$\mathbb{f}^{RM} = \boldsymbol{i} \cdot \mathbf{f}^{RM} \cdot \boldsymbol{i} \tag{4.57}$$

Then, we define the orthogonal projection of a Bending-Gradient compliance tensor $\mathbb{f}$ on a Reissner-Mindlin compliance tensor $\mathbf{f}^{RM}$. For this, we introduce the following inner product:

$$\mathbb{f}_{\alpha\beta\gamma\delta\epsilon\zeta}\mathbb{g}_{\alpha\beta\gamma\delta\epsilon\zeta} = {}^{t}\mathbb{f} ::: \mathbb{g} \tag{4.58}$$

and the related norm:

$$\|\mathbb{f}\| = \sqrt{{}^{t}\mathbb{f} ::: \mathbb{f}} \tag{4.59}$$

We define $\mathbb{f}^{RM}$ the Reissner-Mindlin part of $\mathbb{f}$ as the projection of $\mathbb{f}$ on the linear subspace of tensors writting as $\mathbb{g}^{RM} = \boldsymbol{i} \cdot \mathbf{g}^{RM} \cdot \boldsymbol{i}$:

$$\forall \mathbb{g}^{RM}, \quad {}^{t}\mathbb{f}^{RM} ::: \mathbb{g}^{RM} = {}^{t}\mathbb{f} ::: \mathbb{g}^{RM} \tag{4.60}$$

which is equivalent to:

$$\forall \mathbf{g}^{RM}, \quad {}^{t}\mathbf{f}^{RM} : \mathbf{g}^{RM} = {}^{t}\left(\left(\frac{2}{3}\boldsymbol{i}\right) \therefore \mathbb{f} \therefore \left(\frac{2}{3}\boldsymbol{i}\right)\right) : \mathbf{g}^{RM} \tag{4.61}$$

Thus

$$\mathbf{f}^{RM} = \left(\frac{2}{3}\boldsymbol{i}\right) \therefore \mathbb{f} \therefore \left(\frac{2}{3}\boldsymbol{i}\right) \tag{4.62}$$

defines the projection of $\mathbb{f}$ on Reissner-Mindlin plate model and the Reissner-Mindlin part of $\mathbb{f}$ is:

$$\mathbb{f}^{RM} = \left(\frac{2}{3}\boldsymbol{i} \cdot \boldsymbol{i}\right) \therefore \mathbb{f} \therefore \left(\frac{2}{3}\boldsymbol{i} \cdot \boldsymbol{i}\right) \tag{4.63}$$

The projection $\mathbf{f}^{RM}$ of $\mathbb{f}$ is equivalent to assuming $\mathbb{R} = \frac{2}{3}\boldsymbol{i} \cdot \boldsymbol{Q}$ in $w^{*BG,\mathbb{R}}$ (Equation (4.37)). Actually it is possible to give further mechanical interpretation of this result. Let us consider the following change of generalized shear static variables:

$$Q_\alpha = \mathtt{R}_{\alpha\beta\beta}, \quad \Delta Q_1 = \mathtt{R}_{111} - 2\mathtt{R}_{122}, \quad \Delta Q_2 = 2\mathtt{R}_{121} - \mathtt{R}_{222}, \quad \mathtt{R}_{112} \quad \text{and} \quad \mathtt{R}_{221} \tag{4.64}$$

In that case the four self-equilibrated static unknowns are ΔQ_1, ΔQ_2, $\mathtt{R}_{112}$, and $\mathtt{R}_{221}$. They are clearly set apart from shear forces Q_α. Setting to zero pure warping unknowns in order to keep only "pure shear forces" leads exactly to $\mathbb{R} = \frac{2}{3}\boldsymbol{i} \cdot \boldsymbol{Q}$. From this, $\mathbb{f}^{RM}$ can be considered as the restriction of $\mathbb{f}$ when setting warping unknowns to zero. Consequently, we introduce the pure warping part of $\mathbb{f}$ as

the orthogonal complement of $\mathbb{f}^{RM}$:

$$\mathbb{f}^{\mathrm{W}} = \mathbb{f} - \mathbb{f}^{RM} \tag{4.65}$$

Finally we suggest the following relative distance between the Bending-Gradient plate model and the Reissner-Mindlin one:

$$\Delta^{RM/BG} = \frac{\|\mathbb{f}^{\mathrm{W}}\|}{\|\mathbb{f}\|} \tag{4.66}$$

$\Delta^{RM/BG}$ gives an estimate of the pure warping fraction of the shear stress energy and can be used as a criterion for assessing the need of the Bending-Gradient model. When the plate constitutive equation is restricted to a Reissner-Mindlin one, we have exactly $\Delta^{RM/BG} = 0$.

As illustration, we derived $\Delta^{RM/BG}$ for angle-ply laminates which were considered by Pagano (1970a). Each ply is made of unidirectional fiber-reinforced material oriented at θ relative to the direction x_1. All plies have the same thickness and are perfectly bounded. The overall thickness of the plate is h. A laminate is denoted between brackets by the successive ply-orientations along thickness. For instance $[0°, 90°]$ denotes a 2-ply laminate where the lower ply fibers are oriented in the bending direction. The constitutive behavior of a ply is assumed to be transversely isotropic along the direction of the fibers and engineering constants are chosen similar to those of Pagano (1969):

$$E_L = 25 \times 10^6 psi, \quad E_T = 1 \times 10^6 psi, \quad G_{LT} = G_{LN} = 0.5 \times 10^6 psi,$$
$$G_{NT} = \frac{E_T}{2(1+\nu_{NT})} = 0.4 \times 10^6 psi, \quad \nu_{LT} = \nu_{LN} = \nu_{NT} = 0.25$$

where G_{NT} has been changed to preserve transversely isotropic symmetry. L is the longitudinal direction oriented in the (x_1, x_2) plane at θ with respect to $\widetilde{e}_1$, T is the transverse direction and N is the normal direction coinciding with $\widetilde{e}_3$

On Figure 4.2, $\Delta^{RM/BG}$ is plotted for any 2-ply configuration and on Figure 4.3, for any 4-ply symmetric configurations. It appears clearly that $\Delta^{RM/BG}$, is not negligible (up to 37%). Thus, neglecting warping with a simple Reissner-Mindlin plate model applied to such laminates can lead up to 37% error in the stress energy.

4.7 Conclusion

In this work, applying Reissner's approach for deriving transverse shear stress to a laminated plate revealed that more static shear DOF than the usual shear forces are involved in microscopic fields. Thanks to conventional variational tools, this led to the design of a new higher-order gradient plate theory involving the gradient of the bending moment, instead of shear forces. Statically and kinematically compatible fields as well as constitutive equations were derived. The mechanical meaning of the bending gradient was identified as self-balanced static unknowns associated to warp-

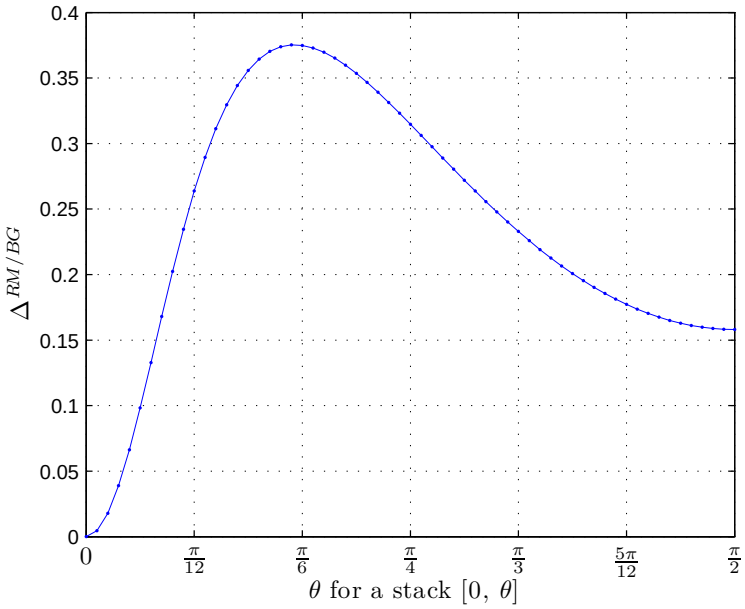

Figure 4.2: Relative distance between the Reissner-Mindlin and the Bending-Gradient plate models $\Delta^{RM/BG}$ for any 2-ply configuration

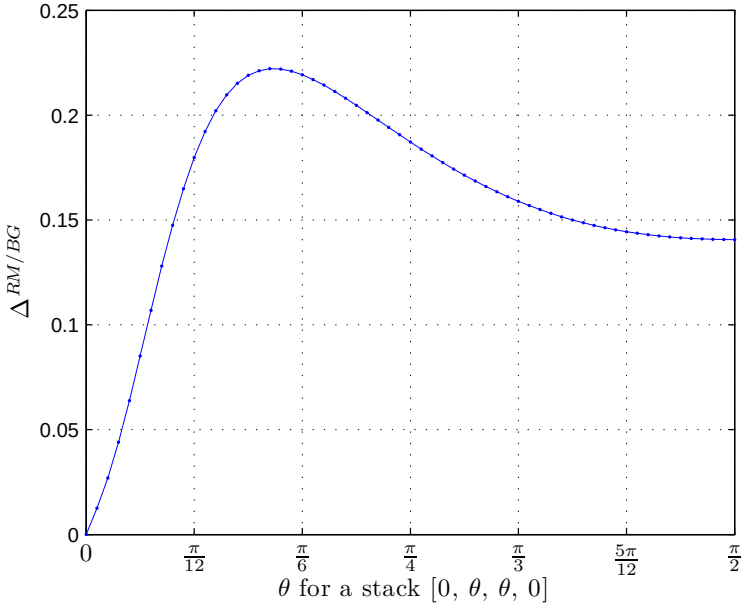

Figure 4.3: Relative distance between the Reissner-Mindlin and the Bending-Gradient plate models $\Delta^{RM/BG}$ for any symmetric 4-ply configuration

ing functions in addition to usual shear forces. The present plate theory does not require any specific constitutive material symmetry and the monoclinic symmetry with respect to plane of $\widetilde{\boldsymbol{e}}_3$ normal was introduced only for convenience. Finally, we demonstrated that the Bending-Gradient plate model is an extension to laminated plates of the Reissner-Mindlin plate model which actually cannot be reduced to a Reissner-Mindlin plate model.

In the second part of this work (Lebée and Sab, 2010a), comparison between models is performed in the cylindrical bending case which makes use of only closed-form solutions. It will be demonstrated that the Bending Gradient model contains most of the relevant aspects of shear effects with very little computation and simple interpretation. The main conclusion is that the Bending-Gradient gives good predictions of both deflection and shear stress distributions in any material configuration and provided the plate follows mirror symmetry ($\boldsymbol{\mathcal{B}} = \boldsymbol{0}$), the Bending-Gradient solution converges to the exact solution when the slenderness ratio h/L goes to 0 faster than other existing models.

4.A Appendix

4.A.1 Symmetries

First, we derive $\mathbf{N}$, $\mathbf{M}$ and $\mathbf{R}$ transformation formulas through orthogonal transformations.

Consider a 3D orthogonal transformation $\widetilde{\mathbf{P}}$ such as $\widetilde{\boldsymbol{x}}^{\dagger} = \widetilde{\mathbf{P}} \cdot \widetilde{\boldsymbol{x}}$ is the image of $\widetilde{\boldsymbol{x}}$, ($^{t}\widetilde{\mathbf{P}} \cdot \widetilde{\mathbf{P}} = \widetilde{\boldsymbol{\delta}}$ and $\det \widetilde{\mathbf{P}} = \pm 1$). A stress field $\widetilde{\boldsymbol{\sigma}}$ has the image $\widetilde{\boldsymbol{\sigma}}^{\dagger}$ given by:

$$\widetilde{\boldsymbol{\sigma}}^{\dagger}\left(\widetilde{\boldsymbol{x}}\right) = \widetilde{\mathbf{P}} \cdot \widetilde{\boldsymbol{\sigma}} \left({}^{t}\widetilde{\mathbf{P}} \cdot \widetilde{\boldsymbol{x}} \right) \cdot {}^{t}\widetilde{\mathbf{P}}$$

The analysis is restricted to planar transformations:

$$\widetilde{\mathbf{P}} = \left(\begin{array}{cc|c} & & 0 \\ & \mathbf{P} & 0 \\ \hline 0 & 0 & \mathsf{P}_{33}=\pm 1 \end{array} \right)$$

where $\mathbf{P}$ is a 2D orthogonal matrix. Then we have:

$$\mathbf{N}^{\dagger}\left(\boldsymbol{x}\right) = \left\langle \boldsymbol{\sigma}^{\dagger}\left(\boldsymbol{x}, x_3\right) \right\rangle = \mathbf{P} \cdot \int_{-\frac{h}{2}}^{\frac{h}{2}} \boldsymbol{\sigma}\left({}^{t}\mathbf{P} \cdot \boldsymbol{x}, \mathsf{P}_{33} x_3 \right) dx_3 \cdot {}^{t}\mathbf{P} = \mathbf{P} \cdot \int_{-\mathsf{P}_{33}\frac{h}{2}}^{\mathsf{P}_{33}\frac{h}{2}} \boldsymbol{\sigma}\left({}^{t}\mathbf{P} \cdot \boldsymbol{x}, y_3 \right) \frac{dy_3}{\mathsf{P}_{33}} \cdot {}^{t}\mathbf{P}$$

$\widetilde{\mathbf{P}}$	N_{11}	N_{22}	N_{12}	M_{11}	M_{22}	M_{12}	$\mathtt{R}_{111}$	$\mathtt{R}_{221}$	$\mathtt{R}_{121}$	$\mathtt{R}_{112}$	$\mathtt{R}_{222}$	$\mathtt{R}_{122}$
a) $\begin{pmatrix}-1&0&0\\0&-1&0\\0&0&1\end{pmatrix}$	+	+	+	+	+	+	−	−	−	−	−	−
b) $\begin{pmatrix}1&0&0\\0&1&0\\0&0&-1\end{pmatrix}$	+	+	+	−	−	−	−	−	−	−	−	−
c) $\begin{pmatrix}1&0&0\\0&-1&0\\0&0&1\end{pmatrix}$	+	+	−	+	+	−	+	+	−	−	−	+

Table 4.1: $\epsilon^{\widetilde{\mathbf{P}}}$ and loads for three main invariances

This equation does not depend on P_{33} sign. Thus we obtain:

$$\mathbf{N}^{\dagger}(\boldsymbol{x}) = \mathbf{P}\cdot\int_{-\frac{h}{2}}^{\frac{h}{2}}\boldsymbol{\sigma}\left({}^{t}\mathbf{P}\cdot\boldsymbol{x},x_3\right)dx_3\cdot{}^{t}\mathbf{P} = \mathbf{P}\cdot\mathbf{N}\left({}^{t}\mathbf{P}\cdot\boldsymbol{x}\right)\cdot{}^{t}\mathbf{P}$$

The same approach leads to the following equation for the bending moment:

$$\mathbf{M}^{\dagger}(\boldsymbol{x}) = \mathsf{P}_{33}\mathbf{P}\cdot\mathbf{M}\left({}^{t}\mathbf{P}\cdot\boldsymbol{x}\right)\cdot{}^{t}\mathbf{P}$$

We have also, $\mathtt{R} = \mathbf{M}\otimes\boldsymbol{\nabla}$. Thus taking the gradient of the previous equation leads to:

$$\mathtt{R}^{\dagger}_{\alpha\beta\gamma}(x_\eta) = \mathsf{P}_{33}\mathsf{P}_{\alpha\delta}\mathsf{P}_{\beta\epsilon}\mathsf{P}_{\gamma\zeta}\mathtt{R}_{\delta\epsilon\zeta}\left(\mathsf{P}_{\theta\eta}x_\theta\right)$$

When $\widetilde{\mathbf{P}}$ is diagonal, the above transformation equations simplify. For instance, we have:

$$\mathsf{M}^{\dagger}_{\alpha\beta}(\boldsymbol{x}) = \epsilon^{\widetilde{\mathbf{P}}}_{\mathsf{M}_{\alpha\beta}}\mathsf{M}_{\alpha\beta}\left({}^{t}\mathbf{P}\cdot\boldsymbol{x}\right)$$

where $\epsilon^{\widetilde{\mathbf{P}}}_{\mathsf{M}_{\alpha\beta}} = \pm 1$ is the symmetry index of $\mathsf{M}_{\alpha\beta}$ with respect to $\widetilde{\mathbf{P}}$. For instance $\epsilon^{\widetilde{\mathbf{P}}}_{\mathsf{N}_{\alpha\beta}} = 1$ indicates that $\mathsf{N}_{\alpha\beta}$ is symmetric with respect to $\widetilde{\mathbf{P}}$ and $\epsilon^{\widetilde{\mathbf{P}}}_{\mathtt{R}_{\alpha\beta\gamma}} = -1$ indicates that $\mathtt{R}_{\alpha\beta\gamma}$ is skew-symmetric with respect to $\widetilde{\mathbf{P}}$. Finally, it is possible to use all the previous transformation equations to derive the transformation of the stress energy. In the case $\widetilde{\mathbf{P}}$ reflects a material symmetry, this energy remains invariant. As a consequence, two components having opposite symmetry indexes with respect to $\widetilde{\mathbf{P}}$ are uncoupled

Table 4.1 summarizes symmetry indexes for three main symmetries. A major observation is that material invariance through π rotation around $\widetilde{\boldsymbol{e}}_3$ axis (case a) ensures uncoupling between shear degrees of freedom $\mathtt{R}$ and Love Kirchhoff degrees of freedom $\mathbf{N}$, and $\mathbf{M}$. A plate where for all values of x_3 the local behavior is symmetric with respect to (x_1, x_2) plane fulfills the π rotation around $\widetilde{\boldsymbol{e}}_3$ symmetry. Thus, uncoupling between $\mathbf{N}, \mathbf{M}$ and $\mathtt{R}$ holds true also for any kind of laminated plate provided the local constitutive behavior is monoclinic relative to (x_1, x_2) plane (which is the case for fibrous plies).

4.A.2 Dualization

Multiplying 4.27a with U_α and integrating by parts on the plate domain ω yield:

$$\int_\omega \mathsf{N}_{\alpha\beta} \frac{1}{2} \left(U_{\alpha,\beta} + U_{\beta,\alpha} \right) d\omega = \int_{\partial\omega} \mathsf{N}_{\alpha\beta} n_\beta U_\alpha dl \tag{4.67}$$

where n_α is the outer normal to $\partial\omega$.

Multiplying 4.27c with U_3 and integrating by parts on the plate domain ω yield:

$$\int_\omega \mathtt{R}_{\alpha\beta\beta} U_{3,\alpha} d\omega = \int_{\partial\omega} \mathtt{R}_{\alpha\beta\beta} n_\alpha U_3 dl + \int_\omega p_3 U_3 d\omega \tag{4.68}$$

Multiplying 4.27b with $\mathtt{\Phi}_{\alpha\beta\gamma}$ and integrating by parts on the plate domain ω yield:

$$\int_\omega \mathsf{M}_{\alpha\beta} \mathtt{\Phi}_{\alpha\beta\gamma,\gamma} + \mathtt{R}_{\alpha\beta\gamma} \mathtt{\Phi}_{\alpha\beta\gamma} d\omega = \int_{\partial\omega} \mathsf{M}_{\alpha\beta} \mathtt{\Phi}_{\alpha\beta\gamma} n_\gamma dl \tag{4.69}$$

Adding all relations developed above leads to the following expression which is separated into three parts:

$$\begin{aligned} \int_\omega \mathsf{N}_{\alpha\beta} \frac{1}{2} \left(U_{\alpha,\beta} + U_{\beta,\alpha} \right) + \mathsf{M}_{\alpha\beta} \mathtt{\Phi}_{\alpha\beta\gamma,\gamma} + \mathtt{R}_{\alpha\beta\gamma} \left(\mathtt{\Phi}_{\alpha\beta\gamma} + \frac{1}{2} \left(\delta_{\beta\gamma} U_{3,\alpha} + \delta_{\alpha\gamma} U_{3,\beta} \right) \right) d\omega = \\ \int_\omega p_3 U_3 d\omega + \int_{\partial\omega} \mathsf{N}_{\alpha\beta} n_\beta U_\alpha + \mathsf{M}_{\alpha\beta} \mathtt{\Phi}_{\alpha\beta\gamma} n_\gamma + \mathtt{R}_{\alpha\beta\beta} n_\alpha U_3 dl \end{aligned} \tag{4.70}$$

4.A.3 Mixed boundary conditions

The edge is separated into two parts: $\partial\omega^k$ where generalized strains $(\widetilde{\boldsymbol{U}}^d, \mathbf{H}^d)$ are enforced and $\partial\omega^s$ where generalized stress $(\boldsymbol{V}^d, \mathbf{M}^d)$ are enforced. $\widetilde{\boldsymbol{U}}^d$ is the forced displacement on the edge, $\mathbf{H}^d$ is a symmetric second-order tensor related to a forced rotation on the edge, $\boldsymbol{V}^d$ is the force per unit length enforced on the edge and $\mathbf{M}^d$ is the full bending moment enforced on the edge

4.A.3.1 Kinematically compatible fields

We define Bending-Gradient kinematically compatible fields for mixt boundary condition plates as:

$$(\mathbf{e}, \boldsymbol{\chi}, \boldsymbol{\Gamma}) \in KC^{BG} \Leftrightarrow \begin{cases} \mathbf{e} = \boldsymbol{i} : (\boldsymbol{\nabla} \otimes \boldsymbol{U}) \text{ on } \omega & \text{(4.71a)} \\ \boldsymbol{\chi} = \boldsymbol{\Phi} \cdot \boldsymbol{\nabla} \text{ on } \omega & \text{(4.71b)} \\ \boldsymbol{\Gamma} = \boldsymbol{\Phi} + \boldsymbol{i} \cdot \boldsymbol{\nabla} U_3 \text{ on } \omega & \text{(4.71c)} \\ \boldsymbol{\Phi} \cdot \boldsymbol{n} = \mathbf{H}^d \text{ on } \partial\omega^k & \text{(4.71d)} \\ \widetilde{\boldsymbol{U}} = \widetilde{\boldsymbol{U}}^d \text{ on } \partial\omega^k & \text{(4.71e)} \end{cases}$$

The potential energy is:

$$P^{BG}(\mathbf{e},\boldsymbol{\chi},\boldsymbol{\Gamma}) = \int_\omega w^{BG}(\mathbf{e},\boldsymbol{\chi},\boldsymbol{\Gamma}) - p_3 U_3 d\omega - \int_{\partial\omega^s} \boldsymbol{V}^d \cdot \boldsymbol{U} + \mathbf{M}^d : (\boldsymbol{\Phi}\cdot\boldsymbol{n}) + V_3^d U_3 dl \tag{4.72}$$

4.A.3.2 Statically admissible fields

Bending-Gradient statically compatible fields for mixt boundary condition are:

$$(\mathbf{N},\mathbf{M},\mathbb{R}) \in SC^{BG} \Leftrightarrow \begin{cases} \mathbf{N}\cdot\boldsymbol{\nabla} = -\boldsymbol{p} \text{ on } \omega & \text{(4.73a)} \\ \mathbf{M}\otimes\boldsymbol{\nabla} - \mathbb{R} = 0 \text{ on } \omega & \text{(4.73b)} \\ \boldsymbol{i}\therefore\mathbb{R}\cdot\boldsymbol{\nabla} = -p_3 \text{ on } \omega & \text{(4.73c)} \\ \mathbf{N}\cdot\boldsymbol{n} = \boldsymbol{V}^d \text{ on } \partial\omega^s & \text{(4.73d)} \\ \mathbf{M} = \mathbf{M}^d \text{ on } \partial\omega^s & \text{(4.73e)} \\ \boldsymbol{i}\therefore\mathbb{R}\cdot\boldsymbol{n} = V_3^d \text{ on } \partial\omega^s & \text{(4.73f)} \end{cases}$$

NB: Having $\mathbf{M}\cdot\boldsymbol{t} = \mathbf{M}^d\cdot\boldsymbol{t}$ on $\partial\omega^s$, where $\boldsymbol{t}$ is orthogonal to $\boldsymbol{n}$ looks unnatural since it involves stresses that do not belong to the edge surface. It is a fourth boundary condition common to higher-order models and related to free edge effects similar to those described in Chapter 8.

The complementary energy is:

$$P^{*BG}(\mathbf{N},\mathbf{M},\mathbb{R}) = \int_\omega w^{*BG}(\mathbf{N},\mathbf{M},\mathbb{R})d\omega + \int_{\partial\omega^k} (\mathbf{N}\cdot\boldsymbol{n})\cdot\boldsymbol{U}^d + \mathbf{M}:\mathbf{H}^d + (\mathbb{R}\therefore\boldsymbol{i}\cdot\boldsymbol{n})\,U_3^d dl \tag{4.74}$$

4.A.4 Generalized-shear compliance kernel properties

In this section we demonstrate that $\mathbb{F}\therefore\mathbb{f}\therefore\boldsymbol{i} = \boldsymbol{i}$ and $\mathbb{f}\therefore\mathbb{F}\therefore\boldsymbol{i} = \boldsymbol{i}$, where $\mathbb{F}$ is Moore-Penrose pseudo inverse. This ensures that the internal constraint $(\mathbb{I} - \mathbb{f}\therefore\mathbb{F})\therefore\boldsymbol{\Gamma} = \mathbf{0}$ is equivalent to $\boldsymbol{\Phi} = \mathbb{f}\therefore\mathbb{F}\therefore\boldsymbol{\Phi}$.

Proof: Since $\left\langle \boldsymbol{\sigma}_{\alpha 3}^{(\mathbb{R})} \right\rangle = Q_\alpha$, then, $\widetilde{\boldsymbol{\sigma}}^{(\mathbb{R})}$ is not uniformly zero through the thickness and $w^{*BG,\mathbb{R}}(\mathbb{R}) > 0$. Thus:

$$\boldsymbol{i}\therefore\mathbb{R} \neq \mathbf{0} \Rightarrow w^{*BG,\mathbb{R}}(\mathbb{R}) > 0 \tag{4.75}$$

Let us define: $\mathbb{R}^* = \frac{2}{3}\boldsymbol{i}\cdot\boldsymbol{Q}, \quad \boldsymbol{Q}\neq\mathbf{0}$. We have $\boldsymbol{i}\therefore\mathbb{R}^* = \boldsymbol{Q}$ and then $\frac{2}{3}\boldsymbol{i}\cdot\boldsymbol{Q} \in Im\,(\mathbb{F})$. Since $\mathbb{F}\therefore\mathbb{f}$ is the projector on the orthogonal complement of $\mathbb{f}$ kernel, we have:

$$\forall\boldsymbol{Q}, \quad \mathbb{F}\therefore\mathbb{f}\therefore\boldsymbol{i}\cdot\boldsymbol{Q} = \boldsymbol{i}\cdot\boldsymbol{Q}$$

which is the first expected result. The second result is straightforward when noticing that $\mathbb{f}$ and $\mathbb{F}$

have the same kernel: since $\mathbb{f}$ and $\mathbb{F}$ are diagonalizable, we have:

$$\mathbb{R} \in Im\left(\mathbb{F}\right)$$

$$\Leftrightarrow \mathbb{R} = \sum_i \mathbb{R}_i \text{ and } \mathbb{f} \therefore \mathbb{R} = \sum_i \lambda_i \mathbb{R}_i, \forall i, \lambda_i \neq 0$$

$$\Leftrightarrow \mathbb{R} = \sum_i \mathbb{R}_i \text{ and } \mathbb{F} \therefore \mathbb{R} = \sum_i \mathbb{R}_i/\lambda_i, \forall i, \lambda_i \neq 0$$

$$\Leftrightarrow \mathbb{R} \in Im\left(\mathbb{f}\right)$$

4.A.5 Degenerated boundary conditions in the homogeneous case

The pseudo inverse in homogeneous case is easy to find:

$$\mathbb{F} = \frac{5h}{6}\frac{4}{9}\boldsymbol{i} \cdot \mathsf{S}^{-1} \cdot \boldsymbol{i} \tag{4.76}$$

and $\mathbb{f} \therefore \mathbb{F} = \frac{2}{3}\boldsymbol{i} \cdot \boldsymbol{i}$. The generalized shear strain, solution of $\mathcal{P}^{BG}$ fulfils $(\mathbb{I} - \mathbb{f} \therefore \mathbb{F}) \therefore \boldsymbol{\Gamma} = 0$, which is equivalent to: $\boldsymbol{\Phi} = \frac{2}{3}\boldsymbol{i} \cdot \boldsymbol{i} \therefore \boldsymbol{\Phi}$ (see Appendix 4.A.4). Then it is possible to rewrite the work of M on the edges $\partial\omega$:

$$\mathsf{M} : (\boldsymbol{\Phi} \cdot \boldsymbol{n}) = (\mathsf{M} \cdot \boldsymbol{n}) \cdot \left(\frac{2}{3}\boldsymbol{i} \therefore \boldsymbol{\Phi}\right)$$

which is identical to the Reissner-Mindlin work on the edge $\partial\omega$ where the rotation pseudo-vector is $\boldsymbol{\varphi} = \frac{2}{3}\boldsymbol{i} \therefore \boldsymbol{\Phi}$.

CHAPTER

5

A full bending gradient plate theory for thick plates Part II: Closed-form solutions for cylindrical bending of laminates

Dans ce chapitre, on propose d'appliquer la théorie de gradient du moment à la flexion cylindrique des plaques stratifiées en fibre de carbone. On se compare à la solution analytique de Pagano (1970a) et on montre que la solution de gradient du moment converge vers la solution exacte lorsque la plaque est symétrique par rapport à son plan moyen. Ce chapitre est la seconde partie d'un article en deux parties soumis le 19/07/2010.

Abstract

In Chapter 4 we have presented a new plate theory for out-of-plane loaded thick plates where the static unknowns are those of the Love-Kirchhoff theory (3 in-plane stresses and 3 bending moments), to which six components are added representing the gradient of the bending moment. The new theory, called Bending-Gradient plate theory is an extension to arbitrary multilayered plates of the Reissner-Mindlin plate theory which appears as a special case when the plate is homogeneous. Moreover, we demonstrated that, in the general case, the Bending-Gradient model cannot be reduced to a Reissner-Mindlin model. In this paper, the Bending-Gradient theory is applied to multilayered plates and its predictions are compared to those of Reissner-Mindlin theory and to full 3D Pagano's exact solutions. The main conclusion is that the Bending-Gradient gives good predictions of both deflection and shear stress distributions in any material configuration. Moreover, under some symmetry conditions, the Bending-Gradient model coincides with the second-order approximation of the exact solution as the slenderness ratio L/h goes to infinity.

5.1 Introduction

Laminated plates are widely used in engineering applications. For instance angle-ply carbon fiber reinforced laminates are commonly used in aeronautics. However, these materials are strongly anisotropic and the plate overall behavior is difficult to capture. The most common plate theory is the Love-Kirchhoff plate model. However, it is well-known that, when the plate slenderness ratio L/h (h is the plate thickness and L the span) is not large enough, transverse shear stresses which are not taken into account in the Love-Kirchhoff theory have an increasing influence on the plate deflection.

In recent decades many suggestions have been made to improve the estimation of transverse shear stresses. Reddy (1989), Noor and Malik (2000) and Carrera (2002) provided detailed reviews for these models. Two main approaches can be found: asymptotic approaches and axiomatic approaches. The first one is mainly based on asymptotic expansions in the small parameter h/L (Caillerie, 1984; Lewinski, 1991c,b,a). However, higher-order terms yield only intricated "Love-Kirchhoff" plate equations and no distinction between relevant fields and unknowns was made. The second main approach is based on assuming *ad hoc* displacement or stress 3D fields. These models can be "Equivalent Single Layer" or "layerwise". Equivalent single layer models treat the whole laminate as an equivalent homogeneous plate. However, when dealing with laminated plates, these models lead systematically to discontinuous transverse shear stress distributions through the thickness as indicated by Reddy (1989). In layerwise models, all plate degrees of freedom are introduced in each layer of the laminate and continuity conditions are enforced between layers. The reader can refer to Reddy (1989) and Carrera (2002) for detailed reviews of kinematic approaches and to (Naciri et al., 1998; Diaz Diaz et al., 2001; Hadj-Ahmed et al., 2001; Caron et al., 2006; Diaz Diaz et al., 2007; Dallot and Sab, 2008) for static approaches. Layerwise models lead to correct estimates of local 3D fields. However, their main drawback is that they involve a number of degrees of freedom proportional to the number of layers. The limitation is immediately pointed out with functionally graded materials, where the plate constituents properties vary continuously through the thickness (Nguyen et al., 2008a,b).

In Chapter 4 we revisited the use of 3D equilibrium in order to derive transverse shear stress as Reissner (1945) did for homogeneous plates. Thanks to standard variational tools, this led us to an Equivalent Single Layer plate theory which takes accurately into account shear effects and does not require any specific constitutive material symmetry: the Bending-Gradient theory. This plate theory is identical to the Reissner-Mindlin plate theory in the case of homogeneous plates. However, for laminated plates, shear forces are replaced by the gradient of the bending moment $\mathbf{R} = \mathbf{M} \otimes \boldsymbol{\nabla}$. Hence, this theory belongs to the family of higher-order gradient models. The mechanical meaning of the bending gradient was identified as self-balanced static unknowns associated to warping functions in addition to classic shear forces.

The purpose of the present paper is to derive closed-form solutions for the Bending-Gradient model in the case of cylindrical bending and compare them to the exact solutions from Pagano (1969, 1970a,b) and to other approaches commonly used.

This paper is organized as follows. First, in Section 5.2, notations are briefly introduced. Then, in Section 5.3, the Bending-Gradient model is recalled, Voigt notation is introduced and the influence of material symmetries is also considered. In Section 5.4, cylindrical bending closed-form solutions are derived and applied to laminates. Finally, comparison with other Equivalent Single Layer approaches and discussion on results is provided in Section 5.5.

5.2 Notations

Plate models involve 2-dimensional (2D) tensors of several orders. Vectors and higher-order tensors are boldfaced and different typefaces are used for each order: vectors are slanted: $\boldsymbol{T}$, $\boldsymbol{u}$. Second order tensors are sans-serif: M, e. Third order tensors are in typewriter style: $\mathtt{\Phi}$, $\mathtt{\Gamma}$. Fourth order tensors are in calligraphic style $\mathcal{D}$, $\mathcal{c}$. Sixth order tensors are double stroked $\mathbb{F}$, $\mathbb{W}$. For instance, the fourth-order tensor $\mathcal{c} = c_{\alpha\beta\gamma\delta}$ with Greek indexes $\alpha, \beta, \gamma.. = 1, 2$, denotes the plane-stress elasticity tensor. The identity for in-plane elasticity is $i_{\alpha\beta\gamma\delta} = \frac{1}{2}(\delta_{\alpha\gamma}\delta_{\beta\delta} + \delta_{\alpha\delta}\delta_{\beta\gamma})$, where $\delta_{\alpha\beta}$ is Kronecker symbol ($\delta_{\alpha\beta} = 1$ if $\alpha = \beta$, $\delta_{\alpha\beta} = 0$ otherwise). The transpose operation ${}^t\bullet$ is applied to any order tensors as follows: $\left({}^tA\right)_{\alpha\beta\ldots\psi\omega} = A_{\omega\psi\ldots\beta\alpha}$.

Three contraction products are defined, the usual dot product ($\boldsymbol{a} \cdot \boldsymbol{b} = a_\alpha b_\alpha$), the double contraction product ($\mathsf{a} : \mathsf{b} = \mathsf{a}_{\alpha\beta}\mathsf{b}_{\alpha\beta}$) and a triple contraction product ($\mathtt{A} \therefore \mathtt{B} = \mathtt{A}_{\alpha\beta\gamma}\mathtt{B}_{\gamma\beta\alpha}$). In these definitions Einstein's notation on repeated indexes is used. It should be noticed that closest indexes are summed together in contraction products. Thus, $\mathtt{\Phi} \cdot \boldsymbol{n} = \mathtt{\Phi}_{\alpha\beta\gamma} n_\gamma$ is different from $\boldsymbol{n} \cdot \mathtt{\Phi} = n_\alpha \mathtt{\Phi}_{\alpha\beta\gamma}$.

The derivation operator $\boldsymbol{\nabla}$ is also formally represented as a vector: $\mathsf{a} \cdot \boldsymbol{\nabla} = \mathsf{a}_{\alpha\beta}\nabla_\beta = \mathsf{a}_{\alpha\beta,\beta}$ is the divergence and $\mathsf{a} \otimes \boldsymbol{\nabla} = \mathsf{a}_{\alpha\beta}\nabla_\gamma = \mathsf{a}_{\alpha\beta,\gamma}$ is the gradient. Here $\otimes$ is the dyadic product.

In this paper, Voigt notation is also introduced. Brackets $[\bullet]$ are used to denote that a tensor is considered in a matrix form. Moreover, matrices and vectors of several dimensions are defined. Vectors and matrices are 2D by default. In other cases, $\widetilde{\bullet}$ denotes dimension 3: $\widetilde{\boldsymbol{U}}$ denotes a 3D vector and $\widetilde{\mathsf{f}}$ denotes a 3×3 matrix. The related components are indexed with Latin indexes, $i, j, k.. = 1, 2, 3$: f_{ij}. $\widehat{\bullet}$ denotes dimension 6: $\widehat{\mathsf{P}}$ denotes a 6×6 matrix.

Finally, the integration through the thickness is noted $\langle\bullet\rangle$: $\int_{-\frac{h}{2}}^{\frac{h}{2}} f(x_3)dx_3 = \langle f \rangle$.

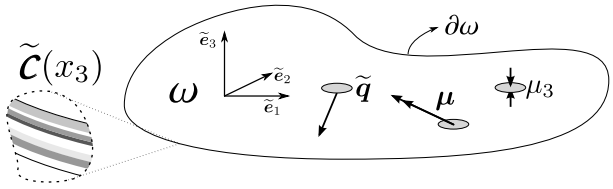

Figure 5.1: The plate configuration

5.3 The Bending-Gradient plate model

5.3.1 Summary of the plate model

We consider a linear elastic plate of thickness h which mid-plane is the 2D domain $\omega \subset \mathbb{R}^2$ (Figure 5.1). Cartesian coordinates (x_1, x_2, x_3) in the reference frame $(\widetilde{\boldsymbol{e}}_1, \widetilde{\boldsymbol{e}}_2, \widetilde{\boldsymbol{e}}_3)$ are used. The local stiffness tensor $\mathcal{C}_{ijkl}(x_3)$ is assumed to be invariant with respect to translations in the (x_1, x_2) plane and the plate is loaded exclusively with the out-of-plane distributed force $p_3\widetilde{\boldsymbol{e}}_3$.

The membrane stress $\mathbf{N}$, the bending moment $\mathbf{M}$, and shear forces $\boldsymbol{Q}$ are related to the actual 3D local stress by the following equations:

$$\begin{cases} \mathsf{N}_{\alpha\beta}\left(x_1, x_2\right) = \langle \sigma_{\alpha\beta} \rangle & \text{(5.1a)} \\ \mathsf{M}_{\alpha\beta}\left(x_1, x_2\right) = \langle x_3 \sigma_{\alpha\beta} \rangle & \text{(5.1b)} \\ Q_{\alpha}\left(x_1, x_2\right) = \langle \sigma_{\alpha 3} \rangle & \text{(5.1c)} \end{cases}$$

Moreover, we introduce the gradient of the bending moment $\mathbb{R} = \mathbf{M} \otimes \boldsymbol{\nabla}$. $\mathbb{R}$ is a 2D third-order tensor with the following symmetry: $\mathbb{R}_{\alpha\beta\gamma} = \mathbb{R}_{\beta\alpha\gamma}$. It is possible to derive shear forces $\boldsymbol{Q}$ from $\mathbb{R}$ as: $\boldsymbol{Q} = \boldsymbol{i} \therefore \mathbb{R}$.

Equilibrium equations and boundary conditions involving stress fields were derived in Chapter 4 and are gathered in the set of statically compatible fields:

$$\begin{cases} \mathbf{N} \cdot \boldsymbol{\nabla} = \mathbf{0} \text{ on } \omega & \text{(5.2a)} \\ \mathbf{M} \otimes \boldsymbol{\nabla} - \mathbb{R} = 0 \text{ on } \omega & \text{(5.2b)} \\ (\boldsymbol{i} \therefore \mathbb{R}) \cdot \boldsymbol{\nabla} = -p_3 \text{ on } \omega & \text{(5.2c)} \\ \mathbf{N} \cdot \boldsymbol{n} = \boldsymbol{V}^d \text{ on } \partial\omega^s & \text{(5.2d)} \\ \mathbf{M} = \mathbf{M}^d \text{ on } \partial\omega^s & \text{(5.2e)} \\ (\boldsymbol{i} \therefore \mathbb{R}) \cdot \boldsymbol{n} = V_3^d \text{ on } \partial\omega^s & \text{(5.2f)} \end{cases}$$

where $\partial\omega^s$ is the portion of edge on which static boundary conditions apply: $\widetilde{\boldsymbol{V}}^d$ is the force per unit length and $\mathbf{M}^d$ the full bending moment enforced on the edge. This set of equations is almost identical

to Reissner-Mindlin equations where shear forces have been replaced by the bending gradient $\mathbf{R}$.

Generalized stresses $\mathbf{N}$, $\mathbf{M}$, and $\mathbf{R}$ work respectively with the associated strain variables: $\mathbf{e}$, the conventional membrane strain, $\boldsymbol{\chi}$ the conventional curvature and $\boldsymbol{\Gamma}$ the generalized shear strain. These strain fields must comply with the following compatibility conditions and boundary conditions:

$$\begin{cases} \mathbf{e} = \boldsymbol{i} : (\boldsymbol{\nabla} \otimes \boldsymbol{U}) \text{ on } \omega & \text{(5.3a)} \\ \boldsymbol{\chi} = \boldsymbol{\Phi} \cdot \boldsymbol{\nabla} \text{ on } \omega & \text{(5.3b)} \\ \boldsymbol{\Gamma} = \boldsymbol{\Phi} + \boldsymbol{i} \cdot \boldsymbol{\nabla} U_3 \text{ on } \omega & \text{(5.3c)} \\ \boldsymbol{\Phi} \cdot \boldsymbol{n} = \mathbf{H}^d \text{ on } \partial\omega^k & \text{(5.3d)} \\ \widetilde{\boldsymbol{U}} = \widetilde{\boldsymbol{U}}^d \text{ on } \partial\omega^k & \text{(5.3e)} \end{cases}$$

where $\widetilde{\boldsymbol{U}}$ is the 3D displacement of the mid-plane of the plate and $\boldsymbol{\Phi}$ is the generalized rotation. $\boldsymbol{\Gamma}$ and $\boldsymbol{\Phi}$ are 2D third-order tensors with the following symmetry: $\Phi_{\alpha\beta\gamma} = \Phi_{\beta\alpha\gamma}$. Moreover, $\partial\omega^k$ is the portion of edge on which kinematic boundary conditions apply: $\widetilde{\boldsymbol{U}}^d$ is a given displacement and $\mathbf{H}^d$ is a symmetric second-order tensor related to a forced rotation on the edge. These fields are almost identical to Reissner-Mindlin kinematically compatible fields where the rotation pseudo-vector is replaced by the generalized rotation $\boldsymbol{\Phi}$.

Finally, for constitutive material following local monoclinic symmetry with respect to (x_1, x_2) plane (uncoupling between $\mathbf{R}$ and $(\mathbf{N}, \mathbf{M})$) the Bending-Gradient plate constitutive equations are written as:

$$\begin{cases} \mathbf{N} = \boldsymbol{\mathcal{A}} : \mathbf{e} + \boldsymbol{\mathcal{B}} : \boldsymbol{\chi} & \text{(5.4a)} \\ \mathbf{M} = {}^t\boldsymbol{\mathcal{B}} : \mathbf{e} + \boldsymbol{\mathcal{D}} : \boldsymbol{\chi} & \text{(5.4b)} \\ \boldsymbol{\Gamma} = \mathbb{f} \therefore \mathbf{R}, \quad \text{where} \quad (\mathbb{I} - \mathbb{f} \therefore \mathbb{F}) \therefore \boldsymbol{\Gamma} = 0 & \text{(5.4c)} \end{cases}$$

where conventional Love-Kirchhoff stiffnesses are defined as $(\boldsymbol{\mathcal{A}}, \boldsymbol{\mathcal{B}}, \boldsymbol{\mathcal{D}}) = \langle (1, x_3, x_3^2)\, \boldsymbol{c}(x_3) \rangle$ and the definition of $\mathbb{f}$ and $\mathbb{F}$ is detailed in Section 5.4.2 of the present work. Here $\mathbb{I}$ is the identity for 2D sixth-order tensors following the generalized shear compliance $\mathbb{f}$ minor and major symmetries [1] ($\mathbb{I}_{\alpha\beta\gamma\delta\epsilon\zeta} = i_{\alpha\beta\epsilon\zeta}\, \delta_{\gamma\delta}$). The solution of the plate model must comply with the three sets of equations (5.2, 5.3, 5.4). The compliance $\mathbb{f}$ is positive. However when $\mathbb{f}$ is not definite, there is a set of solutions, up to a self-stress field.

1. $\mathbb{f}_{\alpha\beta\gamma\delta\epsilon\zeta}$ follows major symmetry: $\mathbb{f}_{\alpha\beta\gamma\delta\epsilon\zeta} = \mathbb{f}_{\zeta\epsilon\delta\gamma\beta\alpha}$ and minor symmetry $\mathbb{f}_{\alpha\beta\gamma\delta\epsilon\zeta} = \mathbb{f}_{\beta\alpha\gamma\delta\epsilon\zeta}$. Thus there are only 21 independent components

5.3.2 Voigt Notations

In this section, we introduce Voigt notation in order to turn contraction products into conventional matrix products. Brackets $[\bullet]$ are used to denote that a tensor is considered in a matrix form. Thus $[\bullet]$ is a linear operator, reallocating tensor components.

For instance, the bending moment is reallocated in a vector form:

$$[\mathbf{M}] = \begin{pmatrix} \mathsf{M}_{11} \\ \mathsf{M}_{22} \\ \sqrt{2}\mathsf{M}_{12} \end{pmatrix} \tag{5.5}$$

as well as $\mathbf{N}$, $\mathbf{e}$ and $\boldsymbol{\chi}$, and the fourth-order compliance tensor $\mathscr{d}$ is reallocated in a matrix form so that constitutive equation (5.4b) becomes a vector-matrix product:

$$[\mathscr{d}] = \begin{pmatrix} d_{1111} & d_{2211} & \sqrt{2}d_{1211} \\ d_{2211} & d_{2222} & \sqrt{2}d_{1222} \\ \sqrt{2}d_{1211} & \sqrt{2}d_{1222} & 2d_{1212} \end{pmatrix} \tag{5.6}$$

as well as the stiffness tensor $\mathscr{D}$. This is also done for the other Love-Kirchhoff compliances $\mathscr{a}$, $\mathscr{b}$, and stiffnesses $\mathscr{A}$, $\mathscr{B}$ and finally to the plane-stress stiffness tensor $\mathscr{c}$.

The same procedure is applied to shear variables and the corresponding constitutive equation. Shear static unknowns are reallocated in a vector form,

$$[\mathbb{R}] = \begin{pmatrix} \mathsf{R}_{111} \\ \mathsf{R}_{221} \\ \sqrt{2}\mathsf{R}_{121} \\ \mathsf{R}_{112} \\ \mathsf{R}_{222} \\ \sqrt{2}\mathsf{R}_{122} \end{pmatrix} \tag{5.7}$$

as well as $\mathbf{\Gamma}$ and $\mathbf{\Phi}$; and the constitutive sixth-order tensor is turned into a 6×6 matrix:

$$[\mathbb{f}] = \begin{pmatrix} \mathbb{f}_{111111} & \mathbb{f}_{111122} & \sqrt{2}\mathbb{f}_{111121} & \mathbb{f}_{111211} & \mathbb{f}_{111222} & \sqrt{2}\mathbb{f}_{111221} \\ \mathbb{f}_{221111} & \mathbb{f}_{221122} & \sqrt{2}\mathbb{f}_{221121} & \mathbb{f}_{221211} & \mathbb{f}_{221222} & \sqrt{2}\mathbb{f}_{221221} \\ \sqrt{2}\mathbb{f}_{121111} & \sqrt{2}\mathbb{f}_{121122} & 2\mathbb{f}_{121121} & \sqrt{2}\mathbb{f}_{121211} & \sqrt{2}\mathbb{f}_{121222} & 2\mathbb{f}_{121221} \\ \mathbb{f}_{112111} & \mathbb{f}_{112122} & \sqrt{2}\mathbb{f}_{112121} & \mathbb{f}_{112211} & \mathbb{f}_{112222} & \sqrt{2}\mathbb{f}_{112221} \\ \mathbb{f}_{222111} & \mathbb{f}_{222122} & \sqrt{2}\mathbb{f}_{222121} & \mathbb{f}_{222211} & \mathbb{f}_{222222} & \sqrt{2}\mathbb{f}_{222221} \\ \sqrt{2}\mathbb{f}_{122111} & \sqrt{2}\mathbb{f}_{122122} & 2\mathbb{f}_{122121} & \sqrt{2}\mathbb{f}_{122211} & \sqrt{2}\mathbb{f}_{122222} & 2\mathbb{f}_{122221} \end{pmatrix} \tag{5.8}$$

Finally, when using Voigt matrices components, the same typeface is used. The number of indexes indicates unambiguously whether it is the tensor component or the matrix component: $\mathbb{f}_{222221}$ is the tensor component of $\mathbb{f}$ and $\mathbb{f}_{56} = \sqrt{2}\mathbb{f}_{222221}$ is the matrix component of $[\mathbb{f}]$.

5.3.3 Symmetries

The effects of material symmetries on uncouplings have been presented in Chapter 4. The main result is that $(\mathbf{N}, \mathbf{M})$ and bending gradient $(\mathbf{R})$ are uncoupled when the local elasticity tensor $\mathcal{C}_{ijkl}(x_3)$ follows monoclinic symmetry with respect to (x_1, x_2) plane for all x_3. Under this assumption, which is valid for most of applications involving laminated materials, it is possible to point out the influence of the invariance of the plate's overall configuration on the constitutive equations. Regarding the Love-Kirchhoff constitutive equation, we just recall that when the plate is overall symmetric with respect to its mid-plane there is uncoupling between membrane stresses and bending moments: $\boldsymbol{\mathcal{B}} = \boldsymbol{0}$. This symmetry is the so-called mirror symmetry. Regarding the generalized shear constitutive equation, the in-plane transformations of $\mathbb{f}$ are identical to those for in-plane strain-gradient elasticity. Auffray et al. (2009) give a detailed analysis of this issue. We provide here a very brief description of their conclusions.

Let us consider an isometry of the (x_1, x_2) plane, $\mathbf{P}$: ${}^t\mathbf{P} \cdot \mathbf{P} = \boldsymbol{\delta}$. The transformation of $\mathbb{f}$ by $\mathbf{P}$, $\mathbb{f}^*$ is given by:

$$\mathbb{f}^*_{\alpha\beta\gamma\delta\epsilon\zeta} = \mathsf{P}_{\alpha\eta}\mathsf{P}_{\beta\theta}\mathsf{P}_{\gamma\iota}\mathsf{P}_{\delta\kappa}\mathsf{P}_{\epsilon\lambda}\mathsf{P}_{\zeta\mu}\mathbb{f}_{\eta\theta\iota\kappa\lambda\mu} \tag{5.9}$$

It can be rewritten with Voigt notation as:

$$[\mathbb{f}]^* = \widehat{\mathbf{P}} \cdot [\mathbb{f}] \cdot {}^t\widehat{\mathbf{P}} \tag{5.10}$$

where $\widehat{\mathbf{P}}$ is a 6×6 matrix which components are explicitly known in terms of the components of $\mathbf{P}$. For a rotation, $\mathbf{P}^r = \left(\begin{smallmatrix} \cos\theta & -\sin\theta \\ \sin\theta & \cos\theta \end{smallmatrix}\right)$, and $\widehat{\mathbf{P}}^r$ is the 6×6 matrix:

$$\widehat{\mathbf{P}}^r = \begin{pmatrix} c^3 & cs^2 & -\sqrt{2}c^2s & -c^2s & -s^3 & \sqrt{2}cs^2 \\ cs^2 & c^3 & \sqrt{2}c^2s & -s^3 & -c^2s & -\sqrt{2}cs^2 \\ \sqrt{2}c^2s & -\sqrt{2}c^2s & (c^2-s^2)c & -\sqrt{2}cs^2 & \sqrt{2}cs^2 & -(c^2-s^2)s \\ c^2s & s^3 & -\sqrt{2}cs^2 & c^3 & cs^2 & -\sqrt{2}c^2s \\ s^3 & c^2s & \sqrt{2}cs^2 & cs^2 & c^3 & \sqrt{2}c^2s \\ \sqrt{2}cs^2 & -\sqrt{2}cs^2 & (c^2-s^2)s & \sqrt{2}c^2s & -\sqrt{2}c^2s & (c^2-s^2)c \end{pmatrix}$$

where c and s stand respectively for $\cos\theta$ and $\sin\theta$. When $\mathbf{P}$ is a reflection through $\boldsymbol{e}_2$ normal plane,

$\mathbf{P}^m = \left(\begin{smallmatrix} 1 & 0 \\ 0 & -1 \end{smallmatrix}\right)$ and we have:

$$\widehat{\mathbf{P}}^m = \begin{pmatrix} 1 & 0 & 0 & 0 & 0 & 0 \\ 0 & 1 & 0 & 0 & 0 & 0 \\ 0 & 0 & -1 & 0 & 0 & 0 \\ 0 & 0 & 0 & -1 & 0 & 0 \\ 0 & 0 & 0 & 0 & -1 & 0 \\ 0 & 0 & 0 & 0 & 0 & 1 \end{pmatrix}$$

If the laminated plate is invariant with respect to an isometry $\mathbf{P}$, then we have the following 21 linearly dependent equations:

$$[\mathbb{f}] = \widehat{\mathbf{P}} \cdot [\mathbb{f}] \cdot {}^t\widehat{\mathbf{P}}$$

5.3.3.0.1 Isotropy A plate configuration is isotropic if its constitutive equation is both invariant by any planar rotation ($\widehat{\mathbf{P}}^r$) and reflection ($\widehat{\mathbf{P}}^m$). With this assumption, four independent constants for isotropic plates ($\mathbb{f}_{11}, \mathbb{f}_{12}, \mathbb{f}_{22}, \mathbb{f}_{26}$) still remain and $\mathbb{f}$ is positive definite:

$$[\mathbb{f}] = \begin{pmatrix} \mathbb{f}_{11} & \mathbb{f}_{12} & 0 & 0 & 0 & \frac{\mathbb{f}_{11}-\mathbb{f}_{22}}{\sqrt{2}} - \mathbb{f}_{26} \\ \mathbb{f}_{12} & \mathbb{f}_{22} & 0 & 0 & 0 & \mathbb{f}_{26} \\ 0 & 0 & \frac{\mathbb{f}_{11}+\mathbb{f}_{22}}{2} - \mathbb{f}_{12} & \mathbb{f}_{26} & \frac{\mathbb{f}_{11}-\mathbb{f}_{22}}{\sqrt{2}} - \mathbb{f}_{26} & 0 \\ 0 & 0 & \mathbb{f}_{26} & \mathbb{f}_{22} & \mathbb{f}_{12} & 0 \\ 0 & 0 & \frac{\mathbb{f}_{11}-\mathbb{f}_{22}}{\sqrt{2}} - \mathbb{f}_{26} & \mathbb{f}_{12} & \mathbb{f}_{11} & 0 \\ \frac{\mathbb{f}_{11}-\mathbb{f}_{22}}{\sqrt{2}} - \mathbb{f}_{26} & \mathbb{f}_{26} & 0 & 0 & 0 & \frac{\mathbb{f}_{11}+\mathbb{f}_{22}}{2} - \mathbb{f}_{12} \end{pmatrix} \tag{5.11}$$

It is possible to simplify further this constitutive equation when a laminate is a stack of plies with different isotropic constitutive materials (this symmetry is also valid for some functionally graded materials (Nguyen et al., 2008a,b)). We use spectral decomposition of plane stress stiffness:

$$\boldsymbol{c}(x_3) = \frac{2\nu(x_3)E(x_3)}{1-\nu^2(x_3)}\boldsymbol{j} + \frac{E(x_3)}{1+\nu(x_3)}\boldsymbol{i}$$

where E is the Young modulus, ν Poisson's ratio and $j_{\alpha\beta\gamma\delta} = 1/2\delta_{\alpha\beta}\delta_{\gamma\delta}$. Deriving directly the constitutive equation (5.29) with this decomposition enables us to demonstrate that $\mathbb{f}_{26} = -\mathbb{f}_{12}$. Three independent constants $\mathbb{f}_{11}, \mathbb{f}_{12}, \mathbb{f}_{22}$ still remain and $\mathbb{f}$ is no more invertible:

$$\mathbb{f} = (\mathbb{f}_{11} + \mathbb{f}_{22} + 2\mathbb{f}_{12})\,\boldsymbol{i}\cdot\boldsymbol{i} - 2\,(\mathbb{f}_{22} + \mathbb{f}_{12})\,(\boldsymbol{j}\cdot\boldsymbol{i} + \boldsymbol{i}\cdot\boldsymbol{j}) + \mathbb{f}_{22}\boldsymbol{j}\cdot\boldsymbol{j} \tag{5.12}$$

Finally, for a plate with a homogeneous and isotropic constitutive material, we have demonstrated that the Bending-Gradient model is turned into a Reissner-Mindlin plate model and that

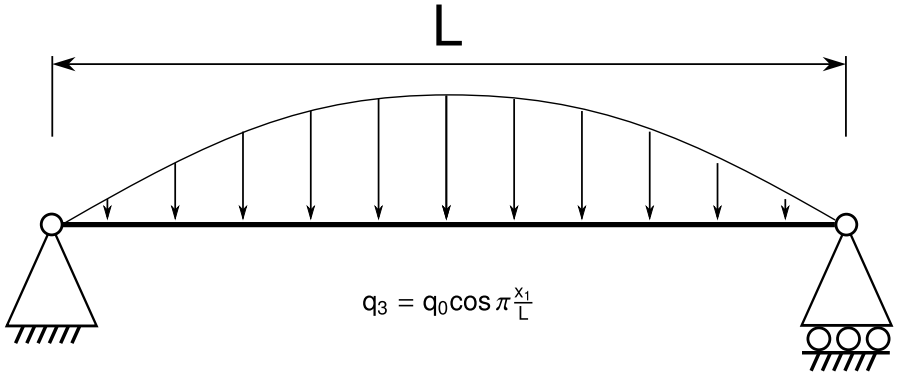

Figure 5.2: Pagano's cylindrical bending configuration

$\mathbb{f} = \frac{6}{5Gh}\boldsymbol{i}\cdot\boldsymbol{i}$ in Chapter 4. This is rewritten as

$$[\mathbb{f}] = \frac{6}{5Gh}\begin{pmatrix} 1 & 0 & 0 & 0 & 0 & 1/\sqrt{2} \\ 0 & 0 & 0 & 0 & 0 & 0 \\ 0 & 0 & 1/2 & 0 & 1/\sqrt{2} & 0 \\ 0 & 0 & 0 & 0 & 0 & 0 \\ 0 & 0 & 1/\sqrt{2} & 0 & 1 & 0 \\ 1/\sqrt{2} & 0 & 0 & 0 & 0 & 1/2 \end{pmatrix} \tag{5.13}$$

In this case: $\mathbb{f}_{11} = \frac{6}{5Gh}$ and $\mathbb{f}_{12} = \mathbb{f}_{22} = 0$ which is different from the general case of a layered plate made of different isotropic constitutive materials (Equation (5.12)). Consequently, for these laminates, the Bending-Gradient model is *a priori* not a Reissner-Mindlin model. This is mainly because the different Poisson's ratios in each layer generates warping. When Poisson's ratio is uniform through the thickness, the constitutive equation is such that $\mathbb{f}_{12} = \mathbb{f}_{22} = 0$ and for conventional isotropic materials, the warping effect remains very limited, leading to a quasi homogeneous constitutive equation.

5.4 Closed-form solution for Pagano's configuration

5.4.1 Plate closed-form solution

Pagano (1969) gives an exact solution for cylindrical bending of simply supported composite laminates. We choose the same configuration for the Bending-Gradient model. The plate is invariant and infinite in x_2 direction. It is out-of-plane loaded with $p_3(x_1) = -p_0 \sin \kappa x_1$ where $\lambda = 1/\kappa = \frac{L}{n\pi},\ n \in \mathbb{N}^{+*}$ is the wavelength of the loading (Figure 5.2).

The plate is simply supported at $x_1 = 0$ and $x_1 = L$ with traction free edges:

$$U_3(0) = 0, \quad U_3(L) = 0, \quad \mathbf{M}(0) = \mathbf{0}, \quad \mathbf{M}(L) = \mathbf{0}, \quad \mathbf{N}(0) \cdot \boldsymbol{e}_1 = \mathbf{0}, \quad \mathbf{N}(L) \cdot \boldsymbol{e}_1 = \mathbf{0} \quad (5.14)$$

$\mathsf{M}_{22}(0) = \mathsf{M}_{22}(L) = 0$ is the additional boundary condition compared to the Reissner-Mindlin plate model as the bimoment vanishes on a free section in Vlasov (1961) beam theory. This additional boundary condition takes into account free edge effects similar to those described in Chapter 8 for periodically layered laminate.

The solution is obtained as follows: First, the x_2-invariance leads to several simplifications and some unknowns vanish. Second, relevant equations and unknowns are gathered into a differential system and the closed-form solution is derived.

5.4.1.1 Simplifications related to x_2-invariance

5.4.1.1.1 Membrane solution Since $(\mathbf{N}, \mathbf{M})$ fields are uncoupled from shear fields, it is possible to solve separately the membrane part of the plate model. Hence, the x_2-invariance in the membrane strain definition (5.3a) enforces $\mathsf{e}_{22} = U_{2,2} = 0$. Moreover, boundary conditions (5.2d) and equilibrium equation (5.2a) for membrane stresses lead easily to $\mathsf{N}_{11} = \mathsf{N}_{12} = 0$. However, N_{22}, e_{11} and e_{12} remain undetermined.

5.4.1.1.2 Curvatures Curvatures are defined by Equation 5.3b: $\chi_{\alpha\beta} = \Phi_{\alpha\beta\gamma,\gamma}$. Taking into account x_2 invariance leads to:

$$[\boldsymbol{\chi}] = \begin{pmatrix} \chi_{11} \\ \chi_{22} \\ \sqrt{2}\chi_{12} \end{pmatrix} = \begin{pmatrix} \Phi_{111,1} \\ \Phi_{221,1} \\ \sqrt{2}\Phi_{121,1} \end{pmatrix} = \begin{pmatrix} \Phi_{1,1} \\ \Phi_{2,1} \\ \Phi_{3,1} \end{pmatrix} \quad (5.15)$$

5.4.1.1.3 Love-Kirchhoff constitutive equation Love-Kirchhoff constitutive equations (5.4a) and (5.4b) are written with Voigt notation in the inverse form as:

$$[\mathbf{e}] = [\boldsymbol{a}] \cdot [\mathbf{N}] + [\boldsymbol{b}] \cdot [\mathbf{M}] \quad (5.16a)$$

$$[\boldsymbol{\chi}] = {}^t[\boldsymbol{b}] \cdot [\mathbf{N}] + [\boldsymbol{d}] \cdot [\mathbf{M}] \quad (5.16b)$$

where $[\boldsymbol{a}]$, $[\boldsymbol{b}]$ and $[\boldsymbol{d}]$ are Love-Kirchhoff compliance matrices.

Taking into account $\mathsf{N}_{11} = \mathsf{N}_{12} = 0$ and $\mathsf{e}_{22} = 0$ enables us to rewrite Love-Kirchhoff constitutive equation in a compact form as:

$$[\boldsymbol{\chi}] = [\boldsymbol{d}]^* \cdot [\mathbf{M}] \quad (5.17)$$

where

$$d^*_{ij} = d_{ij} - \frac{b_{2i} b_{2j}}{a_{22}}$$

is the effective flexural stiffness taking into account $\mathsf{e}_{22} = 0$ constraint. N_{22}, e_{11} and e_{12} are then derived directly from the bending moment using equations:

$$\mathsf{e}_i = \left(b_{ij} - \frac{a_{i2} b_{2j}}{a_{22}} \right) \mathsf{M}_j \quad \text{and} \quad \mathsf{N}_2 = -\frac{b_{2i}}{a_{22}} \mathsf{M}_i \tag{5.18}$$

5.4.1.1.4 Equilibrium The x_2 invariance in the bending gradient equilibrium equation (5.2b) enforces:

$$\begin{pmatrix} \mathtt{R}_1 \\ \mathtt{R}_2 \\ \mathtt{R}_3 \\ \mathtt{R}_4 \\ \mathtt{R}_5 \\ \mathtt{R}_6 \end{pmatrix} = \begin{pmatrix} \mathsf{M}_{11,1} \\ \mathsf{M}_{22,1} \\ \sqrt{2}\mathsf{M}_{12,1} \\ 0 \\ 0 \\ 0 \end{pmatrix} \tag{5.19}$$

and transverse loading equilibrium equation (5.2c) becomes:

$$\mathsf{M}_{11,11} = -p_3(x_1) \tag{5.20}$$

5.4.1.1.5 Shear constitutive equation Taking into account $\mathtt{R}_4 = \mathtt{R}_5 = \mathtt{R}_6 = 0$, $U_{3,2} = 0$ and generalized shear strain definition (5.3c), Shear constitutive equation (5.4c) is rewritten in two parts.

A first part with unknowns involving active boundary conditions:

$$\begin{pmatrix} \Phi_1 \\ \Phi_2 \\ \Phi_3 \end{pmatrix} = \begin{pmatrix} \mathbb{f}_{11} & \mathbb{f}_{12} & \mathbb{f}_{13} \\ \mathbb{f}_{12} & \mathbb{f}_{22} & \mathbb{f}_{23} \\ \mathbb{f}_{13} & \mathbb{f}_{23} & \mathbb{f}_{33} \end{pmatrix} \cdot \begin{pmatrix} \mathsf{M}_{11,1} \\ \mathsf{M}_{22,1} \\ \sqrt{2}\mathsf{M}_{12,1} \end{pmatrix} - \begin{pmatrix} U_{3,1} \\ 0 \\ 0 \end{pmatrix} \tag{5.21}$$

and a second part which enables the derivation of Φ_4, Φ_5, Φ_6 on which no boundary condition applies:

$$\begin{pmatrix} \Phi_4 \\ \Phi_5 \\ \Phi_6 \end{pmatrix} = \begin{pmatrix} \mathbb{f}_{41} & \mathbb{f}_{42} & \mathbb{f}_{43} \\ \mathbb{f}_{52} & \mathbb{f}_{52} & \mathbb{f}_{53} \\ \mathbb{f}_{63} & \mathbb{f}_{63} & \mathbb{f}_{63} \end{pmatrix} \cdot \begin{pmatrix} \mathsf{M}_{11,1} \\ \mathsf{M}_{22,1} \\ \sqrt{2}\mathsf{M}_{12,1} \end{pmatrix} \tag{5.22}$$

5.4.1.2 Resolution

5.4.1.2.1 Final System Finally, combining Equations 5.14, 5.15, 5.17, 5.20 and 5.21, leads to the following set of equations which fully determines the problem:

$$\begin{cases} \mathsf{M}_{11,11} = -p_0 \sin \kappa x_1 & \text{(5.23a)} \\ [\boldsymbol{\mathcal{A}}]^* \cdot [\mathsf{M}] - \widetilde{\mathsf{f}} \cdot [\mathsf{M}]_{,11} = \begin{pmatrix} U_{3,11} \\ 0 \\ 0 \end{pmatrix} & \text{(5.23b)} \\ [\mathsf{M}] = 0 \quad \text{for} \quad x_1 = 0 \quad \text{and} \quad x_1 = L & \text{(5.23c)} \\ U_3 = 0 \quad \text{for} \quad x_1 = 0 \quad \text{and} \quad x_1 = L & \text{(5.23d)} \end{cases}$$

where for convenience, $\widetilde{\mathsf{f}}$ is the 3×3 submatrix of $[\mathbb{f}]$:

$$\widetilde{\mathsf{f}} = \begin{pmatrix} \mathbb{f}_{11} & \mathbb{f}_{12} & \mathbb{f}_{13} \\ \mathbb{f}_{12} & \mathbb{f}_{22} & \mathbb{f}_{23} \\ \mathbb{f}_{13} & \mathbb{f}_{23} & \mathbb{f}_{33} \end{pmatrix}$$

Once $[\mathsf{M}]$ is derived, the non-zero unknowns are derived using Equations 5.18, 5.19 and 5.22.

5.4.1.2.2 Solution Since $\widetilde{\mathsf{f}}$ is positive and $[\boldsymbol{\mathcal{A}}]^*$ is positive definite, the differential system 5.23 is well-posed and the solution is the sum of a particular solution and hyperbolic solutions of the homogeneous equation. Boundary conditions applied to M vanish hyperbolic solutions. There remains the particular solution:

$$[\mathsf{M}] = \begin{pmatrix} 1 \\ -\mathbf{g}^{-1} \cdot \boldsymbol{g} \end{pmatrix} p_0 \lambda^2 \sin \kappa x_1 \quad \text{and} \quad U_3 = p_0 \lambda^4 \left(\mathsf{g}_{11} - {}^t\boldsymbol{g} \cdot \mathbf{g}^{-1} \cdot \boldsymbol{g} \right) \sin \kappa x_1 \tag{5.24}$$

where

$$\widetilde{\mathbf{g}} = [\boldsymbol{\mathcal{A}}]^* + \kappa^2 \widetilde{\mathbf{f}}, \quad \mathbf{g} = \begin{pmatrix} \mathsf{g}_{22} & \mathsf{g}_{23} \\ \mathsf{g}_{23} & \mathsf{g}_{33} \end{pmatrix}, \quad \boldsymbol{g} = \begin{pmatrix} \mathsf{g}_{12} \\ \mathsf{g}_{13} \end{pmatrix}. \tag{5.25}$$

The matrix $\widetilde{\mathbf{g}}$ appears to be the effective flexural stiffness for cylindrical bending, corrected with shear effects. When $\kappa \to 0$, $\widetilde{\mathbf{g}} = \widetilde{\mathbf{d}}^*$ which yields exactly the Love-Kirchhoff solution.

5.4.2 Localization

Once the generalized stresses are derived, it is possible to reconstruct local 3D fields, using the localization procedure described in Chapter 4. The local 3D stress $\widetilde{\boldsymbol{\sigma}}^{BG}$ is the sum of three terms

depending linearly on the generalized stresses:

$$\widetilde{\boldsymbol{\sigma}}^{BG} = \widetilde{\boldsymbol{s}}^{(\mathsf{N})} : \mathbf{N} + \widetilde{\boldsymbol{s}}^{(\mathsf{M})} : \mathbf{M} + \widetilde{\boldsymbol{s}}^{(\mathsf{R})} \therefore \mathbf{R} \tag{5.26}$$

where,

$$\begin{cases} s^{(\mathsf{N})}_{\alpha\beta\epsilon\zeta}(x_3) = c_{\alpha\beta\gamma\delta}(x_3)\,(a_{\delta\gamma\epsilon\zeta} + x_3\, b_{\zeta\epsilon\gamma\delta}) \quad \text{and } s^{(\mathsf{N})}_{i3\epsilon\zeta} = 0 & \text{(5.27a)} \\ s^{(\mathsf{M})}_{\alpha\beta\epsilon\zeta}(x_3) = c_{\alpha\beta\gamma\delta}(x_3)\,(b_{\delta\gamma\epsilon\zeta} + x_3\, d_{\delta\gamma\epsilon\zeta}) \quad \text{and } s^{(\mathsf{M})}_{i3\epsilon\zeta} = 0 & \text{(5.27b)} \\ s^{(\mathsf{R})}_{\alpha 3\eta\zeta\epsilon}(x_3) = -\displaystyle\int_{-\frac{h}{2}}^{x_3} c_{\alpha\eta\gamma\delta}(z)\,(b_{\delta\gamma\epsilon\zeta} + z\, d_{\delta\gamma\epsilon\zeta})\,dz \text{ , } s^{(\mathsf{R})}_{\alpha\beta\eta\zeta\epsilon} = 0 \text{ and } s^{(\mathsf{R})}_{33\eta\zeta\epsilon} = 0 & \text{(5.27c)} \end{cases}$$

and $\boldsymbol{c}(x_3)$ is the local plane-stress stiffness tensor.

It is possible to rewrite Equation (5.26) with Voigt notations as follows:

$$\widetilde{\boldsymbol{\sigma}}^{BG,\backslash\backslash} = \begin{pmatrix} \sigma^{BG}_{11} \\ \sigma^{BG}_{22} \\ \sqrt{2}\sigma^{BG}_{12} \end{pmatrix} = \widetilde{\mathbf{s}}^{(\mathsf{N})} \cdot [\mathbf{N}] + \widetilde{\mathbf{s}}^{(\mathsf{M})} \cdot [\mathbf{M}]$$

$$\boldsymbol{\sigma}^{BG,\perp} = \begin{pmatrix} \sigma^{BG}_{13} \\ \sigma^{BG}_{23} \end{pmatrix} = \overline{\mathbf{s}}^{(\mathsf{R})} \cdot [\mathbf{R}]$$

where

$$\widetilde{\mathbf{s}}^{(\mathsf{N})}(x_3) = [\boldsymbol{c}](x_3) \cdot \left([\boldsymbol{a}] + x_3{}^t[\boldsymbol{b}]\right)$$

$$\widetilde{\mathbf{s}}^{(\mathsf{M})}(x_3) = [\boldsymbol{c}](x_3) \cdot ([\boldsymbol{b}] + x_3[\boldsymbol{d}])$$

$$\overline{\mathbf{s}}^{(\mathsf{R})}(x_3) = \int_{-\frac{h}{2}}^{x_3} [\![\boldsymbol{c}(z) : (\boldsymbol{b} + z\,\boldsymbol{d})]\!]dz$$

$\widetilde{\mathbf{s}}^{(\mathsf{N})}$ and $\widetilde{\mathbf{s}}^{(\mathsf{M})}$ are 3×3 matrices and $\overline{\mathbf{s}}^{(\mathsf{R})}$ is a 2×6 matrix. Straight double stroked brackets $[\![\bullet]\!]$ denote here the following matrix representation of a fourth-order tensor:

$$[\![\mathcal{L}]\!] = \begin{pmatrix} \mathcal{L}_{1111} & \mathcal{L}_{1122} & \sqrt{2}\mathcal{L}_{1121} & \mathcal{L}_{1211} & \mathcal{L}_{1222} & \sqrt{2}\mathcal{L}_{1221} \\ \mathcal{L}_{2111} & \mathcal{L}_{2122} & \sqrt{2}\mathcal{L}_{2121} & \mathcal{L}_{2211} & \mathcal{L}_{2222} & \sqrt{2}\mathcal{L}_{2221} \end{pmatrix} \tag{5.28}$$

This reallocation is also useful for the derivation of the shear compliance tensor derived in Chapter 4:

$$[\mathbb{f}] = \int_{-\frac{h}{2}}^{\frac{h}{2}} \left(\int_{-\frac{h}{2}}^{x_3} {}^t[\![\boldsymbol{c}(z) : (\boldsymbol{b} + z\,\boldsymbol{d})]\!]dz \right) \cdot \mathbf{S}(x_3) \cdot \left(\int_{-\frac{h}{2}}^{x_3} [\![\boldsymbol{c}(z) : (\boldsymbol{b} + z\,\boldsymbol{d})]\!]dz \right) dx_3 \tag{5.29}$$

where $\mathsf{S}_{\alpha\beta}(x_3) = 4\mathcal{S}_{\alpha 3\beta 3}(x_3)$ is the out-of-plane shear compliance tensor.

Since $\mathbb{f}$ is not always invertible, we introduce Moore-Penrose pseudo inverse for the shear stiffness tensor $\mathbb{F}$:

$$\mathbb{F} = \lim_{\kappa \to 0} \left(\mathbb{f} \therefore \mathbb{f} + \kappa \mathbb{I} \right)^{-1} \therefore \mathbb{f}$$

which is used in the constraint on generalized shear strain $\mathbf{\Gamma}$ in Equation (5.4).

5.4.3 Application to laminates

5.4.3.1 Plate configuration

We consider angle-ply laminates. Each ply is made of unidirectional fiber-reinforced material oriented at θ relative to the bending direction x_1. All plies have the same thickness and are perfectly bounded. The overall thickness of the plate is h. A laminate is denoted between brackets by the successive ply-orientations along thickness. For instance $[0°, 90°]$ denotes a 2-ply laminate where the lower ply fibers are oriented in the bending direction. When the laminate follows mirror symmetry described in Section 5.3.3, only half of the stack is given and the subscript s is added. Thus $[30°, -30°]_s$ means $[30°, -30°, -30°, 30°]$.

The constitutive behavior of a ply is assumed to be transversely isotropic along the direction of the fibers and engineering constants are chosen similar to those of Pagano (1969):

$$E_L = 25 \times 10^6 psi, \quad E_T = 1 \times 10^6 psi, \quad G_{LT} = G_{LN} = 0.5 \times 10^6 psi,$$

$$G_{NT} = \frac{E_T}{2(1+\nu_{NT})} = 0.4 \times 10^6 psi, \quad \nu_{LT} = \nu_{LN} = \nu_{NT} = 0.25$$

where G_{NT} has been changed to preserve transversely isotropic symmetry. L is the longitudinal direction oriented in the (x_1, x_2) plane at θ with respect to $\widetilde{\boldsymbol{e}}_1$, T is the transverse direction and N is the normal direction coinciding with $\widetilde{\boldsymbol{e}}_3$

Pagano (1969, 1970a,b) derived exact 3D elasticity solution of this problem for a laminate loaded only on the upper face and free on the lower face. In the present work we assume the plate is identically loaded on its upper and lower face to comply with the plate model: $T_3^+ = T_3^- = \frac{p_3}{2}$ where $T_3^\pm$ is the normal traction on the upper and lower face of the plate.

5.4.3.2 Localization fields

Shear forces are related to the bending gradient as follows: $Q_1 = \mathtt{R}_{111} + \mathtt{R}_{122}$ and $Q_2 = \mathtt{R}_{121} + \mathtt{R}_{222}$. Thus we suggested in Chapter 4 the following signification for the bending gradient components:

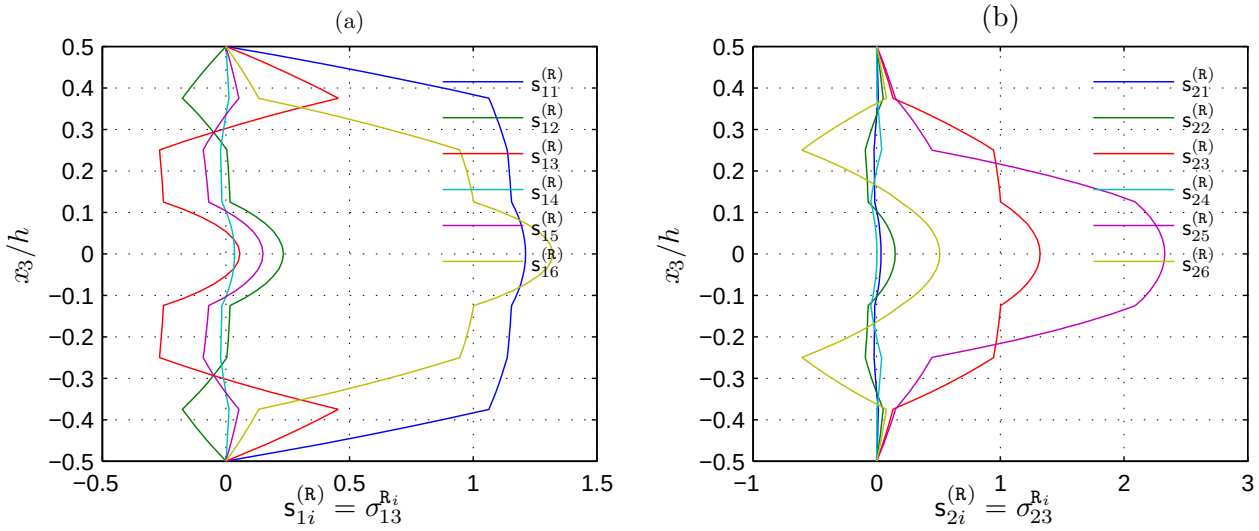

Figure 5.3: Bending-Gradient localization shear distributions through the thickness for a $[0°, -45°, 90°, 45°]_s$ laminate

$\mathtt{R}_{111} - \mathtt{R}_1$: Cylindrical Bending part of Q_1

$\mathtt{R}_{221} - \mathtt{R}_2$: Pure warping

$\mathtt{R}_{121} - \mathtt{R}_3$: Torsional part of Q_2

$\mathtt{R}_{112} - \mathtt{R}_4$: Pure warping

$\mathtt{R}_{222} - \mathtt{R}_5$: Cylindrical Bending part of Q_2

$\mathtt{R}_{122} - \mathtt{R}_6$: Torsional part of Q_1

In Figure 5.3 are plotted localization shear stress distributions $\bar{\mathbf{s}}^{(\mathtt{R})}$ derived in Section 5.4.2 corresponding to each components of $\mathbf{R}$ in both directions for a quasi-isotropic laminate $[0°, -45°, 90°, 45°]_s$. All stress distributions are continuous and fulfill traction free boundary conditions on the upper and lower faces of the plate. For each direction there are four self-equilibrated stress distribution ($\langle \sigma_{\alpha 3} \rangle = 0$) associated to $\mathtt{R}_2, \mathtt{R}_3, \mathtt{R}_4$ and $\mathtt{R}_5$ for direction 1 and $\mathtt{R}_1, \mathtt{R}_2, \mathtt{R}_4$ and $\mathtt{R}_6$ for direction 2. This explains the suggested signification for shear variables. We draw the reader's attention to the fact that, even if there are self-equilibrated stress distributions, all distributions have comparable amplitude and none can be neglected at this stage. Moreover, it is clear that torsion generates different distributions than pure cylindrical bending, except in the homogeneous case.

5.4.3.3 Distance between the Reissner-Mindlin and the Bending-Gradient model

In Chapter 4 we introduced the relative distance between the Bending-Gradient model and a Reissner-Mindlin model, $\Delta^{RM/BG}$:

$$\Delta^{RM/BG} = \frac{\|\mathbb{f}^{\mathrm{W}}\|}{\|\mathbb{f}^{RM}\|} \tag{5.30}$$

where

$$\|\mathbb{f}\| = \sqrt{{}^{t}[\mathbb{f}] : [\mathbb{f}]} \tag{5.31}$$

is the norm for Bending-Gradient compliance tensors and $\mathbb{f}^{\mathrm{W}}$ is the pure warping part of $\mathbb{f}$:

$$[\mathbb{f}]^{\mathrm{W}} = \left([\mathbb{I}] - \frac{2}{3}{}^{t}[\![\boldsymbol{i}]\!] \cdot [\![\boldsymbol{i}]\!]\right) \cdot [\mathbb{f}] \cdot \left([\mathbb{I}] - \frac{2}{3}{}^{t}[\![\boldsymbol{i}]\!] \cdot [\![\boldsymbol{i}]\!]\right) \tag{5.32}$$

$\Delta^{RM/BG}$ gives an estimate of the pure warping fraction of the shear stress energy. When the plate constitutive equation is restricted to a Reissner-Mindlin one we have exactly $\Delta^{RM/BG} = 0$.

In Table 5.1, are given the values of $\Delta^{RM/BG}$ for the laminates considered in this work. For a single ply, the criterion is zero since in Chapter 4 we demonstrated that the Bending-Gradient model is exactly a Reissner-Mindlin model in this case. However, when there are several plies, the distance is greater than 10%. Thus with these laminates, the shear constitutive equation cannot be reduced to a Reissner-Mindlin behavior.

Stack	$[0°]$	$[0°, 90°]$	$[30°, -30°]_s$	$[30°, -30°]$	$[0°, -45°, 90°, 45°]_s$
$\Delta^{RM/BG}$	0	16.0%	16.0%	23.9 %	12.4%

Table 5.1: The criterion $\Delta^{RM/BG}$ for several laminates

5.5 Comparison with other single equivalent layer approaches

5.5.1 Other single equivalent layer approaches

5.5.1.1 The Reissner-Mindlin model with the approach from Whitney (1972)

Closed-form solutions using the Reissner-Mindlin model were derived in order to compare them with the Bending-Gradient. The resolution of the cylindrical bending problem is quite similar so it will not be detailed here. The work of Whitney (1972) was used for deriving transverse shear stress distributions and shear correction factors were taken into account into the shear constitutive equation of the Reissner-Mindlin plate model.

Let us recall briefly the method. Whitney (1972) assumes the plate is under cylindrical bending: $\boldsymbol{Q}_1 = \mathbf{M}_{11,1}$, $\boldsymbol{Q}_2 = \mathbf{M}_{12,1}$, $\mathbf{e}_{22} = 0$ and $\boldsymbol{\chi}_{22} = 0$ and derives transverse shear distribution $\widetilde{\boldsymbol{\sigma}}^{(\boldsymbol{Q}),W}(x_3)$ following a procedure almost identical to the one proposed in Chapter 4. Then he computes the shear correction factor defined as:

$$k_1^2 = \frac{\mathsf{f}_{11}^{FSDT}}{\left\langle \widetilde{\boldsymbol{\sigma}}^{Q_1} : \widetilde{\boldsymbol{\mathcal{S}}}(x_3) : \widetilde{\boldsymbol{\sigma}}^{Q_1} \right\rangle}$$

where f_{11}^{FSDT} is the First Order Shear Deformation Theory shear compliance: $\mathbf{f}^{FSDT} = \left(\mathbf{F}^{FSDT}\right)^{-1}$ where $\mathsf{F}_{\alpha\beta}^{FSDT} = \langle \mathcal{C}_{\alpha 3 \beta 3}(x_3) \rangle$. The shear correction factor in the second direction k_2 is derived in the same way while rotating the plate of $\pi/2$. Once shear correction factors are derived, the corrected shear stiffness $\mathbf{F}^{RM,W}$ is defined as follows:

$$\mathbf{F}^{RM,W} = \mathbf{k} \cdot \mathbf{F}^{FSDT} \cdot \mathbf{k} \tag{5.33}$$

where $\mathbf{k} = \left(\begin{smallmatrix} k_1 & 0 \\ 0 & k_2 \end{smallmatrix}\right)$

5.5.1.2 Finite element analysis

A comparison with a finite elements solution was also performed on ABAQUS (2007b). Since the Bending-Gradient is an Equivalent Single Layer theory, conventional shell elements were chosen (3 displacements and 3 rotations). Transverse shear fields with conventional shell elements in ABAQUS are derived using an approach very similar to Whitney (1972) where it is furthermore assumed that the plate overall constitutive equation is orthotropic with respect to the main bending direction. $S4$, linear quadrangle with full integration elements, were used. A convergence test was performed comparing the FE mid-span deflection $U^{RM,FE}$ to the exact solution from Pagano (1969) U^{Ex} which ensures that the FE error increment is 1/1000 of the error with the exact solution ($(U^{RM,FE} - U^{Ex})/U^{Ex}$). This study enforced the typical size of an element $l_{char} = h/5$ where h is the plate thickness. For instance when the slenderness is $h/L = 1/4$ there are 20 elements. Figure 5.4 shows a typical deformation of this mesh. Periodicity was enforced on lateral edges of the strip in Figure 5.4 by equating corresponding rotations and displacements. Finally 61 section points were required as output and section integration is performed during the analysis. The number of integration points has no incidence on the convergence.

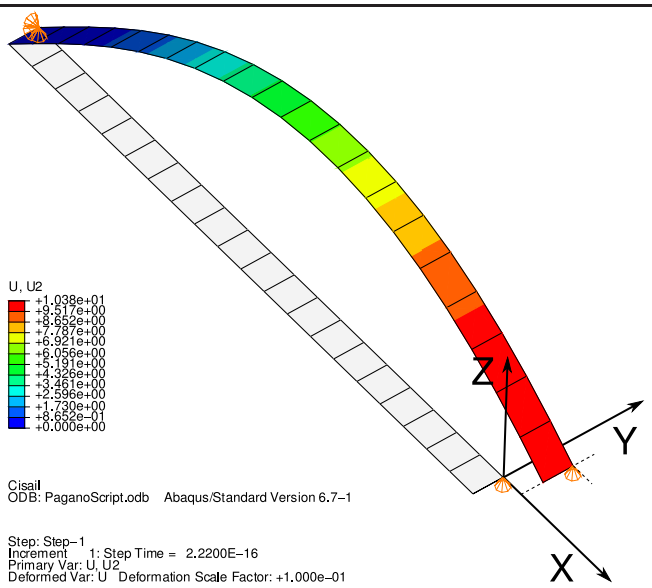

Figure 5.4: Finite Element undeformed and deformed mesh for an anisotropic laminate

5.5.2 Error estimates

Two error estimates are introduced: the first one for the transverse shear part of the stresses for which we introduce the following seminorm:

$$\|\boldsymbol{\sigma}\|^2 = \int_0^L \int_{-\frac{h}{2}}^{\frac{h}{2}} \sigma_{\alpha 3} \mathcal{S}_{\alpha 3 \beta 3} \sigma_{\beta 3} dx_3 dx_1$$

and we define the relative error as:

$$\Delta(\boldsymbol{\sigma}) = \frac{\|\boldsymbol{\sigma}^{Ex} - \boldsymbol{\sigma}\|}{\|\boldsymbol{\sigma}^{Ex}\|}$$

where $\boldsymbol{\sigma}^{Ex}$ is the exact shear stress distribution from Pagano (1969, 1970a,b). The second one is the mid-span deflection relative error:

$$\Delta(U_3) = \frac{U_3^{Ex}(L/2) - U_3(L/2)}{U_3^{Ex}(L/2)}$$

where $U_3^{Ex}(x_1)$ is the plate deflection taken for the exact solution. In Chapter 4 we demonstrated that the plate deflection is related to 3D fields as:

$$U_3^{Ex}(x_1, x_2) = \frac{u_3^{Ex}(x_1, x_2, h/2) + u_3^{Ex}(x_1, x_2, -h/2)}{2} \tag{5.34}$$

where u_3^{Ex} is the vertical displacement field from Pagano (1969, 1970a,b).

5.5.3 Results

5.5.3.1 $[0°, 90°]$ ply

In this section, we consider a skew-symmetric cross ply $[0°, 90°]$ laminate. In this case, the plate configuration fulfills the assumptions made for the finite elements approximation (orthotropic laminate). In Figure 5.5, shear stress distribution in both directions are plotted for the exact solution from Pagano (1969) $\boldsymbol{\sigma}^{Ex}$, the Bending-Gradient solution $\boldsymbol{\sigma}^{(\mathbb{R})}$, Whitney's shear distribution $\boldsymbol{\sigma}^{(\boldsymbol{Q}),W}$ and the finite elements solution $\boldsymbol{\sigma}^{(\boldsymbol{Q}),FE}$. The slenderness ratio is set to $L/h = 4$ as conventionally done when benchmarking plate models. The reader is referred to (Whitney, 1972; Noor and Malik, 2000; Yu et al., 2002b; Nguyen et al., 2005b; Carrera, 2003b) among others. The three approximate solutions yield the same distribution. The discrepancy with the exact solution is well-known and associated to edge effects.

In Figure 5.6 the transverse shear stress distribution error $\Delta(\boldsymbol{\sigma})$ versus the slenderness ratio L/h is plotted for the Bending-Gradient solution (BG), the finite elements solution (RM, FE) and the closed-form Reissner-Mindlin solution (RM, WE). In this case, Whitney's solution converges with L/h whereas finite elements and Bending-Gradient approximations do not converge and lead to rather small errors ($\simeq 10^{-3}$). In Figure 5.7 the mid-span deflection error is also plotted versus the slenderness ratio. The three approximate solutions yields almost the same error.

5.5.3.2 $[30°, -30°]_s$ ply

We consider here a symmetric and non-orthotropic $[30°, -30°]_s$ laminate. This configuration does not comply with the assumptions made for the finite elements approach. In Figure 5.8 shear distributions are compared to the exact solution. The Bending-Gradient solution remains close to the exact solution. However finite elements and Whitney's solution yield a different distribution which is not as accurate as the Bending-Gradient. More precisely, in direction 2, the FE solution does not capture the change of slope associated to the change of ply orientation. In direction 1 the macroscopic equilibrium is respected for all approximated solutions ($\langle \sigma_{13} \rangle = Q_1$). However in direction 2 we can see that $\langle \sigma_{23}^{FE} \rangle \neq Q_2$ for both finite elements and Whitney's solution.

In Figure 5.9 the transverse shear stress distribution error versus the slenderness ratio is plotted. Contrary to the finite elements solution and Whitney's solution, the Bending-Gradient solution converges when the plate is slender. More precisely we have: $\Delta(\boldsymbol{\sigma}^{BG}) \propto \left(\frac{h}{L}\right)^2$ in this case. In Figure 5.10 the mid-span deflection error is also plotted versus the slenderness ratio. The Bending-Gradient solution is the most accurate one for conventional slenderness.

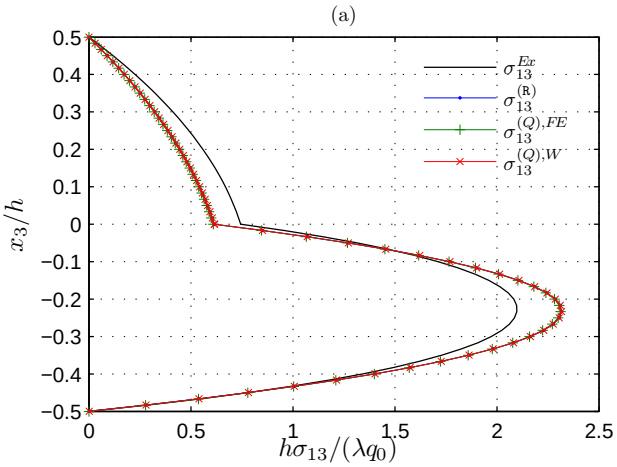

Figure 5.5: Normalized shear distribution σ_{13} at $x_1 = 0$ for a $[0, 90°]$ laminate, $L/h = 4$, ($\sigma_{23} = 0$: symmetry).

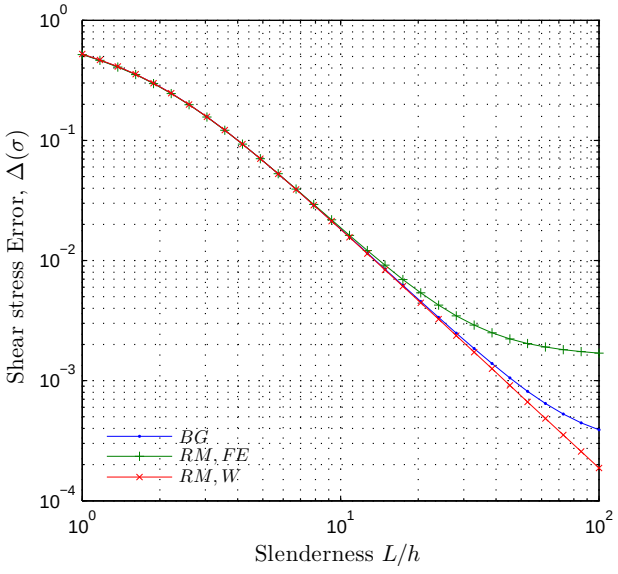

Figure 5.6: Shear stress distribution error versus slenderness ratio for a $[0°, 90°]$ laminate, (BG: Bending-Gradient, RM, FE: finite elements, RM, W:Whitney's distribution)

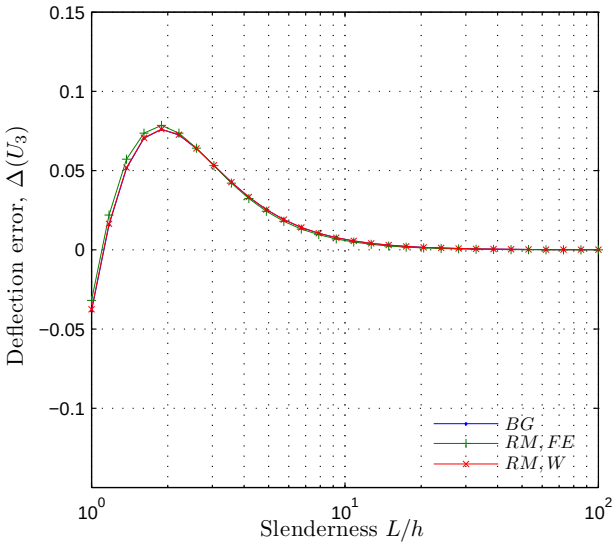

Figure 5.7: Deflection error versus slenderness ratio for a $[0, 90°]$ laminate

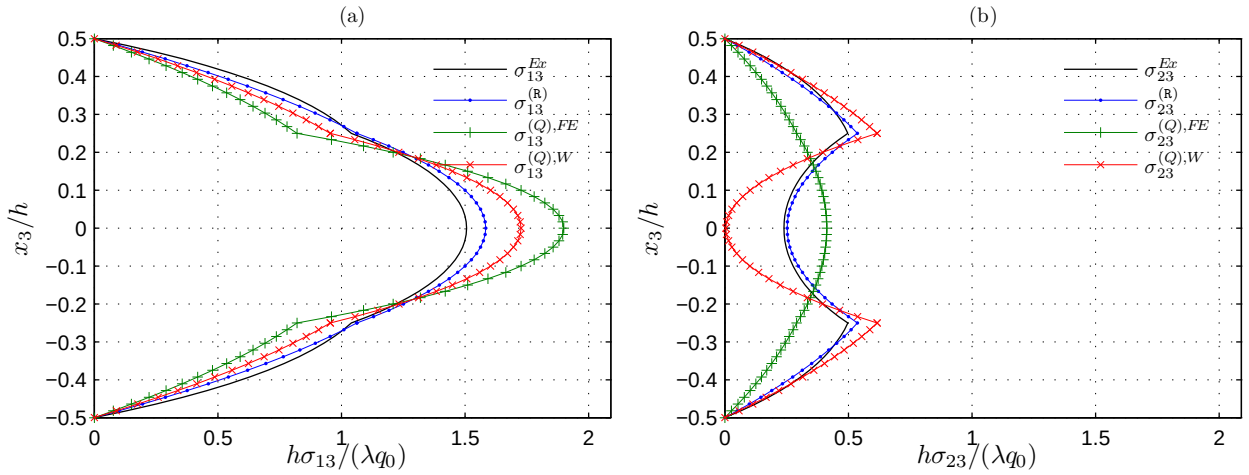

Figure 5.8: Normalized shear distribution in both directions at $x_1 = 0$ for a $[30°, -30°]_s$ laminate, $L/h = 4$, a) σ_{13} b) σ_{23}.

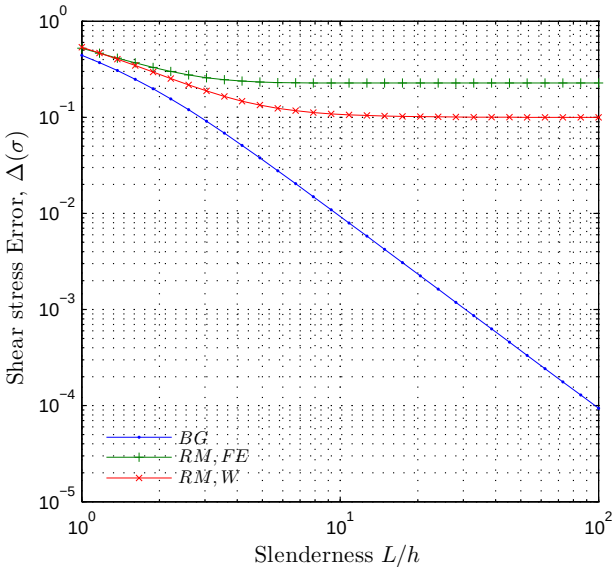

Figure 5.9: Shear stress distribution error versus slenderness ratio for a $[30°, -30°]_s$ laminate

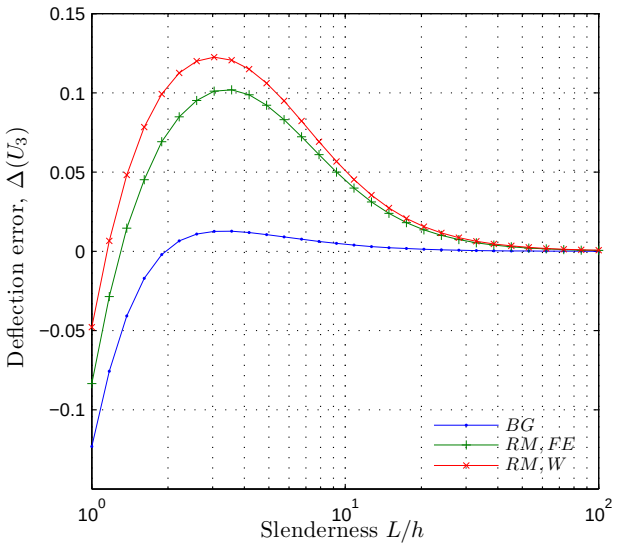

Figure 5.10: Deflection error versus slenderness ratio for a $[30°, -30°]_s$ laminate

5.5.3.3 $[30°, -30°]$ ply

In Figure 5.11 the comparison is made for a non-symmetric and non-orthotropic ply $[30°, -30°]$. Again, this configuration does not comply with the assumptions made for the finite elements approach. The Bending-Gradient solution remains close to the exact solution and Whitney's solution yields acceptable results (except a mismatch for $\sigma_{23}^{(\boldsymbol{Q}),W}$). However in this case, finite elements yields inappropriate results: in direction 1 the stress distribution does not respect macroscopic equilibrium $\left\langle \sigma_{13}^{FE} \right\rangle \neq Q_1$. We checked nevertheless that FE nodal forces fulfills macroscopic equilibrium.

This inaccuracy is also clear in Figure 5.6 showing the transverse shear stress distribution error versus the slenderness ratio whereas the Bending-Gradient converges as $\Delta(\boldsymbol{\sigma}^{BG}) \propto \left(\frac{h}{L}\right)^2$ and both the Whitney and finite elements solutions lead to non negligible errors. Again, in Figure 5.13, the deflection error indicates that FE are too compliant and that the Bending-Gradient is more accurate than the Reissner-Mindlin solution.

5.5.3.4 Influence of the bending direction

As already mentioned, the finite elements approach makes assumption on the overall plate configuration (orthotropy). However, in standard engineering application, even if the plate is orthotropic, the bending direction does not often correspond to the orthotropy axis. In order to illustrate this, we consider here the cross ply $[0°, 90°]$ laminate with fixed slenderness $L/h = 4$ and we rotate the bending directions (*eg.* the plate's overall configuration is rotating relative to x_3 axis). In Figure 5.14 we plotted the deflection error with respect to the bending direction for the different approximations. It is clear that the bending direction has a great influence on the accuracy of the deflection. Even for the Reissner-Mindlin approximation, the error can be four times greater than the error for the Bending-Gradient.

5.5.4 Discussion

We have compared three approaches for deriving an approximation of the exact solution for cylindrical bending suggested by Pagano (1969, 1970a,b).

First we derived closed-form solutions for the Reissner-Mindlin model using shear correction factors and shear distributions from Whitney (1972). This approach yields a fair estimation of the deflection and shear distributions in cylindrical bending but it is not as accurate as the Bending-Gradient approximation in most cases. The main limitation of this approach is the cylindrical bending assumption. It is not sure that shear correction factors and shear distributions will remain valid with more general plate boundary conditions, especially involving torsion, whereas the Bending-Gradient theory is not limited to cylindrical bending.

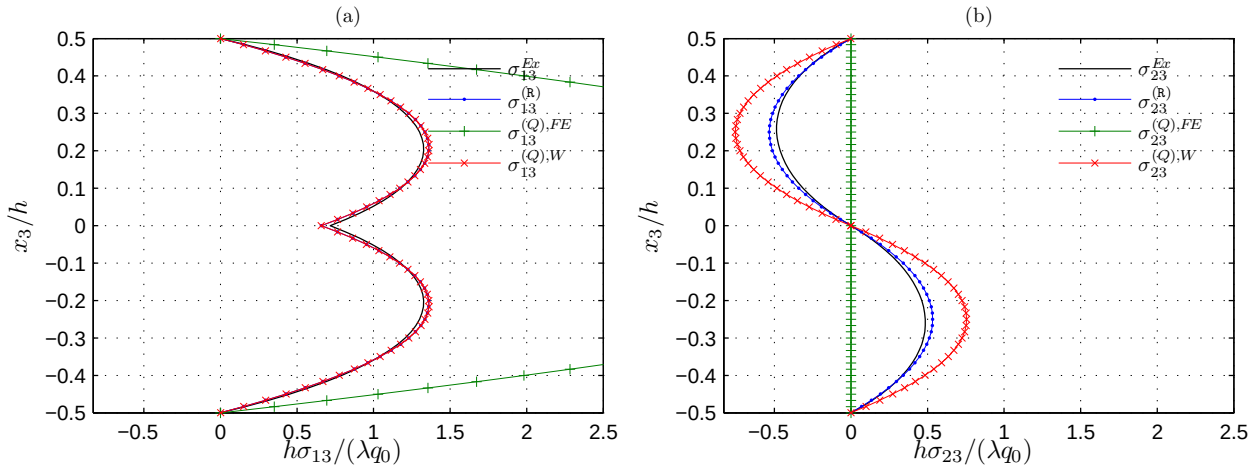

Figure 5.11: Normalized shear distribution in both directions at $x_1 = 0$ for a $[-30°, 30°]$ laminate, $L/h = 4$, a) σ_{13} b) σ_{23}.

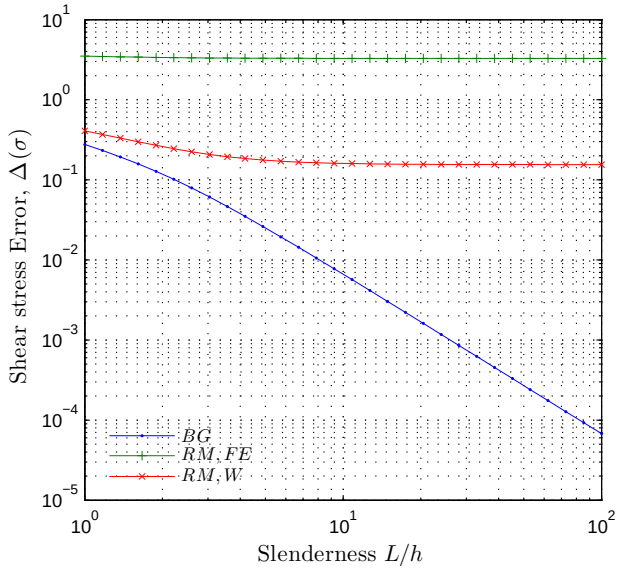

Figure 5.12: Shear stress distribution error versus slenderness ratio for a $[30°, -30°]$ laminate

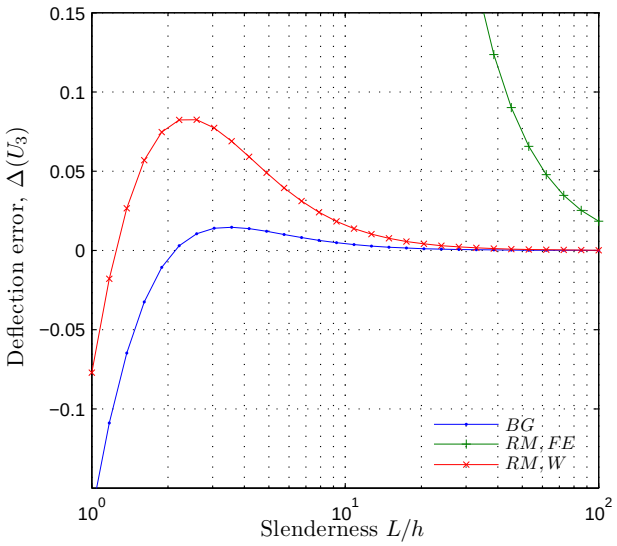

Figure 5.13: Deflection error versus slenderness ratio for a $[30°, -30°]$ laminate

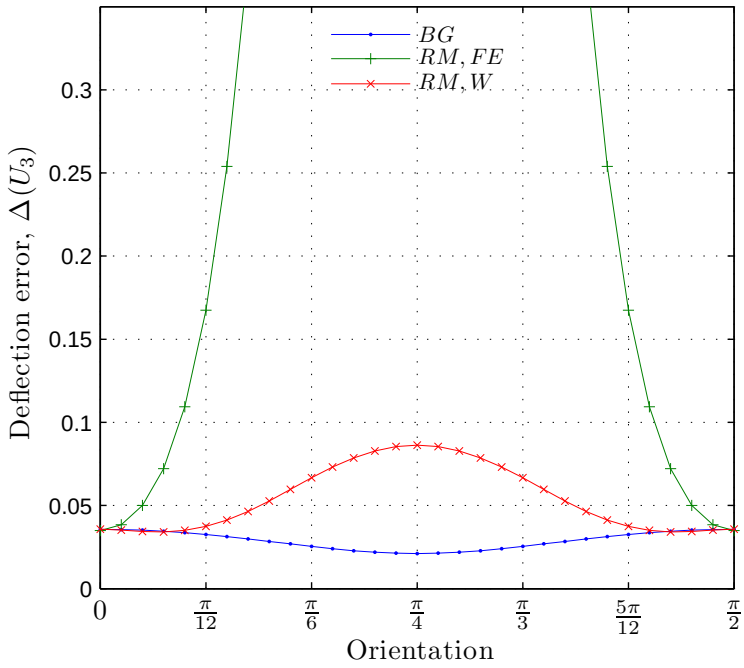

Figure 5.14: Deflection error versus bending direction for a $[0, 90°]$ laminate, $L/h = 4$, maximum value: $\Delta U^{RM,FE}(\pi/4) = 2$

Second, we implemented a finite elements approximation, using conventional shell elements. This approach assumes both cylindrical bending and orthotropy in the same direction. When these assumptions are not valid, the results might be really affected both for deflection and stress distribution as demonstrated for the $[30°, -30°]$ laminate or the rotated $[0°, 90°]$ orthotropic laminate. However, the discrepancy is attenuated, leading to about 15% deflection errors and 25% shear stress errors when increasing the number of layers for configurations similar to the one described in Section 5.5.3.4, (quasi-isotropic laminates).

Finally, the Bending-Gradient solution was presented. This approach enables the derivation of stress distributions and gives good enough deflection and stress distribution estimates whatever the plate configuration and the bending direction are. Moreover, it was numerically demonstrated that in some configurations the Bending-Gradient solution converges with the slenderness ratio.

Let us state this convergence condition precisely. In Chapter 4 we indicated that it was our choice to neglect the gradient of membrane stress $\mathbf{N} \otimes \boldsymbol{\nabla}$ since it is not related to macroscopic stress. In the present application to cylindrical bending, the membrane stress is reduced to N_{22}. When $\mathsf{N}_{22} = 0$, the membrane stress gradient vanishes. This is the case for $[30°, -30°]_s$ and $[30°, -30°]$ since they are balanced laminates (as many θ plies as $-\theta$ plies). In these cases, the Bending-Gradient solution converges because the stress fields related to the membrane stress gradient do not contribute to the final solution. It is possible to generalize this result to any boundary conditions with mirror

symmetric laminates ($\boldsymbol{\mathcal{B}} = 0$) for which the membrane problem is fully uncoupled from the out-of-plane problem. With these laminates, the Bending-Gradient solution is the Saint-Venant solution for an out-of-plane loaded plate. When the plate is not symmetric, an outlook of this work is to estimate the error which comes from this approximation. When looking at the convergence of the skew-symmetric $[0°, 90°]$ laminate in Figure 5.6 one can see that the error seems to remain limited. In this specific case, Whitney's solution converges because it assumes *a priori* $\chi_{22} = 0$ which is not the case with the Bending-Gradient since χ_{22} derives from the generalized rotation $\boldsymbol{\Phi}$ and is not directly related to macroscopic displacements.

Finally, in Chapter 4 we pointed out that the relevance of introducing the full bending gradient might be questionable since the Bending-Gradient is sometimes turned into a Reissner-Mindlin model. In the present paper, we provide answers. First, when dealing with highly anisotropic laminates, it is clear that all localization fields are relevant (see Section 5.4.3.2) and the distance with Reissner-Mindlin presented in Section 5.4.3.3 fully justifies the use of the Bending-Gradient. However, when studying the influence of isotropy on the shear constitutive equation in Section 5.3.3 we indicated that only Poisson's effect has an influence on warping. Since most conventional materials have almost identical Poissons's ratios, it is more relevant to use a Reissner-Mindlin model in these cases.

5.6 Conclusion

In the present chapter, we provided first applications using the Bending-Gradient plate theory. We introduced Voigt notation which enables easier analytical computations and prepares finite elements implementation. Then the influence of material symmetries was associated to in-plane strain gradient elasticity. Closed-form solutions for cylindrical bending were fully derived, applied to laminates and compared to Reissner-Mindlin and finite elements approximations. The main conclusion is that the Bending-Gradient gives good predictions of both deflection and shear stress distributions in any material configuration. It is also the Saint-Venant solution when membrane stresses are fully uncoupled from bending moments and generalized shear stresses. Finally, with usual laminated plates, we demonstrated that the Bending-Gradient cannot be reduced to a Reissner-Mindlin plate model.

Several outlooks are under consideration. First, this plate theory can be extended to periodic plates such as sandwich panels (Lebée and Sab, 2010c,d). Second, the estimation of the influence of the membrane stress gradient on the quality of the shear stress estimation should be studied in detail. Finally, since we have a Saint-Venant solution, it is worth analyzing the shift with more refined approximations such as layerwise models or even full 3D finite elements when it is necessary to locally refine the analysis as illustrated in Amini et al. (2009) among others.

CHAPTER

6

Homogenization of periodic sandwich panels

Since the Bending-Gradient plate theory has been defined for invariant plates in the (x_1, x_2) plane in Chapter 4, we suggest its extension to periodic plates thanks to simple micro/macro energy-equivalence considerations, in this chapter. Once this extension is provided, it is possible to refine the analysis for the specific case of sandwich panels. Finally, we will give full justification of the sandwich theory and identify precisely the underlying assumptions.

6.1 Thick periodic plate homogenization

Exactly as Cecchi and Sab (2007) did for periodic plate Reissner-Mindlin homogenization, it is possible to extend to periodic plates the Bending-Gradient plate theory of Chapter 4. For this, it is implicitly assumed that macroscopic fields $(\mathbf{N}, \mathbf{M}, \mathbf{R})$ and their associated local stress energy density vary slowly with respect to the size of the unit-cell. This is very conventional in homogenization. Then, the average of the local energy (microscopic energy) is assumed equal to the plate energy (macroscopic energy). For a stress approach this is equivalent to setting:

$$w^{*BG}(\mathbf{N}, \mathbf{M}, \mathbf{R}) = \frac{1}{A_Y} \int_Y \widetilde{\boldsymbol{\sigma}}^{BG}(\widetilde{\boldsymbol{y}}) : \widetilde{\boldsymbol{\mathcal{S}}}(\widetilde{\boldsymbol{y}}) : \widetilde{\boldsymbol{\sigma}}^{BG}(\widetilde{\boldsymbol{y}}) dY \tag{6.1}$$

where A_Y is the unit-cell surface and $\widetilde{\boldsymbol{\sigma}}^{BG} = \widetilde{\boldsymbol{s}}^{(\mathsf{N})} : \mathbf{N} + \widetilde{\boldsymbol{s}}^{(\mathsf{M})} : \mathbf{M} + \widetilde{\boldsymbol{s}}^{(\mathsf{R})} \therefore \mathbf{R}$ is the localization field in the unit-cell Y associated to the Bending-Gradient plate model, the derivation of which is described in the following.

6.1.1 The unit-cell configuration

Let us consider a plate generated by periodicity of a unit-cell Y (Figure 6.1). The upper face ∂Y_3^+ and the lower face ∂Y_3^- are traction free and the lateral faces ∂Y_l must fulfil periodicity conditions. V_Y is the unit-cell volume and A_Y is the area of the unit-cell cross section with the plate

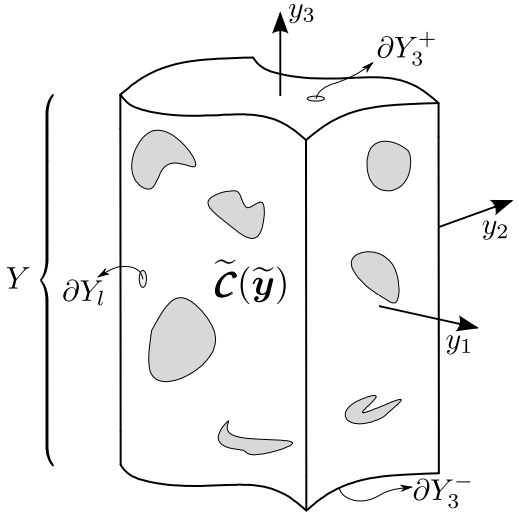

Figure 6.1: The plate unit-cell

mid-plane. (y_1, y_2, y_3) is the set of coordinates in the unit-cell reference frame.

When dealing with laminated plates it was possible to derive localization fields $\boldsymbol{s}^{(\mathbf{N})}(x_3)$, $\boldsymbol{s}^{(\mathbf{M})}(x_3)$ and $\boldsymbol{s}^{(\mathbf{R})}(x_3)$ explicitly from the constitutive material behavior (Equation (4.19) and Equation (4.25)). However, with periodic plates this is not possible in the general case and deriving localization fields necessitates the resolution of auxiliary unit-cell problems. First, the Love-Kirchhoff homogenization auxiliary problem was suggested by Caillerie (1984) and enables the derivation of the effective Love-Kirchhoff membrane and flexural moduli of the periodic plate $\boldsymbol{\mathcal{A}}$, $\boldsymbol{\mathcal{B}}$ and $\boldsymbol{\mathcal{D}}$, as well as the local 3D stresses $\boldsymbol{s}^{(\mathbf{e})}(\widetilde{\boldsymbol{y}})$ and $\boldsymbol{s}^{(\boldsymbol{\chi})}(\widetilde{\boldsymbol{y}})$. Then a Bending-Gradient auxiliary problem is defined, using Love-Kirchhoff localization fields as loading, in order to derive the shear constitutive equation.

6.1.2 Love-Kirchhoff auxiliary problem (Caillerie, 1984)

Love-Kirchhoff homogenization of periodic plates was first proposed by Caillerie (1984) and followed by Kohn and Vogelius (1984). The auxiliary problem is stated as follows:

$$\mathcal{P}^{(\mathsf{e},\chi)} \begin{cases} \widetilde{\boldsymbol{\sigma}}^{LK} \cdot \widetilde{\boldsymbol{\nabla}} = 0 & \text{(6.2a)} \\ \widetilde{\boldsymbol{\sigma}}^{LK} = \widetilde{\boldsymbol{\mathcal{C}}}(\widetilde{\boldsymbol{y}}) : \widetilde{\boldsymbol{\varepsilon}}^{LK} & \text{(6.2b)} \\ \widetilde{\boldsymbol{\varepsilon}}^{LK} = \widetilde{\mathbf{e}} + y_3 \widetilde{\boldsymbol{\chi}} + \widetilde{\boldsymbol{\nabla}} \otimes^s \widetilde{\boldsymbol{u}}^{per} & \text{(6.2c)} \\ \widetilde{\boldsymbol{\sigma}} \cdot \widetilde{\boldsymbol{e}}_3 = 0 \text{ on free faces } \partial Y_3^{\pm} & \text{(6.2d)} \\ \widetilde{\boldsymbol{\sigma}} \cdot \widetilde{\boldsymbol{n}} \text{ skew-periodic on lateral boundaries } \partial Y_l & \text{(6.2e)} \\ \widetilde{\boldsymbol{u}}^{per}(y_1, y_2, y_3) \quad (y_1, y_2)\text{-periodic on lateral boundaries } \partial Y_l & \text{(6.2f)} \end{cases}$$

Basically it enforces the membrane strains $\mathbf{e}$ and the curvatures $\boldsymbol{\chi}$ on average on the unit-cell while taking into account periodicity in the (x_1, x_2)-plane and traction-free conditions on the upper and lower faces of the plate. $\widetilde{\mathbf{e}}$ and $\widetilde{\boldsymbol{\chi}}$ denote the extension to 3D of the 2D tensors $\mathbf{e}$ and $\boldsymbol{\chi}$ with $\mathsf{e}_{i3} = \chi_{i3} = 0$ (as for any 2D tensor: $\mathbf{N}$, $\mathbf{M}$, $\boldsymbol{Q}$, $\boldsymbol{\gamma}$). Solving the problem for each individual component of $\mathbf{e}$ and $\boldsymbol{\chi}$ leads to the localization stress fields $s^{(\mathsf{e})}_{ij\alpha\beta}(\widetilde{\boldsymbol{y}})$ and $s^{(\chi)}_{ij\alpha\beta}(\widetilde{\boldsymbol{y}})$. The complete local stress field can be reconstructed by linear combination:

$$\widetilde{\boldsymbol{\sigma}}^{LK} = \widetilde{\boldsymbol{\sigma}}^{(\mathsf{e})} + \widetilde{\boldsymbol{\sigma}}^{(\chi)} = \widetilde{\boldsymbol{s}}^{(\mathsf{e})}(\widetilde{\boldsymbol{y}}) : \mathbf{e} + \widetilde{\boldsymbol{s}}^{(\chi)}(\widetilde{\boldsymbol{y}}) : \boldsymbol{\chi} \tag{6.3}$$

Love-Kirchhoff plate moduli are then evaluated as follows:

$$\boldsymbol{\mathcal{A}} = \left\langle {}^{t}\widetilde{\boldsymbol{s}}^{(\mathsf{e})} : \widetilde{\boldsymbol{\mathcal{S}}} : \widetilde{\boldsymbol{s}}^{(\mathsf{e})} \right\rangle, \quad \boldsymbol{\mathcal{B}} = \left\langle {}^{t}\widetilde{\boldsymbol{s}}^{(\mathsf{e})} : \widetilde{\boldsymbol{\mathcal{S}}} : \widetilde{\boldsymbol{s}}^{(\chi)} \right\rangle, \quad \boldsymbol{\mathcal{D}} = \left\langle {}^{t}\widetilde{\boldsymbol{s}}^{(\chi)} : \widetilde{\boldsymbol{\mathcal{S}}} : \widetilde{\boldsymbol{s}}^{(\chi)} \right\rangle \tag{6.4}$$

where and $\widetilde{\boldsymbol{\mathcal{S}}}(\widetilde{\boldsymbol{y}})$ is the local 3D compliance tensor and

$$\langle f \rangle = \frac{1}{A_Y} \int_Y f(\widetilde{\boldsymbol{y}}) dY \tag{6.5}$$

is the surface average on the unit-cell and replaces the integration through the thickness in Chapter 4. Variational principles related to $\mathcal{P}^{(\mathsf{e},\chi)}$ problem are recalled in Frame 6.1.

Finally, using the inverted Love-Kirchhoff plate constitutive law,

$$\mathbf{e} = \boldsymbol{a} : \mathbf{N} + \boldsymbol{b} : \mathbf{M}, \qquad \boldsymbol{\chi} = {}^{t}\boldsymbol{b} : \mathbf{N} + \boldsymbol{d} : \mathbf{M} \tag{6.6}$$

and localization tensors $\widetilde{\boldsymbol{s}}^{(\mathsf{e})}(\widetilde{\boldsymbol{y}})$ and $\widetilde{\boldsymbol{s}}^{(\chi)}(\widetilde{\boldsymbol{y}})$, it is possible to write the stress field generated by an imposed bending moment as:

$$\widetilde{\boldsymbol{\sigma}}^{(\mathsf{M})} = \left(\widetilde{\boldsymbol{s}}^{(\mathsf{e})} : \boldsymbol{b} + \widetilde{\boldsymbol{s}}^{(\chi)} : \boldsymbol{d} \right) : \mathbf{M} \tag{6.7}$$

NB: For implementation convenience, the problem $\mathcal{P}^{(\mathsf{e},\chi)}$ can be rewritten in the strictly equivalent

Static approach: The set of statically compatible fields $SC^{(\mathsf{e},\chi)}$ is the set of stress fields $\widetilde{\boldsymbol{\sigma}}$ which fulfil equilibrium equation (6.2a), boundary conditions (6.2d) and periodicity conditions (6.2e).
The stress solution $\widetilde{\boldsymbol{\sigma}}^{LK}$ is the one that minimizes the complementary energy per unit surface $P^{*(\mathsf{e},\chi)}$:

$$P^{*(\mathsf{e},\chi)}\left(\widetilde{\boldsymbol{\sigma}}^{LK}\right) = \min_{\widetilde{\boldsymbol{\sigma}}\in SC^{(\mathsf{e},\chi)}} \left\{ \frac{1}{2}\left\langle {}^t\widetilde{\boldsymbol{\sigma}} : \widetilde{\boldsymbol{\mathcal{S}}}(\widetilde{\boldsymbol{y}}) : \widetilde{\boldsymbol{\sigma}} \right\rangle - \left\langle {}^t\widetilde{\boldsymbol{\sigma}} : (\widetilde{\mathbf{e}} + y_3\widetilde{\boldsymbol{\chi}}) \right\rangle \right\} \tag{6.8}$$

Kinematic approach: The set of kinematically compatible fields $KC^{(\mathsf{e},\chi)}$ is the set of strain fields $\widetilde{\boldsymbol{\varepsilon}}$ which fulfil compatibility conditions (6.2c) and periodicity conditions (6.2f).
The strain solution $\widetilde{\boldsymbol{\varepsilon}}^{LK}$ is the one that minimizes the potential energy per unit surface $P^{(\mathsf{e},\chi)}$:

$$P^{(\mathsf{e},\chi)}\left(\widetilde{\boldsymbol{\varepsilon}}^{LK}\right) = \min_{\widetilde{\boldsymbol{\varepsilon}}\in KC^{(\mathsf{e},\chi)}} \left\{ \frac{1}{2}\left\langle {}^t\widetilde{\boldsymbol{\varepsilon}} : \widetilde{\boldsymbol{\mathcal{C}}}(\widetilde{\boldsymbol{y}}) : \widetilde{\boldsymbol{\varepsilon}} \right\rangle \right\} \tag{6.9}$$

Clapeyron's formula: The following relation holds for the solution:

$$P^{(\mathsf{e},\chi)}\left(\widetilde{\boldsymbol{\varepsilon}}^{LK}\right) = -P^{*(\mathsf{e},\chi)}\left(\widetilde{\boldsymbol{\sigma}}^{LK}\right) = w^{LK}\left(\mathbf{e},\boldsymbol{\chi}\right) = \frac{1}{2}\left(\mathbf{e} : \boldsymbol{\mathcal{A}} : \mathbf{e} + 2\mathbf{e} : \boldsymbol{\mathcal{B}} : \boldsymbol{\chi} + \boldsymbol{\chi} : \boldsymbol{\mathcal{D}} : \boldsymbol{\chi}\right) \tag{6.10}$$

Frame 6.1: Variational Principles for the Love-Kirchhoff auxiliary problem

form:

$$\mathcal{P}^{(\mathsf{e},\chi),bis} \begin{cases} \widetilde{\boldsymbol{\sigma}}^{LK} \cdot \widetilde{\boldsymbol{\nabla}} = 0 & \text{(6.11a)} \\ \widetilde{\boldsymbol{\sigma}}^{LK} = \widetilde{\boldsymbol{\mathcal{C}}}\left(\widetilde{\boldsymbol{y}}\right) : \widetilde{\boldsymbol{\varepsilon}}^{LK} & \text{(6.11b)} \\ \widetilde{\boldsymbol{\varepsilon}}^{LK} = \widetilde{\boldsymbol{\nabla}} \otimes^s \widetilde{\boldsymbol{u}}^{LK} & \text{(6.11c)} \\ \widetilde{\boldsymbol{u}}^{LK} = \widetilde{\boldsymbol{u}}^{per} + \widetilde{\mathbf{e}} \cdot \widetilde{\boldsymbol{y}} + y_3\widetilde{\boldsymbol{\chi}} \cdot \widetilde{\boldsymbol{y}} - \dfrac{1}{2}\left({}^t\widetilde{\boldsymbol{y}} \cdot \widetilde{\boldsymbol{\chi}} \cdot \widetilde{\boldsymbol{y}}\right)\widetilde{\boldsymbol{e}}_3 \quad \text{on } \partial Y_l & \text{(6.11d)} \\ \widetilde{\boldsymbol{\sigma}} \cdot \widetilde{\boldsymbol{e}}_3 = 0 \text{ on free faces } \partial Y_3^{\pm} & \text{(6.11e)} \\ \widetilde{\boldsymbol{\sigma}} \cdot \widetilde{\boldsymbol{n}} \text{ skew-periodic on lateral boundaries } \partial Y_l & \text{(6.11f)} \\ \widetilde{\boldsymbol{u}}^{per}(y_1, y_2, y_3) \quad (y_1, y_2)\text{-periodic on lateral boundaries } \partial Y_l & \text{(6.11g)} \end{cases}$$

where conditions are imposed on the lateral boundaries of the unit cell which is much easier to implement than applying average volume strain.

6.1.3 The Bending-Gradient auxiliary problem

Exactly as for laminated plates (Section 4.5.1), it is possible to bring out a volume force related to $\mathbf{R}$ when assuming a linear variation of the bending moment in the (y_1, y_2)-plane: $\mathbf{M} = \mathbf{R} \cdot \boldsymbol{y}$. Inserting this in the localization equation (6.7) and taking the 3D divergence of the stress, leads to:

$$f_i^{(\mathsf{R})} = \left(s_{ij\beta\alpha}^{(\mathsf{M})}(\widetilde{\boldsymbol{y}})\mathrm{R}_{\alpha\beta\gamma}y_\gamma\right)\nabla_j = s_{i\gamma\beta\alpha}^{(\mathsf{M})}\left(\widetilde{\boldsymbol{y}}\right)\mathrm{R}_{\alpha\beta\gamma} = \left(\widetilde{\boldsymbol{s}}^{(\mathsf{e})} : \boldsymbol{\mathcal{b}} + \widetilde{\boldsymbol{s}}^{(\chi)} : \boldsymbol{\mathcal{d}}\right) \therefore \mathbf{R} \tag{6.12}$$

Then the Bending-Gradient 3D stress $\widetilde{\boldsymbol{\sigma}}^{(\mathtt{R})}$ is defined as the stress field which equilibrates $\widetilde{\boldsymbol{f}}^{(\mathtt{R})}$. Accordingly, the Bending-Gradient auxiliary problem on the unit-cell is defined as:

$$\mathcal{P}^{(\mathtt{R})}\begin{cases}\widetilde{\boldsymbol{\sigma}}^{(\mathtt{R})}\cdot\widetilde{\boldsymbol{\nabla}}+\widetilde{\boldsymbol{f}}^{(\mathtt{R})}(\widetilde{\boldsymbol{y}})=0 & (6.13a)\\ \widetilde{\boldsymbol{\sigma}}^{(\mathtt{R})}=\widetilde{\boldsymbol{\mathcal{C}}}(\widetilde{\boldsymbol{y}}):\left(\widetilde{\boldsymbol{\nabla}}\otimes^{s}\widetilde{\boldsymbol{u}}^{(\mathtt{R})}\right) & (6.13b)\\ \widetilde{\boldsymbol{\sigma}}^{(\mathtt{R})}\cdot\widetilde{\boldsymbol{e}}_3=0 \text{ on free faces } \partial Y_3^{\pm} & (6.13c)\\ \widetilde{\boldsymbol{\sigma}}^{(\mathtt{R})}\cdot\widetilde{\boldsymbol{n}} \text{ skew-periodic on lateral boundaries } \partial Y_l & (6.13d)\\ \widetilde{\boldsymbol{u}}^{(\mathtt{R})}(y_1,y_2,y_3)\quad (y_1,y_2)\text{-periodic on lateral boundaries } \partial Y_l & (6.13e)\end{cases}$$

Variational principles related to $\mathcal{P}^{(\mathtt{R})}$ are recalled in Frame 6.2.

Likewise Equation (6.3), solving $\mathcal{P}^{(\mathtt{R})}$ leads to the localization stress field $s^{(\mathtt{R})}_{ij\alpha\beta\gamma}$ associated to $\mathbf{R}$. The overall stress is obtained by linear combination:

$$\widetilde{\boldsymbol{\sigma}}^{(\mathtt{R})}=\widetilde{\boldsymbol{s}}^{(\mathtt{R})}(\widetilde{\boldsymbol{y}})\therefore\mathbf{R} \tag{6.14}$$

It is then possible to identify the Bending-Gradient compliance tensor as:

$$\mathbb{f}=\left\langle {}^{t}\left(\widetilde{\boldsymbol{s}}^{(\mathtt{R})}\right):\widetilde{\boldsymbol{\mathcal{S}}}(\widetilde{\boldsymbol{y}}):\widetilde{\boldsymbol{s}}^{(\mathtt{R})}\right\rangle \tag{6.15}$$

Moreover, if the unit-cell does not comply with the rotational symmetry with respect to a vertical axis there is coupling between $(\mathbf{N},\mathbf{M})$ and $\mathbf{R}$ (*cf.* Section 4.A.1). The fifth order compliance tensors related to this coupling are derived using:

$$\mathbb{n}=\left\langle {}^{t}\left(\widetilde{\boldsymbol{s}}^{(\mathtt{N})}\right):\widetilde{\boldsymbol{\mathcal{S}}}(\widetilde{\boldsymbol{y}}):\widetilde{\boldsymbol{s}}^{(\mathtt{R})}\right\rangle \tag{6.16}$$

for coupling between $\mathbf{R}$ and the membrane stress, and:

$$\mathbb{m}=\left\langle {}^{t}\left(\widetilde{\boldsymbol{s}}^{(\mathtt{M})}\right):\widetilde{\boldsymbol{\mathcal{S}}}(\widetilde{\boldsymbol{y}}):\widetilde{\boldsymbol{s}}^{(\mathtt{R})}\right\rangle \tag{6.17}$$

for coupling between $\mathbf{R}$ and the bending moment. Then, the full constitutive equation is written as:

$$\begin{cases}\mathbf{e}=\boldsymbol{a}:\mathbf{N}+\boldsymbol{b}:\mathbf{M}+\mathbb{n}\therefore\mathbf{R} & (6.18a)\\ \boldsymbol{\chi}={}^{t}\boldsymbol{b}:\mathbf{N}+\boldsymbol{d}:\mathbf{M}+\mathbb{m}\therefore\mathbf{R} & (6.18b)\\ \boldsymbol{\Gamma}={}^{t}\mathbb{n}:\mathbf{N}+{}^{t}\mathbb{m}:\mathbf{M}+\mathbb{f}\therefore\mathbf{R} & (6.18c)\end{cases}$$

Contrary to axiomatic approaches, the main asset of this approach is that no assumption is made on the strain or stress related to shear forces. Actually, the effect of generalized shear plate force on

the local stress distribution is introduced with the volume force $\widetilde{\boldsymbol{f}}^{(\mathrm{R})}$ which cannot be chosen *a priori* but derives from the bending moment localization field.

Static approach: The set of statically compatible fields $SC^{(\mathrm{R})}$ is the set of stress fields $\widetilde{\boldsymbol{\sigma}}$ which fulfil equilibrium equation (6.13a), boundary conditions (6.13c) and periodicity conditions (6.13d).
The stress solution $\widetilde{\boldsymbol{\sigma}}^{(\mathrm{R})}$ is the one that minimizes the complementary energy $P^{*(\mathrm{R})}$:

$$P^{*(\mathrm{R})}\left(\widetilde{\boldsymbol{\sigma}}^{(\mathrm{R})}\right) = \min_{\widetilde{\boldsymbol{\sigma}} \in SC^{(\mathrm{R})}} \left\{ \frac{1}{2} \left\langle {}^{t}\widetilde{\boldsymbol{\sigma}} : \widetilde{\boldsymbol{\mathcal{S}}}(\widetilde{\boldsymbol{y}}) : \widetilde{\boldsymbol{\sigma}} \right\rangle \right\} \tag{6.19}$$

Kinematic approach: The set of kinematically compatible fields $KC^{(\mathrm{R})}$ is the set of strain fields $\widetilde{\boldsymbol{\varepsilon}}$ which derive from a displacement field which fulfils periodicity conditions (6.13e).
The strain solution $\widetilde{\boldsymbol{\varepsilon}}^{(\mathrm{R})}$ is the one that minimizes the potential energy $P^{(\mathrm{R})}$:

$$P^{(\mathrm{R})}\left(\widetilde{\boldsymbol{\varepsilon}}^{(\mathrm{R})}\right) = \min_{\widetilde{\boldsymbol{\varepsilon}} \in KC^{(\mathrm{R})}} \left\{ \frac{1}{2} \left\langle {}^{t}\widetilde{\boldsymbol{\varepsilon}} : \widetilde{\boldsymbol{\mathcal{C}}}(\widetilde{\boldsymbol{y}}) : \widetilde{\boldsymbol{\varepsilon}} \right\rangle - \left\langle \widetilde{\boldsymbol{f}}^{(\mathrm{R})} \cdot \widetilde{\boldsymbol{u}}\left(\widetilde{\boldsymbol{\varepsilon}}\right) \right\rangle \right\} \tag{6.20}$$

Clapeyron's formula: The following relation holds for the solution:

$$P^{(\mathrm{R})}\left(\widetilde{\boldsymbol{\varepsilon}}^{(\mathrm{R})}\right) = -P^{*(\mathrm{R})}\left(\widetilde{\boldsymbol{\sigma}}^{(\mathrm{R})}\right) = w^{*BG,(\mathrm{R})}\left(\mathbb{R}\right) = \frac{1}{2}{}^{t}\mathbb{R} \therefore \mathbb{f} \therefore \mathbb{R} \tag{6.21}$$

Frame 6.2: Variational Principles for the Bending-Gradient auxiliary problem

The present extension to periodic plate of the Bending-Gradient theory is provided using simple energy equivalence. This approach will be validated in the specific case of a sandwich panel including the chevron pattern in the next chapter. However, it would be of interest to compare this theory to the rigorous one from Lewinski (1991c). This was performed in the case of periodic beam by Buannic and Cartraud (2001a) and could be extended to periodic plates.

6.2 Sandwich Theory justification

As we indicated in Chapter 2, deriving sandwich panels constitutive equations is based on a contrast assumption. Provided this assumption, it is admitted that only the skins are involved in the flexural behavior and only the core affects the shear forces behavior of the sandwich panel.

Let us recall the conventional approach for deriving flexural and shear forces stiffnesses of sandwich panels, called the 2-step homogenization method. First, the core is homogenized in order to derive both in-plane and out-of-plane effective properties using standard methods. Once the effective properties are derived, the Classical Laminates Theory (CLT) is applied for the flexural behavior and the First Order Shear Deformation Theory (FOSDT) is used for the shear forces stiffness assuming the contribution from the skins negligible (thin skins), (Hohe, 2003).

This approach raises two difficulties. First, the homogenization scheme for the core is not always justified. Generally, one assumes that the core is infinite in the thickness direction and performes 3D homogenization for periodic media. This is possible with honeycomb, but what would be an infinite pattern for the chevron pattern? Moreover, it is generally recognized that 3D homogenization fails to capture the influence of the stiff skins on the core. Second, whereas using the CLT for deriving flexural stiffnesses is commonly accepted, using the FOSDT for the shear forces stiffness is valid only for thin skins. When the skins are thick and the core heterogeneous, the contribution of the skins to the shear forces stiffness is controversial. Given the homogenized transverse shear stiffness of the core $\mathsf{C}^{\text{eff}}_{\alpha\beta}$, Kelsey et al. (1958) suggest, with neither justification nor reference, the following shear forces stiffness:

$$\mathsf{F}_{\alpha\beta} = \frac{t_c}{k_s^2}\mathsf{C}^{\text{eff}}_{\alpha\beta}, \quad \text{where} \quad k_s = \frac{3}{2}\frac{t_c(h^2 - t_c^2)}{h^3 - t_c^3}. \tag{6.22}$$

Allen (1969) suggests:

$$\mathsf{F}_{\alpha\beta} = \frac{(t_c + t_s)^2}{t_c}\mathsf{C}^{\text{eff}}_{\alpha\beta}. \tag{6.23}$$

which is the same as the one from Kelsey et al. (1958) at first order in t_s/t_c. Many authors use: $\mathsf{F}_{\alpha\beta} = t_c\mathsf{C}^{\text{eff}}_{\alpha\beta}$ which is the same as Kelsey et al. (1958) at zeroth order in t_s/t_c. Finally, some directly use the FOSDT uniform shear strain assumption which leads to: $\mathsf{F}_{\alpha\beta} = t_c\mathsf{C}^{\text{eff}}_{\alpha\beta} + 2t_s\mathsf{C}^{s}_{\alpha\beta}$ where $\mathsf{C}^{s}_{\alpha\beta} = \mathcal{C}^{s}_{\alpha 3\beta 3}$ is the transverse shear stiffness of the skins.

In order to give a better insight of these questions, we apply in the following the Bending-Gradient homogenization scheme from Section 6.1 to a sandwich panel. First, the Love-Kirchhoff auxiliary problem leads to a quantitative definition of the contrast assumption. Then, adopting the Bending-Gradient auxiliary problem reveals that the actual shear behavior of a sandwich panel under the contrast assumption is a Reissner-Mindlin one. Finally, we derive the already known bounds for the shear forces stiffness in sandwich panels and give their extension to the case of thick skins.

6.2.1 The sandwich panel unit-cell

Let us consider the sandwich panel unit-cell in Figure 6.2. The unit-cell, Y, is separated in three parts, the upper skin Y^{s+}, the lower skin Y^{s-} and the core Y^c: $Y = Y^{s+} \cup Y^c \cup Y^{s-}$. Both skins have the same thickness t_s and the same homogeneous elasticity tensor $\widetilde{\boldsymbol{\mathcal{C}}}^s$ which is symmetric with respect to (y_1, y_2) plane ($\mathcal{C}^s_{i333} = 0$). The core is heterogeneous $\widetilde{\boldsymbol{\mathcal{C}}}^c(\widetilde{\boldsymbol{y}})$ and its thickness is t_c. The total thickness of the plate is: $h = t_c + 2t_s$. The interfaces between core and skins are also introduced. ∂Y^+_{int} is the interface between the core and the upper skin, and ∂Y^-_{int} is the interface between the core and the lower skin (Figure 6.2).

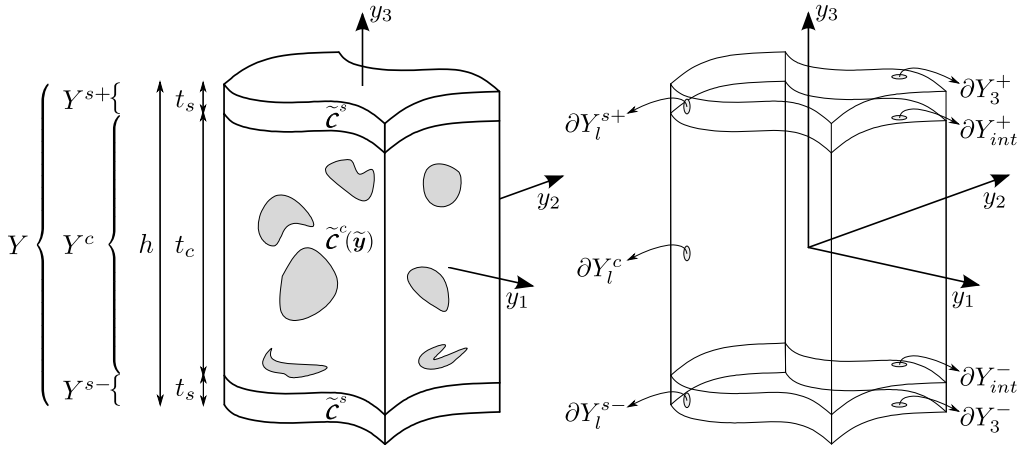

Figure 6.2: Periodic sandwich panel unit-cell

6.2.2 Neglecting the core in Love-Kirchhoff constitutive equation

In order to determine the contrast assumption implicitly made in sandwich theory, we apply variational principles for the Love-Kirchhoff auxiliary problem introduced in Section 6.1.2 to the sandwich panel unit-cell (Figure 6.2). This is done in two steps. First, strain and stress compatible trial fields are defined. Then, the related energies are derived and compared to the exact solution.

6.2.2.1 Compatible trial fields

For the lower bound, we choose $\boldsymbol{\sigma}^- \in SC^{(\mathsf{e},\chi)}$ of the form:

$$\boldsymbol{\sigma}^- = \begin{cases} \boldsymbol{c}^s : (\mathbf{e} + x_3\boldsymbol{\chi}) & \text{on } Y^{s\pm} \\ \mathbf{0} & \text{on } Y^c \end{cases} \qquad \text{and} \quad \sigma_{i3}^- = 0 \quad \text{on } Y \tag{6.24}$$

$\widetilde{\boldsymbol{\sigma}}^-$ is null in the core and plane-stress in the skins. $\boldsymbol{c}^s$ is the plane-stress stiffness tensor in the skins. As already mentionned, it is the inverse of the in-plane part of the 3D compliance: $\boldsymbol{c}^s = (\boldsymbol{\mathcal{S}}^s)^{-1}$. The complementary energy (6.8) related to $\widetilde{\boldsymbol{\sigma}}^-$ involves only the skins and is written as:

$$P^{*(\mathsf{e},\chi)}\left(\widetilde{\boldsymbol{\sigma}}^-\right) = -\frac{1}{2}\left\langle {}^t(\mathbf{e} + y_3\boldsymbol{\chi}) : \boldsymbol{c}^s : (\mathbf{e} + y_3\boldsymbol{\chi})\right\rangle_s \tag{6.25}$$

where

$$\langle f(\widetilde{\boldsymbol{y}})\rangle_s = \frac{1}{A_Y}\int_{Y^{s+}\bigcup Y^{s-}} f(\widetilde{\boldsymbol{y}})\, d\widetilde{\boldsymbol{y}} \tag{6.26}$$

is the surface average restricted to the skins.

For the upper bound, we choose the following kinematically compatible strain field:

$$\widetilde{\boldsymbol{\varepsilon}}^{+} = \begin{cases} \widetilde{\mathbf{e}} + x_3\widetilde{\boldsymbol{\chi}} - \frac{\mathcal{C}^s_{33\alpha\beta}}{\mathcal{C}^s_{3333}}(\mathsf{e}_{\alpha\beta} + x_3\chi_{\alpha\beta})\widetilde{\boldsymbol{e}}_3 \otimes \widetilde{\boldsymbol{e}}_3 & \text{on } Y^{s\pm} \\ \widetilde{\mathbf{e}} + x_3\widetilde{\boldsymbol{\chi}} & \text{on } Y^c \end{cases} \tag{6.27}$$

$\widetilde{\boldsymbol{\varepsilon}}^{+}$ is plane-strain in the core and is plane-stress in the skins (this is the purpose of the ε_{33} correction which takes into account Poisson's effect). Assuming plane-stress in the core would lead to discontinuous strain fields in the general case. The potential energy (6.9) related to $\widetilde{\boldsymbol{\varepsilon}}^{+}$ is written as:

$$P^{(\mathsf{e},\chi)}\left(\widetilde{\boldsymbol{\varepsilon}}^{+}\right) = \frac{1}{2}\left\langle {}^t(\mathbf{e} + y_3\boldsymbol{\chi}) : \boldsymbol{\mathcal{c}}^s : (\mathbf{e} + y_3\boldsymbol{\chi})\right\rangle_s + \frac{1}{2}\left\langle {}^t(\widetilde{\mathbf{e}} + y_3\widetilde{\boldsymbol{\chi}}) : \widetilde{\boldsymbol{\mathcal{C}}}^c : (\widetilde{\mathbf{e}} + y_3\widetilde{\boldsymbol{\chi}})\right\rangle_c \tag{6.28}$$

where

$$\langle f(\widetilde{\boldsymbol{y}})\rangle_c = \frac{1}{A_Y}\int_{Y^c} f(\widetilde{\boldsymbol{y}})\, d\widetilde{\boldsymbol{y}} \tag{6.29}$$

is the surface average restricted to the core.

6.2.2.2 Definition of the contrast assumption

Using variational principles derived in Section 6.1.2 leads directly to the bounds for Love-Kirchhoff stiffnesses:

$$w^{LK,s} < w^{LK} < w^{LK,s} + w^{LK,c} \tag{6.30}$$

where

$$w^{LK,s}(\mathbf{e},\boldsymbol{\chi}) = \frac{1}{2}\left\langle {}^t(\mathbf{e} + y_3\boldsymbol{\chi}) : \boldsymbol{\mathcal{c}}^s : (\mathbf{e} + y_3\boldsymbol{\chi})\right\rangle_s \tag{6.31}$$

is the Love-Kirchhoff energy density restricted to the skins and

$$w^{LK,c}(\mathbf{e},\boldsymbol{\chi}) = \frac{1}{2}\left\langle {}^t(\widetilde{\mathbf{e}} + y_3\widetilde{\boldsymbol{\chi}}) : \widetilde{\boldsymbol{\mathcal{C}}}^c : (\widetilde{\mathbf{e}} + y_3\widetilde{\boldsymbol{\chi}})\right\rangle_c \tag{6.32}$$

is the Love-Kirchhoff energy density restricted to the core.

The contrast assumption consists in neglecting the contribution of the core in the energy:

$$\forall(\mathbf{e},\boldsymbol{\chi}),\ w^{LK,c}(\mathbf{e},\boldsymbol{\chi}) \ll w^{LK,s}(\mathbf{e},\boldsymbol{\chi}) \tag{6.33}$$

which is equivalent to:

$$\forall\mathbf{e},\quad \mathbf{e} : \langle\boldsymbol{\mathcal{C}}^c\rangle_c : \mathbf{e} \ll 2t_s\, \mathbf{e} : \boldsymbol{\mathcal{c}}^s : \mathbf{e} \tag{6.34}$$

We draw the reader's attention to the fact that $\langle\boldsymbol{\mathcal{C}}^c\rangle_c$ is proportional to t_c in the general case. Thus the comparison between core and skin stiffnesses is weighted by their respective thicknesses. This

is *a priori* in contradiction with the thin skins assumption ($t_s \ll t_c$). Further discussion is given in Chapter 7. Here the contrast assumption is stated whatever the skins thickness is.

Under the contrast assumption the lower bound for Love-Kirchhoff stiffnesses becomes:

$$\boldsymbol{\mathcal{A}}^- = 2t_s \boldsymbol{\mathfrak{c}}^s, \quad \boldsymbol{\mathcal{B}}^- = \boldsymbol{0} \quad \boldsymbol{\mathcal{D}}^- = \frac{h^3 - t_c^3}{12} \boldsymbol{\mathfrak{c}}^s \tag{6.35}$$

and the stress distribution related to this lower bound is a good approximation for the actual stress generated by the bending moment:

$$\boldsymbol{\sigma}^{(\mathsf{M})-} = \begin{cases} \pm \frac{12 y_3}{h^3 - t_c^3} \mathbf{M} & \text{on } Y^{s\pm} \\ \mathbf{0} \quad \text{on } Y^c \end{cases} \qquad \text{and} \quad \sigma_{i3}^{(\mathsf{M})-} = 0 \quad \text{on } Y \tag{6.36}$$

With this lower bound, the core is completely negligible in the flexural behavior of the sandwich panel.

We have also the following upper bound for Love-Kirchhoff stiffnesses:

$$\boldsymbol{\mathcal{A}}^+ = 2t_s \boldsymbol{\mathfrak{c}}^s + \left\langle \boldsymbol{\mathcal{C}}^c \right\rangle_c, \quad \boldsymbol{\mathcal{B}}^+ = \left\langle x_3 \boldsymbol{\mathcal{C}}^c \right\rangle_c \quad \boldsymbol{\mathcal{D}}^+ = \frac{h^3 - t_c^3}{12} \boldsymbol{\mathfrak{c}}^s + \left\langle x_3^2 \boldsymbol{\mathcal{C}}^c \right\rangle_c \tag{6.37}$$

where the contribution of the core is related to the Voigt upper bound of 3D elasticity for the core.

6.2.3 Degeneration of the Bending-Gradient into a Reissner-Mindlin plate model

Under the contrast assumption, the volume loading definition (Equation (6.12)) applied to the stress distribution under contrast assumption (Equation (6.36)) becomes:

$$\boldsymbol{f}^{(\mathbb{R})-} = \begin{cases} \pm \frac{12 y_3}{h^3 - t_c^3} \boldsymbol{i} \therefore \mathbf{R} & \text{on } Y^{s\pm} \\ \mathbf{0} \quad \text{on } Y^c \end{cases} \qquad \text{and} \quad f_3^{(\mathbb{R})-} = 0 \quad \text{on } Y \tag{6.38}$$

where we identify directly shear forces: $\boldsymbol{Q} = \boldsymbol{i} \therefore \mathbf{R}$. Thus, as in the homogeneous case, with sandwich panels under contrast assumption the Bending-Gradient model is turned into a Reissner-Mindlin model.

Accordingly, we define the volume force related to shear forces as:

$$\boldsymbol{f}^{(Q)} = \begin{cases} \pm \frac{12 y_3}{h^3 - t_c^3} \boldsymbol{Q} & \text{on } Y^{s\pm} \\ \mathbf{0} \quad \text{on } Y^c \end{cases} \qquad \text{and} \quad f_3^{(Q)} = 0 \quad \text{on } Y \tag{6.39}$$

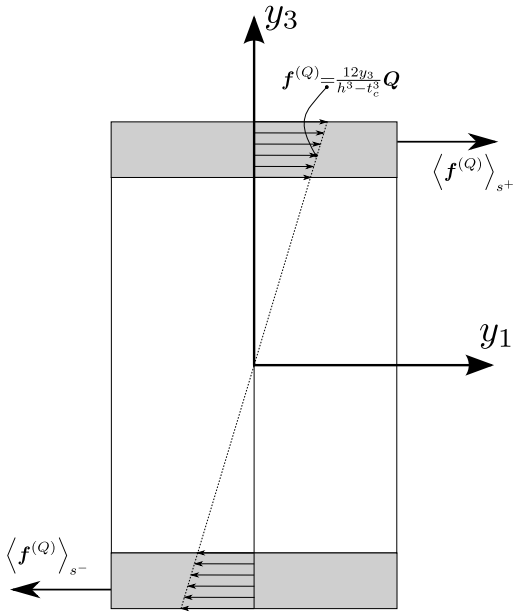

Figure 6.3: Shear force loading $\boldsymbol{f}^{(Q)-}$ for a sandwich panel with thin skins

Basically, it enforces volume forces in the skins so that the core is put into shearing exactly as suggested in sandwich theory (Figure 6.3).

Exactly as for $\mathtt{R}$, the 3D stress field $\widetilde{\boldsymbol{\sigma}}^{(Q)}$ related to shear forces is the stress field which equilibrates $\widetilde{\boldsymbol{f}}^{(Q)}$ and the Bending-Gradient auxiliary problem on the unit-cell is defined as:

$$\mathcal{P}^{(Q)} \begin{cases} \widetilde{\boldsymbol{\sigma}}^{(Q)} \cdot \widetilde{\boldsymbol{\nabla}} + \widetilde{\boldsymbol{f}}^{(Q)}(\widetilde{\boldsymbol{y}}) = 0 & \text{(6.40a)} \\ \widetilde{\boldsymbol{\sigma}}^{(Q)} = \widetilde{\boldsymbol{\mathcal{C}}}(\widetilde{\boldsymbol{y}}) : \left(\widetilde{\boldsymbol{\nabla}} \otimes^s \widetilde{\boldsymbol{u}}^{(Q)} \right) & \text{(6.40b)} \\ \widetilde{\boldsymbol{\sigma}}^{(Q)} \cdot \widetilde{\boldsymbol{e}}_3 = 0 \text{ on free faces } \partial Y_3^{\pm} & \text{(6.40c)} \\ \widetilde{\boldsymbol{\sigma}}^{(Q)} \cdot \widetilde{\boldsymbol{n}} \text{ skew-periodic on lateral boundaries } \partial Y_l & \text{(6.40d)} \\ \widetilde{\boldsymbol{u}}^{(Q)}(y_1, y_2, y_3) \quad (y_1, y_2)\text{-periodic on lateral boundaries } \partial Y_l & \text{(6.40e)} \end{cases}$$

This problem is exactly Cecchi and Sab (2007) auxiliary problem for deriving shear forces stiffness without needing the assumption of cylindrical bending.

Again, solving $\mathcal{P}^{(Q)}$ leads to the localization stress field $s_{ij\alpha}^{(Q)}(\widetilde{\boldsymbol{y}})$ associated to shear forces, obtained by linear combination:

$$\widetilde{\boldsymbol{\sigma}}^{(Q)} = \widetilde{\boldsymbol{s}}^{(Q)}(\widetilde{\boldsymbol{y}}) \cdot \boldsymbol{Q} \tag{6.41}$$

It is then possible to identify the shear forces compliance tensor with:

$$\mathsf{f} = \left\langle {}^t\left(\widetilde{\boldsymbol{s}}^{(Q)} \right) : \widetilde{\boldsymbol{\mathcal{S}}}(\widetilde{\boldsymbol{y}}) : \widetilde{\boldsymbol{s}}^{(Q)} \right\rangle \tag{6.42}$$

$\mathbf{f}$ is the second order tensor such as: $\boldsymbol{\gamma} = \mathbf{f} \cdot \boldsymbol{Q}$, where $\boldsymbol{\gamma}$ is the conventional Reissner-Mindlin shear strain (cf. Chapter 1). We recall that the shear forces stiffness tensor is $\mathbf{F} = \mathbf{f}^{-1}$ and $\boldsymbol{Q} = \mathbf{F} \cdot \boldsymbol{\gamma}$.

The variational principles related to $\mathcal{P}^{(Q)}$ are strictly identical to those introduced in Frame 6.2 replacing "$\mathbb{R}$" by "Q" so they are not recalled here.

Finally, the contrast assumption enable a direct derivation of shear forces stiffness with $\widetilde{\boldsymbol{f}}^{(Q)}$ loading and do not request the derivation of Love-Kirchhoff localization fields.

6.2.4 Bounds for sandwich panels shear forces stiffness

In Chapter 3, bounds for the shear forces stiffness of sandwich panels including the chevron pattern were derived using the method from Kelsey et al. (1958). However, no real justification of these bounds is provided. Moreover, when the skins are thick, their contribution to the shear forces stiffness is controversial. Since the actual shear forces loading is known for a sandwich panel, we apply variational principles to the Bending-Gradient auxiliary problem $\mathcal{P}^{(Q)}$ for deriving these bounds.

6.2.4.1 Voigt and Reuss bounds

Assuming uniform displacement in the skins and uniform shear strain in the core enables the derivation of a Voigt type upper bound for sandwich panels shear forces stiffness. Computation details are given in Appendix A.2. Finally, we have:

$$\forall \boldsymbol{\gamma}, \quad {}^t\boldsymbol{\gamma} \cdot \mathbf{F} \cdot \boldsymbol{\gamma} < {}^t\boldsymbol{\gamma} \cdot \frac{\langle \mathbf{C}^c \rangle_c}{k_s^2} \cdot \boldsymbol{\gamma} \tag{6.43}$$

where $\mathbf{F}$ is the actual shear forces stiffness, $\mathsf{C}^c_{\alpha\beta} = \mathcal{C}^c_{\alpha 3 \beta 3}$ is the transverse shear part of the 3D stiffness tensor and $k_s = \frac{3}{2}\frac{t_c(h^2 - t_c^2)}{h^3 - t_c^3} \simeq 1 - \frac{t_s}{t_c}$ is the correction suggested by Kelsey et al. (1958) related to the relative thickness of the skins.

Here the effective transverse shear stiffness for the core appears as: $\mathsf{C}^{\text{eff}}_{\alpha\beta} = \langle \mathbf{C}^c \rangle_c / t_c$. It is the Voigt upper bound for transverse shear stiffness in 3D elasticity. Thus, we define the Voigt upper bound for shear forces stiffness as: $\mathbf{F}^{\text{V}} = \frac{\langle \mathbf{C}^c \rangle_c}{k_s^2}$.

The correction affects Voigt upper bound with thin skins proportionally to $1 + 2t_s/t_c$ which might not be negligible in standard sandwich panels applications. For instance, with the sandwich panel of Figure 2.10, $t_s \simeq 1mm$ and $t_s \simeq 1,6cm$ lead to a correction of 12.5%.

This correction does not depend on the skins stiffness. It is not surprising since the trial strain field assumes no strain in the skins. The correction is simply related to a geometric effect: the thicker the skins are, the further from the midplane the resultant of $\boldsymbol{f}^{(Q)}$ in the skin is. Thus the lever effect of the resultant of $\boldsymbol{f}^{(Q)}$ in the skin is greater (Figure 6.3). Finally, using directly FOSDT leads to

a correction which depends on the skins stiffness. The present result confirms that such approach might overestimate the Reissner-Mindlin stiffness of the sandwich panel.

It is also possible to derive a Reuss lower bound, assuming *ad hoc* compatible stress distribution in the skins and a uniform shear stress in the core. Computation details are given in Appendix A.2. This leads to the following Reuss bound:

$$\forall \boldsymbol{\gamma}, \quad {}^t\boldsymbol{\gamma} \cdot \frac{1}{k_s^2} \left(\frac{\langle \mathbf{S}^c \rangle_c}{t_c^2} + \frac{t_s \left(6t_s^2 - 15t_s h + 10h^2\right)}{15t_c^2 (h - t_s)^2} \mathbf{S}^s \right)^{-1} \cdot \boldsymbol{\gamma} < {}^t\boldsymbol{\gamma} \cdot \mathbf{F} \cdot \boldsymbol{\gamma} \tag{6.44}$$

where $\mathsf{S}^c_{\alpha\beta} = 4\mathcal{S}^c_{\alpha 3 \beta 3}$ and $\mathsf{S}^s_{\alpha\beta} = 4\mathcal{S}^s_{\alpha 3 \beta 3}$ are the transverse shear parts of the 3D compliances.

There is no *a priori* reason for neglecting the skins contribution since the contrast hypothesis involves only the plane part of 3D stiffnesses (Section 6.2.1). For instance with carbon fiber reinforced composite skins, the transverse shear stiffness of the skins is quite low. Yet, if the skins are thin and their constitutive material is isotropic, their contribution is negligible.

Again, in the present case, the effective transverse shear stiffness appears as: $\mathsf{C}^{\text{eff}}_{\alpha\beta} = \left(\langle \mathbf{S}^c \rangle_c / t_c\right)^{-1}$. It is the Reuss lower bound for transverse shear stiffness in 3D elasticity. Thus we define the Reuss lower bound for shear forces stiffness as: $\mathbf{F}^{\text{R}} = \frac{t_c^2}{k_s^2} \langle \mathbf{S}^c \rangle_c^{-1}$.

Since most of cores used in applications are porous, this bound is often null. In order to overcome this difficulty, Kelsey et al. (1958) suggested improved bounds for sandwich panels.

6.2.4.2 The bounds from Kelsey et al.

The approach from Kelsey et al. (1958) is detailed in Chapter 3. Let us recall that for the upper bound, a unit displacement is enforced only on the core, replacing the skins action on it (the unit displacement method). For the lower bound, it is an arbitrary stress distribution which is applied on the core (unit force method). It is possible to give partial justification to these bounds while separating the Bending-Gradient auxiliary problem $\mathcal{P}^{(Q)}$ in three parts, a part dedicated to the core and two parts dedicated to the skins. Then, the solution in the skins is taken similar to the one used for Voigt and Reuss bounds and the problem for the core is exactly the one suggested by Kelsey et al. (1958).

For the upper bound, we still assume a uniform displacement in the the skins: $\widetilde{\boldsymbol{u}}^{K+} = \frac{t_c}{2}\widetilde{\boldsymbol{\gamma}}$. Enforcing displacements continuity at the skin/core interface $\partial Y^{\pm}_{int}$ leads to the following auxiliary

problem in the core:

$$\mathcal{P}^{K+}\begin{cases}\widetilde{\boldsymbol{\sigma}}^{K+}\cdot\widetilde{\boldsymbol{\nabla}}=0 & \text{(6.45a)}\\ \widetilde{\boldsymbol{\sigma}}^{K+}=\widetilde{\boldsymbol{\mathcal{C}}}\left(\widetilde{\boldsymbol{y}}\right):\left(\widetilde{\boldsymbol{\nabla}}\otimes^{s}\widetilde{\boldsymbol{u}}^{K+}\right) & \text{(6.45b)}\\ \widetilde{\boldsymbol{u}}^{K+}=\pm\dfrac{t_c}{2}\widetilde{\boldsymbol{\gamma}}\text{ on interface faces }\partial Y_{int}^{\pm} & \text{(6.45c)}\\ \widetilde{\boldsymbol{\sigma}}^{K+}\cdot\widetilde{\boldsymbol{n}}\text{ skew-periodic on }\partial Y_l^c & \text{(6.45d)}\\ \widetilde{\boldsymbol{u}}^{K+}(y_1,y_2,y_3)\quad (y_1,y_2)\text{-periodic on }\partial Y_l^c & \text{(6.45e)}\end{cases}$$

which is exactly the unit displacement method suggested by Kelsey et al. (1958). The application of variational principles for the Bending-Gradient auxiliary problem $\mathcal{P}^{(Q)}$, detailled in Appendix A.2, leads to the following upper bound:

$$\forall\boldsymbol{\gamma},\quad {}^{t}\boldsymbol{\gamma}\cdot\mathbf{F}\cdot\boldsymbol{\gamma}<{}^{t}\boldsymbol{\gamma}\cdot\mathbf{F}^{K+}\cdot\boldsymbol{\gamma} \tag{6.46}$$

where $\mathbf{F}^{K+}$ is the original upper bound from Kelsey et al. (1958).

The lower bound raises more difficulties. Separating the Bending-Gradient auxiliary problem into three parts brings out the interface stress $\widetilde{\boldsymbol{\sigma}}^{(Q)}\left(y_1,y_2,\pm t_c/2\right)\cdot(\pm\widetilde{\boldsymbol{e}}_3)$ located on $\partial Y_{int}^{\pm}$. This stress interface must respect macroscopic equilibrium for each part:

$$\frac{1}{A_Y}\int_{\partial Y_{int}^{\pm}}\widetilde{\boldsymbol{\sigma}}^{(Q)}\left(y_1,y_2,\pm t_c/2\right)\cdot\widetilde{\boldsymbol{e}}_3dy_1dy_2=\pm\frac{k_s}{h}\widetilde{\boldsymbol{Q}} \tag{6.47}$$

The derivation of the lower bound consists in choosing *a priori* this interfacial stress distribution. Let us introduce such arbitrary surface traction $\widetilde{\boldsymbol{T}}^{d\pm}(y_1,y_2)$ fullfilling:

$$\frac{1}{A_Y}\int_{\partial Y_{int}^{\pm}}\widetilde{\boldsymbol{T}}^{d\pm}d\boldsymbol{y}=\frac{k_s}{h}\widetilde{\boldsymbol{Q}} \tag{6.48}$$

Given $\widetilde{\boldsymbol{T}}^{d\pm}(y_1,y_2)$, the problem in the core is stated as:

$$\mathcal{P}^{K-}\begin{cases}\widetilde{\boldsymbol{\sigma}}^{K-}\cdot\widetilde{\boldsymbol{\nabla}}=0 & \text{(6.49a)}\\ \widetilde{\boldsymbol{\sigma}}^{K-}=\widetilde{\boldsymbol{\mathcal{C}}}\left(\widetilde{\boldsymbol{y}}\right):\left(\widetilde{\boldsymbol{\nabla}}\otimes^{s}\widetilde{\boldsymbol{u}}^{K-}\right) & \text{(6.49b)}\\ \widetilde{\boldsymbol{\sigma}}^{K-}\cdot\widetilde{\boldsymbol{e}}_3=\pm\widetilde{\boldsymbol{T}}^{d\pm},\text{ on interface }\partial Y_{int}^{\pm} & \text{(6.49c)}\\ \widetilde{\boldsymbol{\sigma}}^{K-}\cdot\widetilde{\boldsymbol{n}}\text{ skew-periodic on lateral boundaries }\partial Y_l^c & \text{(6.49d)}\\ \widetilde{\boldsymbol{u}}^{K-}(y_1,y_2,y_3)\quad (y_1,y_2)\text{-periodic on lateral boundaries }\partial Y_l^c & \text{(6.49e)}\end{cases}$$

When $k_s=1$, this problem is exactly the one suggested by Kelsey et al. (1958) for deriving the lower bound.

Then, the problems in the skins are stated as:

$$\mathcal{P}^{K-,s\pm}\begin{cases} \widetilde{\boldsymbol{\sigma}}^{K-}\cdot\widetilde{\boldsymbol{\nabla}}\pm\dfrac{\boldsymbol{Q}}{t^s h}=0 & (6.50a)\\ \widetilde{\boldsymbol{\sigma}}^{K-}=\widetilde{\boldsymbol{\mathcal{C}}}\left(\widetilde{\boldsymbol{y}}\right):\left(\widetilde{\boldsymbol{\nabla}}\otimes^s\widetilde{\boldsymbol{u}}^{K-}\right) & (6.50b)\\ \widetilde{\boldsymbol{\sigma}}^{K-}\cdot\widetilde{\boldsymbol{e}}_3=\pm\widetilde{\boldsymbol{T}}^{d\pm},\ \text{on interface } \partial Y^{\pm}_{int} & (6.50c)\\ \widetilde{\boldsymbol{\sigma}}^{K-}\cdot\widetilde{\boldsymbol{e}}_3=\widetilde{\boldsymbol{0}}\ \text{on free face } \partial Y^{\pm}_{3} & (6.50d)\\ \widetilde{\boldsymbol{\sigma}}^{K-}\cdot\widetilde{\boldsymbol{n}}\ \text{skew-periodic on lateral boundaries } \partial Y^{s}_{l} & (6.50e)\\ \widetilde{\boldsymbol{u}}^{K-}(y_1,y_2,y_3)\quad (y_1,y_2)\text{-periodic on lateral boundaries } \partial Y^{s}_{l} & (6.50f)\end{cases}$$

The combination of variational principles related to the three problems is detailed in Appendix A.2. This leads to the following lower bound for shear forces stiffness:

$$\forall\boldsymbol{\gamma},\quad {}^t\boldsymbol{\gamma}\cdot\left(\mathbf{f}^{K-}+\mathbf{f}^{K-,s+}+\mathbf{f}^{K-,s-}\right)^{-1}\cdot\boldsymbol{\gamma}<{}^t\boldsymbol{\gamma}\cdot\mathbf{F}\cdot\boldsymbol{\gamma} \tag{6.51}$$

where $\mathbf{f}^{K-}$ is the transverse shear compliance of the lower bound from Kelsey et al. (1958), and $\mathbf{f}^{K-,s\pm}$ are the contribution of the skins.

Demonstrating that the stress energy in the skins is negligible (even with thin skins) is not straightforward and might be wrong in the general case. Yet this seems to be a very common implicit assumption. At best, one can hope that the skins contribution is of the same amplitude as the one in the case of the Reuss lower bound (Equation (6.44)).

6.2.5 Conclusion

When applying the Love-Kirchhoff auxiliary problem to a sandwich panel we brought out the contrast assumption (Equation (6.34)). Then, we demonstrated that under this assumption, the shear constitutive equation for a sandwich panel is turned into a Reissner-Mindlin model as it is the case for homogeneous plates. Moreover, we identified the loading related to shear forces as a volume force distributed in the skins. This loading confirms the common intuition that the core is put into shear by the skins and enables the direct derivation of shear forces stiffness for a sandwich panel. Finally, we provided justification for bounds which are commonly used in sandwich panel design, taking into account the thickness of the skins.

As allready mentioned, these bounds do not take into account a possible interaction between the skins and the core. Moreover, we demonstrated in Chapter 3 that for the chevron pattern, they are not sufficient for estimating accurately the shear forces stiffness. Hence, in the following chapter, the Bending-Gradient homogenization scheme is applied to a sandwich panel including the chevron pattern so that a better understanding of the gap between bounds is provided.

CHAPTER

7

Application to sandwich panels including chevron pattern

7.1 Introduction

In Chapter 3, the bounds from Kelsey et al. (1958) for a sandwich panel including the chevron pattern were derived. The main conclusion was that for both analytical and finite element approaches, the bounds remained very loose. The interpretation suggested is that the interaction between the skins and the core is not taken into account. Moreover, the Bending-Gradient homogenization scheme provides a means to estimate shear forces stiffness of the whole sandwich panel unit-cell including the skins. Thus, in this chapter we apply the Bending-Gradient homogenization scheme to a sandwich panel including the chevron pattern.

First, we identify relevant parameters involved in the design of sandwich panels and corresponding assumptions. Then, we apply the homogenization scheme. This enables the specification of the assumptions validity range. It confirms also the bounds from Kelsey et al. (1958) including the thick skins correction and provides explanation of the gap between bounds. Finally, the homogenization scheme itself is validated trough comparison with full 3D simulation.

7.2 Relevant parameters for the sandwich panel including the chevron pattern

Here we consider a sandwich panel fully made of aluminum sheets with $E_m = 73\,GPa$ and $\nu_m = 0.3$ (related to the stiffness tensor $\widetilde{\mathcal{C}}^m$). Assuming the same constitutive material for the core and the skins simplifies the presentation. The investigated geometric parameters are again similar to Nguyen et al. (2005a). $a_0 = 30\,mm,\ t_c = 28.5\,mm$, $\delta = 72°$, $\zeta = 34°$ are fixed parameters in the present study. Varying $b_0 \in [20\,mm, 60\,mm]$ as in Chapter 3 enables the investigation of the facets shape ratio. Figure 7.1 shows configurations without skins for several shape ratios, a_0/b_0. There remains to choose t_f the facets thickness and t_s the skins thickness.

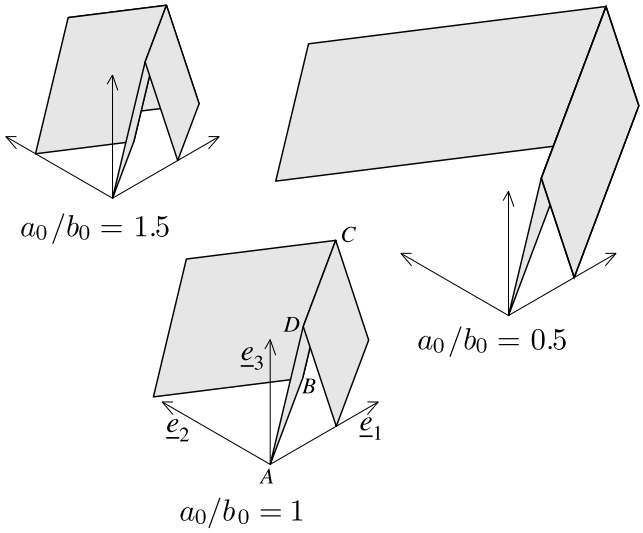

Figure 7.1: Chevron pattern investigated configurations

Let us state the thin skins assumption and the contrast assumption in the present case. First, the thin skins assumption is direct: $t_s \ll h$. Second, since skins and core are made of the same constitutive material, the contrast assumption (Equation (6.34)) becomes:

$$\forall \mathbf{e}, \qquad \mathbf{e} : t_c \rho \boldsymbol{\mathcal{C}}^m : \mathbf{e} \ll 2 t_s \, \mathbf{e} : \boldsymbol{c}^m : \mathbf{e} \tag{7.1}$$

where $\boldsymbol{c}^m$ is the constitutive material plane-stress stiffness tensor and ρ its volume fraction in the core:

$$\rho = \frac{t_f}{t_c \sin\zeta \cos\delta} \simeq 6 \frac{t_f}{t_c} \tag{7.2}$$

Provided the Poisson's ratio is not too close to 0.5 (detailed justification is given in Appendix A.4), the contrast assumption becomes:

$$3 t_f \ll t_s \tag{7.3}$$

and we suggest to call t_s/t_f the contrast ratio.

Combining both assumptions leads the following hierarchy between thicknesses:

$$3 t_f \ll t_s \ll h \tag{7.4}$$

Actually, fullfilling *a priori* this double scale separation is too much restrictive for conventional sandwich panels applications. For instance, an acceptable choice would be $h = 34.5\,mm$, $t_s = 3\,mm$ and $t_f = 0.1\,mm$. However, this would lead to up to 20% error, given the error estimates introduced in Chapter 6 for the Love-Kirchhoff stiffnesses and for the shear forces stiffness. Thus, in this work, we suggest to perform all computations as if there were neither contrast assumption nor

thin skins assumption and implement all the Bending-Gradient homogenization scheme. Once the results are obtained, it will be possible to precisely estimate the validity range of the assumptions.

Finally we suggest the following range for the facet thickness: $t_f \in [0.02\,mm, 0.5\,mm]$ and for the skin thickness: $t_f \in [0.1\,mm, 5\,mm]$. The facet thickness range is a bit wider than producible thicknesses and the skins thickness range is rather wide. This leads to a very wide range for the contrast ratio and will provide a comprehensive view of the influence of these parameters on the sandwich panel overall behavior. Let us just recall the reader that having $t_s/t_f > 100$ is not interesting in sandwich panel design since it leads inevitably to a failure of the core under shear forces. On the other side, having $t_s/t_f < 1$ leads to systematic wrinkling of the skins and is neither interesting in sandwich panel design.

7.3 Implementation

In this section, the most important points concerning the numerical implementation are given.

7.3.1 Modeling the unit-cell with shell elements

Since the facets constituting the unit-cell are slender, it is more relevant to use shell finite elements than 3D finite elements for implementing the auxiliary problems introduced in Chapter 6. This necessitates some adaptions to shell models. A fully detailed justification is provided in Appendix A.3 as well as some technical implementation details. We just recall here that displacement field $\widetilde{\boldsymbol{u}}$ at nodes is replaced by a plate displacement field $\widetilde{\boldsymbol{U}}$ *and* a plate rotation field $\widetilde{\boldsymbol{\theta}}$. Moreover, stress field $\widetilde{\boldsymbol{\sigma}}$ in the elements is replaced by plate generalized stress fields $(\mathbf{n}, \mathbf{m}, \boldsymbol{q})$ expressed in the facets' local reference frame. The facets' local reference frame and related transformation formulas were given in details in Section 3.2.

We choose $S4R$ quadrangle linear shell elements with reduced integration in ABAQUS. Since the facets are homogeneous, using Reissner-Mindlin elements is consistent with the results on the transverse shear behavior of laminates derived in Chapter 5. A convergence study, not detailed here, was performed and led to a mesh with ten elements per edge. Linear elements with reduced integration were used for implementation convenience. With such an element, there is only one value per element for stress and strain fields (otherwise there are several integrations points). Moreover there is no weighting related to elements shape functions when applying concentrated loads at nodes. Obviously, it is possible to extend the method to any kind of plate elements.

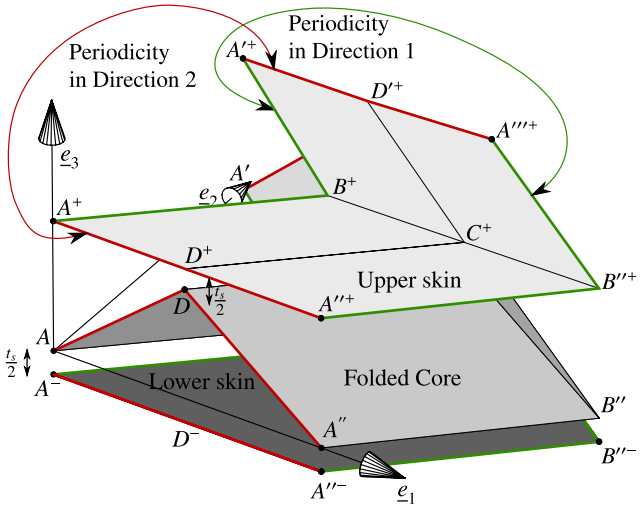

Figure 7.2: The chevron pattern sandwich panel unit-cell and periodicity conditions

7.3.2 The detailed geometry of the unit-cell

The geometry of the core itself has been fully detailed in Section 3.2. It comprises four tilted parallelogram-shaped faces which vertices are $A, B, C, D, A', D', A'', B''$ and A'''. Moreover, skins are glued or welded along D, C, D' (upper skin) and A, B, A' (lower skin). In order to take into account the skins thickness, the mid-plane of the skins is set with a $t_s/2$ offset (Figure 7.2). The upper and lower skins vertices are denoted with $A^{\pm}, B^{\pm}, C^{\pm}, D^{\pm}, A'^{\pm}, D'^{\pm}, A''^{\pm}, B''^{\pm}$ and $A'''^{\pm}$. Their coordinates are detailed in Table 7.1. In order to bind the core to teh skins, a rigid motion is

Vertex	A	B	C	D	A'	D'	A''	B''	A'''
x_1	0	v	$a+v$	a	0	a	$2a$	$2a+v$	$2a$
x_2	0	s	s	0	$2s$	$2s$	0	s	$2s$
x_3	0	0	t_c	t_c	0	t_c	0	0	0
Vertex	A^-	B^-	C^-	D^-	A'^-	D'^-	A''^-	B''^-	A'''^-
x_1	0	v	$a+v$	a	0	a	$2a$	$2a+v$	$2a$
x_2	0	s	s	0	$2s$	$2s$	0	s	$2s$
x_3	$-\frac{t_s}{2}$	$-\frac{t_s}{2}$	$-\frac{t_s}{2}$	$-\frac{t_s}{2}$	$-\frac{t_s}{2}$	$-\frac{t_s}{2}$	$-\frac{t_s}{2}$	$-\frac{t_s}{2}$	$-\frac{t_s}{2}$
Vertex	A^+	B^+	C^+	D^+	A'^+	D'^+	A''^+	B''^+	A'''^+
x_1	0	v	$a+v$	a	0	a	$2a$	$2a+v$	$2a$
x_2	0	s	s	0	$2s$	$2s$	0	s	$2s$
x_3	$t_c+\frac{t_s}{2}$	$t_c+\frac{t_s}{2}$	$t_c+\frac{t_s}{2}$	$t_c+\frac{t_s}{2}$	$t_c+\frac{t_s}{2}$	$t_c+\frac{t_s}{2}$	$t_c+\frac{t_s}{2}$	$t_c+\frac{t_s}{2}$	$t_c+\frac{t_s}{2}$

Table 7.1: Vertices' coordinates

$\widetilde{\mathsf{P}}$	N_{11}	N_{22}	N_{12}	M_{11}	M_{22}	M_{12}	R_{111}	R_{221}	R_{121}	R_{112}	R_{222}	R_{122}
$\mathcal{S}$ $\left(\begin{smallmatrix}-1&0&0\\0&-1&0\\0&0&1\end{smallmatrix}\right)$	+	+	+	+	+	+	−	−	−	−	−	−
$\mathcal{R}$ $\left(\begin{smallmatrix}-1&0&0\\0&-1&0\\0&0&-1\end{smallmatrix}\right)$	+	+	+	−	−	−	+	+	+	+	+	+
$\mathcal{N}$ $\left(\begin{smallmatrix}1&0&0\\0&-1&0\\0&0&1\end{smallmatrix}\right)$	+	+	−	+	+	−	+	+	−	−	−	+

Table 7.2: $\epsilon^{\widetilde{\mathsf{P}}}$ and loads for the chevron pattern symmetries

enforced between skins and core along D, C, D' for the upper skin:

$$\begin{cases} \widetilde{\boldsymbol{U}}^{DCD'} = \widetilde{\boldsymbol{U}}^{D^+C^+D'^+} + \widetilde{\boldsymbol{\theta}}^{D^+C^+D'^+} \times \frac{t_s}{2}\widetilde{\boldsymbol{e}}_3 \\ \widetilde{\boldsymbol{\theta}}^{DCD'} = \widetilde{\boldsymbol{\theta}}^{D^+C^+D'^+} \end{cases}$$

and along A, B, A' for the lower skin:

$$\begin{cases} \widetilde{\boldsymbol{U}}^{ABA'} = \widetilde{\boldsymbol{U}}^{A^+B^+A'^-} + \widetilde{\boldsymbol{\theta}}^{A^+B^+A'^-} \times \left(-\frac{t_s}{2}\widetilde{\boldsymbol{e}}_3\right) \\ \widetilde{\boldsymbol{\theta}}^{ABA'} = \widetilde{\boldsymbol{\theta}}^{A^+B^+A'^-} \end{cases}$$

Finally, periodicity conditions must be applied: $A^{\pm}D^{\pm}A''^{\pm}$ matches $A'^{\pm}D'^{\pm}A'''^{\pm}$, $A^{\pm}B^{\pm}A'^{\pm}$ matches $A''^{\pm}B''^{\pm}A'''^{\pm}$ and ADA'' matches $A'D'A'''$ (Figure 7.2).

The influence of the symmetries of the plate material configuration on uncouplings was provided in details in Section 4.A.1 for laminates. These results are easily extended to periodic plates when considering the symmetries of the whole unit-cell of the periodic plate. The chevron pattern unit-cell including skins follows exactly the same symmetries as detailed for the chevron pattern alone in Chapter 3. The correspondning uncouplings are recalled in Table 7.2. Finally, under the contrast assumption there are only height Love-Kirchhoff moduli and two Reissner-Mindlin transverse shear moduli to derive (orthotropic symmetry).

7.4 Results

7.4.1 Love-Kirchhoff homogenization

7.4.1.1 Unit load fields

In Figure 7.3 and Figure 7.4 are plotted the deformed unit-cell under Love-Kirchhoff unit strain loads. The facets thickness is $0.1\,mm$, the skins thickness is $1\,mm$ and the shape ratio is, $a_0/b_0 = 1.2$. The original geometry is given by a wireframe and the contour plot displays Von Mises

stress. One can clearly identify the average strains enforced on the overall unit-cell similar to those described in Figure 3.4. When computing the Love-Kirchhoff stiffnesses, expected uncouplings were obtained.

The main observation is that for both membrane and curvature loadings, most of the stress is concentrated in the skins and the core is almost not stressed.

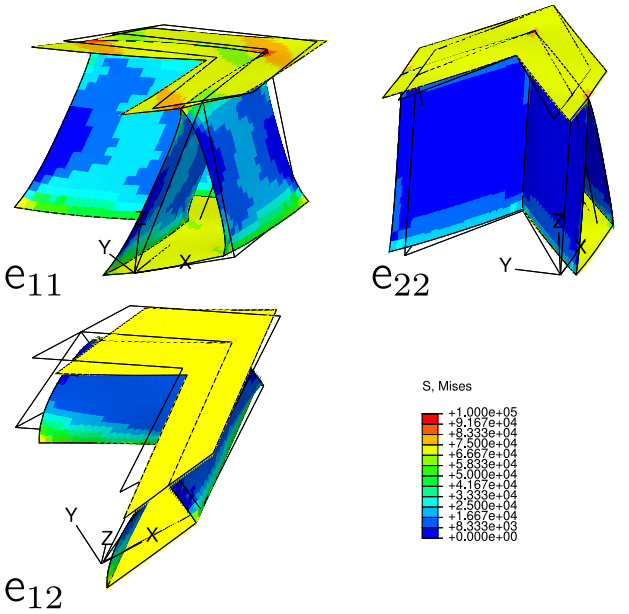

Figure 7.3: Deformed unit-cell under Membrane **e** loading ($a_0/b_0 = 1.2$, $t_f = 0.1\,mm$, $t_s = 1\,mm$). The contour plot displays Von Mises stress.

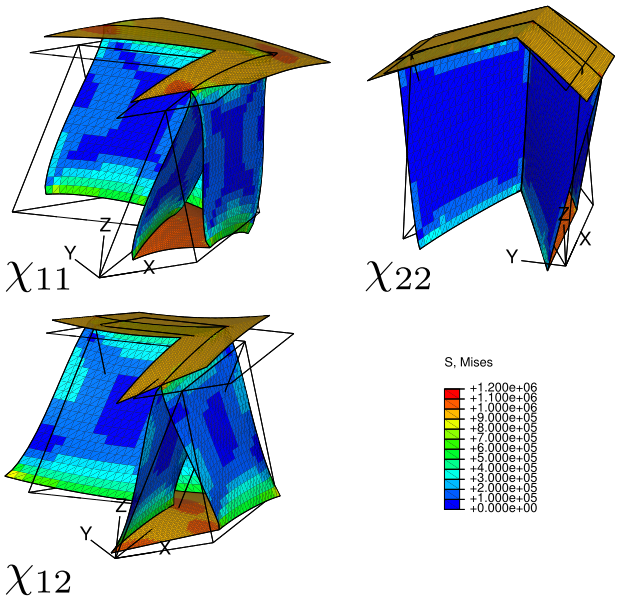

Figure 7.4: Deformed unit-cell under Curvature $\boldsymbol{\chi}$ loading ($a_0/b_0 = 1.2$, $t_f = 0.1\,mm$, $t_s = 1\,mm$). The contour plot displays Von Mises stress.

7.4.1.2 Validity range of the contrast assumption

This remark is confirmed when deriving Love-Kirchhoff stiffness moduli.

In Figure 7.5 is plotted the bending stiffness in Direction 1, $\mathcal{D}_{1111}$ versus the contrast ratio t_s/t_f for several facets thicknesses. It is normalized with the lower bound $\mathcal{D}^-_{1111}$ (Equation (6.35) derived in Section 6.2.2.2. The upper bound has also been plotted.

Clearly, the larger is t_s/t_f, the smaller is the error as expected with the contrast assumption. Moreover, the lower bound is a much better approximation than the upper bound, even for low contrasts. This has been observed whatever the Love-Kirchhoff moduli is. Here is a plausible explanation: contrary to homogeneous sandwich panels, the core alone is not a structure: it has barely no membrane stiffness and a small bending stiffness. Thus, its contribution in the sandwich panel remains very weak. However, this observation might not hold with other core geometries (honeycomb for instance).

Finally it is possible to specify the validity range of the contrast assumption. Based on Figure 7.5 we suggest $t_s > 5t_f$ which is much less restrictive than expected in previous discussion (Section 7.2).

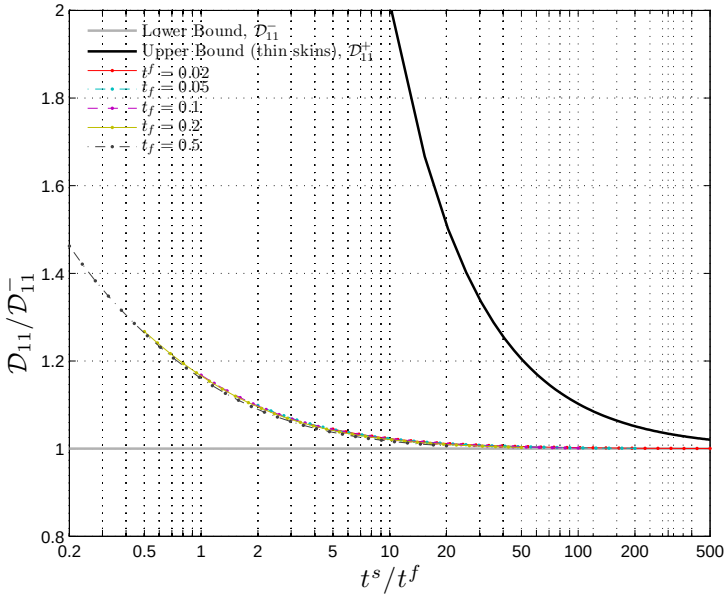

Figure 7.5: Normalized Bending stiffness $\mathcal{D}_{1111}$ versus t_f/t_s

7.4.2 Reissner-Mindlin homogenization

7.4.2.1 Unit load fields

Since the validity range of the contrast assumption is broader than expected, one can expect that the Bending-Gradient model is turned into a Reissner-Mindlin model even for rather thin skins. This is quantified when looking at the distance between the Bending-Gradient model and the Reissner-Mindlin model (cf. Section 4.6.2). This distance is plotted in Figure 7.6 versus the contrast ratio for several facets' thickness. For $t_s = 2t_f$ the distance is already smaller than 2%. It is globally decreasing with the contrast ratio and when $t_s/t_f < 3$, the distance between models seems to depend only on the contrast ratio and not on the facets' relative thickness t_f/f. For contrast ratios greater than 10, the distance is very small (2‰) and becomes steady with respect to the contrast ratio. No satisfying explanation for this observation was found.

Since for all configurations the distance is very small, results are focused only on the Reissner-Mindlin part of the Bending-Gradient simulations in the following.

On Figure 7.7 are plotted the deformed unit-cell under shear force unit loads. The overall deformation of the unit-cell looks like uniform shear strain as expected with sandwich panels. The

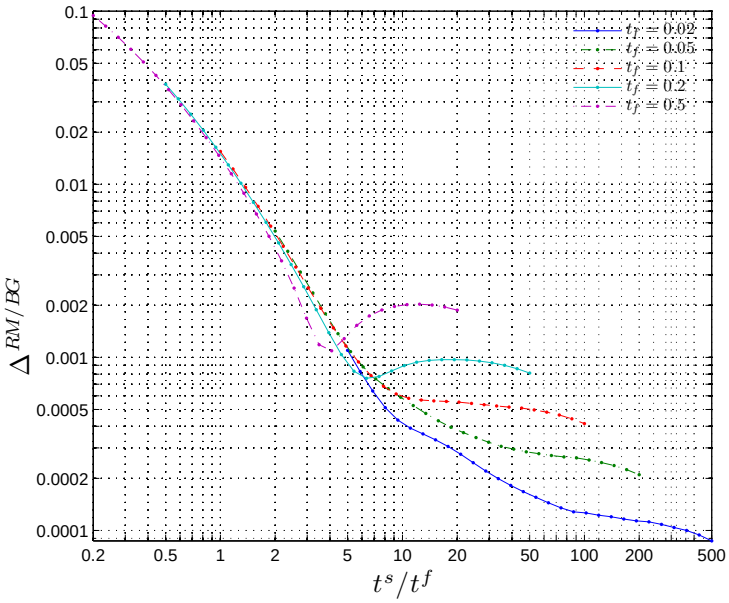

Figure 7.6: Distance between Reissner-Mindlin and Bending-Gradient plate model with respect to the contrast ratio

core is more stressed than the skins and the fields are similar to those derived in Chapter 3. In Direction 1, the main stress is still $\mathsf{n}_{11}^{(Q)}$ (σ_{uu} in Chapter 3) and in Direction 2, it is $\mathsf{n}_{12}^{(Q)}$ (σ_{uv}).

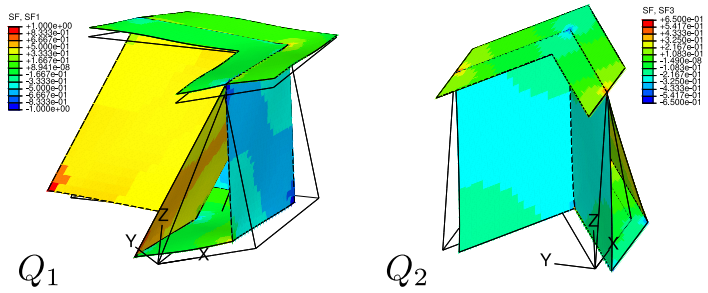

Figure 7.7: Deformed unit-cell under shear forces loading ($a_0/b_0 = 1.2$, $t_f = 0.1\,mm$, $t_s = 1\,mm$). The contour plot displays local membrane stress $\mathsf{n}_{11}^{(Q)}$ for Q_1 loading and $\mathsf{n}_{12}^{(Q)}$ for Q_2 loading

Finally, whereas in Direction 2 the skins remain planar under Q_2 loading, in Direction 1 the skins are distorted (Figure 7.8). The out-of-plane displacement of the skin is about 1/3 of the skins relative displacement. This explains the gap between bounds in this direction.

7.4.2.2 Shear forces stiffness

In Figures 7.9 and 7.10, the shear forces stiffness is plotted in each direction versus the shape ratio a_0/b_0. As in Chapter 3, it is normalized with Voigt upper bound. Here we used the corrected bound $\mathsf{F}^{\mathrm{V}}_{\alpha\beta} = \rho G_m t_c/k_s^2$ since skins might be thick. The correction is very strong: it is up to 40%

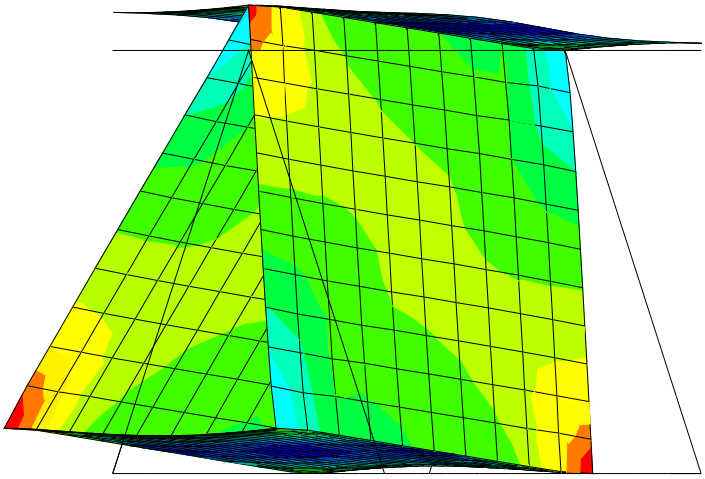

Figure 7.8: Deformed unit-cell under Q_1 loading ($a_0/b_0 = 1.2$, $t_f = 0.1\,mm$, $t_s = 1\,mm$). View from $\widetilde{e}_2$

when $t_s = 5\,mm$. The bounds from Kelsey et al. (1958) derived with finite elements in Chapter 3 are recalled.

The facet thickness is set to $t_f = 0.1\,mm$ and several skins thicknesses are investigated. The upper bound from Kelsey et al. (1958) is always respected whereas the lower bound is not when the contrast ratio is rather low. As already pointed out with the bounds in Chapter 3, the shape ratio has a strong influence on the actual shear forces stiffness in both directions.

It is noticeable that the stiffnesses derived with the Bending-Gradient homogenization scheme cover all the range between the bounds from Kelsey et al. (1958) when varying the skins thickness. Thus we conclude that these bounds cannot be improved without a detailed analysis of the interaction between the skins and the core.

Finally, in both directions, the thicker the skins are, the closer to the upper bound the shear forces stiffness is. This confirms the interpretation given by Kelsey et al. (1958) for their bounds: the upper bound is relevant for thick skins and the lower one for thin skins. Further analysis of this phenomenon is provided in Section 7.5.

7.4.3 Comparison with full 3D simulation

In order to validate the Bending-Gradient model, the homogenized solution derived with the Bending-Gradient homogenization scheme is compared with a full 3D simulation of the sandwich panel under Pagano's cylindrical bending.

The Bending-Gradient solution for Pagano's configuration was derived in Chapter 5. Or-

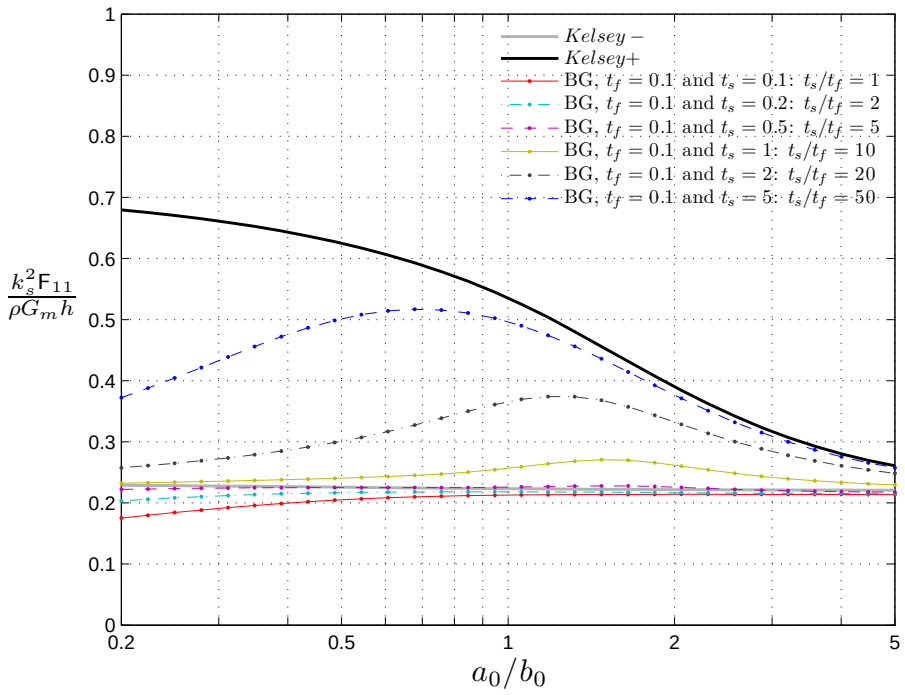

Figure 7.9: The normalized shear forces stiffness in Direction 1 vs. the shape ratio for several skin thicknesses ($t_f = 0.1$)

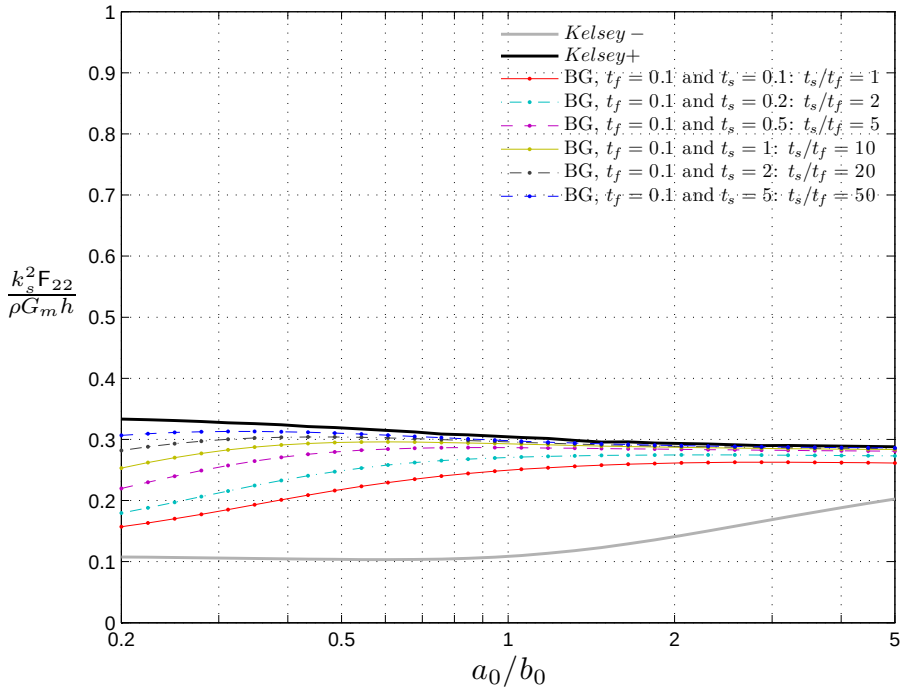

Figure 7.10: The normalized shear forces stiffness in Direction 2 vs. the shape ratio for several skin thicknesses ($t_f = 0.1$)

thotropic uncouplings lead directly to the deflection in Direction 1:

$$U_3(x_1) = p_0 \left(\frac{L}{\pi}\right)^4 \left(\frac{1}{\mathcal{D}_{1111}} + \frac{\pi^2}{L^2 \mathsf{F}_{11}}\right) \sin \frac{\pi x_1}{L} \tag{7.5}$$

where $\mathcal{D}_{1111}$ and F_{11} are the stiffness moduli derived from the homogenization scheme.

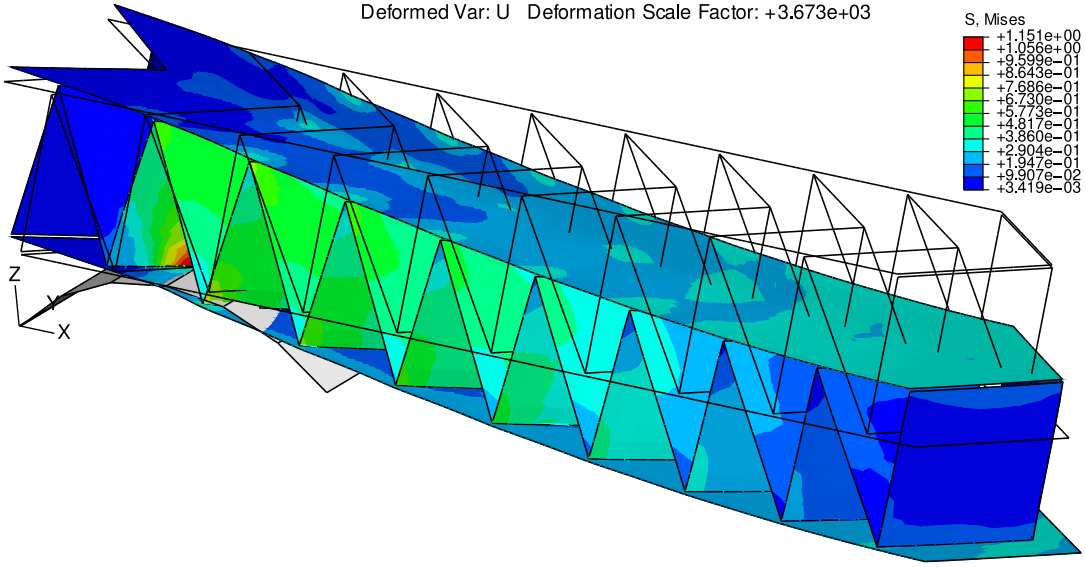

Figure 7.11: Overview of the full 3D finite elements cylindrical bending, $t_s = 1\,mm$ and $t_f = 0.1\,mm$

An illustration of the full 3D simulation is given in Figure 7.11. The sandwich panel is loaded on the lower and upper skins with $\widetilde{\boldsymbol{T}}^{\pm} = \frac{p_3}{2}\widetilde{\boldsymbol{e}}_3$ where $p_3 = -p_0 \sin \frac{\pi x_1}{L}$. Simply supported boundary conditions in Pagano's configuration cannot be applied to a heterogeneous sandwich panel. Here they are replaced by rigid rolls which diameter is equal to $3t_c$. Actually these boundary conditions are much closer to the reality than those implicitly defined in plate models. Periodicity conditions are enforced along the edge of the 9.5 cells strip in Figure 7.11. At mid-span, the rotational symmetry $\mathcal{S}$ with respect to a vertical axis is used to enforce boundary conditions. This symmetry was detailed in Section 3.2.

The unit-cell geometry is the same as in Figure 7.3. Two arbitrary facet thicknesses are investigated: $t_f = 0.1\,mm$ and $t_f = 2\,mm$ as well as two skin thicknesses: $t_s = 5\,mm$ and $t_s = 1\,mm$. The span covers 18 cells: $L = 308\,mm \simeq 10h$.

The same elements as for the homogenization are used. Because of the supporting rolls, contact with the sandwich panel is taken into account. However, large strains are not allowed.

On Figure 7.11 is plotted the deformed mesh. The skins distorsion is clearly visible. In order to compare with the prediction from the Bending-Gradient model, the plate deflection from the 3D simulation is derived as the average between the upper skin and the lower skin deflections as defined

in Equation (4.35) from Chapter 4. Moreover, this deflection is averaged in the x_2 direction. On Figures 7.12 to 7.15 are plotted the deflection curves. For each sandwich panel configuration, four deflection curves are plotted: the full simulation and the Bending-Gradient gradient prediction, but also the deflections using only the bounds from Kelsey et al. (1958) for the shear forces stiffness. The deflection is normalized with the Love-Kirchhoff deflection of the plate ($\mathsf{F}_{11} = \infty$).

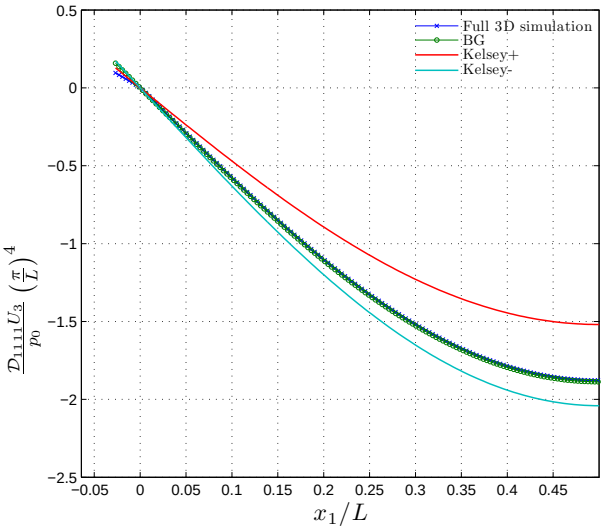

Figure 7.12: Deflection along the span for $t_s = 1\,mm$ and $t_f = 0.1\,mm$

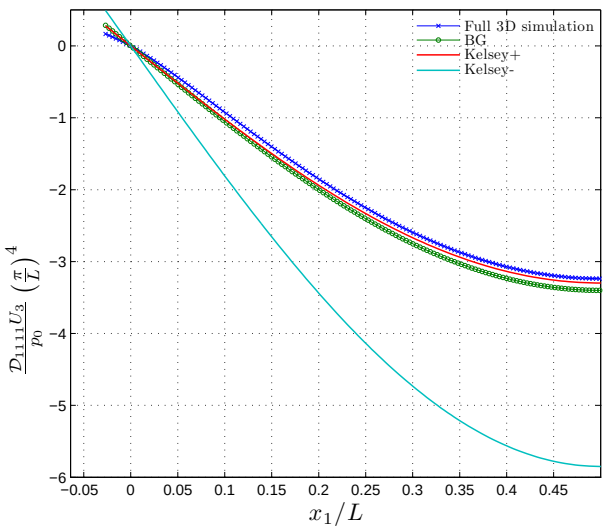

Figure 7.13: Deflection along the span for $t_s = 5\,mm$ and $t_f = 0.1\,mm$

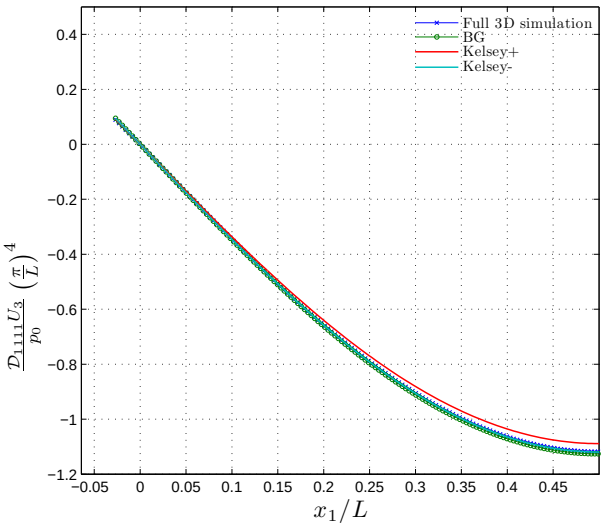

Figure 7.14: Deflection along the span for $t_s = 1\,mm$ and $t_f = 2\,mm$

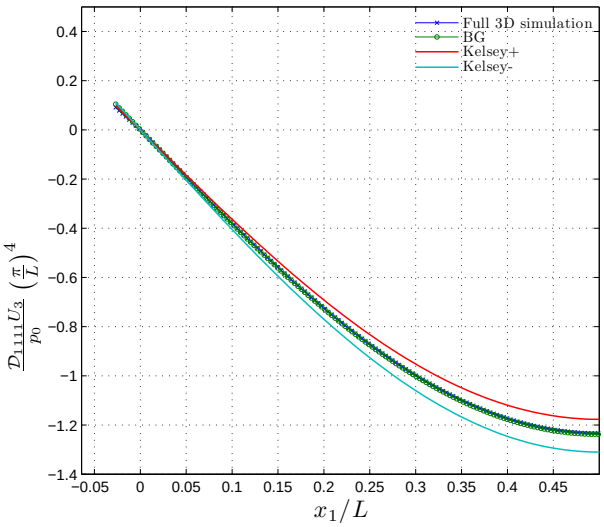

Figure 7.15: Deflection along the span for $t_s = 5\,mm$ and $t_f = 2\,mm$

For all configurations, their is a very good agreement between the Bending-Gradient predictions and the 3D solution. Because of the supporting condition difference between the Bending-Gradient solution and the 3D simulation, it is not possible to give a quantitative comparison of deflections.

For instance, in Figure 7.13, the skins flexural stiffness generates an offset in the deflection. The qualitative comparison is nevertheless convincing.

7.5 Discussion on shear forces stiffness

7.5.1 The case of honeycomb structures

The interaction between the skins and the core has already been observed with honeycomb. In order to compare with the case of the chevron pattern, it is of interest to recall the existing work on that matter.

In the case of honeycomb structures, the interaction is mainly caused by an incompatibility between shear strain fields in the core and the skins stiffness. This phenomenon is a boundary effect.

The incompatibility itself is caused by the non-uniform shear strain in the core far form the skins. Especially this generates out-of-plane warping of the honeycomb core. Close to the skins, this warping is restrained which generates flexion in the skins. Since warping involves honeycomb's facets in-plane shearing, this phenomenon is driven by a trade-off between the skins flexural stiffness and the honeycomb's facets membrane stiffness.

This incompatibility phenomenon is a boundary effect because of a structural effect. In many sandwich panels including honeycomb, the in-plane size l of the unit-cell is rather small compared to the core thickness t_c (Figure 7.16). Thus, when t_c/l is large enough, the unit-cell can be considered as a beam doubly clamped to the skins. The strain incompatibility caused by clamping remains localized close to the skins. This phenomenon is directly driven by the aspect ratio of the unit-cell t_c/l. Following a completely different approach, a model is proposed for analyzing such boundary effects caused by strains incompatibility on the edge in Chapter 8 and an illustration for a doubly clamped infinite laminate under transverse shear is given in Figure 8.3.

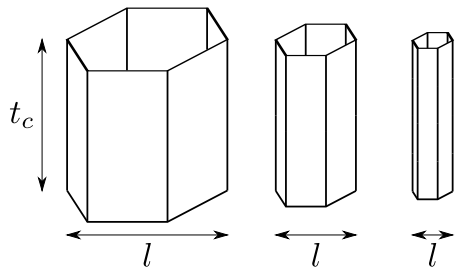

Figure 7.16: The honeycomb unit-cell for several apsect ratio

The structural effect was pointed out by Grediac (1993) when applying the unit displacement method from Kelsey et al. (1958) with finite elements exactly as done for the chevron pattern in

Chapter 3. Grediac (1993) demonstrated the influence of the unit-cell aspect ratio on the upper bound for shear forces stiffness. His work was followed by an analytical approach from Chen and Davalos (2005) where the strain incompatibility is treated as a boundary effect. However both these works assume fully rigid skins. Thus the trade-off between the skins stiffness and the facets membrane stiffness was not pointed out.

In order to take into account the full interaction between skins and core under transverse shear loading, Shi and Tong (1995) suggested to apply a uniform transverse shear strain on average in the core (as done in periodic homogenization schemes) to which are welded the skins. This enabled them to bring out both the unit-cell aspect ratio and the skins flexural stiffness on the actual shear forces stiffness of honeycomb. Their approach was applied to several honeycomb geometries by Hohe (2003) who calls it the direct homogenization method.

Even if this approach is based on a relevant analysis on the mechanical behavior of sandwich panels under shear forces, its main limitation is that it is valid only for thin skins. As demonstrated in the present work, the contribution of the skins thickness is not so often negligible. Actually there is an inherent contradiction when assuming thin skins and trying to assess the influence of their thickness on the shear forces stiffness. The Bending-Gradient homogenization scheme is not limited by the skins thickness.

7.5.2 The case of chevron pattern

In the case of the chevron pattern, three combined phenomenon could explain the shear forces stiffness variations.

First, as for honeycomb, their is a shape ratio: a_0/b_0. As indicated in Section 7.4.2.2 this shape ratio has a strong influence on the shear forces stiffness. However, it is difficult to relate a_0/b_0 to some scale separation or structural effect. Moreover in practical case $a_0/b_0 \in [0.25, 1.5]$ (Zakirov et al., 2006) thus it would be irrelevant to look for asymptotic behavior.

Second, since the facets are clamped on the skins, there can be local flexion in the facets or in the skins. In Chapter 3 we indicated that facets mostly behave as membranes. However, when the skins are thin and the facets thick enough, there could be a competition between flexion in the skins or flexion in the facets. This phenomenon is driven by a trade-off between facets and skins flexural stiffnesses. In the present case, this trade-off is proportional to the cube of the contrast ratio t_s/t_f.

Third, exactly as for the honeycomb, the shear forces stiffness is nevertheless mostly driven by the facets membrane stiffness which compete with the skins own flexural stiffness. In the present case, this trade-off is proportional to the ratio between the skins flexural stiffness and the facets membrane stiffness: $t_s/(t_f h^2)^{1/3}$ which we call the skins relative flexural stiffness (an equivalent parameter was suggested by Shi and Tong (1995)).

The influence of the shape ratio was studied in Section 7.4.2.2. In order to illustrate the two last phenomena, the shape ratio is chosen as $a_0/b_0 = 1$ in the following.

In Figure 7.17 the shear forces stiffness in Direction 1 is plotted versus the contrast ratio t_s/t_f for several facets thicknesses. The bounds from Kelsey et al. (1958) derived with finite elements are recalled. Globally, the shear forces stiffness increase with the contrast ratio and the upper bound from Kelsey et al. (1958) is always respected. For low contrasts (< 2), the lower bound from Kelsey et al. (1958) in not fully respected. Again, this is not surprising since it is not a "true" bound and the contrast assumption is not fullfilled here. Moreover the shear forces stiffness is only function of the contrast ratio t_s/t_f: it does not depend on the facets relative thickness (t_f/h). Hence, for this range of contrast ratios with thin skins, it is the competition between flexion in the core or in the skins which drives the stiffness. Large skins deformation were observed with finite elements computations. For contrast ratio larger than 2, a shift between the lower bound and the upper bound occurs. This shift depends on both the contrast ratio and the facets relative thickness. When the shift occurs, no more skins distorsion is observed in finite elements computations.

In Figure 7.18 the shear forces stiffness in Direction 1 is plotted versus the skins relative flexural stiffness $t_s/(t_f h^2)^{1/3}$ for several facet thicknesses. All shifts occur for the same value of this parameter ($t_s/(t_f h^2)^{1/3} \simeq 0.4$). This justifies the interpretation of the skins distorsion as a trade-off between skins flexural stiffness and facets membrane stiffness suggested above.

In Direction 2, the shear forces stiffness is only function of the contrast ratio t_s/t_f and does not depend on the facets relative thickness (Figure 7.19). Contrary to Direction 1, there is no clear shift between the upper and the lower bound. Very small out-of-plane skins deformations were observed in finite elements results. Here, it is only the competition between flexion in the core or in the skins which drives the stiffness.

7.6 Conclusion

In this chapter, a detailed analysis of the behavior of sandwich panels including the chevron pattern under shear forces loading was performed. For this, relevant length scales were identified (the sandwich, the skins and the facets thicknesses) and corresponding assumptions stated. Then, the Bending-Gradient homogenization scheme was applied and validated thanks to full 3D simulations. The first conclusion is that the contrast assumption validity range is much wider with the chevron pattern than in the general case and that assuming thin skins might really affect shear forces stiffness estimates. It is not recommended when designing sandwich panels. The second conclusion is that two phenomena drive the shear forces stiffness. The most important one is the out-of-plane skins distorsion. This phenomenon is driven by the relative flexural stiffness of the skins. The second one is the competition of flexion between the skins and the core. This phenomenon is driven directly by

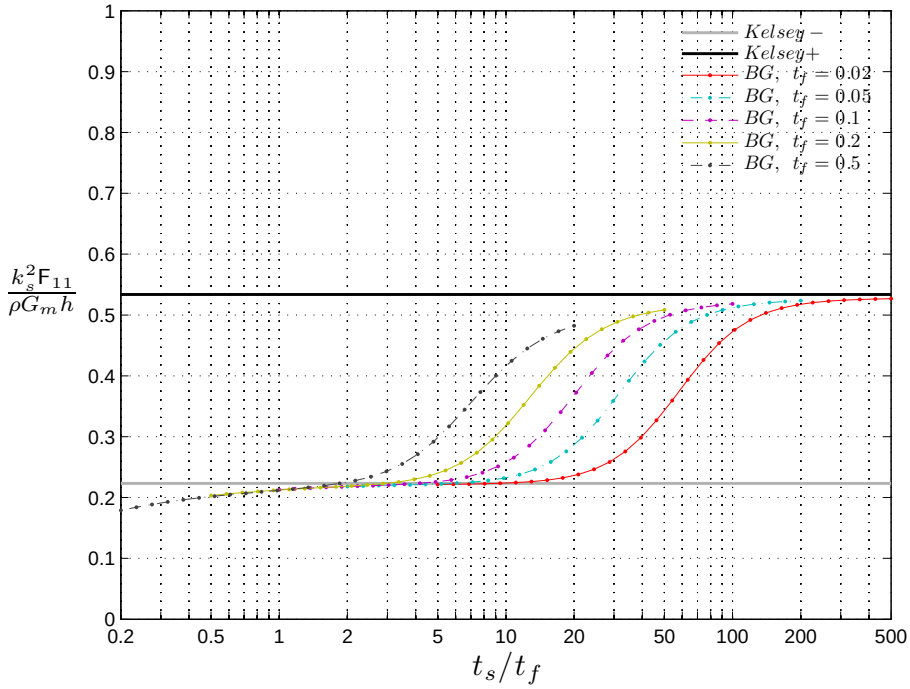

Figure 7.17: The normalized shear forces stiffness in Direction 1 vs. the contrast ratio for several facets thicknesses ($a_0/b_0 = 1$)

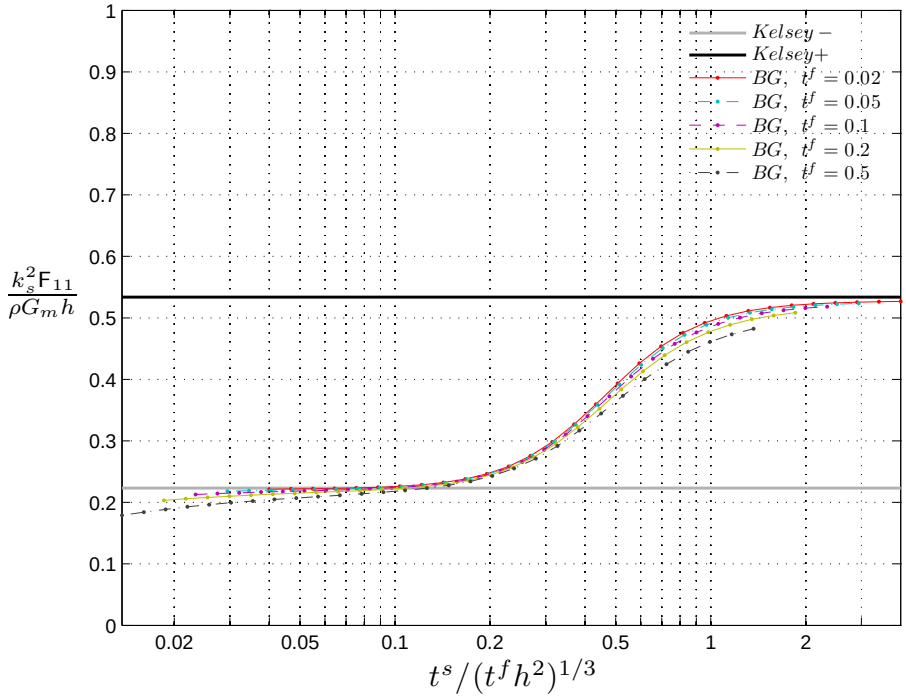

Figure 7.18: The normalized shear forces stiffness in Direction 1 vs. skins relative flexural stiffness for several facets thicknesses ($a_0/b_0 = 1$)

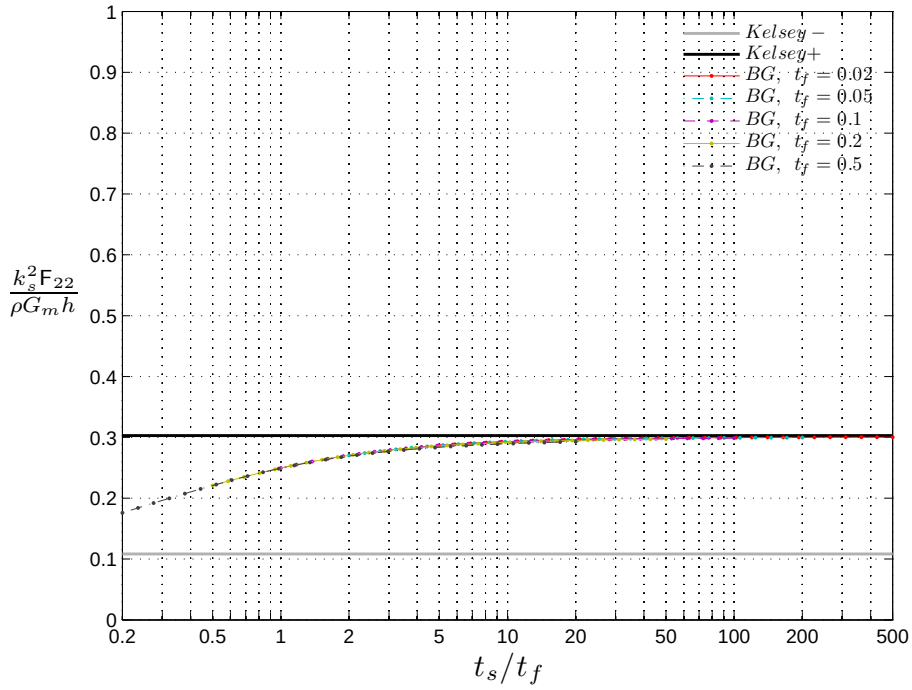

Figure 7.19: The normalized shear forces stiffness in Direction 2 vs. the contrast ratio for several facets thicknesses ($a_0/b_0 = 1$)

the contrast ratio.

One can wonder if the distorsion effect has to be taken into account with conventional sandwich panel applications including the chevron pattern.

Here is a first answer in the linear elastic domain. Let us consider such a sandwich panel under Pagano's cylindrical bending. The mid-span deflection (Equation (7.5)) can be rewritten as:

$$U_3 = \frac{p_0}{\mathcal{D}_{1111}} \left(\frac{L}{\pi}\right)^4 \left(1 + \left(\frac{L^*}{L}\right)^2\right)$$

where $L^* = \pi\sqrt{\frac{\mathcal{D}_{1111}}{\mathsf{F}_{11}}}$ is a characteristic length to which the span must be compared. When $L \gg L^*$ the contribution of the shear forces stiffness to the deflection is negligible. In Figure 7.20 L^*/h is plotted as a function of the contrast ratio. This leads to three remarks.

First, we have $L^*/h > 1$. Having $L^*/h \ll 1$ would mean that the plate behavior is completely dominated by flexion. Actually, in such a case, one can wonder the meaning of a shear effect which is negligible compared to the unit-cell size and the homogenization approach becomes inconsistent.

Second, in the present case, the shear deflection cannot be neglected. For instance, in standard sandwich panel applications, the slenderness ratios L/h are barely larger than 40. Here, with a contrast ratio of $t_s/t_f = 10$, we have $L^*/h \simeq 10$.

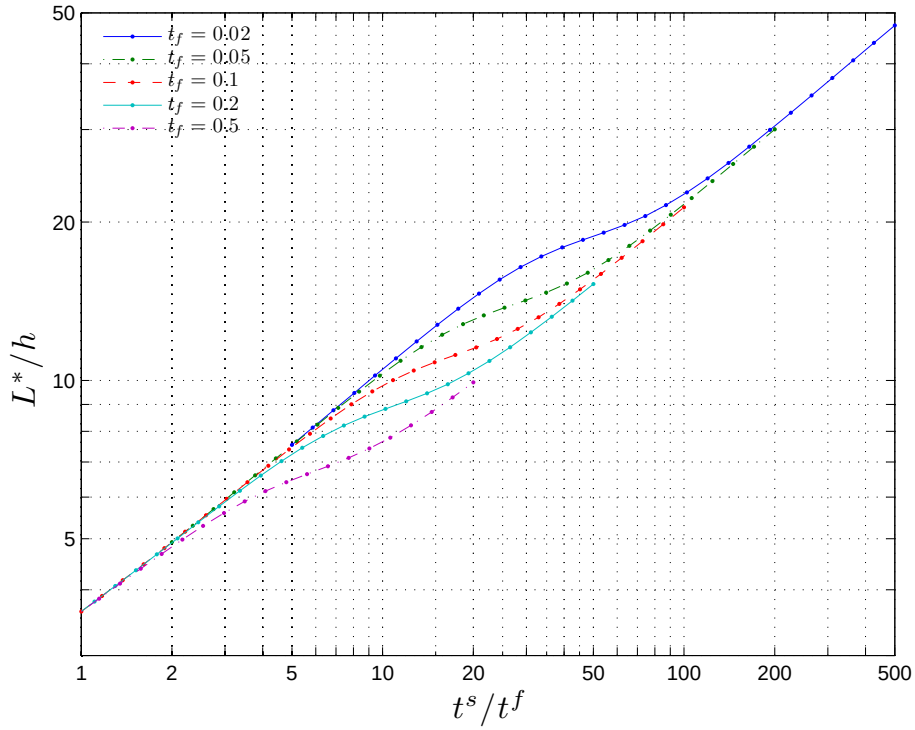

Figure 7.20: Shear deflection correction vs. contrast ratio for several facets thicknesses ($a_0/b_0 = 1$)

Third, the skins distorsion occurs exactly in the standard range for contrast ratio. We conclude that this phenomenon has a central role when one wants to predict accurately sandwich panels deflection including the chevron pattern.

The non-linear elasticity is out of the scope of this work. Yet, as already mentioned, the failure of sandwich panels is mainly due to buckling. The work from Petras and Sutcliffe (1999) has been given as illustration for an analytical and experimental approach of honeycomb sandwich panels failure map. It is also very interesting to consider the work from Pahr and Rammerstorfer (2006) and Rammerstorfer et al. (2006) were the numerous failure modes are numerically investigated. In many of these failure, the out-of-plane displacement of the skins is involved. Thus, in the case of the chevron pattern, the skins distorsion might really affect the bifurcation point. Moreover, Pahr and Rammerstorfer (2006) use the direct homogenization method from Shi and Tong (1995). As already noticed, this method does not take accurately the thickness of the skins into account. It would be interesting to apply the Bending-Gradient homogenization scheme in order to estimate the sensitivity of bifurcation point when the skins becomes thick.

CHAPTER

8

A Cosserat multiparticle model for periodically layered materials

Au Chapitre 4, on a montré que la théorie de gradient du moment présente une quatrième condition au bord sur le moment de flexion dans la direction orthogonale à celui-ci. Prendre en compte des contraintes qui ne font pas partie la surface tridimensionnelle sur laquelle s'appliquent les conditions au limites peut sembler artificiel au premier abord. En réalité cette condition supplémentaire traduit l'existence d'un effet de bord. Certains l'interprêteraient comme une tension de surface. Dans le cas de la théorie de gradient du moment, il s'agit plutôt de l'incompatibilité entre le gauchissement de la section dans la partie courante et l'encastrement imposé au bord. Ce type d'effet de bord se retrouve aussi dans ce qu'on a décrit comme l'interaction entre peaux et âme dans le cas du nid d'abeilles. En effet, loin des peaux, le nid d'abeilles présente une déformation de gauchissement sous cisaillement uniforme qui est empêchée au niveau des peaux. Enfin il existe aussi des effets de bord libre. Dans le cas des plaques stratifiées sous chargement membranaire, on a très rapidement identifié des concentrations de contraintes interlaminaires au niveau des bords libres provoquant des délaminages prématurés. Une étude détaillée de ce phénomène est présentée dans l'ouvrage de Pagano (1989).

Ces trois phénomènes sont en réalité associés à l'apparition de singularités des contraintes tridimensionnelles générées par les incompatibilités sur les bords (Leguillon, 1999). Une approche pour les étudier consiste à les régulariser par des fonctions exponentielles (finies) qui tendent rapidement vers 0 loin du bord. Cela passe donc par la construction de modèles d'ordre supérieurs (une dérivation supplémentaire dans les équations différentielles) qui font apparaître ce type de solutions. Les nombreux travaux sur les milieux continus généralisés (Cosserat, second gradient etc.) illustre cette régularisation.

Dans le cas présent, on considère un milieu stratifié de n couches reproduit à l'infini par périodicité. On utilise des outils similaires à ceux introduit pour la théorie de gradient du moment ainsi que pour les modèles multi-particulaires construits au Laboratoire Navier (Diaz Diaz et al., 2001).

On aboutit à un modèle de type Cosserat dans chaque couche (modèle multi-particulaire). Les effets de bords sont donc pris en compte en faisant apparaître un moment de flexion localisé dans chaque couche.

Ce chapitre est paru dans la revue Mechanics Research Communications sous la référence Lebée and Sab (2010b).

Abstract

In this paper, the Cosserat Multiparticle Model (CM2) for 3D periodically layered materials is proposed in order to reproduce both size and boundary effects in these materials. This model can handle $n-$ phase periodically layered materials with $4n+1$ kinematic variables at each 3D geometric point: 2 in-plane displacements and 2 rotations per phase + 1 common out-of-plane displacement. The model gives excellent agreement with full finite element results for out-of-plane shearing.

8.1 Introduction

In this paper, a new continuum multiparticle model for *3D periodically layered materials* is proposed in order to reproduce both size effects and boundary effects in these materials.

As example, a two-phase linear elastic periodically layered material with free body forces is submitted to out-of-plane shearing as following Figure 8.1. The domain considered is infinite in the x_2 and x_3 directions, with $|x_1| \leq \frac{L}{2}$, and the displacement vector, $\mathbf{u} = (u_1, u_2, u_3)$, is imposed at the boundary $x_1 = \pm\frac{L}{2}$, $\mathbf{u} = (0, 0, \pm w)$. The phase-1 material is situated between $x_3 = 0$ and $x_3 = t_1$ and the phase-2 material is situated between $x_3 = t_1$ and $x_3 = t_1 + t_2 = t$. This pattern is reproduced by periodicity in the x_3 direction.

The full 3D solution of this $(x_1, x_3)-$plane strain problem is periodic in the x_3 direction. Hence, it can be obtained by restricting the analysis to the domain $(x_1, x_3) \in \mathcal{D} \equiv \left]-\frac{L}{2}, \frac{L}{2}\right[\times]0, t[$, and by applying suitable displacement and stress periodicity conditions to the boundaries $x_3 = 0$ and $x_3 = t$.

One may also use the well-known standard homogenization procedure to solve the same problem: First, the effective overall elastic constants of the periodic material are determined by solving an auxiliary boundary value problem on the unit cell. Then, the overall elastic constants are used to solve the initial boundary value problem. Finally, an estimation of the real 3D stresses is obtained by a suitable localization of the overall stresses in the unit cell. When applying this procedure to periodically layered materials, the unit cell boundary value problem, as well as the stress localization problem, are 1D in the x_3 direction, and closed-form solution are obtained. Moreover, in the case of the above described out-of-plane shearing problem with isotropic constituents (Young's modulus E^γ,

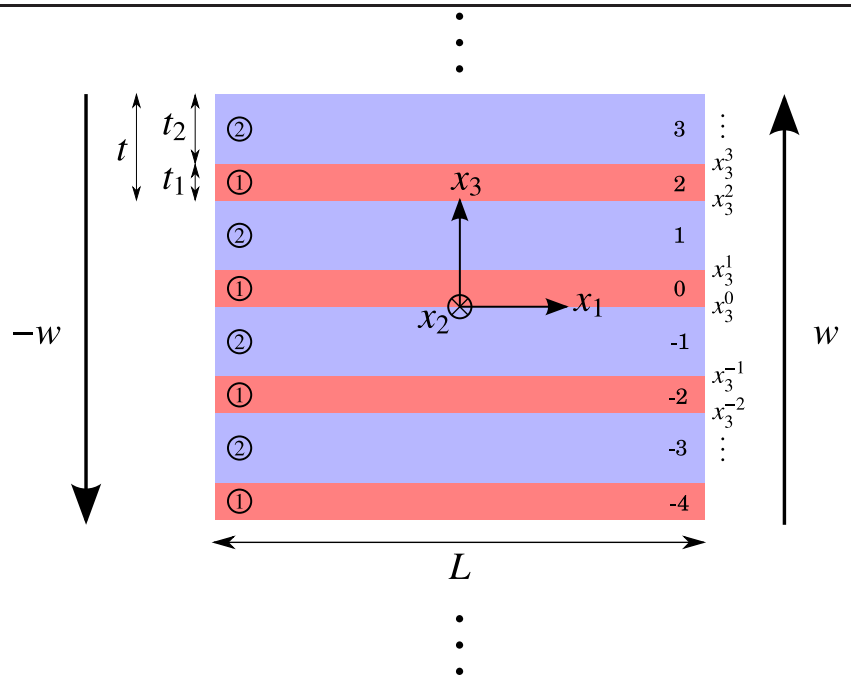

Figure 8.1: Two-phase periodically layered material

shear modulus G^γ, Poisson's ratio ν^γ, $\gamma = 1, 2$), the homogenized solution is straightforward: the displacement is linear in x_3, $\left(0, 0, \frac{2x_3}{L}w\right)$, and the predicted $(1,3)-$ shear stress after localization is uniform in both layers, $\sigma_{13}^{\text{hom}} = 2G^{\text{hom}}\frac{w}{L}$. Here, $G^{\text{hom}} = \left(\overline{G^{-1}}\right)^{-1}$ is the homogenized $(1,3)-$ shear modulus where the following notation is used:

$$\overline{X} = \frac{t_1}{t}X^1 + \frac{t_2}{t}X^2$$

It is expected that the full 3D solution converges to the homogenized one as the slenderness ratio $\frac{L}{t}$ goes to infinity.

The Finite Element ABAQUS software (ABAQUS, 2007b) has been used to numerically solve the above described plane strain problem on $\mathcal{D}$. Figure 8.2 shows the normalized effective shear modulus[1], G^{eff}/G^{hom}, versus $\frac{L}{t}$ for $\frac{t_1}{t_2} = 4$, $\frac{E^1}{E^2} = 10$ and $\nu^1 = \nu^2 = 0.3$ and Figure 8.3 shows the normalized shear stress distribution with respect to its average value for $\frac{L}{t} = 8$. Clearly, a size effect on the effective shear modulus is exhibited for small values of $\frac{L}{t}$. Moreover, even for large values of $\frac{L}{t}$, the stress distribution near the vertical boundaries does not fit the one predicted by the homogenization procedure because of its incompatibility with the displacement boundary conditions.

Many works have tried to capture these size and boundary effects by adopting higher-order

1. defined as the ratio of the FE and homogenized strain energy of $\mathcal{D}$.

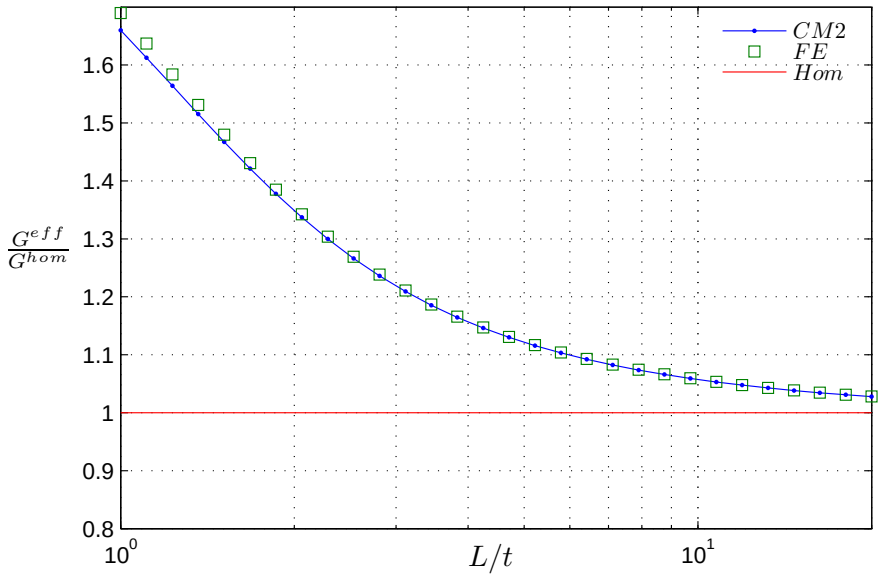

Figure 8.2: Size effect. Normalized effective shear modulus vs. slenderness ratio for $t_1/t_2 = 4$, $E^1/E^2 = 10$ and $\nu^1 = \nu^2 = 0.3$.

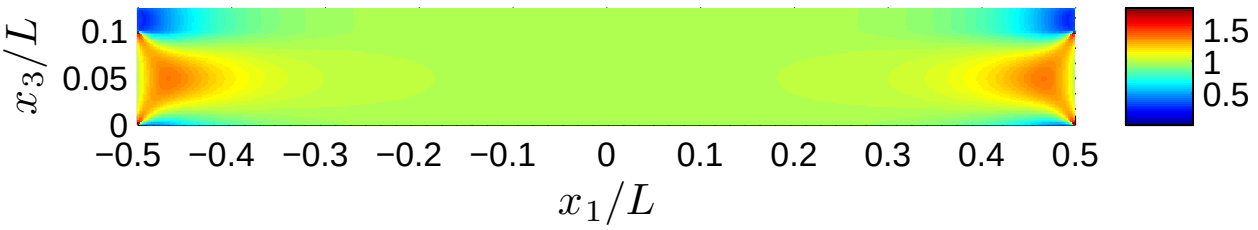

Figure 8.3: Boundary effect. FE normalized shear stress $\sigma_{13}/\overline{\Sigma}_{13}$ for $t_1/t_2 = 4$, $E^1/E^2 = 10$ and $\nu^1 = \nu^2 = 0.3$.

homogenized models. See among others (Boutin, 1996), (Adhikary and Dyskin, 1997), (Forest and Sab, 1998), (de Buhan and Sudret, 2000), (Kouznetsova et al., 2002), (Bigoni and Drugan, 2007) and (Yuan et al., 2008). In most of these papers, general procedures based on some modified unit cell boundary value problems are proposed to derive Cosserat-type or second-gradient-type macroscopic equivalent homogeneous descriptions of the periodic medium. Actually these procedures are not specific to periodically layered materials. Yet, the behavior of multilayered *plate structures* (non periodic with small thickness in the x_3 direction) has been studied for many years. See, for example, (Carrera, 2002) for a review. The most common approach is to substitute the heterogeneous plate with a homogeneous equivalent one, with or without taking into account shear effects. Another class of plate models initiated by Pagano (1978) is based on layerwise approach. These models called M4 (Multiparticle Model for Multilayered Materials) have been developed at Ecole des Ponts ParisTech by Ehrlacher, Caron, Foret, Sab and their co-workers (Diaz Diaz et al., 2001), (Hadj-Ahmed et al., 2001), (Caron et al., 2006), (Diaz Diaz et al., 2007) and (Dallot and Sab, 2008). The main interest of these models is to make the study of local fields possible, especially at the interfaces between layers (stress concentration in adhesive joints , delamination in composite materials, limit analysis of reinforced plates...).

The idea of the present paper is to combine higher ordrer homogenization procedures and layerwise plate models. It consists in using the M4 model for the periodically layered material, and then in homogenizing this model obtaining a Cosserat Multiparticle Model (CM2). The proposed CM2 is described in Section 8.2 and its application, in Section 8.3, to the shearing problem of Figure 8.1 will demonstrate its ability to reproduce both size and boundary effects.

8.2 The proposed model

The elasticity tensor $\boldsymbol{L}$ at every point $\mathbf{x} = (x_1, x_2, x_3)$ is piecewise uniform and periodic in x_3:

$$\boldsymbol{L}(\mathbf{x}) = \boldsymbol{L}(x_3) = \boldsymbol{L}^{\gamma(k)} \text{ for } x_3^k < x_3 < x_3^{k+1},\ k \in \mathbb{Z},$$

where x_3^k is the coordinate of the the interface between layer $k-1$ and layer k with $x_3^0 = 0$, $\gamma(k)$ is equal to 1 for even k and to 2 for odd k, and $\boldsymbol{L}^\gamma$ is the elasticity tensor of phase γ, $\gamma = 1, 2$. Hence, even layers $(\cdots, -2, 0, +2, \cdots)$ are occupied by phase 1 and odd layers $(\cdots -3, -1, +1, +3, \cdots)$ are occupied by phase 2. The coordinate of the middle surface of layer k is $\bar{x}_3^k = \frac{x_3^{k+1}+x_3^k}{2}$. The multilayered material being periodic, the thickness $x_3^{k+1} - x_3^k$ of layer k is $t_{\gamma(k)}$ and its inertia is $I_{\gamma(k)} = \frac{t_{\gamma(k)}^2}{12}$. The period in the x_3 direction is $t = t_1 + t_2$.

8.2.1 Statics

The idea is to model the 3D layered material as a collection of Reissner-Mindlin plates interacting at their interfaces.

The following notations are introduced: Greek index $\alpha, \beta, \gamma = 1, 2$. Latin index $i, j = 1, 2, 3$. For layer k , $\mathbf{N}^k = \left(N^k_{\alpha\beta}\right)$ is the in-plane (membrane) stress resultant, $\mathbf{M}^k = \left(M^k_{\alpha\beta}\right)$ is the out-of-plane (flexural) stress resultant with respect to the middle surface, $\bar{x}^k_3$, and $\mathbf{Q}^k = \left(Q^k_\alpha\right)$ is the out-of-plane shear stress resultant. We have:

$$\begin{cases} N^k_{\alpha\beta}(x_1, x_2) = \int_{x^k_3}^{x^{k+1}_3} \sigma_{\alpha\beta}(x_1, x_2, x_3)\, dx_3, \\ M^k_{\alpha\beta}(x_1, x_2) = \int_{x^k_3}^{x^{k+1}_3} \left(x_3 - \bar{x}^k_3\right) \sigma_{\alpha\beta}(x_1, x_2, x_3)\, dx_3, \\ Q^k_\alpha(x_1, x_2) = \int_{x^k_3}^{x^{k+1}_3} \sigma_{\alpha 3}(x_1, x_2, x_3)\, dx_3, \end{cases}$$

where $\boldsymbol{\sigma} = (\sigma_{ij})$ is the 3D-stress tensor field. It is easily established that the 3D balance equation div $\boldsymbol{\sigma} = 0$ leads to the following balance equations for each layer k (Caron and Sab, 2001), (Nguyen et al., 2005b):

$$N^k_{\alpha\beta,\beta} + \sigma^{k+1}_{\alpha 3} - \sigma^k_{\alpha 3} = 0, \tag{8.1}$$

$$Q^k_{\alpha,\alpha} + \sigma^{k+1}_{33} - \sigma^k_{33} = 0, \tag{8.2}$$

$$M^k_{\alpha\beta,\beta} - Q^k_\alpha + \left(x^{k+1}_3 - x^k_3\right) \frac{\sigma^{k+1}_{\alpha 3} + \sigma^k_{\alpha 3}}{2} = 0, \tag{8.3}$$

where $\sigma^k_{i3} \equiv \sigma_{i3}(x_1, x_2, x^k_3)$ is the $i-$component of the vector stress at the interface between layer $k-1$ and layer k.

It is assumed that the above introduced plate resultant stresses and moments $\mathbf{N}^k$, $\mathbf{M}^k$ and $\mathbf{Q}^k$ are the traces at $(x_1, x_2, \bar{x}^k_3)$ of regular functions for each phase γ. More precisely, we write:

$$N^k_{\alpha\beta}(x_1, x_2) = t_{\gamma(k)} \Sigma^{\gamma(k)}_{\alpha\beta}\left(x_1, x_2, \bar{x}^k_3\right), \tag{8.4}$$

$$Q^k_\alpha(x_1, x_2) = t_{\gamma(k)} \Sigma^{\gamma(k)}_{3\alpha}\left(x_1, x_2, \bar{x}^k_3\right), \tag{8.5}$$

$$M^k_{\alpha\beta}(x_1, x_2) = t_{\gamma(k)} \mu^{\gamma(k)}_{\alpha\beta}\left(x_1, x_2, \bar{x}^k_3\right), \tag{8.6}$$

$$\sigma^k_{i3}(x_1, x_2) = S^{\gamma(k)}_i\left(x_1, x_2, x^k_3\right), \tag{8.7}$$

where $\Sigma^\gamma_{\alpha\beta} = \Sigma^\gamma_{\beta\alpha}$, $\mu^\gamma_{\alpha\beta} = \mu^\gamma_{\beta\alpha}$, $\Sigma^\gamma_{3\alpha}$ and S^γ_i are functions of (x_1, x_2, x_3). These functions are actually regular interpolations on the x_3-coordinate of their corresponding plate stresses.

Using Taylor series expansion in x_3 of order 1 for S_i^γ, it is found that:

$$\frac{\sigma_{i3}^{k+1}+\sigma_{i3}^{k}}{2} \approx \Sigma_{i3}+\frac{(-1)^{\gamma(k)}}{4}t_{\gamma(k)}\Delta_{i,3}, \tag{8.8}$$

$$\sigma_{i3}^{k+1}-\sigma_{i3}^{k} \approx (-1)^{\gamma(k)}\,\Delta_i+t_{\gamma(k)}\Sigma_{i3,3}, \tag{8.9}$$

where the values of the functions Σ_{i3}, Δ_i, $\Sigma_{i3,3}$ and $\Delta_{i,3}$, with

$$\Sigma_{i3}=\frac{S_i^1+S_i^2}{2}, \quad \Delta_i=S_i^1-S_i^2,$$

are taken at point $\left(x_1,x_2,\bar{x}_3^k\right)$. Moreover, it is assumed that Δ_i and $t\Sigma_{i3,3}$ are of the same order:

$$\Delta_i \sim t\Sigma_{i3,3} \tag{8.10}$$

Hence, using the notations

$$\boldsymbol{\Sigma}^\gamma=\begin{pmatrix}\Sigma_{11}^\gamma & \Sigma_{12}^\gamma & \Sigma_{13}\\ \Sigma_{12}^\gamma & \Sigma_{22}^\gamma & \Sigma_{23}\\ \Sigma_{31}^\gamma & \Sigma_{32}^\gamma & \Sigma_{33}\end{pmatrix}, \quad \boldsymbol{\mu}^{(\gamma)}=\begin{pmatrix}\mu_{11}^\gamma & \mu_{12}^\gamma\\ \mu_{12}^\gamma & \mu_{22}^\gamma\end{pmatrix}, \tag{8.11}$$

the following stress balance equations are derived for $\gamma=1,2$ from (8.1), (8.2), (8.4), (8.5) and (8.9):

$$\Sigma_{ij,j}^\gamma+(-1)^\gamma\frac{\Delta_i}{t_\gamma}=0 \tag{8.12}$$

As a consequence of the assumption (8.10), the term $t_\gamma\Delta_{i,3}$ in (8.8) is of the same order as $t^2\Sigma_{i3,33}$ and is neglected when compared to Σ_{i3}. Hence, the following momentum balance equations are obtained from (8.3), (8.5), (8.6) and (8.8):

$$\mu_{\alpha\beta,\beta}^\gamma-\Sigma_{3\alpha}^\gamma+\Sigma_{\alpha 3}=0 \tag{8.13}$$

The balance equations (8.12-8.13) are those of a Cosserat continuum model for each phase, the two Cosserat models being coupled by the interface stresses Σ_{i3} and Δ_i. Note that the out-of-plane couple-stresses are null, $\mu_{3i}^\gamma=\mu_{i3}^\gamma=0$, $\Sigma_{3\alpha}^\gamma\neq\Sigma_{\alpha 3}$ in the general case whereas the in-plane tensors $\Sigma_{\alpha\beta}^\gamma$ and $\mu_{\alpha\beta}^\gamma$ are symmetric.

8.2.2 The generalized stress energy

For given $\boldsymbol{\Sigma}^\gamma$, $\boldsymbol{\mu}^\gamma$, $\gamma = 1,2$, of the form (8.11), and given in-plane interface stresses, Δ_α, $\alpha = 1,2$, the stress energy density $\mathcal{W}^*$ of the Cosserat Multiparticle Model (CM2) is identified as the average energy per unit period in the x_3 direction,

$$\mathcal{W}^*\left(\boldsymbol{\Sigma}^\gamma, \boldsymbol{\mu}^\gamma, \Delta_\alpha\right) \equiv \frac{1}{2t}\int_0^t \boldsymbol{\sigma}^{per}\left(x_3\right) : \boldsymbol{L}^{-1}\left(x_3\right) : \boldsymbol{\sigma}^{per}\left(x_3\right) dx_3,$$

of the periodic 3D-stress tensor field $\boldsymbol{\sigma}^{per}\left(x_3\right)$ defined as follows: For $x_3^k < x_3 < x_3^{k+1}$, $\hat{x}_3 = x_3 - \bar{x}_3^k$,

$$\sigma_{\alpha\beta}^{per}\left(x_3\right) = \Sigma_{\alpha\beta}^{\gamma(k)} + \mu_{\alpha\beta}^{\gamma(k)}\frac{\hat{x}_3}{I_{\gamma(k)}},\ \sigma_{33}^{per}\left(x_3\right) = \Sigma_{33}, \tag{8.14}$$

$$\sigma_{\alpha 3}^{per}\left(x_3\right) = \Sigma_{3\alpha}^{\gamma(k)} + \frac{\Sigma_{\alpha 3} - \Sigma_{3\alpha}^{\gamma(k)}}{2}\left(\frac{\hat{x}_3^2}{I_{\gamma(k)}} - 1\right) + (-1)^{\gamma(k)}\Delta_\alpha\frac{\hat{x}_3}{t_{\gamma(k)}}. \tag{8.15}$$

The in-plane stress components $\sigma_{\alpha\beta}^{per}\left(x_3\right)$ are piecewise linear in x_3 and completely determined by $\Sigma_{\alpha\beta}^\gamma$ and $\mu_{\alpha\beta}^\gamma$ in phase-γ layers; The out-of-plane shear stresses $\sigma_{\alpha 3}^{per}\left(x_3\right)$ are piecewise quadratic in x_3. They are equal to $S_\alpha^{\gamma(k)} = \Sigma_{\alpha 3} - \frac{(-1)^{\gamma(k)}}{2}\Delta_\alpha$ at the interface x^k an their average over layer k is $\Sigma_{3\alpha}^{\gamma(k)}$. Finally, $\sigma_{33}^{per}\left(x_3\right) = \Sigma_{33}$ is uniform..

8.2.3 Kinematics

Since the out-of-plane interface stress Δ_3 does not enter in the expression of the stress energy, it must be eliminated from the balance equations. Hence, the reduced balance equations are: the four in-plane stress balance equations (8.12) for $i = 1,2$ and $\gamma = 1,2$, the four momentum balance equations (8.13) for $\alpha = 1,2$ and $\gamma = 1,2$, and the reduced out-of-plane stress balance equation obtained by a combination of (8.12) for $i = 3$ and $\gamma = 1,2$:

$$\overline{\Sigma}_{31,1} + \overline{\Sigma}_{32,2} + \Sigma_{33,3} = 0. \tag{8.16}$$

The weak formulation of the nine balance equations of the CM2 is obtained by introducing nine corresponding kinematic fields: four in-plane displacement fields, U_α^γ, four rotation fields, ϕ_α^γ and one out-of-plane displacement field U_3. The CM2 balance equations are equivalent to:

$$\int_\Omega \overline{\Sigma_{ij}E_{ij}} + \overline{\mu_{\alpha\beta}\chi_{\alpha\beta}} + \Delta_\alpha D_\alpha\, d\Omega = \int_{\partial\Omega} \overline{\Sigma_{ij}n_j U_i} + \overline{\mu_{\alpha\beta}n_\beta\phi_\alpha}\, dS \tag{8.17}$$

for all regular fields $(U_\alpha^\gamma, U_3, \phi_\alpha^\gamma)$. Here, Ω is a 3D domain with a smooth boundary $\partial\Omega$, $\mathbf{n}$ is the outer normal vector to $\partial\Omega$, and the CM2 generalized strains are given by:

$$\begin{aligned} E^\gamma_{\alpha\beta} &= \frac{1}{2}\left(U^\gamma_{\beta,\alpha}+U^\gamma_{\alpha,\beta}\right),\ E^\gamma_{3\alpha}=U_{3,\alpha}+\phi^\gamma_\alpha,\ E_{\alpha 3}=\overline{U}_{\alpha,3}-\overline{\phi}_\alpha,\ E_{33}=U_{3,3},\\ \chi^\gamma_{\alpha\beta} &= \frac{1}{2}\left(\phi^\gamma_{\beta,\alpha}+\phi^\gamma_{\alpha,\beta}\right),\ D_\alpha=\frac{1}{t}\left(U^1_\alpha-U^2_\alpha\right). \end{aligned} \tag{8.18}$$

The above CM2 strains and the usual 3D strains, $\boldsymbol{\varepsilon}$, are related by the following generalized Hill-Mandel property which is consistent with the assumptions made for the identification of the CM2 stress energy density: assume that $\boldsymbol{\varepsilon}$ is locally periodic in x_3, then, for every $\left(\boldsymbol{\Sigma}^{(\gamma)},\boldsymbol{\mu}^{(\gamma)},\Delta_\alpha\right)$, we should have:

$$\overline{\Sigma_{ij}E_{ij}}+\overline{\mu_{\alpha\beta}\chi_{\alpha\beta}}+\Delta_\alpha D_\alpha \equiv \frac{1}{t}\int_{-\frac{t}{2}}^{+\frac{t}{2}} \boldsymbol{\sigma}^{per}(z):\boldsymbol{\varepsilon}\ (x_1,x_2,x_3+z)\,dz.$$

where $\boldsymbol{\sigma}^{per}$ is given by (8.14-8.15). Substituting $\boldsymbol{\sigma}^{per}$ by its expression in the above identity, the CM2 strains are identified to weighted averages of the 3D strain components. In particular, $E^{(\gamma)}_{\alpha\beta}$ and $\chi^{(\gamma)}_{\alpha\beta}$ are respectively the moving partial averages of $\varepsilon_{\alpha\beta}$ and $\frac{\hat{x}_3}{I_\gamma}\varepsilon_{\alpha\beta}$ on phase γ, and E_{33} is the moving average of ε_{33} on a period. Therefore, $U^{(\gamma)}_\alpha$ and $\phi^{(\gamma)}_\alpha$ are respectively the moving partial averages of u_α and $\frac{\hat{x}_3}{I_\gamma}u_\alpha$ on phase γ, and U_3 is the moving average of u_3 on a period. Here, $\mathbf{u}=(u_i)$ is the 3D displacement vector field.

8.2.4 The constitutive law

The CM2 strains can be expressed in terms of their corresponding dual stresses by the partial derivation of $\mathcal{W}^*$. For example, $\frac{t_\gamma}{t}E^\gamma_{\alpha\beta}$ is the dual of $\Sigma^\gamma_{\alpha\beta}$ and $E^\gamma_{\alpha\beta}=\frac{t}{t_\gamma}\frac{\partial\mathcal{W}^*}{\partial\Sigma^\gamma_{\alpha\beta}}$. In the case of two isotropic phases (Young's modulus E^γ, shear modulus G^γ, Poisson's ratio ν^γ), the following constitutive relations are obtained:

$$\begin{aligned} E^\gamma_{11} &= \frac{\Sigma^\gamma_{11}}{E^\gamma}-\frac{\nu^\gamma}{E^\gamma}\left(\Sigma^\gamma_{22}+\Sigma_{33}\right),\ E^\gamma_{22}=\frac{\Sigma^\gamma_{22}}{E^\gamma}-\frac{\nu^\gamma}{E^\gamma}\left(\Sigma^\gamma_{11}+\Sigma_{33}\right),\\ E^\gamma_{3\alpha} &= \frac{1}{G^\gamma}\left(\frac{6}{5}\Sigma^\gamma_{3\alpha}-\frac{1}{5}\Sigma_{\alpha 3}\right),\ E_{\alpha 3}=\frac{1}{5}\left(\frac{\Sigma_{\alpha 3}}{G^{\hom}}-\overline{\left(\frac{\Sigma_{3\alpha}}{G}\right)}\right),\\ E^\gamma_{12} &= \frac{\Sigma^\gamma_{12}}{2G^\gamma},\ E_{33}=\overline{\left(\frac{1}{E}\right)}\Sigma_{33}-\overline{\frac{\nu}{E}\left(\Sigma_{11}+\Sigma_{22}\right)},\\ \chi^\gamma_{11} &= \frac{1}{E^\gamma I_\gamma}\left(\mu^\gamma_{11}-\nu^\gamma\mu^\gamma_{22}\right),\ \chi^\gamma_{22}=\frac{1}{E^\gamma I_\gamma}\left(\mu^\gamma_{22}-\nu^\gamma\mu^\gamma_{11}\right) \end{aligned} \tag{8.19}$$

and

$$\chi_{12}^{\gamma} = \frac{\mu_{12}^{\gamma}}{2G^{\gamma}I_{\gamma}},\ D_{\alpha} = \frac{\Delta_{\alpha}}{12G^{\hom}}.$$

Let us summarize the CM2: the generalized stresses and displacements are, respectively, $(\boldsymbol{\Sigma}^{\gamma}, \boldsymbol{\mu}^{\gamma}, \Delta_{\alpha})$ with (8.11) and $(U_{\alpha}^{\gamma}, U_3, \phi_{\alpha}^{\gamma})$, $\alpha, \gamma = 1, 2$. The generalized strains are given by (8.18) and they are related to the generalized stresses by the above constitutive equations. The nine balance equations are (8.12), $i, \gamma = 1, 2$, (8.13), $\alpha, \gamma = 1, 2$, and (8.16). The weak formulation of the balance equations (8.17) exhibits nine pairs of dual unknowns (static↔kinematic) on the boundary $\partial\Omega$: $\mu_{\alpha\beta}^{\gamma} n_{\beta} \leftrightarrow \phi_{\alpha}^{\gamma}$,

$\Sigma_{\alpha\beta}^{\gamma} n_{\beta} + \Sigma_{\alpha 3} n_3 \leftrightarrow U_{\alpha}^{\gamma}$, $\overline{\Sigma}_{3\alpha} n_{\alpha} + \Sigma_{33} n_3 \leftrightarrow U_3$. Therefore, boundary conditions are obtained by fixing one unknown for each of these pairs. For example, free boundary conditions are those for which all the static unknowns are null.

Once the CM2 solution has been found, an estimation of the full 3D stresses is obtained by using the localization operator $\boldsymbol{\sigma}^{per}$ given by (8.14-8.15) which relates the 3D stresses to the CM2 stresses.

8.3 Application to out-of-plane shearing

The CM2 solution of the shearing problem of Figure 8.1 is as follows: U_3 and $\phi_1^{(\gamma)}$, $\gamma = 1, 2$, are the only non null CM2 displacement and rotations and they are function of x_1. The compatibility equations (8.18) and the constitutive law are used to determine the non null components: $E_{31}^{\gamma} = U_{3,1} + \phi_1^{\gamma}$ and $E_{13} = -\overline{\phi}_1$ for the strains; and $\chi_{11}^{\gamma} = \phi_{1,1}^{\gamma}$ for the curvatures; Σ_{31}^{γ}, Σ_{13} given by (8.19), $\alpha = 1$, or equivalently by:

$$\Sigma_{31}^{\gamma} = G^{\hom}\left(E_{13} + \frac{1}{6}\overline{E}_{31}\right) + \frac{5}{6}G^{\gamma}E_{31}^{\gamma},\ \Sigma_{13} = G^{\hom}\left(6E_{13} + \overline{E}_{31}\right)$$

for the stresses; and μ_{11}^{γ}, $\mu_{22}^{\gamma} = \nu^{\gamma}\mu_{11}^{\gamma}$ with

$$\mu_{11}^{\gamma} = \frac{E^{\gamma}I_{\gamma}}{1 - \left(\nu^{\gamma}\right)^2}\chi_{11}^{\gamma}$$

for the couple-stresses. Inserting these expressions in the balance equation (8.16), $\overline{\Sigma}_{31,1} = 0$ ($\overline{\Sigma}_{31}$ is uniform), and in the momentum equation (8.13), $\alpha = 1$, $\gamma = 1, 2$, $\mu_{11,1}^{\gamma} - \Sigma_{31}^{\gamma} + \Sigma_{\alpha 3} = 0$, gives a system of three second order differential equations in U_3 and ϕ_1^{γ} which have six fundamental solutions. Due to the symmetry of the problem, the solution (U_3, ϕ_1^{γ}) is a linear combination of only three fundamental solutions: one fundamental solution is such that U_3 is linear and ϕ_1^{γ} is constant, $(V_* x_1, \phi_*^{\gamma})$, and two fundamental solutions are of the form $(U_{\pm}\sinh(s_{\pm}x_1), \phi_{\pm}^{\gamma}\cosh(s_{\pm}x_1))$ where $V_*, \phi_*^{\gamma}, s_{\pm}, U_{\pm}$ and $\phi_{\pm}^{\gamma}$ are constants that are analytically determined in terms of the elastic constants,

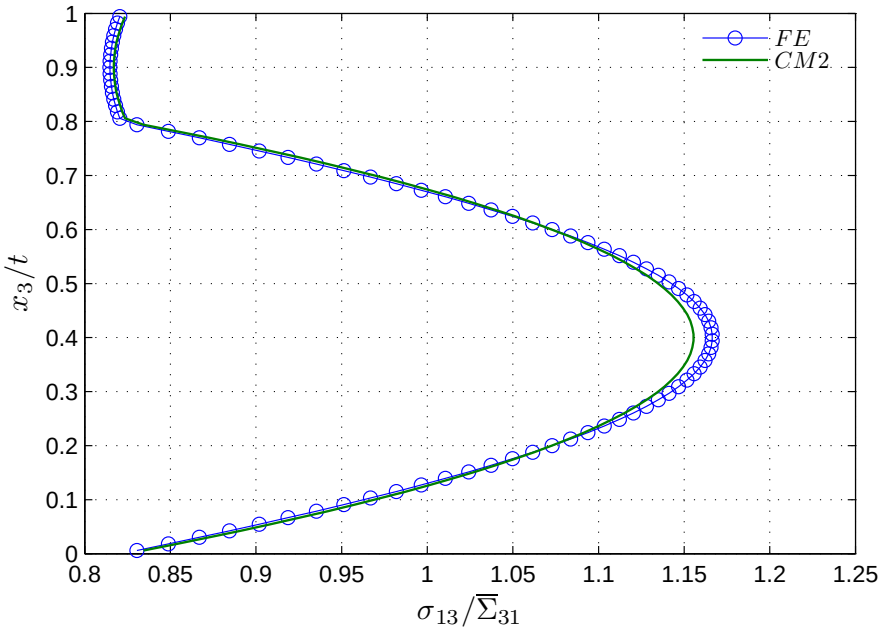

Figure 8.4: Normalized shear stress distribution in section $x_1 = -0.4L$ for $t_1/t_2 = 4$, $E^1/E^2 = 10$ and $\nu^1 = \nu^2 = 0.3$.

t_1 and t_2. The three integration constants (cofactors of the fundamental solutions) are determined thanks to the boundary conditions: $U_3\left(\frac{L}{2}\right) = w$ and $\phi_1^\gamma\left(\frac{L}{2}\right) = 0$.

The effective shear modulus is estimated as $G^{eff} \approx \frac{\overline{\Sigma}_{31}}{2w/L}$ and is plotted in Figure 8.2 versus L/t. Excellent agreement with the FE results is obtained even for small values of the slenderness ratio. In Figures 8.4 and 8.5 the normalized shear and in-plane stresses, respectively $\sigma_{13}/\overline{\Sigma}_{31}$ and $\sigma_{11}/\overline{\Sigma}_{31}$, are plotted at section $x_3 = -0.4L$ and compared to FE results. Here again the agreement is excellent. These Figures show that the assumptions of piecewise-linear σ_{11} and piecewise-quadratic σ_{13} are consistent with the FE results. This is less true as x_3 goes to the boundaries at $\pm L/2$ since the true 3D stress becomes singular. See (Leguillon, 1999). Figure 8.5 shows that both CM2 and FEM σ_{11} are of the same order as $\overline{\Sigma}_{31}$ while σ_{11} is zero in the homogenized theory. Finally, Figure 8.6 shows the normalized external couple applied to layer 1 at the boundaries versus L/t for both CM2 and FEM. A small discrepancy, probably due to numerical integration in the FEM, is observed. It is clear from this Figure that the boundary effect is well captured by CM2 and that it does not vanish as L/t goes to infinity.

In conclusion, we have proposed in this paper a model for 3D periodically layered materials able to reproduce both size and boundary effects. This model can handle $n-$phase periodically layered materials with $4n+1$ kinematic variables at each geometric point: 2 in-plane displacements and 2 rotations per phase + 1 common out-of-plane displacement.

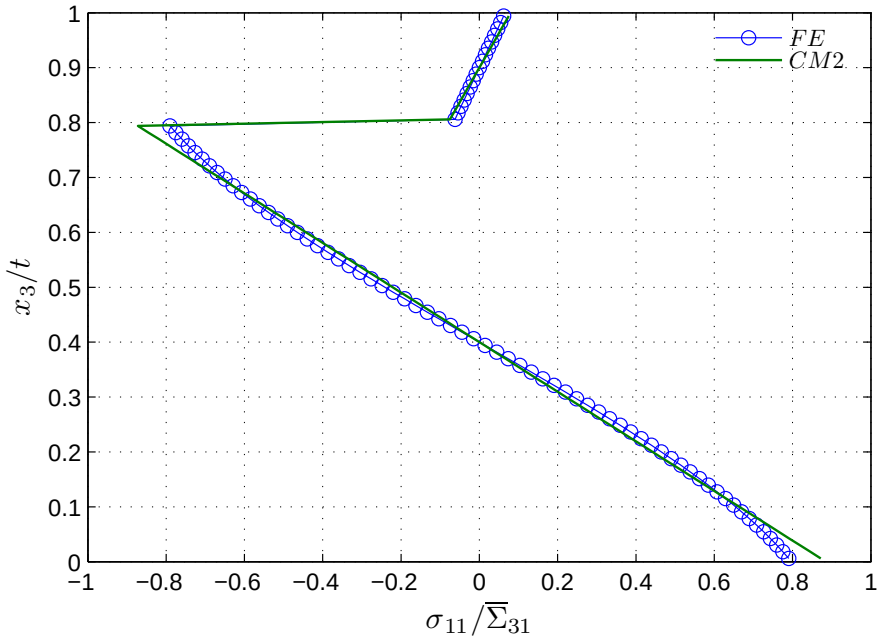

Figure 8.5: Normalized in-plane stress distribution in section $x_1 = -0.4L$ for $t_1/t_2 = 4$, $E^1/E^2 = 10$ and $\nu^1 = \nu^2 = 0.3$.

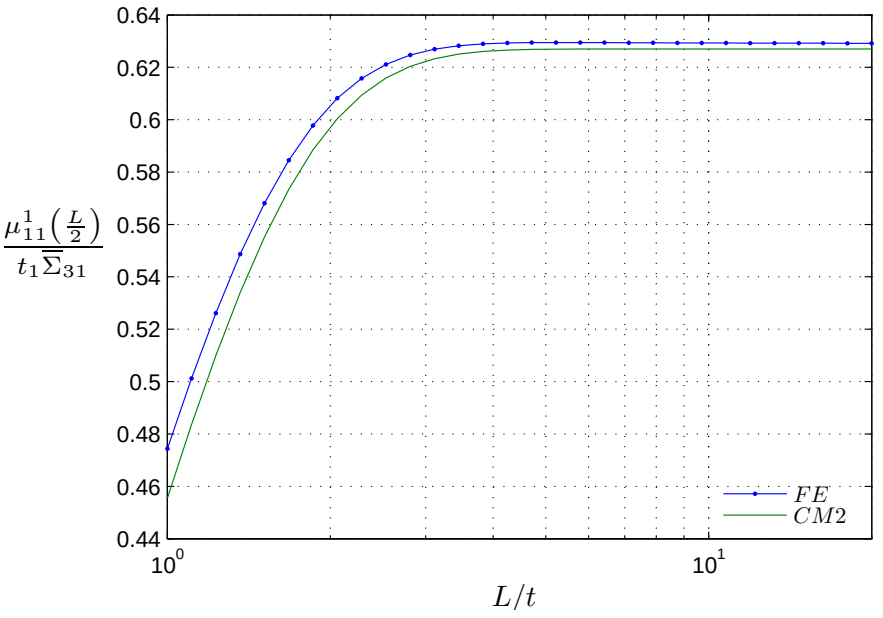

Figure 8.6: Normalized external couple $\frac{\mu^1_{11}}{t_1\overline{\Sigma}_{31}}$ at $x_1 = 0.5L$ vs. L/t for $t_1/t_2 = 4$, $E^1/E^2 = 10$ and $\nu^1 = \nu^2 = 0.3$.

Conclusion Générale

Partant de l'étude d'un nouveau type d'âme de panneau sandwich, ce travail de doctorat a été l'occasion d'approfondir la question du cisaillement transverse dans les plaques. En effet, comme le Chapitre 1 l'a montré, il existe un grand nombre d'approches différentes pour déterminer le comportement des plaques soumises à l'effort tranchant. L'origine principale de cette abondance de travaux est que le modèle de Reissner-Mindlin est différent du second ordre des développements asymptotiques. D'un côté le modèle de Reissner-Mindlin présente une approche assez intuitive du fonctionnement de la plaque et est apprécié des ingénieurs. De l'autre côté, les développements asymptotiques sont une approche rigoureuse pour élaborer un modèle de plaque. D'une certaine façon, en reprenant l'approche de Reissner pour construire un modèle de plaque dans le cas hétérogène au Chapitre 4, on réalise un compromis entre ces deux visions qui donne à la fois une estimation précise de l'état de contrainte généré par l'effort tranchant mais conserve un formalisme analogue au modèle de Reissner-Mindlin (Chapitre 5).

La façon dont nous avons obtenu le modèle de gradient du moment l'apparente aux théories de gradient supérieur. Ces théories sont souvent considérées comme complexes car chaque ordre fait apparaître un grand nombre de variables supplémentaires auxquelles sont respectivement associées des échelles caractéristiques (du type L^* au Chapitre 7). Cependant, on a montré au Chapitre 8 qu'elles permettent aussi de capter des effets de bord en les régularisant.

Enfin, dans le cas général, le modèle de gradient du moment ne peut pas être réduit à un modèle de Reissner-Mindlin. Cet écart entre modèles peut devenir suffisamment important dans le cas des plaques stratifiées anisotropes pour justifier une implémentation complète en éléments finis de ce nouveau modèle. D'un autre côté, on a pu voir aussi que la théorie de gradient du moment se simplifie en une théorie de Reissner-Mindlin dans le cas des plaques homogènes mais aussi dans le cas des panneaux sandwichs pour lesquels l'hypothèse de contraste a été formulée de façon précise.

Dans le cas plus particulier des panneaux sandwichs qui est à l'origine de ce travail de doctorat, nous avons élaboré un schéma direct d'homogénéisation pour la raideur à l'effort tranchant et donné une assise théorique plus forte aux bornes utilisées dans ce domaine (Chapitre 6). Finalement, en

appliquant cet outil au cas d'un panneau sandwich incluant le module à chevrons au Chapitre 7, on a mis en évidence un phénomène de distorsion des peaux, déjà connu dans le cas des nid d'abeilles mais qui est beaucoup plus important dans le cas du module à chevrons. Le phénomène a lieu pour des valeurs de contraste assez fortes et pour un possible doublement de la raideur à l'effort tranchant ce qui explique l'écart entre les bornes obtenues au Chapitre 3.

L'intérêt de cette nouvelle méthode pour calculer la raideur à l'effort tranchant est qu'elle permet d'estimer plus précisément non seulement la flèche d'un panneau sandwich (qui n'est pas négligeable) mais aussi l'état de contrainte local dans le panneau. Cette maîtrise de la localisation des champs offre de nouvelles perspectives dans le calcul de la résistance à l'effort tranchant, ce qui est au cœur des enjeux technologiques du marché des panneaux sandwichs comme l'a montré le Chapitre 2.

Ce travail apporte donc un éclairage supplémentaire sur les questions posées par les effets de l'effort tranchant dans les plaques en général et plus particulièrement dans le cas des panneaux sandwichs. Néanmoins, il soulève un certain nombre de questions qui pourront faire l'objet de développements ultérieurs.

Tout d'abord, en ce qui concerne la théorie de gradient du moment, il est nécessaire de faire une analyse détaillée de ses différences avec le second ordre des développements asymptotiques. Plus particulièrement, comme cela a été indiqué, nous n'avons pas tenu compte du gradient des efforts membranaires, ni de la correction au deuxième ordre de la localisation des champs associés à la flexion et aux efforts membranaires. L'erreur introduite par ces choix devra être estimée. Ensuite, on peut se poser la question de la dégénérescence du modèle de gradient du moment en modèle de Reissner-Mindlin d'une façon plus systématique que les deux cas, homogène et panneau sandwich. Dans le cas des stratifiés, on peut s'intéresser aux travaux de Vannucci and Verchery (2001, 2002) qui utilisent une méthode de décomposition polaire des tenseurs de raideur de Love-Kirchhoff afin d'identifier les configurations menant à des comportement quasi isotropes. Dans le cas des plaques périodiques, il serait intéressant d'identifier les motifs dont la raideur en cisaillement n'est pas négligeable mais qui mènent à des comportements très éloignés du modèle de Reissner-Mindlin ($\Delta^{RM/BG}$ grand) pour mieux comprendre la signification cinématique des variables de gauchissement introduites avec le modèle de gradient du moment. Enfin, comme on l'a indiqué, le modèle de gradient du moment présente des effets de bords car c'est un modèle de gradient supérieur (tout comme le modèle de Reissner-Mindlin). Il serait intéressant d'essayer de séparer le modèle complet en deux problèmes : un problème intérieur, sans effet de bord, et un problème sur le bord qui ne traite que des incompatibilités. Une proposition est faite par Nosier et al. (2001) dans le cas du modèle de Reissner-Mindlin et pourrait être poussée plus avant.

En ce qui concerne le module à chevrons utilisé comme âme de panneau sandwich, il n'a pas vraiment été possible de démontrer une supériorité sur le nid d'abeilles. En effet, même s'il existe

des configurations où le module à chevrons est plus raide à l'effort tranchant que le nid d'abeilles, le critère déterminant est la résistance de l'âme. Cette analyse passe en partie par l'étude numérique des différents modes de ruine comme l'effectuent Pahr and Rammerstorfer (2006) dans le cas du nid d'abeilles, mais aussi par un travail expérimental poussé, qui n'a pas été entrepris au cours de ce doctorat. En effet, même si la simulation numérique est un excellent outil d'investigation systématique, la méthode expérimentale reste le seul moyen pour comparer les comportements prédits par les différents modèles et la réalité.

ANNEXE

A

Annexes

A.1 The Reissner-Mindlin homogeneous plate

We recall here in details the Reissner-Mindlin model for a homogeneous plate.

A.1.1 The 3D model

We consider a linear elastic plate of thickness h occupying the 3D domain $\Omega = \omega \times]-h/2, h/2[$, where $\omega \subset \mathbb{R}^2$ is the mid-plane of the plate (Figure A.1). Cartesian coordinates (x_1, x_2, x_3) in the reference frame $(\widetilde{\boldsymbol{e}}_1, \widetilde{\boldsymbol{e}}_2, \widetilde{\boldsymbol{e}}_3)$ are used. The constitutive material is assumed to be homogeneous. The plate is loaded on its upper and lower faces $\omega^{\pm} = \omega \times \{\pm h/2\}$ with the distributed force $\widetilde{\boldsymbol{T}}^{\pm}$. There are also body forces $\widetilde{\boldsymbol{f}}(x_3)$ and the plate is clamped on its lateral edge, $\partial\omega \times]-h/2, h/2[$ where $\partial\omega$ is the edge of ω.

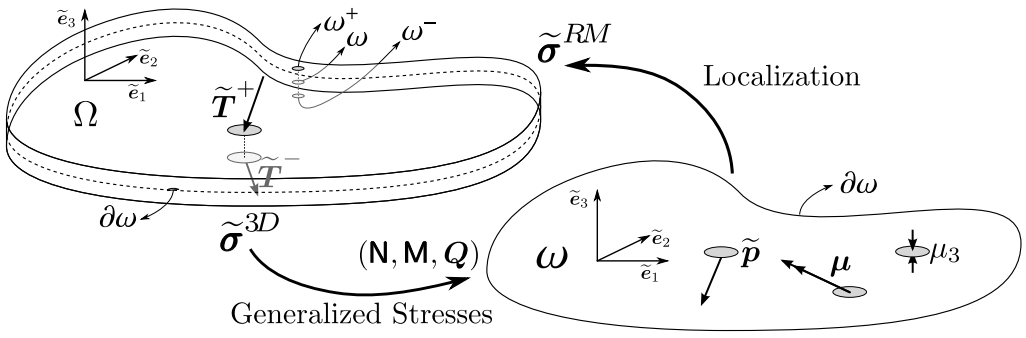

Figure A.1: The homogeneous plate configuration

The 3D problem $\mathcal{P}^{3D}$ is summarized as follows:

$$\mathcal{P}^{3D}\begin{cases}\widetilde{\boldsymbol{\sigma}}\cdot\widetilde{\boldsymbol{\nabla}}=0 \quad \text{on } \Omega. & \text{(A.1a)}\\ \widetilde{\boldsymbol{\sigma}}=\widetilde{\boldsymbol{\mathcal{C}}}:\widetilde{\boldsymbol{\varepsilon}} \quad \text{on } \Omega. & \text{(A.1b)}\\ \widetilde{\boldsymbol{\sigma}}\cdot\widetilde{\boldsymbol{e}}_3=\widetilde{\boldsymbol{T}}^{\pm} \quad \text{on } \omega^{\pm}. & \text{(A.1c)}\\ \widetilde{\boldsymbol{\varepsilon}}=\dfrac{1}{2}\left(\widetilde{\boldsymbol{\nabla}}\otimes\widetilde{\boldsymbol{u}}+\widetilde{\boldsymbol{u}}\otimes\widetilde{\boldsymbol{\nabla}}\right) \quad \text{on } \Omega. & \text{(A.1d)}\\ \widetilde{\boldsymbol{u}}=0 \quad \text{on } \partial\omega\times]-h/2,h/2[. & \text{(A.1e)}\end{cases}$$

where $\widetilde{\boldsymbol{u}}$ is the 3D displacement vector field, $\widetilde{\boldsymbol{\varepsilon}}$ is the strain tensor field and $\widetilde{\boldsymbol{\sigma}}$ is the stress tensor field. The external work is:

$$V_{ext}^{3D}=\int_{\omega}\widetilde{\boldsymbol{T}}^{+}\cdot\widetilde{\boldsymbol{u}}^{3D+}+\widetilde{\boldsymbol{T}}^{-}\cdot\widetilde{\boldsymbol{u}}^{3D-}+\left\langle\widetilde{\boldsymbol{f}}\cdot\widetilde{\boldsymbol{u}}^{3D}\right\rangle d\omega, \tag{A.2}$$

The 3D elasticity stiffness tensor is written using the spectrum decomposition:

$$\widetilde{\boldsymbol{\mathcal{C}}}=\frac{E}{1+\nu}\widetilde{\boldsymbol{I}}+\frac{3\nu E}{(1+\nu)(1-2\nu)}\widetilde{\boldsymbol{\jmath}} \tag{A.3}$$

where $I_{ijkl}=\frac{1}{2}\left(\delta_{ik}\delta_{jl}+\delta_{il}\delta_{jk}\right)$ is the identity for 3D elasticity and $\jmath_{ijkl}=\frac{1}{3}\delta_{ij}\delta_{kl}$.

A.1.2 Reissner-Mindlin compatible fields

A.1.2.1 Statically compatible fields

The generalized Reissner-Mindlin stresses associated to the 3D stress field $\widetilde{\boldsymbol{\sigma}}$ are:

$$\begin{cases}\mathsf{N}_{\alpha\beta}\left(x_1,x_2\right)=\langle\sigma_{\alpha\beta}\rangle & \text{(A.4a)}\\ \mathsf{M}_{\alpha\beta}\left(x_1,x_2\right)=\langle x_3\sigma_{\alpha\beta}\rangle & \text{(A.4b)}\\ Q_{\alpha}\left(x_1,x_2\right)=\langle\sigma_{\alpha3}\rangle & \text{(A.4c)}\end{cases}$$

where N is the membrane stress, M the bending moment, and $\boldsymbol{Q}$ the shear forces.

Reissner-Mindlin equilibrium equations are obtained by integrating Equations (A.1a) and $x_3\times$(A.1a) with respect to x_3 leading to:

$$\begin{cases}\langle\sigma_{\alpha\beta,\beta}\rangle+\left[\sigma_{\alpha3}\right]_{-h/2}^{h/2}+\langle f_{\alpha}\rangle=0\\ \langle\sigma_{\alpha3,\alpha}\rangle+\left[\sigma_{33}\right]_{-h/2}^{h/2}+\langle f_3\rangle=0\\ \langle x_3\sigma_{\alpha\beta,\beta}\rangle-\langle\sigma_{\alpha3}\rangle+\left[x_3\sigma_{\alpha3}\right]_{-h/2}^{h/2}+\langle x_3f_{\alpha}\rangle=0\end{cases}$$

Using boundary conditions (A.1c) and volume forces yields:

$$\begin{cases} \mathsf{N}_{\alpha\beta,\beta} + p_\alpha = 0 & \text{(A.5a)} \\ Q_{\alpha,\alpha} + p_3 = 0 & \text{(A.5b)} \\ \mathsf{M}_{\alpha\beta,\beta} - Q_\alpha + \mu_\alpha = 0 & \text{(A.5c)} \end{cases}$$

where $p_i = T_i^+ + T_i^- + \langle f_i \rangle$ are symmetric loadings per unit surface and $\mu_i = \frac{h}{2}(T_i^+ - T_i^-) + \langle x_3 f_i \rangle$ are skew-symmetric loadings per unit surface. More precisely, $\boldsymbol{p} = (p_\alpha)$ are membrane loadings per unit surface, p_3 is the out-of-plane loading per unit surface, $\boldsymbol{\mu} = (\mu_\alpha)$ are couples per unit surface and μ_3 is the transverse bulk loading.

Following Nguyen et al. (2005b) a fourth equilibrium equation involving transverse bulk is introduced:

$$Q_3 = \mu_3 \tag{A.6}$$

where $Q_3 = \frac{h}{2}\left(\sigma_{33}\left(x_1, x_2, \frac{h}{2}\right) + \sigma_{33}\left(x_1, x_2, -\frac{h}{2}\right)\right)$.

A.1.2.2 Kinematically compatible fields

Multiplying Equation (A.5) with U_α, Equation (A.5) with U_3, Equation (A.5) with φ_α and Equation (A.6) with φ_3, integrating by parts on the domain ω and summing all equations leads to the weak formulation of the plate model:

$$V_{int}^{RM} = V_{ext}^{RM}$$

where

$$V_{int}^{RM} = \int_\omega \mathbf{N} : (\boldsymbol{i} : (\boldsymbol{\nabla} \otimes \boldsymbol{U})) + \mathbf{M} : (\boldsymbol{i} : (\boldsymbol{\nabla} \otimes \boldsymbol{\varphi})) + \boldsymbol{Q} \cdot (\boldsymbol{\varphi} + \boldsymbol{\nabla} U_3) + Q_3 \varphi_3 d\omega \tag{A.7}$$

$$V_{ext}^{RM} = \int_\omega \widetilde{\boldsymbol{p}} \cdot \widetilde{\boldsymbol{U}} + \widetilde{\boldsymbol{\mu}} \cdot \widetilde{\boldsymbol{\varphi}} d\omega + \int_{\partial\omega} (\mathbf{N} \cdot \boldsymbol{n}) \cdot \boldsymbol{U} + (\mathbf{M} \cdot \boldsymbol{n}) \cdot \boldsymbol{\varphi} + (\boldsymbol{Q} \cdot \boldsymbol{n}) U_3 dl \tag{A.8}$$

and $\boldsymbol{n}$ is the in-plane unit vector outwardly normal to ω.

Dual strains are identified in V_{int}^{RM} as:

$$\mathbf{e} = \boldsymbol{i} : (\boldsymbol{\nabla} \otimes \boldsymbol{U}), \quad \boldsymbol{\chi} = \boldsymbol{i} : (\boldsymbol{\nabla} \otimes \boldsymbol{\varphi}), \quad \boldsymbol{\gamma} = \boldsymbol{\varphi} + \boldsymbol{\nabla} U_3 \quad \text{and} \quad \varphi_3 \tag{A.9}$$

where $\mathsf{e}_{\alpha\beta}$ is the membrane strain, $\chi_{\alpha\beta}$ is the curvature, γ_α is the shear strain and φ_3 the transverse bulk. Since we have assumed the plate is clamped, there is no external work on the edge $\partial\omega$ in V_{ext}^{RM} (Equation A.8). This leads to the following condition on $\widetilde{\boldsymbol{U}}$ and $\boldsymbol{\varphi}$ for clamped edges:

$$\widetilde{\boldsymbol{\varphi}} = \widetilde{\mathbf{0}} \quad \text{and} \quad \widetilde{\boldsymbol{U}} = \widetilde{\mathbf{0}} \quad \text{on } \partial\omega$$

and finally:

$$V_{ext}^{RM} = \int_\omega \widetilde{\boldsymbol{p}} \cdot \widetilde{\boldsymbol{U}} + \widetilde{\boldsymbol{\mu}} \cdot \widetilde{\boldsymbol{\varphi}} d\omega \tag{A.10}$$

Dual strains have been defined previously using standard dualization techniques. In order to recover a physical meaning for $(\mathbf{e}, \boldsymbol{\chi}, \boldsymbol{\gamma}, \varphi_3)$ it is of interest to compare the external work for the Reissner-Mindlin plate model and the external work for the $3D$ problem (Equation A.2).

First, if we assume no volume force $\widetilde{\boldsymbol{f}} = \widetilde{\mathbf{0}}$, we have:

$$V_{ext}^{3D} = \int_\omega \widetilde{\boldsymbol{T}}^+ \cdot \widetilde{\boldsymbol{u}}^{3D+} + \widetilde{\boldsymbol{T}}^- \cdot \widetilde{\boldsymbol{u}}^{3D-} d\omega \tag{A.11}$$

which can be rewritten as:

$$V_{ext}^{3D} = \int_\omega \widetilde{\boldsymbol{p}} \cdot \widetilde{\boldsymbol{U}}^{3D} + \widetilde{\boldsymbol{\mu}} \cdot \widetilde{\boldsymbol{\varphi}}^{3D} d\omega \tag{A.12}$$

with the following definitions:

$$\widetilde{\boldsymbol{U}}^{3D} = \frac{\widetilde{\boldsymbol{u}}^{3D+} + \widetilde{\boldsymbol{u}}^{3D-}}{2}, \quad \widetilde{\boldsymbol{\varphi}}^{3D} = \frac{\widetilde{\boldsymbol{u}}^{3D+} - \widetilde{\boldsymbol{u}}^{3D-}}{h} \tag{A.13}$$

Thus setting $\widetilde{\boldsymbol{U}} = \widetilde{\boldsymbol{U}}^{3D}$ and $\widetilde{\boldsymbol{\varphi}} = \widetilde{\boldsymbol{\varphi}}^{3D}$ ensures identical external work for the Reissner-Mindlin plate model and the $3D$ model.

However, another choice is possible. Let us assume $\widetilde{\boldsymbol{T}}^{\pm} = \widetilde{\mathbf{0}}$ and $\widetilde{\boldsymbol{f}}(x_3) = \widetilde{\boldsymbol{r}} + x_3 \widetilde{\boldsymbol{s}}$. We have: $\widetilde{\boldsymbol{p}} = h\widetilde{\boldsymbol{r}}$ and $\widetilde{\boldsymbol{\mu}} = \frac{h^3}{12}\widetilde{\boldsymbol{s}}$ and:

$$V_{ext}^{3D} = \int_\omega \left\langle \widetilde{\boldsymbol{f}} \cdot \widetilde{\boldsymbol{u}}^{3D} \right\rangle d\omega \tag{A.14}$$

which can be rewritten as:

$$V_{ext}^{3D} = \int_\omega \widetilde{\boldsymbol{p}} \cdot \widetilde{\boldsymbol{U}}^{3D} + \widetilde{\boldsymbol{\mu}} \cdot \widetilde{\boldsymbol{\varphi}}^{3D} d\omega \tag{A.15}$$

with the following definitions:

$$\widetilde{\boldsymbol{U}}^{3D} = \frac{\left\langle \widetilde{\boldsymbol{u}}^{3D} \right\rangle}{h}, \quad \widetilde{\boldsymbol{\varphi}}^{3D} = \frac{12 \left\langle x_3 \widetilde{\boldsymbol{u}}^{3D} \right\rangle}{h^3} \tag{A.16}$$

Thus setting $\widetilde{\boldsymbol{U}} = \widetilde{\boldsymbol{U}}^{3D}$ and $\widetilde{\boldsymbol{\varphi}} = \widetilde{\boldsymbol{\varphi}}^{3D}$ ensures also identical external work for the Reissner-Mindlin plate model and the $3D$ model.

Actually, both definition are very close when the plate is homogeneous and slender. In this case, it is possible to perform a Taylor expansion of the $3D$ displacement in x_3 direction:

$$u_i^{3D} = u_i^{3D}(x_1, x_2, 0) + x_3 u_{i,3}^{3D}(x_1, x_2, 0) + \frac{x_3^2}{2} u_{i,33}^{3D}(x_1, x_2, 0) + \frac{x_3^3}{6} u_{i,333}^{3D}(x_1, x_2, 0)$$

$$u_i^{3D} = \overline{u}_i^{3D} + x_3\overline{u}_{i,3}^{3D} + \frac{x_3^2}{2}\overline{u}_{i,33}^{3D} + \frac{x_3^3}{6}\overline{u}_{i,333}^{3D}$$

and we have:

$$\frac{\widetilde{\boldsymbol{u}}^{3D+} + \widetilde{\boldsymbol{u}}^{3D-}}{2} = \overline{u}_i^{3D} + \frac{h^2}{4}\overline{u}_{i,33}^{3D}, \quad \frac{\widetilde{\boldsymbol{u}}^{3D+} - \widetilde{\boldsymbol{u}}^{3D-}}{h} = \overline{u}_{i,3}^{3D} + \frac{h^2}{48}\overline{u}_{i,333}^{3D} \tag{A.17}$$

$$\frac{\left\langle \widetilde{\boldsymbol{u}}^{3D} \right\rangle}{h} = \overline{u}_i^{3D} + \frac{h^2}{24}\overline{u}_{i,33}^{3D}, \quad \frac{12\left\langle x_3\widetilde{\boldsymbol{u}}^{3D} \right\rangle}{h^3} = \overline{u}_{i,3}^{3D} + \frac{h^2}{32}\overline{u}_{i,333}^{3D} \tag{A.18}$$

Thus, both definitions are identical at first order and we have:

$$\widetilde{\boldsymbol{U}} \simeq \frac{\widetilde{\boldsymbol{u}}^{3D+} + \widetilde{\boldsymbol{u}}^{3D-}}{2} \simeq \frac{\left\langle \widetilde{\boldsymbol{u}}^{3D} \right\rangle}{h} \simeq \overline{u}_i^{3D} \tag{A.19}$$

$$\widetilde{\boldsymbol{\varphi}} \simeq \frac{\widetilde{\boldsymbol{u}}^{3D+} - \widetilde{\boldsymbol{u}}^{3D-}}{h} \simeq \frac{12\left\langle x_3\widetilde{\boldsymbol{u}}^{3D} \right\rangle}{h^3} \simeq \overline{u}_{i,3}^{3D} \tag{A.20}$$

Finally, U_i is the translation of the plate mid-plane, φ_α is a vector related to the local rotation with respect to in-plane axes and φ_3 is a variable related to Poisson's effect in the transverse direction. The actual rotation pseudo vector corresponding to $\boldsymbol{\varphi}$ is $\boldsymbol{\theta} = \left(\begin{smallmatrix} -\varphi_2 \\ \varphi_1 \end{smallmatrix}\right)$.

A.1.3 Localization

The derivation of localization fields is the same as the one performed in Chapter 4.

The stress field is:

$$\begin{cases} \boldsymbol{\sigma}^{(\mathsf{N})}(x_1,x_2,x_3) = \dfrac{1}{h}\mathbf{N}(x_1,x_2) \quad \text{and } \sigma_{i3}^{(\mathsf{N})} = 0 & \text{(A.21a)} \\ \boldsymbol{\sigma}^{(\mathsf{M})}(x_1,x_2,x_3) = \dfrac{12x_3}{h^3}\mathbf{M}(x_1,x_2) \quad \text{and } \sigma_{i3}^{(\mathsf{M})} = 0 & \text{(A.21b)} \\ \sigma_{\alpha3}^{(Q)} = \dfrac{3}{2}\left(1 - \left(\dfrac{2x_3}{h}\right)^2\right)\dfrac{Q_\alpha}{h}, \quad \sigma_{\alpha\beta}^{(Q)} = 0 \quad \text{and} \quad \sigma_{33}^{(Q)} = 0 & \text{(A.21c)} \end{cases}$$

The strain field is derived using the $3D$ constitutive equation:

$$\begin{cases} \boldsymbol{\varepsilon}^{(\mathsf{e})}(x_1,x_2,x_3) = \mathbf{e}(x_1,x_2) \quad \text{and } \varepsilon_{i3}^{(\mathsf{e})} = 0 & \text{(A.22a)} \\ \boldsymbol{\varepsilon}^{(\chi)}(x_1,x_2,x_3) = x_3\boldsymbol{\chi}(x_1,x_2) \quad \text{and } \varepsilon_{i3}^{(\chi)} = 0 & \text{(A.22b)} \\ \varepsilon_{\alpha3}^{(\gamma)} = \dfrac{5}{8}\left(1 - \left(\dfrac{2x_3}{h}\right)^2\right)\gamma_\alpha, \quad \varepsilon_{\alpha\beta}^{(\gamma)} = 0 \quad \text{and} \quad \varepsilon_{33}^{(\gamma)} = 0 & \text{(A.22c)} \end{cases}$$

A.1.4 Constitutive equations

Constitutive equations a derived using localization fields and:

$$w^{*RM}(\mathbf{N}, \mathbf{M}, \boldsymbol{Q}) = \frac{1}{2} \left\langle \widetilde{\boldsymbol{\sigma}}^{RM} : \widetilde{\boldsymbol{\mathcal{S}}} : \widetilde{\boldsymbol{\sigma}}^{RM} \right\rangle \tag{A.23}$$

This leads to:

$$\mathbf{N} = h\boldsymbol{c} : \mathbf{e}, \quad \mathbf{M} = \frac{h^3}{12}\boldsymbol{c} : \boldsymbol{\chi}, \quad \boldsymbol{Q} = \frac{5}{6}Gh\boldsymbol{\gamma} \tag{A.24}$$

where $\boldsymbol{c}$ is the plane-stress 2D stiffness tensor. Its spectrum decomposition is:

$$\boldsymbol{c} = \frac{E}{1+\nu}\boldsymbol{i} + \frac{2\nu E}{1-\nu^2}\boldsymbol{j} \tag{A.25}$$

where $i_{\alpha\beta\gamma\delta} = \frac{1}{2}\left(\delta_{\alpha\gamma}\delta_{\beta\delta} + \delta_{\alpha\delta}\delta_{\beta\gamma}\right)$ is the identity for 2D elasticity and $j_{\alpha\beta\gamma\delta} = \frac{1}{3}\delta_{\alpha\beta}\delta_{\gamma\delta}$.

A.2 Justification of bounds for the shear forces stiffness of sandwich panels

In Chapter 6, Section 6.2.4, is provided justification of bounds for the transverse shear stiffness of sandwich panels. Here the computation details are given.

A.2.1 Upper bounds for sandwich panels shear forces stiffness

A.2.1.1 Voigt upper bound

We choose the following kinematically compatible strain field:

$$\varepsilon^+_{\alpha 3} = \begin{cases} 0 & \text{on } Y^{s\pm} \\ \frac{\gamma}{2} & \text{on } Y^c \end{cases} \qquad \text{and} \quad \varepsilon^+_{\alpha\beta} = \varepsilon^+_{33} = 0 \tag{A.26}$$

$\boldsymbol{\varepsilon}^+$ enforces a uniform transverse shear strain in the core. $\boldsymbol{\varepsilon}^+$ is related to the following displacement field:

$$\boldsymbol{u}^+ = \begin{cases} \pm\frac{t_c}{2}\boldsymbol{\gamma} & \text{on } Y^{s\pm} \\ \boldsymbol{\gamma} y_3 & \text{on } Y^c \end{cases} \qquad \text{and} \quad u^+_3 = 0 \tag{A.27}$$

With this trial strain field $\boldsymbol{\varepsilon}^+$ the potential energy (6.20) of the Reissner-Mindlin shear auxiliary problem $\mathcal{P}^{(Q)}$ becomes:

$$P^{(Q)}\left(\widetilde{\boldsymbol{\varepsilon}}^+\right) = \frac{1}{2}\gamma_\alpha \left\langle \mathcal{C}^c_{\alpha 3\beta 3}\right\rangle_c \gamma_\beta - \frac{3}{2}\frac{t_c(h^2 - t_c^2)}{h^3 - t_c^3}\gamma_\alpha Q_\alpha \tag{A.28}$$

We denote the correction related to skins thickness: $k_s = \frac{3}{2}\frac{t_c(h^2-t_c^2)}{h^3-t_c^3} \simeq 1 - \frac{t_s}{t_c}$.

Minimizing $P^{(Q)}\left(\widetilde{\boldsymbol{\varepsilon}}^+\right)$ with respect to $\boldsymbol{\gamma}$ leads to:

$$\boldsymbol{\gamma} = k_s \left\langle \mathbf{C}^c\right\rangle_c^{-1} \cdot \boldsymbol{Q} \tag{A.29}$$

where $\mathsf{C}^c_{\alpha\beta} = \mathcal{C}^c_{\alpha 3\beta 3}$ is the transverse shear part of the 3D stiffness tensor. Finally the potential energy for the Reissner-Mindlin auxiliary problem is:

$$P^{(Q)}\left(\widetilde{\boldsymbol{\varepsilon}}^+\right) = -\frac{1}{2}{}^t\boldsymbol{Q} \cdot k_s^2 \left\langle \mathbf{C}^c\right\rangle_c^{-1} \cdot \boldsymbol{Q} \tag{A.30}$$

which leads to the Voigt upper bound:

$$\forall \boldsymbol{Q}, \quad {}^t\boldsymbol{Q} \cdot k_s^2 \left\langle \mathbf{C}^c\right\rangle_c^{-1} \cdot \boldsymbol{Q} < {}^t\boldsymbol{Q} \cdot \mathbf{f} \cdot \boldsymbol{Q} \tag{A.31}$$

A.2.1.2 The upper bound from Kelsey et al.

It is possible to give a sharper bound. We still assume a uniform displacement $\widetilde{\boldsymbol{u}}^{K+} = \frac{t_c}{2}\widetilde{\boldsymbol{\gamma}}$ in the the skins and suggest the following auxiliary problem in the core:

$$\mathcal{P}^{K+}\begin{cases} \widetilde{\boldsymbol{\sigma}}^{K+} \cdot \widetilde{\boldsymbol{\nabla}} = 0 & \text{(A.32a)} \\ \widetilde{\boldsymbol{\sigma}}^{K+} = \widetilde{\boldsymbol{\mathcal{C}}}\left(\widetilde{\boldsymbol{y}}\right) : \left(\widetilde{\boldsymbol{\nabla}} \otimes^{s} \widetilde{\boldsymbol{u}}^{K+}\right) & \text{(A.32b)} \\ \widetilde{\boldsymbol{u}}^{K+} = \pm\dfrac{t_c}{2}\boldsymbol{\gamma} \text{ on interface faces } \partial Y_{int}^{\pm} & \text{(A.32c)} \\ \widetilde{\boldsymbol{\sigma}}^{K+} \cdot \widetilde{\boldsymbol{n}} \text{ skew-periodic on } \partial Y_l^c & \text{(A.32d)} \\ \widetilde{\boldsymbol{u}}^{K+}(y_1, y_2, y_3) \quad (y_1, y_2)\text{-periodic on } \partial Y_l^c & \text{(A.32e)} \end{cases}$$

This auxiliary problem is exactly the one suggested by Kelsey et al. (1958) for deriving upper bounds of sandwich panels shear forces stiffness. The potential energy of this problem is:

$$P^{K+}\left(\widetilde{\boldsymbol{\varepsilon}}^{K+}\right) = \frac{1}{2}\left\langle {}^{t}\widetilde{\boldsymbol{\varepsilon}} : \widetilde{\boldsymbol{\mathcal{C}}}^{c}(\widetilde{\boldsymbol{y}}) : \widetilde{\boldsymbol{\varepsilon}}\right\rangle_{c} \tag{A.33}$$

it is a quadratic form of $\boldsymbol{\gamma}$ which can be written as:

$$P^{K+}\left(\widetilde{\boldsymbol{\varepsilon}}^{K+}\right) = \frac{1}{2}{}^{t}\boldsymbol{\gamma} \cdot t_c \mathsf{C}_{\alpha\beta}^{K+} \cdot \boldsymbol{\gamma} \tag{A.34}$$

Then the potential energy of the core and the skins becomes:

$$P^{(Q)}\left(\widetilde{\boldsymbol{\varepsilon}}^{K+}\right) = \frac{1}{2}{}^{t}\boldsymbol{\gamma} \cdot t_c \mathsf{C}_{\alpha\beta}^{K+} \cdot \boldsymbol{\gamma} - k_s \boldsymbol{\gamma} \cdot \boldsymbol{Q} \tag{A.35}$$

and the minimization over $\boldsymbol{\gamma}$ leads to:

$$P^{(Q)}\left(\widetilde{\boldsymbol{\varepsilon}}^{K+}\right) = -\frac{1}{2}{}^{t}\boldsymbol{Q} \cdot k_s^2 \left(t_c \mathsf{C}_{\alpha\beta}^{K+}\right)^{-1} \cdot \boldsymbol{Q} \tag{A.36}$$

Then the related shear forces stiffness is: $\mathsf{F}^{K+} = \frac{t_c \mathsf{C}_{\alpha\beta}^{K+}}{k_s^2}$ which is the upper bound for shear forces stiffness from Kelsey et al..

A.2.2 Lower bound for sandwich panels shear forces stiffness

A.2.2.1 Reuss lower bound

We choose a statically compatible stress field of the form:

$$\sigma^-_{\alpha 3} = \begin{cases} \pm\frac{3}{2}\frac{h^2}{h^3-t_c^3}\left(1-\left(\frac{2y_3}{h}\right)^2\right)Q_\alpha & \text{on } Y^{s\pm} \\ \frac{3}{2}\frac{h^2-t_c^2}{h^3-t_c^3}Q_\alpha & \text{on } Y^c \end{cases} \qquad \text{and} \quad \sigma^-_{\alpha\beta} = \sigma^-_{33} = 0 \tag{A.37}$$

$\boldsymbol{\sigma}^-$ is uniform in the core and fulfils traction free boundary conditions on the upper and lower faces. With this definition of $\boldsymbol{\sigma}^-$, the complementary energy becomes:

$$P^{*(Q)}\left(\widetilde{\boldsymbol{\sigma}}^-\right) = \frac{1}{2}{}^t\boldsymbol{Q}\cdot\left(\frac{k_s^2}{t_c^2}\left\langle \mathsf{S}^c\right\rangle_c + \frac{k_s^2}{15}\frac{t_s\left(6t_s^2-15t_sh+10h^2\right)}{t_c^2(h-t_s)^2}\mathsf{S}^s\right)\cdot\boldsymbol{Q} \tag{A.38}$$

where $\mathsf{S}^c_{\alpha\beta} = 4\mathcal{S}^c_{\alpha 3\beta 3}$ and $\mathsf{S}^s_{\alpha\beta} = 4\mathcal{S}^s_{\alpha 3\beta 3}$ are the transverse shear parts of the 3D compliances.

A.2.2.2 The lower bound from Kelsey et al.

The complementary energy of the $\mathcal{P}^{K-}$ problem is (Equation (6.49)) :

$$P^{*K-}\left(\widetilde{\boldsymbol{\sigma}}^{K-}\right) = \frac{1}{2}\left\langle {}^t\widetilde{\boldsymbol{\sigma}}^{K-} : \widetilde{\boldsymbol{\mathcal{S}}}^c(\widetilde{\boldsymbol{y}}) : \widetilde{\boldsymbol{\sigma}}^{K-}\right\rangle_c \tag{A.39}$$

it is a quadratic form of $\boldsymbol{Q}$ which can be written as:

$$P^{*K-}\left(\widetilde{\boldsymbol{\sigma}}^{K-}\right) = \frac{1}{2}{}^t\boldsymbol{Q}\cdot k_s^2\frac{\mathsf{S}^{K-}_{\alpha\beta}}{t_c}\cdot\boldsymbol{Q} \tag{A.40}$$

Again, the complementary energy of problems in the skins $\mathcal{P}^{K-,s\pm}$ is (Equation (6.50)):

$$P^{*K-,s\pm}\left(\widetilde{\boldsymbol{\sigma}}^{K-}\right) = \frac{1}{2}\left\langle {}^t\widetilde{\boldsymbol{\sigma}}^{K-} : \widetilde{\boldsymbol{\mathcal{S}}}^c(\widetilde{\boldsymbol{y}}) : \widetilde{\boldsymbol{\sigma}}^{K-}\right\rangle_s \tag{A.41}$$

it is a quadratic form of $\boldsymbol{Q}$ where it is possible to bring out the correction for thick skins:

$$P^{*K-,s\pm}\left(\widetilde{\boldsymbol{\sigma}}^{K-}\right) = \frac{1}{2}{}^t\boldsymbol{Q}\cdot\mathbf{f}^{K-,s\pm}\cdot\boldsymbol{Q} \tag{A.42}$$

Then the complementary energy of the core and the skins becomes:

$$P^{*(Q)}\left(\widetilde{\boldsymbol{\sigma}}^{K-}\right) = \frac{1}{2}{}^t\boldsymbol{Q}\cdot\left(\mathbf{f}^{K-}+\mathbf{f}^{K-,s+}+\mathbf{f}^{K-,s-}\right)\cdot\boldsymbol{Q} \tag{A.43}$$

where $\mathbf{f}^{K-} = k_s^2\frac{\mathsf{S}^{K-}_{\alpha\beta}}{t_c}$ is the lower bound for shear forces stiffness from Kelsey et al..

A.3 Implementation of the Bending-Gradient homogenization scheme with plate elements

All the developments in Chapter 6 for deriving the Bending-Gradient localization fields of periodic plates are valid for 3D continuum mechanics. However, sandwich panels with core made of honeycomb structures or folded material are mostly made of thin facets. In order to limit computational cost, it is much more relevant to model the unit-cell of these panels with plate elements: the facets. In this case, the 3D fields in the auxiliary problems $\mathcal{P}^{(\mathtt{e},\chi),bis}$ and $\mathcal{P}^{(\mathtt{R})}$ are replaced by plate generalized stresses, translations and rotations. In this section we provide some adaptation of auxiliary problems to plate fields.

First, boundary conditions in the Love-Kirchhoff auxiliary problem are modified so that it takes into account the rotation sfield. Then the volume force related to $\mathbf{R}$ is turned into plates loadings $\widetilde{\boldsymbol{p}}$ and $\boldsymbol{\mu}$.

A.3.1 Boundary conditions in the Love-Kirchhoff auxiliary problem

In the Love-Kirchhoff auxiliary problem $\mathcal{P}^{(\mathtt{e},\chi),bis}$ (Equation (6.11)), displacements are enforced on the edge of the cell. These displacements are related to the Love-Kirchhoff kinematics on the overall unit-cell. Since the facets are small plates, one have to adapt these boundary conditions to the facets local kinematics: the displacement $\widetilde{\boldsymbol{U}}^{\dagger}$ and the rotation $\boldsymbol{\theta}^{\dagger}$.

First, let us recall the overall Love-Kirchhoff kinematic on the unit-cell (Equation (6.11), Figure 1.1):

$$\widetilde{\boldsymbol{U}}^{LK} = \widetilde{\boldsymbol{U}}^{per} + \widetilde{\boldsymbol{e}} \cdot \widetilde{\boldsymbol{y}} + y_3 \widetilde{\boldsymbol{\chi}} \cdot \widetilde{\boldsymbol{y}} - \frac{1}{2} \left({}^t\widetilde{\boldsymbol{y}} \cdot \widetilde{\boldsymbol{\chi}} \cdot \widetilde{\boldsymbol{y}} \right) \widetilde{\boldsymbol{e}}_3 \tag{A.44}$$

Since the size of the unit-cell in its plane is not negligible with respect to its thickness, one have to take also into account rotation fields. Rotations are related to the skew-symmetric part of the gradient of the displacement:

$$\widetilde{\boldsymbol{\Theta}} = \frac{1}{2} \left(\widetilde{\boldsymbol{U}} \otimes \widetilde{\boldsymbol{\nabla}} - \widetilde{\boldsymbol{\nabla}} \otimes \widetilde{\boldsymbol{U}} \right)$$

$\widetilde{\boldsymbol{\Theta}}$ is a skew-symmetric matrix and $\widetilde{\boldsymbol{\theta}}$ is the pseudo-vector derived from $\widetilde{\boldsymbol{\Theta}}$ (Forest et al., 2001):

$$\forall \widetilde{\boldsymbol{n}}, \quad \widetilde{\boldsymbol{\Theta}} \cdot \widetilde{\boldsymbol{n}} = \widetilde{\boldsymbol{\theta}} \times \widetilde{\boldsymbol{n}}.$$

The skew-symmetric part of $\widetilde{\boldsymbol{U}}^{LK} \otimes \widetilde{\boldsymbol{\nabla}}$ is :

$$\widetilde{\boldsymbol{\Theta}}^{LK} = \widetilde{\boldsymbol{\Theta}}^{per} + (\widetilde{\boldsymbol{\chi}} \cdot \widetilde{\boldsymbol{y}}) \otimes \widetilde{\boldsymbol{e}}_3 - \widetilde{\boldsymbol{e}}_3 \otimes (\widetilde{\boldsymbol{\chi}} \cdot \widetilde{\boldsymbol{y}}) \tag{A.45}$$

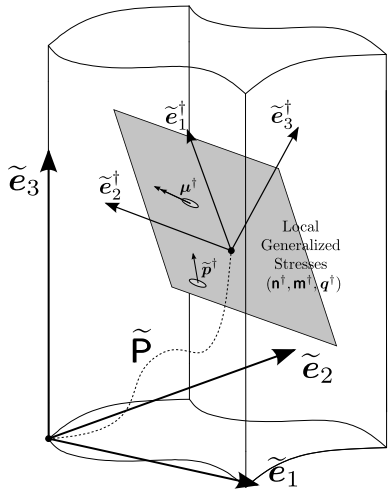

Figure A.2: Local orientation of a facet belonging to the unit-cell

and the corresponding rotation pseudo-vector is:

$$\widetilde{\boldsymbol{\theta}}^{LK} = \widetilde{\boldsymbol{\theta}}^{per} + (\widetilde{\boldsymbol{e}}_2 \otimes \widetilde{\boldsymbol{e}}_1 - \widetilde{\boldsymbol{e}}_1 \otimes \widetilde{\boldsymbol{e}}_2) \cdot (\widetilde{\boldsymbol{\chi}} \cdot \widetilde{\boldsymbol{y}}) \tag{A.46}$$

When two edges are matching with periodicity conditions, the difference between displacements is written in the main reference frame as:

$$\begin{cases} \Delta\widetilde{\boldsymbol{U}}^{LK} = \widetilde{\boldsymbol{e}} \cdot \Delta\widetilde{\boldsymbol{y}} + y_3\widetilde{\boldsymbol{\chi}} \cdot \Delta\widetilde{\boldsymbol{y}} - \left({}^t\left(\frac{\widetilde{\boldsymbol{y}}^+ + \widetilde{\boldsymbol{y}}^-}{2}\right) \cdot \widetilde{\boldsymbol{\chi}} \cdot \Delta\widetilde{\boldsymbol{y}} \right) \widetilde{\boldsymbol{e}}_3 \\ \Delta\widetilde{\boldsymbol{\theta}}^{LK} = (\widetilde{\boldsymbol{e}}_2 \otimes \widetilde{\boldsymbol{e}}_1 - \widetilde{\boldsymbol{e}}_1 \otimes \widetilde{\boldsymbol{e}}_2) \cdot (\widetilde{\boldsymbol{\chi}} \cdot \Delta\widetilde{\boldsymbol{y}}) \end{cases} \tag{A.47}$$

where $\widetilde{\boldsymbol{y}}^-$ and $\widetilde{\boldsymbol{y}}^+$ are the coordinates of the first and the second corresponding edges and $\Delta\widetilde{\boldsymbol{y}} = \widetilde{\boldsymbol{y}}^+ - \widetilde{\boldsymbol{y}}^-$.

The periodicity condition between two matching edges $+$ and $-$ are enforced as:

$$\begin{cases} \widetilde{\boldsymbol{U}}^+ = \widetilde{\boldsymbol{U}}^- + \Delta\widetilde{\boldsymbol{U}}^{LK} \\ \widetilde{\boldsymbol{\theta}}^+ = \widetilde{\boldsymbol{\theta}}^- + \Delta\widetilde{\boldsymbol{\theta}}^{LK} \end{cases} \tag{A.48}$$

These periodicity conditions generalize to any unit-cell configuration those suggested by Hohe (2003) and Pahr and Rammerstorfer (2006) which where restricted to rectangular unit-cell.

In the present case, the unit-cell is constituted of facets which have their own local orientation (†) with respect to the main reference frame. Thus $\widetilde{\boldsymbol{y}}^\dagger$ denote the coordinates in the local reference frame and $\widetilde{\boldsymbol{y}}^\dagger = \widetilde{\mathsf{P}} \cdot \widetilde{\boldsymbol{y}}$, where $\widetilde{\mathsf{P}}$ is an isometry of the 3D space (Figure A.2). For a facet, only rotations with respect to $\widetilde{\boldsymbol{e}}_1^\dagger$ and $\widetilde{\boldsymbol{e}}_2^\dagger$ are defined. Thus it is also necessary to restrict $\widetilde{\boldsymbol{\theta}}^{LK}$ to its in-plane part in the local reference frame. The actual rotation offset between matching edges implemented in

finite elements code in the main reference frame is finally:

$$\Delta\widetilde{\boldsymbol{\theta}}^{FE} = {}^{t}\widetilde{\mathbf{P}} \cdot \widetilde{\mathbf{p}} \cdot \widetilde{\mathbf{P}} \cdot \Delta\widetilde{\boldsymbol{\theta}}^{LK}$$

where $\widetilde{\mathbf{p}} = \begin{pmatrix} 1 & 0 & 0 \\ 0 & 1 & 0 \\ 0 & 0 & 0 \end{pmatrix}$ is the in-plane projection operator.

A.3.2 Localization of Love-Kirchhoff fields

Again, since we are dealing with facets, the local 3D stress $\widetilde{\boldsymbol{\sigma}}(\widetilde{\boldsymbol{y}})$ is replaced by plate generalized-stress fields $\mathbf{n}^{\dagger}(\widetilde{\boldsymbol{y}}), \mathbf{m}^{\dagger}(\widetilde{\boldsymbol{y}}), \boldsymbol{q}^{\dagger}(\widetilde{\boldsymbol{y}})$ which are written in the local reference frame. Thus, solving the Love-Kirchhoff auxiliary problem for each individual component of $\mathbf{e}$ and $\boldsymbol{\chi}$ leads to the localization of generalized-stress fields $n_{\alpha\beta\gamma\delta}$, $m_{\alpha\beta\gamma\delta}$ and $q_{\alpha\beta\gamma}$. The local generalized-stress field can be reconstructed by linear combination:

$$\begin{cases} \mathbf{n}^{\dagger LK} = \boldsymbol{n}^{(\mathsf{e})} : \mathbf{e} + \boldsymbol{n}^{(\chi)} : \boldsymbol{\chi} \\ \mathbf{m}^{\dagger LK} = \boldsymbol{m}^{(\mathsf{e})} : \mathbf{e} + \boldsymbol{m}^{(\chi)} : \boldsymbol{\chi} \\ \boldsymbol{q}^{\dagger LK} = \boldsymbol{q}^{(\mathsf{e})} : \mathbf{e} + \boldsymbol{q}^{(\chi)} : \boldsymbol{\chi} \end{cases} \tag{A.49}$$

We recall that $\mathbf{e}$ and $\boldsymbol{\chi}$ are considered in the main reference frame whereas the resulting generalized-stresses $\mathbf{n}^{\dagger LK}$, $\mathbf{m}^{\dagger LK}$ and $\boldsymbol{q}^{\dagger LK}$ are written in the local reference frame.

Using the inverted Love-Kirchhoff plate constitutive law, it is possible to write the generalized-stress field generated by imposed bending moment:

$$\begin{cases} \mathbf{n}^{\dagger(\mathsf{M})} = \boldsymbol{n}^{(\mathsf{M})} : \mathbf{M} = \left(\boldsymbol{n}^{(\mathsf{e})} : \boldsymbol{b} + \boldsymbol{n}^{(\chi)} : \boldsymbol{d}\right) : \mathbf{M} \\ \mathbf{m}^{\dagger(\mathsf{M})} = \boldsymbol{m}^{(\mathsf{M})} : \mathbf{M} = \left(\boldsymbol{m}^{(\mathsf{e})} : \boldsymbol{b} + \boldsymbol{m}^{(\chi)} : \boldsymbol{d}\right) : \mathbf{M} \\ \boldsymbol{q}^{\dagger(\mathsf{M})} = \boldsymbol{q}^{(\mathsf{M})} : \mathbf{M} = \left(\boldsymbol{q}^{(\mathsf{e})} : \boldsymbol{b} + \boldsymbol{q}^{(\chi)} : \boldsymbol{d}\right) : \mathbf{M} \end{cases} \tag{A.50}$$

A.3.3 Shear auxiliary problem loading

Finally, the volume force $\widetilde{\boldsymbol{f}}^{(\mathbb{R})}$ involved in the shear auxiliary problem $\mathcal{P}^{(\mathbb{R})}$ has to be turned into plate local loading $\widetilde{\boldsymbol{p}}^{\dagger(\mathbb{R})}$ and $\boldsymbol{\mu}^{\dagger(\mathbb{R})}$ in the facet's reference frame. Since it involves different reference frames and respective derivatives, we suggest the following step by step procedure:

The local stress field in the homogeneous plates which constitutes the unit-cell is written as (Appendix A.1):

$$\widetilde{\boldsymbol{\sigma}}^{\dagger(\mathsf{M})} = \frac{1}{t}\mathbf{n}^{\dagger(\mathsf{M})} + \frac{12y_3^{\dagger}}{t^3}\mathbf{m}^{\dagger(\mathsf{M})} + \frac{3}{2}\left(1 - \left(\frac{2y_3^{\dagger}}{t}\right)^2\right)\left(\boldsymbol{q}^{\dagger(\mathsf{M})} \otimes \widetilde{\boldsymbol{e}}_3^{\dagger} + \widetilde{\boldsymbol{e}}_3^{\dagger} \otimes \boldsymbol{q}^{\dagger(\mathsf{M})}\right) \tag{A.51}$$

where t is the facet's thickness.

Using transformation formula, the stress field is expressed in the main reference frame: $\widetilde{\boldsymbol{\sigma}}^{(\mathsf{M})} = \widetilde{\mathbf{P}} \cdot \widetilde{\boldsymbol{\sigma}}^{\dagger(\mathsf{M})} \cdot {}^{t}\widetilde{\mathbf{P}}$. Now it is possible to apply the procedure detailled in Section 6.1.3 for deriving $\widetilde{\boldsymbol{f}}^{(\mathsf{R})}$ in the main reference frame. The volume force in the local reference frame is then: $\widetilde{\boldsymbol{f}}^{\dagger(\mathsf{R})} = {}^{t}\widetilde{\mathbf{P}} \cdot \widetilde{\boldsymbol{f}}^{(\mathsf{R})}$. Then, we derive the plate loads $\widetilde{\boldsymbol{p}}^{\dagger(\mathsf{R})}$ and $\boldsymbol{\mu}^{\dagger(\mathsf{R})}$ from $\widetilde{\boldsymbol{f}}^{\dagger(\mathsf{R})}$ while integrating through the thickness as indicated for a homogeneous plate with a volume loading in Appendix A.1.

All these steps lead to the following definition of plate loads in the local reference frame generated by a uniform bending gradient in the unit-cell:

$$\begin{cases} p_i^{\dagger(\mathsf{R})} = \left(n_{ij\beta\alpha}^{(\mathsf{M})} + q_{i\beta\alpha}^{(\mathsf{M})} \delta_{j3} + q_{j\beta\alpha}^{(\mathsf{M})} \delta_{i3} \right) \mathsf{R}_{\alpha\beta\gamma} \mathsf{P}_{\gamma j} \\ \mu_\delta^{\dagger(\mathsf{R})} = m_{\delta\epsilon\beta\alpha}^{(\mathsf{M})} \mathsf{R}_{\alpha\beta\gamma} \mathsf{P}_{\gamma\epsilon} \end{cases} \tag{A.52}$$

Finite element softwares do not always implement the moment-per-unit-surface loading $\boldsymbol{\mu}$ with plate elements. However, it is always possible to load with concentrated $\widetilde{\boldsymbol{F}}$ force and moments $\widetilde{\boldsymbol{M}}$ at nodes. The preceding plate loads are then converted into concentrated loads in the main reference frame with:

$$\begin{cases} F_i^{(\mathsf{R})} = \mathsf{P}_{ik} \left(n_{kj\beta\alpha}^{(\mathsf{M})} + q_{k\beta\alpha}^{(\mathsf{M})} \delta_{j3} + q_{j\beta\alpha}^{(\mathsf{M})} \delta_{k3} \right) \mathsf{R}_{\alpha\beta\gamma} \mathsf{P}_{\gamma j} S^n \\ M_i^{(\mathsf{R})} = \mathsf{P}_{i\zeta} \left(\delta_{\zeta 2} \delta_{\delta 1} - \delta_{\zeta 1} \delta_{\delta 2} \right) m_{\delta\epsilon\beta\alpha}^{(\mathsf{M})} \mathsf{R}_{\alpha\beta\gamma} \mathsf{P}_{\gamma\epsilon} S^n \end{cases} \tag{A.53}$$

where $(\delta_{\zeta 2}\delta_{\delta 1} - \delta_{\zeta 1}\delta_{\delta 2})$ turns $\boldsymbol{\mu}$ into a moment pseudo-vector and S^n is the nodal area.

A.4 Contrast assumption in the case of a sandwich panel made of only one isotropic material

The contrast assumption for a sandwich panel made of the same isotropic material for the skins and the core is stated as (Equation 7.1):

$$\forall \mathbf{e}, \quad \mathbf{e} : t_c \rho \boldsymbol{\mathcal{C}}^m : \mathbf{e} \ll 2t_s \, \mathbf{e} : \boldsymbol{c}^m : \mathbf{e} \tag{A.54}$$

where ρ is the volume fraction of material in the core, $\boldsymbol{\mathcal{C}}^m$ is the plane-strain stiffness and $\boldsymbol{c}^m$ is the plane-stress stiffness.

Both tensors are *a priori* not simultaneously diagonalizable. Thus we suggest to compare the largest eigenvalue of $t_c \rho \boldsymbol{\mathcal{C}}^m$ to the smallest eigenvalue of $2t_s \boldsymbol{c}^m$. This will yield a sufficient condition for fullfilling the contrast assumption.

With Voigt notations we have:

$$[\boldsymbol{\mathcal{C}}]^m = \frac{E^m}{(1+\nu^m)(1-2\nu^m)} \begin{pmatrix} 1-\nu^m & \nu^m & 0 \\ \nu^m & 1-\nu^m & 0 \\ 0 & 0 & 1-2\nu^m \end{pmatrix}$$

and

$$[\boldsymbol{c}]^m = \frac{E^m}{(1+\nu^m)(1-\nu^m)} \begin{pmatrix} 1 & \nu^m & 0 \\ \nu^m & 1 & 0 \\ 0 & 0 & 1-\nu^m \end{pmatrix}$$

$[\boldsymbol{\mathcal{C}}]^m$ eigenvalues are $\frac{E^m}{(1+\nu^m)(1-2\nu^m)}$ and $\frac{E^m}{1+\nu^m}$; $[\boldsymbol{c}]^m$ eigenvalues are $\frac{E^m}{1+\nu^m}$ and $\frac{E^m}{1-\nu^m}$. Thus the constrast assumption is rewritten, depending on Poisson's ratio, as:

$$\begin{cases} \rho \frac{t_c}{2t_s} \ll \frac{(1+\nu^m)(1-2\nu^m)}{1-\nu^m} & \text{if} \quad \nu^m > 0 \\ \rho \frac{t_c}{2t_s} \ll 1 & \text{if} \quad \nu^m \leq 0 \end{cases}$$

When $\nu^m = 0.5$ the constrast assumption becomes ill-defined. However, in practical cases, $\nu^m \approx 0.3$ and the condition is equivalent to $\rho \frac{t_c}{2t_s} \ll 1$.

Bibliography

ABAQUS, 2007a. ABAQUS theory manual, version 6.7. ABAQUS.

ABAQUS, 2007b. ABAQUS/Standard user's manual, version 6.7.

Adhikary, D. P., Dyskin, A. V., 1997. A cosserat continuum model for layered materials. Computers And Geotechnics 20 (1), 15–45.

Akishev, N., Zakirov, I., Nikitin, A., Patent no. WO 2005/056209 A1, 06 2005a. Device for sheet material corrugation.

Akishev, N., Zakirov, I., Nikitin, A., Patent no. WO 2005/056208 A1, 06 2005b. Device for sheet material corrugation.

Akishev, N., Zakirov, I. A., Patent no. WO 2005/058521, 06 2005a. Foldable mandrel for production of a single curvature folded core for a sandwich panel.

Akishev, N., Zakirov, I. A., Patent no. WO 2005/049307 A1, 06 2005b. Method for curvilinear structure production.

Akishev, N., Zakirov, I. A., Patent no. WO 2005/049247 A1, 06 2005c. Method for production of sandwich panels with zigzag corrugated core.

Akishev, N., Zakirov, I. A., Patent no. WO 2005/058593 A1, 06 2005d. Sandwich panel.

Akishev, N., Zakirov, I. A., Patent no. WO 2005/056285 A1, 06 2005e. Sandwich panel core.

Allen, H., 1969. Analysis and design of structural sandwich panels. Pergamon Press.

Ambartsumian, S., 1969. Theory of anisotropic plates. Ashton Technomic Publishing Co, translated from Russian by T. Cheron.

Amini, A. M., Dureisseix, D., Cartraud, P., 2009. Multi-scale domain decomposition method for large-scale structural analysis with a zooming technique: Application to plate assembly. International Journal for Numerical Methods in Engineering 79 (4), 417–443.

Ashby, M. F., 2000. Multi-objective optimization in material design and selection. Acta Materialia 48 (1), 359 – 369.

Auffray, N., Bouchet, R., Bréchet, Y., 2009. Derivation of anisotropic matrix for bi-dimensional strain-gradient elasticity behavior. International Journal of Solids and Structures 46 (2), 440 – 454.

Baranger, E., Guidault, P.-A., Cluzel, C., Fischer, S., 2010. Generation of physical defects for the prediction of the behaviour of folded cores. In: European Conference on Computational Mechanics Palais des Congrès, Paris, France, May 16-21, 2010.

Basily, B., Elsayed, A., 2004a. A continuous folding process for sheet materials. International Journal of Materials and Product Technology 21, 217–238.

Basily, B., Elsayed, A., Patent no. US 2007004576, 01 2007. Technology for continuous folding of sheet materials into a honeycomb-like configuration.

Basily, B., Elsayed, A., Kling, D. H., Patent no. US 7, 115, 089 B2, 10 2006. Technology for continuous folding of sheet materials.

Basily, B., Elsayed, E., 2004b. Dynamic axial crushing of multi-layer core structures of folded chevron patterns. International Journal of Materials and Product Technology 21, 169–185.

Berdichevsky, V. L., Mar. 2010. An asymptotic theory of sandwich plates. International Journal of Engineering Science 48 (3), 383–404.

Bigoni, D., Drugan, W. J., Jul. 2007. Analytical derivation of cosserat moduli via homogenization of heterogeneous elastic materials. Journal Of Applied Mechanics-Transactions Of The Asme 74 (4), 741–753.

Boussinesq, J., 1871. étude nouvelle sur l'équilibre et le mouvement des corps solides élastiques dont certaines dimensions sont très petites par rapport à d'autres. Journal de Mathématiques 16, 125–274.

Boutin, C., Mar. 1996. Microstructural effects in elastic composites. International Journal Of Solids And Structures 33 (7), 1023–1051.

Buannic, N., Cartraud, P., Oct. 2001a. Higher-order effective modeling of periodic heterogeneous beams. i. asymptotic expansion method. International Journal of Solids and Structures 38 (40-41), 7139–7161.

Buannic, N., Cartraud, P., Oct. 2001b. Higher-order effective modeling of periodic heterogeneous beams. ii. derivation of the proper boundary conditions for the interior asymptotic solution. International Journal of Solids and Structures 38 (40-41), 7163–7180.

Buannic, N., Cartraud, P., Quesnel, T., 2003. Homogenization of corrugated core sandwich panels. Composite Structures 59 (3), 299–312.

Caillerie, D., 1984. Thin elastic and periodic plates. Mathematical Methods in the Applied Sciences 6 (2), 159 – 191.

Caron, J. F., Diaz, A. D., Carreira, R. P., Chabot, A., Ehrlacher, A., May 2006. Multi-particle modelling for the prediction of delamination in multi-layered materials. Composites Science And Technology 66 (6), 755–765.

Caron, J.-F., Sab, K., Aug. 2001. Un nouveau modèle de plaque multicouche épaisse. a new model for thick laminates. Comptes Rendus de l'Académie des Sciences - Series IIB - Mechanics 329 (8), 595–600.

Carrera, E., 2002. Theories and finite elements for multilayered, anisotropic, composite plates and shells. Archives Of Computational Methods In Engineering 9 (2), 87–140.

Carrera, E., May 2003a. Historical review of zig-zag theories for multilayered plates and shells. Appl. Mech. Rev. 56 (3), 287–308.

Carrera, E., Sep. 2003b. Theories and finite elements for multilayered plates and shells: A unified compact formulation with numerical assessment and benchmarking. Archives of Computational Methods in Engineering 10 (3), 215–296.

Cecchi, A., Sab, K., 2002. Out of plane model for heterogeneous periodic materials: the case of masonry. European Journal of Mechanics - A/Solids 21 (5), 715–746.

Cecchi, A., Sab, K., May 2004. A comparison between a 3d discrete model and two homogenised plate models for periodic elastic brickwork. International Journal of Solids and Structures 41 (9-10), 2259–2276.

Cecchi, A., Sab, K., Sep. 2007. A homogenized reissner-mindlin model for orthotropic periodic plates: Application to brickwork panels. International Journal of Solids and Structures 44 (18-19), 6055–6079.

Cerda, E., Mahadevan, L., Mar. 2005. Confined developable elastic surfaces: cylinders, cones and the elastica. Proceedings of the Royal Society A: Mathematical, Physical and Engineering Sciences 461 (2055), 671–700.

Chen, A., Davalos, J. F., 2005. A solution including skin effect for stiffness and stress field of sandwich honeycomb core. International Journal of Solids and Structures 42 (9-10), 2711 – 2739.

Ciarlet, P. G., Destuynder, P., 1979. Justification of the 2-dimensional linear plate model. Journal De Mecanique 18 (2), 315–344.

Corus, 2010. Trisomet 333 System. Corus, http://www.corusconstruction.com/.

Cote, F., Biagi, R., Bart-Smith, H., Deshpande, V. S., May 2007. Structural response of pyramidal core sandwich columns. International Journal of Solids and Structures 44 (10), 3533–3556.

Dallot, J., Sab, K., 2008. Limit analysis of multi-layered plates. part ii: Shear effects. Journal Of The Mechanics And Physics Of Solids 56 (2), 581–612.

de Buhan, P., Sudret, B., Jul. 2000. Micropolar multiphase model for materials reinforced by linear inclusions. European Journal Of Mechanics A-Solids 19 (4), 669–687.

Demaine, E., Demaine, M., 03 2001. Recent results in computational origami. In: Proceedings of the 3rd International Meeting of Origami Science, Math, and Education (OSME 2001).

Diaz Diaz, A., Caron, J.-F., Carreira, R. P., Dec. 2001. Model for laminates. Comptes Rendus de l'Académie des Sciences - Series IIB - Mechanics 329 (12), 873–879.

Diaz Diaz, A., Caron, J. F., Ehrlacher, A., May 2007. Analytical determination of the modes i, ii and iii energy release rates in a delaminated laminate and validation of a delamination criterion. Composite Structures 78 (3), 424–432.

Doherty, K. J., Yiournas, A., Wagner, J. A., Murty, Y., 2009. Structural performance of aluminum and stainless steel pyramidal truss core sandwich panels. Tech. rep., Army Research Laboratory.

Duncan, J. P., Duncan, J. L., Sep. 1982. Folded developables. Proceedings of the Royal Society of London. Series A, Mathematical and Physical Sciences 383 (1784), 191–205.

El-Sawi, A., Wifi, A., Younan, M., Elsayed, E., Basily, B., Jun. 2010. Application of folded sheet metal in flat bed solar air collectors. Applied Thermal Engineering 30 (8-9), 864–871.

Fischer, S., Drechsler, K., Kilchert, S., Johnson, A., Dec. 2009. Mechanical tests for foldcore base material properties. Composites Part A: Applied Science and Manufacturing 40 (12), 1941–1952.

Florence, C., Sab, K., 2006. A rigorous homogenization method for the determination of the overall ultimate strength of periodic discrete media and an application to general hexagonal lattices of beams. European Journal of Mechanics - A/Solids 25 (1), 72 – 97.

Forest, S., Pradel, F., Sab, K., Jun. 2001. Asymptotic analysis of heterogeneous cosserat media. International Journal of Solids and Structures 38 (26-27), 4585–4608.

Forest, S., Sab, K., Jul. 1998. Cosserat overall modeling of heterogeneous materials. Mechanics Research Communications 25 (4), 449–454.

Gewiss, L. V., Patent no. FR 1197941, 12 1960. Dispositifs pour le façonnage mécanique en continu de structures chevronnées développables.

Gewiss, L. V., Patent no. FR 1532509, 06 1968. Procédé et machines pour le façonnage de structures chevronnées et de structures dérivant des structures chevronnées.

Gewiss, L. V., Patent no. US 3,461, 013, 04 1969a. Method and apparatus for sandwiching corrugated core between skin layers.

Gewiss, L. V., Patent no. US 3,433, 692, 03 1969b. Method for forming herringbone configurations for sandwich structures.

Gewiss, L. V., Patent no. US 3992162, 11 1976. Dispositifs pour le façonnage mécanique en continu de structures chevronnées développables.

Gewiss, L. V., Patent no. US 4,012, 932, 03 1977. Machine for manufacturing herringbone-pleated structures.

Gibson, L. J., Ashby, M. F., 1988. Cellular solids. Pergamon Press.

Glenn, J. H., 2000. Nasa image of glass reinforced aluminum (glare) honeycomb composite sandwich structure. web, 25 January 2007.

Grediac, M., 1993. A finite-element study of the transverse-shear in honeycomb-cores. International Journal Of Solids And Structures 30 (13), 1777–1788.

Hadj-Ahmed, R., Foret, G., Ehrlacher, A., Aug. 2001. Stress analysis in adhesive joints with a multiparticle model of multilayered materials (m4). International Journal Of Adhesion And Adhesives 21 (4), 297–307.

Heimbs, S., 2009. Virtual testing of sandwich core structures using dynamic finite element simulations. Computational Materials Science 45 (2), 205–216.

Heimbs, S., Cichosz, J., Klaus, M., Kilchert, S., Johnson, A., May 2010. Sandwich structures with textile-reinforced composite foldcores under impact loads. Composite Structures 92 (6), 1485–1497.

Heimbs, S., Mehrens, T., Middendorf, P., Maier, A., Schumacher, M., 2006. Numerical determination of the nonlinear effective mechanical properties of folded core structures for aircraft sandwich panels. 6^{th} European LS DYNA User's Conference.

Heimbs, S., Middendorf, P., Kilchert, S., Johnson, A., Maier, M., Nov. 2007. Experimental and numerical analysis of composite folded sandwich core structures under compression. Applied Composite Materials 14 (5), 363–377.

Herrmann, A., Zahlen, P., Zuardy, I., 2005. Sandwich Structures 7: Advancing with Sandwich Structures and Materials. Springer Netherlands, Ch. Sandwich Structures Technology in Commercial Aviation, pp. 13–26.

Hochfeld, H., Patent no. US2901951, 09 1959. Process and machine for pleating pliable materials.

Hohe, J., Oct. 2003. A direct homogenisation approach for determination of the stiffness matrix for microheterogeneous plates with application to sandwich panels. Composites Part B: Engineering 34 (7), 615–626.

Hohe, J., Becker, W., May 2001. A refined analysis of the effective elasticity tensor for general cellular sandwich cores. International Journal of Solids and Structures 38 (21), 3689–3717.

Hohe, J., Becker, W., 2002. Effective stress-strain relations for two-dimensional cellular sandwich cores: Homogenization, material models, and properties. Applied Mechanics Reviews 55 (1), 61–87.

Isaksson, P., Krusper, A., Gradin, P., Sep. 2007. Shear correction factors for corrugated core structures. Composite Structures 80 (1), 123–130.

Kawasaki, T., 1989. On the relation between mountain-creases and valley-creases of a flat origami. In: Proceedings of the 1st International Meeting of Origami Science and Technology. pp. 229–237.

Kayumov, R., Zakirov, I., Alekseev, K., Alekseev, K., Zinnurov, R., Dec. 2007. Determination of load-carrying capacity in panels with chevron-type cores. Russian Aeronautics (Iz VUZ) 50 (4), 357–361.

Kehrle, R., Patent no. WO 2004/043685, 05 2004. Method for the production of a sandwich structure for a sandwich composite.

Kehrle, R., Patent no. DE 10 2007 050 356 A1, 04 2009. Core layer for a sandwich structure, comprises a structure folded out of semi-finished product, which has a layer out of tearproof flat material and a layer out of stiff flat material.

Kehrle, R., Patent no. WO 2010/022311 A1, 02 2010. Folded core having a high compression modulus and articles made from the same.

Kelsey, S., Gellatly, R., Clark, B., 1958. The shear modulus of foil honeycomb cores: A theoretical and experimental investigation on cores used in sandwich construction. Aircraft Engineering and Aerospace Technology 30 (10), 294 – 302.

Khaliulin, V., 2005. A technique for synthesizing the structures of folded cores of sandwich panels. Russian Aeronautics 48 (1), 8 – 16.

Khaliulin, V., Batrakov, V., 2005. Technological schemes of zigzag crimp shaping. Russian Aeronautics 48 (2), 106 – 114.

Khaliulin, V., Batrakov, V., 2006. A technique for calculating the z-crimp springing at its shaping from aramide papers. Russian Aeronautics 49 (4), 106 – 115, sandwich panels;Aramide paper;Springing;.

Khaliulin, V., Razdaibedin, A., Menyashkin, D., 2005. Evaluation of influence of processing parameter instability on the accuracy of folded cores. Russian Aeronautics 48 (3), 94 – 101.

Khaliulin, V. I., 1999. Construction of-nodal zone deformation model during forming fold-shaped structures. Izvestiya Vysshikh Uchebnykh Zavedenii Aviatsionaya Tekhnika (4), 61–65.

Kintscher, M., Karger, L., Wetzel, A., Hartung, D., May 2007. Stiffness and failure behaviour of folded sandwich cores under combined transverse shear and compression. Composites Part A: Applied Science and Manufacturing 38 (5), 1288–1295.

Kling, D., oct 1997. Doubly periodic flat surfaces in three-space. Ph.D. thesis, Rutgers Univ.

Kling, D. H., Patent no. US 6,935, 997 B2, 08 2005. Paterning technology for folded sheet structures.

Kling, D. H., Patent no. US2007/0023987, 02 2007. Folding methods, structures and apparatuses.

Kohn, R. V., Vogelius, M., 1984. A new model for thin plates with rapidly varying thickness. International Journal of Solids and Structures 20 (4), 333–350.

Kouznetsova, V., Geers, M. G. D., Brekelmans, W. A. M., Jul. 2002. Multi-scale constitutive modelling of heterogeneous materials with a gradient-enhanced computational homogenization scheme. International Journal For Numerical Methods In Engineering 54 (8), 1235–1260.

Lachihab, A., Sab, K., Jun. 2005. Aggregate composites: a contact based modeling. Computational Materials Science 33 (4), 467–490.

Laroussi, M., Sab, K., Alaoui, A., 2002. Foam mechanics: nonlinear response of an elastic 3d-periodic microstructure. International Journal of Solids and Structures 39 (13-14), 3599 – 3623.

Laszczyk, L. Dendievel, R. B. Y. B. O., 2010. Shape optimization of the periodic architecture of lightweight flexural panels. In: Actes des Journées Annuelles de la Société Française de Métallurgie et de Matériaux.

Lebée, A., Sab, K., 2010a. A bending gradient model for thick plates, part ii: Closed-form solutions for cylindrical bending. *submitted*.

Lebée, A., Sab, K., Apr. 2010b. A cosserat multiparticle model for periodically layered materials. Mechanics Research Communications 37 (3), 293–297.

Lebée, A., Sab, K., 2010c. Reissner-mindlin shear moduli of a sandwich panel with periodic core material. In: Mechanics of Generalized Continua. Vol. 21 of Advances in Mechanics and Mathematics. Springer New York, pp. 169–177.

Lebée, A., Sab, K., Sep. 2010d. Transverse shear stiffness of a chevron folded core used in sandwich construction. International Journal of Solids and Structures 47 (18-19), 2620–2629.

Leguillon, D., 1999. A method based on singularity theory to predict edge delamination of laminates. International Journal Of Fracture 100 (1), 105–120.

Lewinski, T., 1991a. Effective models of composite periodic plates .1. asymptotic solution. International Journal Of Solids And Structures 27 (9), 1155–1172.

Lewinski, T., 1991b. Effective models of composite periodic plates .2. simplifications due to symmetries. International Journal Of Solids And Structures 27 (9), 1173–1184.

Lewinski, T., 1991c. Effective models of composite periodic plates .3. 2-dimensional approaches. International Journal Of Solids And Structures 27 (9), 1185–1203.

Lognon, 2010. Pleated dress from atelier gérard lognon (france). http://lesateliersgerardlognon.com/.

Love, A. E. H., 1888. The small free vibrations and deformation of a thin elastic shell. Philosophical Transactions of the Royal Society of London. (A.) 179, 491–546.

Miara, B., Podio-Guidugli, P., Nov. 2006. Une approche formelle unifiée des théories de plaques et poutres linéairement élastiques. Comptes Rendus Mathematique 343 (10), 675–678.

Mindlin, R., Mar. 1951. Influence of rotatory inertia and shear on flexural motions of isotropic, elastic plates. Journal of Applied Mechanics 18, 31–38.

Miura, K., 1972. Zeta-core sandwich - its concept and realization. ISAS report 37 (6), 137–164.

Miura, K., 1980. Design of zeta-stiffened panels. ISAS report.

Miura, K., 1994. Map fold a la miura style, its physical characteristics and application to the space science. In: Research of Pattern Formation, ktk scientific publishers Edition. R. Takaki, pp. 77–90.

Mohr, D., Doyoyo, M., Jun. 2004. Deformation-induced folding systems in thin-walled monolithic hexagonal metallic honeycomb. International Journal of Solids and Structures 41 (11-12), 3353–3377.

Movchan, G., Dec. 2007. Analysis of folded structures for impact resistance. Russian Aeronautics (Iz VUZ) 50 (4), 439–441.

Murakami, H., Sep. 1986. Laminated composite plate-theory with improved inplane responses. Journal Of Applied Mechanics-Transactions Of The Asme 53 (3), 661–666.

Naciri, T., Ehrlacher, A., Chabot, A., Mar. 1998. Interlaminar stress analysis with a new multiparticle modelization of multilayered materials (m4). Composites Science and Technology 58 (3-4), 337–343.

Nguyen, M., Jacombs, S., Thomson, R., Hachenberg, D., Scott, M., Feb. 2005a. Simulation of impact on sandwich structures. Composite Structures 67 (2), 217–227.

Nguyen, T. K., Sab, K., Bonnet, G., 2007. Shear correction factors for functionally graded plates. Mechanics of Advanced Materials and Structures 14 (8), 567–575.

Nguyen, T.-K., Sab, K., Bonnet, G., Mar. 2008a. First-order shear deformation plate models for functionally graded materials. Composite Structures 83 (1), 25–36.

Nguyen, T.-K., Sab, K., Bonnet, G., Dec. 2008b. Green's operator for a periodic medium with traction-free boundary conditions and computation of the effective properties of thin plates. International Journal of Solids and Structures 45 (25-26), 6518–6534.

Nguyen, V.-T., Caron, J.-F., Sab, K., 2005b. A model for thick laminates and sandwich plates. Composites Science and Technology 65 (3-4), 475 – 489.

Noor, A. K., Malik, M., Feb. 2000. An assessment of five modeling approaches for thermomechanical stress analysis of laminated composite panels. Computational Mechanics 25 (1), 43–58.

Nosier, A., Yavari, A., Sarkani, S., Sep. 2001. A study of the edge-zone equation of mindlin-reissner plate theory in bending of laminated rectangular plates. Acta Mechanica 146 (3), 227–238.

Pagano, N., 1969. Exact solutions for composite laminates in cylindrical bending. Journal of Composite Materials 3 (3), 398–411.

Pagano, N., 1970a. Exact solutions for rectangular bidirectional composites and sandwich plates. Journal of Composite Materials 4 (1), 20–34.

Pagano, N., 1970b. Influence of shear coupling in cylindrical. bending of anisotropic laminates. Journal of Composite Materials 4 (3), 330–343.

Pagano, N., 1989. Interlaminar response of composite materials. Vol. 5 of Composite Materials Series. Elsevier Science Publishers.

Pagano, N. J., 1978. Stress fields in composite laminates. International Journal Of Solids And Structures 14 (5), 385–400.

Pahr, D. H., Rammerstorfer, F. G., Apr. 2006. Buckling of honeycomb sandwiches: Periodic finite element considerations. Cmes-Computer Modeling In Engineering & Sciences 12 (3), 229–241.

Petras, A., Sutcliffe, M. P. F., Apr. 1999. Failure mode maps for honeycomb sandwich panels. Composite Structures 44 (4), 237–252.

Pradel, F., Sab, K., 1998. Homogenization of discrete media. Journal De Physique. IV : JP 8 (8), 317 – 324.

Rammerstorfer, F. G., Pahr, D. H., Daxner, T., Vonach, W. K., May 2006. Buckling in thin walled micro and meso structures of lightweight materials and material compounds. Computational Mechanics 37 (6), 470–478.

Rapp, E., Patent no. US19580729815, 06 1960. Sandwich-type structural element.

Reddy, J. N., 1984. A simple higher-order theory for laminated composite plates. Journal Of Applied Mechanics-Transactions Of The Asme 51 (4), 745–752.

Reddy, J. N., Sep. 1989. On refined computational models of composite laminates. International Journal For Numerical Methods In Engineering 27 (2), 361–382.

Reissner, E., 1945. The effect of transverse shear deformation on the bending of elastic plates. Journal of Applied Mechanics 12, 68–77.

Reissner, E., 1985. Reflections on the theory of elastic plates. Applied Mechanics Reviews 38 (11), 1453 – 1464.

Reissner, E., Stavsky, Y., 1961. Bending and stretching of certain types of heterogeneous aeolotropic elastic plates. Journal of Applied Mechanics 28, 402–408.

Sab, K., May 1996. Microscopic and macroscopic strains in a dense collection of rigid particles. Comptes Rendus de l'Academie Des Sciences Serie II Fascicule B-Mecanique Physique Chimie Astronomie 322 (10), 715–721.

Shi, G., Tong, P., 1995. Equivalent transverse shear stiffness of honeycomb cores. International Journal of Solids and Structures 32 (10), 1383 – 1393.

Sid, 2009. Detail from a pleating mold. Blog "de Brique et de Brock" http://debriqueetdebrock.blogspot.com/2009/02/laiguille-en-fete-1ere-partie_19.html.

Tachi, T., 2009. Generalization of rigid-foldable quadrilateral-mesh origami. In: Journal of the International Association for Shell and Spatial Structures. Vol. 50. Int. Association for Shell and Spatial Structures, Alfonso XII, 3, Madrid, 28014, Spain, pp. 173–179.

Thompson, D. W., 1917. On Growth and Form.

Touratier, M., 1991. An efficient standard plate-theory. International Journal Of Engineering Science 29 (8), 901–916.

Vannucci, P., Verchery, G., Dec. 2001. Stiffness design of laminates using the polar method. International Journal Of Solids And Structures 38 (50-51), 9281–9294.

Vannucci, P., Verchery, G., Oct. 2002. A new method for generating fully isotropic laminates. Composite Structures 58 (1), 75–82.

Vidal, P., Polit, O., Jun. 2008. A family of sinus finite elements for the analysis of rectangular laminated beams. Composite Structures 84 (1), 56–72.

Vlasov, V. Z., 1961. Thin-walled elastic beams. National Science Foundation and Department of Commerce.

Wadley, H., 2002. Cellular metals manufacturing. Advanced Engineering Materials 4 (10), 726–733.

Whitney, J., 1969a. Cylindrical bending of unsymmetrically laminated plates. Journal of Composite Materials 3, 715–719.

Whitney, J., 1969b. The effect of transverse shear deformation on bending of laminated plate. Journal of Composite Materials 3, 534–547.

Whitney, J., 1972. Stress analysis of thick laminated composite and sandwich plates. Journal of Composite Materials 6 (4), 426–440.

Whitney, J. M., Leissa, A. W., june 1969. Analysis of heterogeneous anisotropic plates. Journal of applied mechanics, 261–266.

Wicks, N., Hutchinson, J. W., Jul. 2001. Optimal truss plates. International Journal of Solids and Structures 38 (30-31), 5165–5183.

Wierzbicki, T., 1983. Crushing analysis of metal honeycombs. International Journal of Impact Engineering 1 (2), 157 – 174.

Xu, X. F., Qiao, P., 2002. Homogenized elastic properties of honeycomb sandwich with skin effect. International Journal of Solids and Structures 39 (8), 2153 – 2188.

Xu, X. F., Qiao, P., Davalos, J. F., 2001. Transverse shear stiffness of composite honeycomb core with general configuration. Journal of Engineering Mechanics 127 (11), 1144–1151.

Yu, W., Hodges, D. H., Volovoi, V. V., Oct. 2002a. Asymptotic construction of reissner-like composite plate theory with accurate strain recovery. International Journal of Solids and Structures 39 (20), 5185–5203.

Yu, W., Hodges, D. H., Volovoi, V. V., Oct. 2002b. Asymptotic generalization of reissner-mindlin theory: accurate three-dimensional recovery for composite shells. Computer Methods in Applied Mechanics and Engineering 191 (44), 5087–5109.

Yuan, X., Tomita, Y., Andou, T., Jan. 2008. A micromechanical approach of nonlocal modeling for media with periodic microstructures. Mechanics Research Communications 35 (1-2), 126–133.

Zakirov, I., Alekseev, K., Movchan, G., 2008. Influence of coating thickness on geometric parameters of a chevron core. Russian Aeronautics 51 (3), 326 – 329.

Zakirov, I., Alekseyev, K., 2005. Determination of four-beam spiral folded structure parameters. Russian Aeronautics 48 (4), 91 – 99, spiral folded structure;Folded core;.

Zakirov, I., Alekseyev, K., Mudra, C., 2006. A technique for designing highly-stiffened chevron folded cores. Russian Aeronautics 49 (4), 1 – 7, folded cores;Internal structure;Stiffening;.

Zhang, J., Kundu, J., Manglik, R. M., Apr. 2004. Effect of fin waviness and spacing on the lateral vortex structure and laminar heat transfer in wavy-plate-fin cores. International Journal of Heat and Mass Transfer 47 (8-9), 1719–1730.

Homogénéisation de plaques périodiques épaisses, application aux panneaux sandwichs à âme pliable en chevrons

Les panneaux sandwichs sont des éléments de structure omniprésents au quotidien. Leur efficacité structurelle n'est plus à démontrer. Elle est même un élément déterminant dans le marché qui leur est associé. Ce mémoire de doctorat s'intéresse à un nouveau type d'âme de panneau sandwich qui pourrait être amené à supplanter le nid d'abeilles dans certaines applications, le module à chevrons. L'objectif est donc de pouvoir faire une estimation précise du comportement de ces nouvelles âmes. Cependant le gain en efficacité structurelle des panneaux sandwichs se paye par une augmentation considérable de la complexité de leur comportement mécanique. C'est en particulier le cas de la raideur à l'effort tranchant qui est déterminante pour estimer l'efficacité d'une âme de panneau sandwich. Ainsi, ce travail nous a amené à reconsidérer en profondeur les méthodes pour calculer le comportement à l'effort tranchant des plaques en général. Il nous a conduit à proposer une nouvelle théorie des plaques ainsi qu'une méthode d'homogénéisation associée dans le cas périodique. Cette théorie peut être considérée comme l'extension de la théorie bien connue de Reissner-Mindlin au cas des plaques hétérogènes. Elle ne peut cependant pas être réduite au modèle de Reissner-Mindlin dans le cas général. Dans le cas particulier des panneaux sandwichs incluant le module à chevrons, l'application de cette méthode d'homogénéisation permet de mettre en évidence un phénomène de distorsion des peaux qui affecte de façon notable la raideur à l'effort tranchant de ces panneaux.

Mots-clés Théorie des plaques, Homogénéisation, Panneaux sandwichs, Âmes pliées, Plaques stratifiées,

Thick periodic plates homogenization, application to sandwich panels including chevron folded core

Sandwich panels are widespread in everyday life. Their structural efficiency is well-known and is a central criterion in possible applications. This Ph.D. thesis is dedicated to the study of a new sandwich panel core which might replace honeycomb in some applications: the chevron pattern. In order to compare this new core to other ones, an accurate knowledge of its mechanical behavior is necessary. However, the price for structural efficiency is a more complex mechanical behavior. This is the case for the shear forces stiffness which is critical when comparing sandwich panels cores. Thus, in this work we reconsider in details and in the general case how to derive plates behavior under shear forces. A new plate theory is suggested as well as the related homogenization scheme for periodic plates. This plate theory is the extension of the well-known Reissner-Mindlin plate theory in the case of heterogeneous plates. However, it cannot be reduced to a Reissner-Mindlin plate theory in the general case. In the special case of sandwich panels including the chevron pattern, applying the homogenization scheme brings out a skins distorsion phenomenon which affects a lot their shear forces stiffness.

Keywords Plate theory, Homogenization, Sandwich panels Folded cores, Laminated plates